Dissertation

submitted to the

Combined Faculty of Mathematics, Engineering and Natural Sciences

of Heidelberg University, Germany

for the degree of

Doctor of Natural Sciences

Put forward by

Vikas Shridhar Bothe

born in: Shrirampur

Oral examination: 24.10.2024

Application of Artificial Neural Networks in GERDA
for the search of
neutrinoless double β-decay of ^{76}Ge

Referees :

Prof. Dr. James Hinton
Priv. Doz. Dr. Teresa Marrodán Undagoitia

Anwendung künstlicher neuronaler Netze in GERDA für die Suche nach neutrinoloser doppelter β-Zerfall von ^{76}Ge

Das GERmanium Detector Array (GERDA)-Experiment, das sich unterirdisch in den Laboratori Nazionali del Gran Sasso (LNGS) in Italien befindet, ist der Suche nach dem neutrinolosen doppelten Betazerfall (0νββ) in ^{76}Ge gewidmet. Ein solcher Fund würde den Nachweis erbringen, dass Neutrinos Majorana-Teilchen sind, und das Standardmodell der Teilchenphysik durch Verletzung der Leptonenzahlerhaltung infrage stellen. Diese Dissertation stellt die Entwicklung und Anwendung robuster, auf künstlichen neuronalen Netzen (ANN) basierender Klassifikationsmodelle zur Pulssignal-Diskriminierung (PSD) im GERDA-Experiment vor, die speziell für HPGe detektoren mit semi-koaxialer Geometrie entwickelt wurde. Das Ziel ist es, die experimentelle Empfindlichkeit für 0νββ-Ereignisse zu verbessern, indem der Untergrund in GERDA unterdrückt wird. Die semi-koaxialen Detektoren machen etwa 49% der gesamten 127,2 kg·Jahre-Exposition in GERDA aus. Für jeden der semi-koaxialen Detektoren wurden 1D-CNN-basierte Modelle für Klassifikationsaufgaben trainiert, um zwischen Oberflächen- und gammastrahlungsinduzierten Untergründen zu unterscheiden, wodurch der Untergrundindex bei Qββ um etwa 65% reduziert werden konnte. Dies führte zu einem Untergrundindex von 8.3×10^{-3}cts/(keV·kg·Jahr) in Phase I und 0.59×10^{-3}cts/(keV·kg·Jahr) in Phase II. Es wurde kein Signal beobachtet, und die Halbwertszeit des 0νββ-Zerfalls von ^{76}Ge wurde mit einer Grenze von $T^{0\upsilon}_{1/2} > 1.8 \times 10^{26}\, yr$ Jahren bei einem Konfidenzniveau von 90% festgelegt Und die Empfindlichkeit fällt mit der Grenze zusammen.

Application of Artificial Neural Networks in GERDA for the search of neutrinoless double β-decay of ^{76}Ge

The GERmanium Detector Array (GERDA) experiment, located underground at the Laboratori Nazionali del Gran Sasso (LNGS) in Italy, is dedicated to the search for neutrinoless double beta decay (0νββ) in ^{76}Ge. Such a discovery would provide evidence that neutrinos are Majorana particles and challenge the Standard Model of particle physics by violating lepton number conservation. This thesis presents the development and application of robust artificial neural network (ANN)-based classification models for pulse shape discrimination (PSD) within the GERDA experiment, specifically tailored for the high-purity germanium (HPGe) detectors of semi-coaxial geometry. The goal is to improve the experimental sensitivity to 0νββ events by suppressing the background in GERDA. The semi-coaxial detectors represent ~49% of total 127.2 kg.yr exposure in GERDA. For each of the semi-coaxial detectors, 1-d CNN-based models were trained for classification tasks to discriminate the surface and gamma-induced backgrounds, which suppress the background index at $Q_{\beta\beta}$ by ~65%, achieving a background index of $8.3 \times 10^{-3}\, cts/(keV.\, kg.\, yr)$ and $0.59 \times 10^{-3}\, cts/(keV.\, kg.\, yr)$ in Phase I and PhaseII, respectively. No signal is observed, and a limit on the half-life of 0νββ decay of ^{76}Ge is set at $T^{0\upsilon}_{1/2} > 1.8 \times 10^{26}\, yr$ at 90% C.L and the sensitivity coincides with the limit.

List of abbreviations:

ML : Machine learning
ANN : Artificial neural network
MLP : Multi-layer Perceptron
LSTM : Long short term memory
RNN : Recurrent neural network
IV : Input variable
GERDA : Germanium Detector Array
LEGEND : Large Enriched Germanium Experiment for Neutrinoless double beta Decay
LNGS : Laboratori Nazionali del Gran Sasso
DAQ : data acquisition
DSP : digital signal processing
FADC : flash analog-to-digital converter
LAr : liquid argon
BL : baseline
TP : test pulse
MWA : moving window average
PMT : photomultiplier tube
SiPM : silicon photomultiplier
PSA : pulse shape analysis
PSD : pulse shape discrimination
ROI : region of interest
RT : risetime
MSE : multi-site event
SSE : single-site event
DEP : double escape peak
FEP : Full energy peak
TlDEP : ^{208}Tl Double Escape Peak
TlSEP : ^{208}Tl Single Escape Peak
TlFEP : ^{208}Tl Full Energy Peak
BiFEP : ^{212}Bi Full Energy Peak
FWHM : full width at half maximum
IO : Inverted Ordering
NO : Normal Ordering
PMNS : Pontecorvo-Maki-Nakagawa-Sakata
2vββ : two neutrino double beta
0vββ : neutrinoless double beta
QFT : quantum field theory

HPGe : high purity germanium
BEGe : broad energy germanium
COAX : Coaxial
IC : inverted coaxial
GTF : Genius Test Facility
RG : Rico Grande
ANG : angereichert
GEANT 4: GEometry ANd Tracking 4
GELATIO : GErda LAyouT for Input/Output
MaGe : Majorana-GERDA
MGDO : Majorana-GERDA Data Objects

Table of Contents :

1. Introduction

The neutrino, first postulated by Wolfgang Pauli in the early 1930s, has long been a focal point of research in fundamental particle physics. Reines and Cowan experimentally confirmed the existence of the neutrino in 1956 [Cow56], nearly three decades after it was first proposed, despite the particle's elusive nature caused by its extremely small interaction cross-section. Ever since, the neutrino has continued to captivate the scientific community, playing a critical role in both validating and challenging the prevailing Standard Model (SM) of particle physics. The discovery of neutrino oscillations, in which neutrinos undergo flavor changes while traveling, has produced strong evidence that neutrinos have a mass, which defies the original Standard Model (SM), which held that neutrinos had no mass at all. It also suggests that there may be new physics beyond the Standard Model.

The search for neutrinoless double beta decay (0νββ) is one of the most interesting experimental and theoretical endeavors involving neutrinos. This rare process, if observed, would confirm that neutrinos are Majorana particles—meaning they are their own antiparticles—and such a decay would violate the conservation of lepton number by two units. Such a discovery would have profound implications for our understanding of the universe, from the mechanisms behind the matter-antimatter asymmetry to the development of a more comprehensive theory beyond the Standard Model. Additionally, 0νββ decay offers a unique opportunity to determine the absolute mass scale of neutrinos, which remains one of the most pressing unanswered questions in modern physics.

The GERmanium Detector Array (GERDA) experiment, located at the Laboratori Nazionali del Gran Sasso (LNGS) in Italy, was at the forefront of this search with ^{76}Ge as a candidate isotope. GERDA employs high-purity germanium (HPGe) detectors that are enriched with 76Ge, a promising isotope for the study of neutrinoless double beta (0νββ) decay. The experimental setup, which includes sophisticated shielding mechanisms such as being situated underground, submersion of detector array in liquid argon (LAr) and additional water shielding, is designed to minimize background and maximize the sensitivity to potential 0νββ events. In its first and second phase of operation, GERDA achieved a significant reduction in background levels, improving upon previous experiments such as the Heidelberg-Moscow (HdM) and the International Germanium Experiment (Igex). The pursuit of increased sensitivity and reduced background is a continuous endeavor, with pulse shape discrimination (PSD) being instrumental in the differentiation of potential 0νββ events from background.

This thesis focuses on the development and optimization of advanced artificial neural networks (ANNs) for pulse shape discrimination (PSD) in the GERDA experiment specifically tailored for semi-coaxial geometry of HPGe detectors. By analyzing the pulse topologies produced by particle interactions within the HPGe detectors, these models are trained to accurately identify and suppress background events. The analysis presented in this thesis is comprehensive, involving the application of various ANN architectures to GERDA data with proper handling of inputs to avoid inducing biases during training. A thorough study was conducted to determine the optimal network configurations and training strategies, with a particular focus on avoiding biases that could be introduced by improper signal proxies or data handling. The use of TensorFlow for model development not only facilitated the creation of these sophisticated neural networks but also ensured their accessibility and transparency for the entire GERDA collaboration. This represents a substantial advancement over the legacy ROOT-TMVA package-based networks. The multivariate approach optimized as part of this study, which employs ANN-based models to eliminate surface events, has demonstrated superior performance in suppressing the surface component of background compared to the legacy monoparametric method.

The result of this research is a collection of PSD techniques that have been optimized for the GERDA experiment. The objective is to increase the sensitivity to the 0νββ signal by suppressing background while preserving high signal efficiency. This thesis is structured as follows: An overview of the current state of neutrino physics is provided in Chapter 2, with a particular emphasis on the theoretical and experimental endeavors to detect 0νββ decay. Chapter 3 details the GERDA experiment, including its design, detection principles, data acquisition, and elements of passive background reduction. Chapter 4 discusses the development of the Artificial Neural Network-based Pulse Shape Discrimination techniques, their implementation, and the results obtained from applying them to GERDA data. Novel approaches with input processing and choice of signal proxy and their contribution to improvement in performance and robustness of the trained models is discussed in detail. Finally, Chapter 5 discusses the implications of the findings from the GERDA experiment and evaluation of the lower limit on half-life of potential neutrinoless double beta decay ($T^{0\upsilon}_{1/2}$) in ^{76}Ge.

In addition to the ANN-based model development, this thesis also explores the use of Geant4-based Monte Carlo simulations to simulate energy depositions inside HPGe detectors and subsequent pulse shape simulations with ADL4 to validate the performance of the developed PSD methods. Though these simulations are limited by the absence of dead layer modeling and the absence of detailed information on impurity concentration gradients in older semi-coaxial detectors, they offer valuable qualitative and quantitative insights. While the simulations were not used to derive the efficiency of the PSD methods due to these limitations, they nevertheless offer a deeper understanding of the underlying processes and are discussed in detail in Appendix A.

2. Introduction to the standard model of particle physics

The Standard Model of Particle Physics is a theoretical framework that attempts to describe all the fundamental interactions except gravitational interactions. The standard model has been a cornerstone of particle physics for decades, despite several experimental findings showing its inadequacy. The standard model describes electromagnetic, weak, and strong interactions using quantum field theory. Bosons and fermions are the two types of fundamental particles. Fermions are spin ½ particles which are the basic building blocks of matter, while gauge bosons with spin 1 facilitate interactions between them. Fermions include six different types of quarks and leptons, while bosons include photons, W and Z bosons, gluons, and spin 0 Higg's bosons. Fermions are further classified into quarks and leptons. Quarks are the building blocks of protons and neutrons, which in turn make up the nucleus of an atom. Quarks are classified into six types: up, down, charm, strange, top, and bottom. Electrons, muons, tau particles, and their corresponding neutrinos make up the leptons. Fermions are further grouped into three generations or flavors, each composed of two quarks, a charged lepton, and its corresponding neutrino.

Interactions between fermions are mediated by the exchange of gauge bosons, and different gauge bosons make possible different kinds of interactions. Photons mediate electromagnetic interactions between charged particles, while gluons mediate strong interactions between quarks. The weak interaction, responsible for beta decay, is mediated by the exchange of massive W and Z bosons. The gravitational force, the weakest of the four fundamental forces, is theorized to be mediated by graviton, an electrically neutral particle analogous to photon but with a spin-2. It is expected to be massless due to a very long range of gravitational force, and recent observations of gravitational waves from a binary black hole merger [Abb16] put an upper bound on its mass of 1.2×10^{-22} eV/c^2. The standard model can explain many of the interactions between subatomic particles, and it was able to predict the existence of some fundamental particles that were later discovered experimentally.

Fundamental Force	Force mediator	Range (m)	Relative Strength*
Strong	gluon	$<10^{-15}$	$\sim10^{-1}$
Electromagnetic	photon	∞	$\sim10^{-2}$
Weak	W & Z bosons	$<10^{-18}$	$\sim10^{-5}$
Gravitational	Graviton (theorised)	∞	$\sim10^{-38}$

Table 1: Here the values of coupling constants taken from [PDG booklet] are used to represent relative strength.

The four fundamental forces differ significantly in terms of their range and relative strengths, or coupling constants, as shown in table 1.

The electron and nucleus were discovered in the early 20th century, followed by the subsequent development of quantum mechanics, which could be argued to be the start of the development of the standard model. In the 1960s, a new class of particles composed of quarks known as mesons and baryons were discovered, leading to the development of the quark model, which explained the properties of these particles in terms of their constituent quarks.

In the late 1960s, physicists discovered the weak force, responsible for radioactive decay and neutrino interactions. The electroweak theory, which combined the electromagnetic and weak forces, predicted the existence of a massive, neutral spin-0 boson called the Higgs boson, which was discovered in 2012 at the LHC, validating this theory. The puzzle was completed with the discovery of the strong force that holds quarks together and the development of quantum chromodynamics.

The trivial observation that there is matter in the universe points to the mechanism beyond the SM that must exist to create observed matter-antimatter asymmetry. 0νββ decay is indeed a matter creating process, and its observation will be an important test for baryogenesis.

2.1. Introduction to Neutrino and Solar Neutrino Problem

Neutrino, as we know it, dates back its roots to the 1930s, when physicists were puzzled by peculiar observations of physics in the form of nuclear beta decay. Numerous unstable nuclei undergo this radioactive decay process, wherein a neutron in the nucleus decays via electroweak interaction into a proton by emitting an electron.

$$n \rightarrow p + e^{-}$$

Under this assumption of a two-body decay, the emitted electron should carry discrete energy. But the observed beta-decay spectrum showed a continuous energy distribution, which resulted in a clear violation of the conservation of energy and momentum. Also, the spin of the decaying system was not conserved anymore. This puzzling observation even led Niels Bohr to propose the radical idea that the energy may not be conserved in case of the beta decay. W. Pauli had an even more radical proposal: to hypothesize a completely new particle participating in the beta decay process, which would take away the missing energy and momentum. To provide for conservation of charge and angular momentum, this hypothetical particle would be electrically neutral with spin ½. He termed it “neutrino”, which is Italian for “little neutral one”. Upon postulating this elusive particle, Pauli remarked, “I have done a terrible thing. I have postulated a particle that cannot be detected”. The neutrino remained a hypothetical particle until 1956, when the first experimental evidence [Cow56] for its existence was accomplished by C. Cowan and F. Reines at the Savannah River Experiment by detecting the antineutrinos emitted by a nuclear reactor.

The handedness of a particle describes the direction of it's spin with respect to the direction of its linear momentum. A particle is said to be right handed if the spin points in the same direction as that of its motion, and on the contrary, left-handed particles have spin that points in a direction opposite to that of the linear momentum. In 1958, at Brookhaven National Laboratory [Gol58], M. Goldhaber observed the inverse beta decay of Europeam-152 nucleus by electron capture, which produced a neutrino and an unstable Samarium-152 nucleus, which decayed instantaneously by emitting a gamma ray. In order to conserve the angular momentum, the handedness of the emitted neutrino and gamma ray had to be the same. By measuring the helicity[1] of the emitted gamma rays using a polarized ferrous filter, it was discovered that the neutrinos are always left-handed and no right-handed neutrinos are found to exist. This had a serious implication: neutrinos had to be massless and hence travel at speed of light since helicity is not Lorentz invariant. This was also consistent with the SM interpretation of how particles acquire their masses via interaction with the Higgs boson, changing their helicity. Since no right-handed neutrino state exists, neutrinos should be unable to interact with Higgs field and hence acquire no mass.

In the standard model, neutrinos are massless leptons with no electric or colour charge and therefore can interact only via weak force. There are three families of leptons and quarks, and to study the weak interaction, they are grouped together based on weak isospin (T) and hypercharge (Y) quantum numbers. Associated with each of the charged leptons, i.e., electron, muon, and tau particle, is an electron-neutrino ν_e , a muon-neutrino ν_μ and a tau-neutrino, ν_τ respectively.

$$\begin{pmatrix} \nu_e \\ e^- \end{pmatrix}, \begin{pmatrix} u \\ d \end{pmatrix}; \qquad \begin{pmatrix} \nu_\mu \\ \mu^- \end{pmatrix}, \begin{pmatrix} c \\ s \end{pmatrix}; \qquad \begin{pmatrix} \nu_\tau \\ \tau^- \end{pmatrix}, \begin{pmatrix} t \\ b \end{pmatrix}$$

Across the three families, a left-handed charged lepton and its corresponding neutrino are paired into a doublet with weak isospin T=½ and weak hypercharge Y=-1. But their weak isospin projections differ: a charged left-handed lepton with T3=-½ and corresponding left handed neutrino with T3=½. The right-handed charged leptons are expressed as singlets with weak isospin T=0 and weak hypercharge Y=-2.

Then the electric charge of the particle expressed in terms of weak isospin projection and hypercharge is:

$$Q = T3 + Y/2$$

---

[1] Helicity of a particle is defined as sign of the projection of its spin vector **σ** onto the direction of its linear momentum vector **P**/|**P**|. Helicity is not Lorentz invariant.

Neutrinos are the least well understood fundamental particles among the ones found in the standard model. Since its postulation by Pauli, the neutrino has played a vital role in unraveling the fundamentals of particle physics and challenging the long-invincible standard model. Being electrically neutral, neutrinos interact solely via weak force, and this offers a window to study it without the background noise of electromagnetic or strong force.

2.2. Solar Neutrino Problem

The solar neutrino problem, in essence, is the observation of a discrepancy in the predicted flux of neutrinos emitted by the Sun based on its luminosity and energy versus what we actually detected on earth in various experiments.

Our Sun, as any other bright star in the night sky, generates energy via nuclear fusion of hydrogen to Helium and avoids a gravitational collapse. Based on the mass of the star, the route taken to achieve this differs. Stars much heavier than our Sun follow the so called Carbon-Nitrogen-Oxygen (CNO) cycle, where four protons fuse using the mentioned heavier nuclei as catalysts to form a stable helium nuclei in a six step process emitting two positrons and two electron neutrinos. But lighter stars like the Sun follow the so-called proton-proton (pp) chain reaction, wherein four hydrogen nuclei fuse to form helium nuclei, emitting a positron and an electron neutrino in the process. This predominant mechanism that drives the nuclear fusion can be described in the following steps:

a) Two Hydrogen nucleus fuse together to form a deuterium with emission of a an electron neutrino and an electron. Occasionally, it can follow the "pep" reaction where an incoming electron replaces the outgoing positron.

$^{1}H + ^{1}H \rightarrow ^{2}H + e + v$

$^{1}H + ^{1}H + e \rightarrow ^{2}H + v$

b)The resultant deuterium fuses with a Hydrogen nucleus to produce Helium-3 nucleus accompanied by energy release(5.493 MeV) carried away by a photon.

$^{2}H + ^{1}H \rightarrow ^{3}He + \gamma$

c)The Helium-3 nucleus then can fuse with another Helium-3 nucleus to produce stable Helium-4 and two hydrogen nuclei

$^{3}He + ^{3}He \rightarrow ^{4}He + ^{1}H + ^{1}H$: PPI chain

Although this is the predominant reaction pathway for Helium-3, it can also undergo alternative fusion reactions: Either it fuses with a Hydrogen nucleus to form Helium-4 nucleus and with emission of a positron and an electron neutrino

$^{3}He + ^{1}H \rightarrow ^{4}He + e^{+} + v$

Or it fuses with Helium-4 nucleus to form Beryllium-7 nucleus emitting a photon.

$^{3}He + ^{4}He \rightarrow ^{7}Be + \gamma$

d)The Beryllium-7 decays to Lithium-7 by absorbing an electron and emits an electron neutrino. The resultant Lithium-7 absorbs a hydrogen nucleus and decays into two helium-4 nuclei.

$^{7}Be + e^{-} \rightarrow {}^{7}Li + v$

$^{7}Li + {}^{1}H \rightarrow {}^{4}He + {}^{4}He$: PPII chain

Rarely, Beryllium-7 can absorb a Hydrogen nucleus to form Boron-8, which in turn decays to an excited state of Beryllium-8 nucleus which further decays into two Helium-4 nuclei.

$^{7}Be + {}^{1}H \rightarrow {}^{8}B + \gamma$

$^{8}B \rightarrow {}^{8}Be^{*} + e^{+} + v$

$^{8}Be^{*} \rightarrow {}^{4}He + {}^{4}He$: PPIII chain

Although PPIII chain is not a dominant mode of decay for ^{7}Be, it is of importance in the Solar neutrino problem since it produces very high energy neutrinos, and most past and present detectors are sensitive to only such high energy electron neutrinos.

So simply put, nuclear fusion reactions in the Sun fuse four hydrogen nuclei to form Helium-4 nucleus and two positrons and two electron neutrinos.

$4({}^{1}H) \rightarrow {}^{4}He + e^{+} + v + \gamma$

Note that, only one flavor of neutrinos, the electron neutrinos, is produced in all the chain reactions.

In the late 1960s, Raymond David Jr. and John Bahcall [Bah64] proposed an experiment to test whether the above mentioned process is the mechanism driving nuclear fusion in Sun. In Homestake mine, the setup consisted of a massive chlorine tank for the neutrinos to interact with. The detection of a neutrino interaction was determined by measuring the amount of radioactive Argon nuclei produced in the tank via :

$$^{37}Cl + v_{e} \rightarrow {}^{37}Ar + e$$

The measured number of radioactive ^{37}Ar allowed to draw an inference about the flux of neutrinos. In 1968, Davis announced the first results [Dav68], and the observed number of ^{37}Ar atoms accounted for only one-third of the neutrino flux predicted by the Standard Solar Model [Bah64]. Over the course of time, various explanations, such as possible inconsistencies in the Standard Solar Model or the Davis experiment, were all ruled out. Subsequently, more recent experimental observations have only strengthened the evidence for missing neutrinos. Observations by GALLEX and SAGE that were sensitive to the most abundant low energy solar neutrinos also confirmed that even lower energy neutrinos are missing, although not in the same proportion as the high energy neutrinos.

The deficiency in observed solar neutrino flux could be explained by allowing neutrinos to change flavors as they travel through space. Because of the change in flavor, some fraction of the solar electron neutrinos are no longer detectable as they have changed into another type: muon or tau neutrinos. The neutrino oscillations are possible only if the three neutrino flavors have differing masses; thus, at least two flavors of neutrino have non-zero mass and the lightest one could be massless.

2.3. Neutrino Oscillations : Resolving the solar neutrino problem

The idea of neutrino mixing was introduced by B. Pountecorvo in 1957, who proposed neutrino-antineutrino transitions may be possible. This idea later led to the development of the quantitative theory of neutrino flavor oscillations put forward by Maki, Nakagawa and Sakata in 1962 [Mak62] and further expanded by B. Pounecorvo [Pou67] and V. Gribov [Gri69].

The basic idea behind neutrino oscillations is that there are three generations, or "flavors," of neutrinos: electron neutrinos, muon neutrinos, and tau neutrinos and neutrinos could change from one flavor to another as they traveled through space. The neutrinos are assumed to be massive, contrary to contemporary belief that they are massless. This is because the three neutrino flavor eigenstates are not mass eigenstates, which means that they do not have a fixed mass associated with them. Instead, each flavor eigenstate is a combination of three different mass eigenstates with different masses and energies. These neutrino flavor and mass eigenstates are superpositions of each other, and their mixing is described by a unitary transformation:

$$|\nu_\alpha\rangle = \sum_i U^*_{\alpha i}|\nu_i\rangle \qquad\qquad |\nu_i\rangle = \sum_\alpha U_{\alpha i}|\nu_\alpha\rangle$$

Where $\boldsymbol{\alpha}$=e,μ,τ refers to flavor eigenstates while *i*=1,2,3 refers to different mass eigenstates. $U_{\boldsymbol{\alpha} i}$ refers to corresponding matrix elements of unitary *Pontecorvo–Maki–Nakagawa–Sakata (PMNS) matrix*. Considering standard three neutrino mixing, the *PMNS* matrix is represented in terms of CP violating phase factor □ and mixing angles θ as:

$$U = \begin{pmatrix} U_{e1} & U_{e2} & U_{e3} \\ U_{\mu 1} & U_{\mu 2} & U_{\mu 3} \\ U_{\tau 1} & U_{\tau 2} & U_{\tau 3} \end{pmatrix} = \begin{bmatrix} c_{12}c_{13} & s_{12}c_{13} & s_{13}e^{-i\delta} \\ -s_{12}c_{23} - c_{12}s_{23}s_{13}e^{i\delta} & c_{12}c_{23} - s_{12}s_{23}s_{13}e^{i\delta} & s_{23}c_{13} \\ s_{12}s_{23} - c_{12}c_{23}s_{13}e^{i\delta} & -c_{12}s_{23} - s_{12}c_{23}s_{13}e^{i\delta} & c_{23}c_{13} \end{bmatrix} \begin{bmatrix} e^{i\alpha_1/2} & 0 & 0 \\ 0 & e^{i\alpha_2/2} & 0 \\ 0 & 0 & 1 \end{bmatrix}$$

where c_{ij} and s_{ij} are cosines and sines of mixing angles θ_{ij} respectively. The additional two phase factors $\boldsymbol{\alpha}_1$ and $\boldsymbol{\alpha}_2$ are non-zero only if the neutrinos are Majorana particles and do not affect the observable oscillation regardless. These Majorana phase factors could be probed with lepton number violating processes like neutrinoless double beta decay.

In principle, when a neutrino is produced, it is in a specific flavor eigenstate. For example, if a neutrino is produced in an electron flavor state, it can be written as a linear combination of the three mass eigenstates as:

$$|v_e(t=0)> = U^*_{e1}|v_1> + U^*_{e2}|v_2> + U^*_{e3}|v_3>$$

Similarly, the flavor states for muon and tau neutrinos can be written as linear combinations of the three mass eigenstates, with the corresponding PMNS matrix elements $U_{\mu i}$ and $U_{\tau i}$.

As the neutrino travels, each mass eigenstate propagates with its own phase factor determined by its mass and energy. This leads to a change in the relative phases of the different mass eigenstates and the flavor eigenstate modifies to:

$$|\nu(t)\rangle = \sum_i U^*_{\alpha i}\, e^{-iE_i t}|\nu_i\rangle = \sum_i U^*_{\alpha i} e^{-iE_i t} \sum_\beta U_{\beta i}|\nu_\beta\rangle$$

which is no longer a coherent superposition of mass eigenstates. Here e^{-iEt} is phase factor of mass eigenstate with energy $E = \sqrt{p^2 + m^2}$.

Upon interaction, one of the flavor eigenstates is realized and since mass eigenstates are superpositions of the flavor eigenstates, the detected neutrino flavor could be different from the initial neutrino flavor. The probability that neutrino produced with flavor $\boldsymbol{\alpha}$ and energy E is detected as neutrino with flavor $\boldsymbol{\beta}$ after time t is given by

$$P(\nu_\alpha \to \nu_\beta) = \left|\langle \nu_\beta | \nu(t)\rangle\right|^2 = \left|\sum_i U_{\beta i} U^*_{\alpha i} e^{-iE_i t}\right|^2$$

Assuming neutrinos to be ultra-relativistic and substituting time with distance travelled L≃ct, the above transition probability is expressed as [Gig18]:

$$P(\nu_\alpha \to \nu_\beta) = \delta_{\alpha\beta} - 4\sum_{i<j} \mathrm{Re}\left[U_{\alpha i}U^*_{\beta i}U^*_{\alpha j}U_{\beta j}\right] \sin^2\left(\frac{\Delta m^2_{ji} L}{4E}\right)$$
$$+\ 2\sum_{i<j} \mathrm{Im}\left[U_{\alpha i}U^*_{\beta i}U^*_{\alpha j}U_{\beta j}\right] \sin\left(\frac{\Delta m^2_{ji} L}{2E}\right),$$

where $\Delta m^2_{ji} = m^2_j - m^2_i$ are the squared mass differences. Since $\Delta m^2_{32} = \Delta m^2_{31} - \Delta m^2_{21}$, there are two independent squared mass differences. Clearly, neutrino oscillations require neutrinos to have different masses $\Delta m^2_{ji} \neq 0$ and non-trivial flavor mixing, i.e. $U \neq 1$ (otherwise flavor eigenstates would be the same as mass eigenstates). As evident from above, the observable neutrino oscillations depend on six parameters: three mixing angles θ_{ij}, the

CP-violating phase factor, δ and two of the three squared mass differences Δm_{ij}^2. Current best fit values for these parameters are summarized in table 2. Thus, neutrino oscillation experiments can neither provide any insight about the absolute mass scale of neutrinos nor about their mass hierarchy. Since the Majorana phase factors do not participate in the oscillation probabilities, the oscillation probabilities are the same irrespective of the Dirac or Majorana nature of neutrinos.

Parameter	Mass ordering	Best fit	2σ range
Δm_{21}^2 (10^{-5}eV^2)	NO or IO	7.50	7.12-7.93
$\lvert\Delta m_{31}^2\rvert$ (10^{-3}eV^2)	NO	2.55	2.49-2.60
	IO	2.45	2.39-2.50
$\sin^2\theta_{12}/10^{-1}$	NO or IO	3.18	2.86-3.52
$\sin^2\theta_{23}/10^{-1}$	NO	5.74	5.41-5.99
	IO	5.78	5.41-5.98
$\sin^2\theta_{13}/10^{-2}$	NO	2.200	2.069-2.337
	IO	2.225	2.086-2.356
δ/π	NO	1.08	0.84-1.42
	IO	1.58	1.26-1.85

Table 2: Neutrino oscillation parameter values and 2σ ranges with respect to the mass ordering(NO or IO). The data is taken from [Sal21] and is compiled using global results from neutrino oscillation experiments.

2.4. Neutrino mass hierarchy and experimental evidence

The standard model has three generations of fermions in which masses of quarks and charged leptons exhibit a particular ordering: Gen I > Gen II > Gen III. Neutrino masses are many orders of magnitudes smaller than those of charged leptons and their relative order is not precisely known. Since the sign of the atmospheric mass splitting Δm_{31}^2 remains unknown, two distinct mass orderings are possible: normal ordering(NO) and inverted ordering(IO). In the normal ordering, the lightest neutrino is the electron neutrino, while the heaviest is the tau neutrino, which is reversed in inverted ordering.

Normal Ordering (NO) : $m_1 << m_2 << m_3$
Inverted Ordering (IO) : $m_3 << m_1 < m_2$

Using best fit values for Δm^2_{31} and Δm^2_{21}, it is evident that at least two neutrinos have a mass greater than $\sqrt{\Delta m^2_{21}} \approx 8\, meV$ and one of them is massive than $\sqrt{|\Delta m^2_{31}|} \approx 50\, meV$. Similarly the lower bounds on the sum of the absolute neutrino masses can be expressed as:

$$Normal\ ordering: \quad \sum m_\nu = m_1 + \sqrt{\Delta m^2_{21} + m^2_1} + \sqrt{\Delta m^2_{31} + m^2_1} \ > \ 0.06\ eV$$

$$Inverted\ ordering: \quad \sum m_\nu = m_3 + \sqrt{|\Delta m^2_{31}| + m^2_3} + \sqrt{\Delta m^2_{21} + |\Delta m^2_{31}| + m^2_3} \ > \ 0.10\ eV$$

Apart from determination of sign of atmospheric mass splitting Δm^2_{31} ,

To study the absolute scale of neutrino masses, three of the most significant probes are kinematic measurements of β-decay, search for the neutrinoless double beta decay and constraints through cosmological observations.

2.4.1. β-decay

Spectral measurement of β-decay near the endpoint is the most reliable model-independent probe to assess absolute neutrino masses. In case of β-decay of tritium (^{3}H), a proton inside the nucleus decays into a neutron emitting an electron and corresponding anti-neutrino.

$$^3H \rightarrow \ ^3He^+ + e^- + \overline{\nu_e}$$

Neglecting the recoil of nucleus, the energy(Q_β) released during β-decay and the neutrino's mass define the endpoint of the beta decay spectrum which is well defined if neutrinos are considered massless. In case of neutrinos with non-vanishing mass, the endpoint energy is reduced and spectral shape is distorted at the endpoint. Current β-decay experiments are not sensitive to individual neutrino mass eigenstates but measure the so-called effective neutrino mass (m_β) expressed as an incoherent superposition of neutrino mass eigenstates.

$$m^2_\beta = \sum_{i=1}^{3} |U_{ei}|^2 m^2_i \ = c^2_{12} c^2_{13} m^2_1 + s^2_{12} c^2_{13} m^2_2 + s^2_{13} m^2_3$$

The strongest upper bound on m_β is currently set by KATRIN [Kat19] with m_β <1.1 eV at 90% C.L, which holds regardless of Dirac or Majorana nature of neutrinos.

2.4.2. Cosmological constraints:

Massive neutrinos affect the evolution of the universe and, in turn, the cosmological observables such as CMB anisotropies and large scale structures in a different way, which is utilized to put constraints on neutrino mass scale. Cosmological observables are mainly sensitive to the sum of neutrino masses ∑mν, defined simply as

$$\sum m = \sum_{i=1}^{3} m_i = m_1 + m_2 + m_3$$

The spatially flat ΛCDM model with adiabatic, nearly scale-invariant initial conditions for scalar perturbations describes the universe effectively. This model can fit almost all the data well. Cold dark matter, baryons, photons, and neutrinos provide matter and radiation in the base CDM model, which is spatially flat (Ωk = 0). Dark energy is a cosmological constant (w = −1). This simple, successful model can be extended in several ways. A one-parameter extension using the sum of neutrino masses as a free parameter is most popular for studying the neutrino mass scale leading to ΛCDM+$\sum m_\nu$, a seven-parameter model. . Photon energy density is fixed by CMB temperature measurements, while neutrinos are assumed to be very light, usually fixing the sum of their masses to m_ν = 0.06 eV, the minimum allowed by oscillation experiments. The limits weaken when one moves from the seven-parameter CDM (Lambda cold dark matter model) plus neutrino mass (ΛCDM+$\sum m_\nu$) framework to frameworks with more cosmological parameters.

Considering the results from a combination of cosmological and neutrino oscillation data,
Global fit analysis with ordering-agnostic priors and parameters provides a 2.7σ [Gar22] preference for the normal ordering over the inverted ordering.

2.5. Neutrinoless Double Beta Decay:

Double-beta (ββ) decay is a second-order weak decay where a parent nucleus (A, Z) decays to a daughter nucleus (A, Z + 2) with the emission of two electrons and two electron antineutrinos.

$$(A, Z) \rightarrow (A, Z + 2) + 2\,e^- + 2\,\bar{\nu}_e + Q_{\beta\beta}$$

Neutrino accompanied double beta decay is SM-allowed second order decay, and the lepton number is conserved.

Neutrinoless double-beta decay is a forbidden, lepton-number-violating nuclear decay that, if observed, would reveal the nature of neutrinos and has implications for theories beyond the

Standard Model, and cosmology. $0\nu\beta\beta\, decay$ involves no emission of neutrinos and violates Lepton number conservation by $\Delta L = 2$.

$$(A, Z) \rightarrow (A, Z + 2) + 2\, e^- + Q_{\beta\beta}$$

The signature of the $0\nu\beta\beta$ decay is a peak in energy spectrum at $Q_{\beta\beta}$ as all the energy released in the decay is carried by the electrons and no energy is lost to neutrinos that do not interact with detectors.

Ettore Majorana first suggested the possibility of a Majorana nature of neutral spin-1/2 particles in 1937 [Maj37]. The neutrino is the only candidate for a Majorana particle in the Standard Model because it is the only neutral fermion. As the dominant process, light massive neutrinos that satisfy the Majorana condition ν=ν are the usual explanation for $0\nu\beta\beta$ decay.

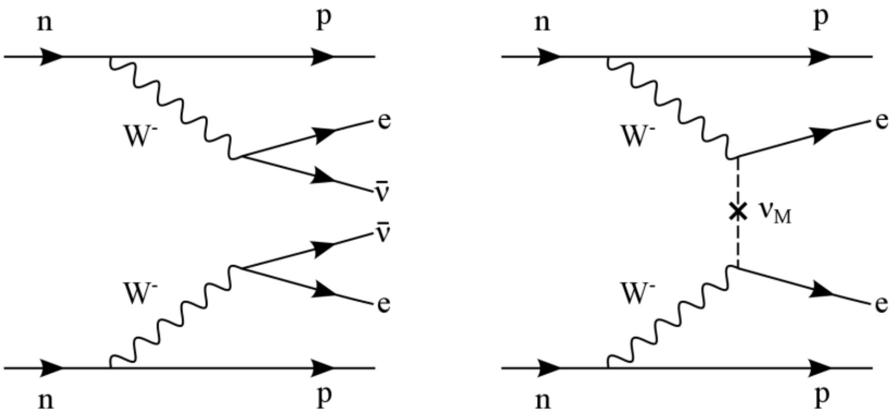

Figure 1: The Feynmann diagrams for well understood $2\nu\beta\beta$ decay (left) and $0\nu\beta\beta$ decay (right) mediated by Majorana neutrinos.

In the case of light neutrino exchange, the 0νββ-decay half-life relates to effective Majorana mass and is given by

$$(T^{0\nu}_{1/2})^{-1} = G_{0\nu}(Q_{\beta\beta}, Z)|\mathcal{M}_{0\nu}|^2 \left(\frac{m_{\beta\beta}}{m_e}\right)^2$$

where m_e is the electron mass, $G_{0\nu}$ is the phase space factor, $M_{0\nu}$ is the nuclear matrix element (NME) of the neutrinoless double beta decay process, and $m_{\beta\beta}$ is the effective Majorana mass. The above conversion between half-life and effective majorana mass depends on NME calculations which is difficult to compute and presents a significant source of uncertainty.

In the three Majorana neutrino paradigm, the effective Majorana mass is expressed as:

$$m_{\beta\beta} = |\sum_{i=1}^{3} U^2_{ei} m_i| \overset{\text{Eq. 2.32}}{=} |c^2_{12}c^2_{13}m_1 + s^2_{12}c^2_{12}m_2 e^{2i\alpha} + s^2_{13}m_3 e^{2i\beta}|\ .$$

With the known mixing parameters and considering three Majorana neutrinos, we find that mββ depends on the mass ordering only for $m_{lightest} < 40$ meV. Thus, if the lightest neutrino has a mass above ~40 meV, which is allowed by all current constraints on the neutrino mass scale, neutrinoless double beta decay experiments will never be able to differentiate the two mass orderings. For smaller values of $m_{lightest}$, $m_{\beta\beta}$ becomes independent, and in the region $m_{lightest}$-10 meV, the effective Majorana mass $m_{\beta\beta}$ is constrained by the mass splittings to be larger than 10 meV for inverted ordering and below 7 meV for normal ordering. Experiments that test $m_{\beta\beta} <$ 10 meV can rule out the inverted scenario. However, a positive detection of $T_{0v1/2}$ in the range that corresponds to $m_{\beta\beta} <$ 10 meV would not provide enough information to determine the mass ordering without determining $m_{lightest}$. In the context of three neutrino mixing, neutrinoless double beta decay experiments alone can only rule out the inverted scheme if the ordering is normal and $m_{lightest} <$ 10 meV.

2.5.1. Experimental Considerations for 0vββ decay experiment:

Direct searches of 0vββ decay study the two electrons' kinematic parameters as observable. A typical experiment measures the total energy (E) of the two electrons, and since no antineutrinos are emitted, the 0vββ-decay signal is monoenergetic peak at $Q_{\beta\beta}$. The signal search can be performed over a narrow energy window around $Q_{\beta\beta}$, termed the Region of Interest (ROI) whose width is based on the detector's energy resolution.

The number of true signal events, N_{sig} can be expressed as:

$$N_{sig} = \left(\frac{ln2}{T^{0v}_{1/2}}\right)\frac{N_A}{m}\eta\epsilon Mt$$

where N_A is the Avagadro number, m is the molar mass of candidate isotope, η is the enrichment fraction, ϵ is the signal detection efficiency and M is total mass of the source and t is the measurement time.

The number of background events in ROI scales linearly with the detector mass M and can be expressed as:

$$N_{bkg} = M.\Delta E.BI.t$$

where ΔE represents the width of ROI and BI is refers to background index in units of counts/(keV.kg.yr).

In the context of a 0vββ decay experiment, the criterion for the discovery potential can be expressed in terms of the number of signal events (N_{sig}) and the number of background events (N_{bkg}) with a confidence level (C_1) measured in units of the standard deviation (σ) of a Poisson distribution [Avi05]. For a certain requirement of signal to background ratio , $R_{sb}=N_{sig}/N_{bkg}$ one can write,

$$N_{sig}= C_1\sqrt{N_{sig} + N_{bkg}} = C_1\sqrt{(R_{sb} + 1)N_{bkg}} = C_1\gamma\sqrt{N_{bkg}}$$

where $\gamma = \sqrt{(R_{sb} + 1)}$.

Combining above three equations, the sensitivity of the experimental measurement depends on the number of events (including the background events) observed in the region of interest and can be written as:

$$T^{0v}_{1/2} \propto \eta\epsilon Mt \quad \text{; Background free}$$

$$T^{0v}_{1/2} \propto \eta\epsilon\sqrt{\frac{Mt}{BI.\Delta E}} \quad \text{; with Background}$$

Above expression underlines the importance of background free experiment for 0vββ search as the sensitivity of the experiment scales linearly with the exposure (Mt) in case of background free conditions instead of $\sqrt{Mt}$ in presence of the significant background. It is evident from above expression that sensitivity can be enhanced by increasing the source mass (M) and measurement time (t) and by minimizing the background (BI). Source material is often limited and expensive, and measurement time is constrained. Hence, the most effective approach to improve sensitivity lies in significantly reducing the background, enabling a more accurate and precise detection of the rare 0vββ decay signal.

2.5.2. Choice of the isotope:

As evident from the above equation, an ideal isotope for the 0vββ search should have high isotopic abundance, η and it should be scalable, to be deployed in large quantities (M). It should be capable of being deployed as detectors with excellent energy resolution (ΔE). Unfortunately, no such ideal double beta decaying isotope exist and experiments have to make design choices to optimize some of these parameters. The candidate isotope is also required to have a large Q in order to place the region of interest above the end point of many potential background sources. A large Q value also ensures a relatively fast 0vββ rate, which is proportional to the phase space factor which in turn relates to $Q_{\beta\beta}$ as $G_{0v} \propto Q^5$ [Avi08].

When the source material is integrated as the detector medium, the detection efficiency of the 0vββ -decay signal is significantly improved. In such a case, excellent energy resolution is achievable because the path lengths of the two signal electrons are much shorter than the size of the active medium in such a coalesced configuration. When the source material is located outside of the detector, the likelihood of at least one of the two electrons escaping detection or having their energy degraded increases due to self-absorption and worsens the energy resolution.

Isotope	**$Q_{\beta\beta}$**	$T^{0v}_{1/2}\,(10^{25}\,yr)$	**$<m_{\beta\beta}>$ (eV)**	**Experiment**
^{48}Ca	4.263	$>5.8 \times 10^{-3}$	<3.5–22	ELEGANT-IV
^{76}Ge	2.039	>18	<0.079-0.180	GERDA
^{82}Se	2.998	$>3.6 \times 10^{-2}$	<0.89–2.43	NEMO-3
^{96}Zr	3.348	$>9.2 \times 10^{-4}$	<7.2–19.5	NEMO-3
^{100}Mo	3.035	$>1.1 \times 10^{-1}$	<0.33–0.62	NEMO-3
^{116}Cd	2.813	$>2.2 \times 10^{-2}$	<1.0–1.7	Aurora
^{130}Te	2.527	>1.5	<0.11–0.52	CUORE
^{136}Xe	2.459	>10.7	<0.061–0.165	KamLAND-Zen
^{150}Nd	3.371	$>2.0 \times 10^{-3}$	<1.6–5.3	NEMO-3

Table 3: Characteristic 0vββ decaying isotopes and 90% CL limits on half-life from various experiments. Data taken from [Dol19]

2.5.3. Background suppression:

In any search for new physics, the detector design must distinguish signal from background while maximising signal detection efficiency. Energy resolution, typically intrinsic to the detection medium, is the most common method for this discrimination.

Neutrinoless double-beta decay has a characteristic event topology with the emission of two ~1MeV electrons. Low-density-gas tracking detectors can theoretically resolve the two electron tracks, leaving only the irreducible background from 2vββ decay. For detectors with higher densities, such as semiconductor detectors or liquid scintillator detectors, these electrons deposit their energy within a few millimeters, allowing a less powerful but still useful discrimination between "compact" signal-like events and compton-scattered gamma ray background, which scatter and deposit energy at multiple sites. Depending on position resolution, detector size, and type, a pulse-shape discrimination or reconstructed event topology can distinguish "single-site" and "multi-site" events. Scintillation and ionization detectors can distinguish particles from α and beta backgrounds. Timing is another important variable for signal-background separation.

Although conclusive observations of neutrino oscillations were a significant stride in understanding these enigmatic particles, many more questions remain unanswered. For now, the absolute masses of neutrinos, the mass ordering, the mechanism that imparts neutrinos mass, and even the very nature of the neutrinos (whether they are Dirac or Majorana particles) remain unknown.

Bibliography (Chapter 2):

[Gol58] M. Goldhaber et al. , Helicity of Neutrinos , Rhys. Rev., 1015-1017 , 491-494, 1958.

[Cow56] C. L. Cowan Jr.; F. Reines; F. B. Harrison; H. W. Kruse; A. D. McGuire (July 20, 1956). "Detection of the Free Neutrino: a Confirmation". Science. 124 (3212)

[Bah64] Bahcall, John N., Solar Neutrinos. I. Theoretical. Physical Review Letters. Volume 12, Number 11.1964

[Dav68] Davis R. Jr., Harmer D. S. and Hoffman K. C. (1968) A search for neutrinos from the Sun. Phys. Rev. Lett. 20, 1205-1209

[Abb16] Abbott, B. P. et al. (2016). "Observation of Gravitational Waves from a Binary Black Hole Merger". Physical Review Letters. 116 (6): 061102. arXiv:1602.03837. Bibcode:2016PhRvL.116f1102A. doi:10.1103/PhysRevLett.116.061102.

[Mak62] Z. Maki, M. Nakagawa, S. Sakata “Remarks on the Unified Model of Elementary Particles” Progress of Theoretical Physics, Volume 28, Issue 5, November 1962, Pages 870–880, https://doi.org/10.1143/PTP.28.870

[Pou68] B. Pontecorvo (May 1968). "Neutrino Experiments and the Problem of Conservation of Leptonic Charge". Zh. Eksp. Teor. Fiz. 53: 1717–1725.

[Gri69] Gribov, V.; Pontecorvo, B. (1969). "Neutrino astronomy and lepton charge". Physics Letters B. 28 (7): 493–496. doi:10.1016/0370-2693(69)90525-5

[Gig18] C. Giganti et al. “ Neutrino oscillations: The rise of the PMNS paradigm”/ Progress in Particle and Nuclear Physics 98 (2018)

[Sal21] de Salas, P.F., Forero, D.V., Gariazzo, S. et al. 2020 global reassessment of the neutrino oscillation picture. J. High Energ. Phys. 2021, 71 (2021). https://doi.org/10.1007/JHEP02(2021)071

[Kat19] KATRIN collaboration, Improved Upper Limit on the Neutrino Mass from a Direct Kinematic Method by KATRIN, Phys. Rev. Lett. 123 (2019) 221802

[Sal18] de Salas, P. F., Gariazzo, S., Mena, O., Ternes, C. A., & Tórtola, M. (2018, September 12). Neutrino Mass Ordering from Oscillations and Beyond: 2018 Status and Future Prospects. Frontiers. https://doi.org/10.3389/fspas.2018.00036

[Avi08] F. Avignone, S. R. Elliott, and J. Engel, Double Beta Decay, Majorana Neutrinos, and Neutrino Mass, Rev.Mod.Phys. 80 (2008) 481{516, [arXiv:0708.1033].

[Dol19] “Neutrinoless Double-Beta Decay: Status and Prospects” ,Annual Review of Nuclear and Particle Science, https://doi.org/10.1146/annurev-nucl-101918-023407

[Gar22] “Neutrino mass and mass ordering: no conclusive evidence for normal ordering”, Stefano Gariazzo et al JCAP10(2022)010 DOI: 10.1088/1475-7516/2022/10/010

[Maj37] Majorana, E. Teoria simmetrica dell’elettrone e del positrone. Il Nuovo Cimento (1924-1942), volume 14(4):pp. 171, 1937. doi:10.1007/BF02961314

[Avi05] F T Avignone III et al 2005 New J. Phys. 7 6, doi:10.1088/1367-2630/7/1/006

3. The GERDA Experiment

3.1: Introduction and Physics Goals

The GERDA experiment was first proposed in March 2004 [Abt04] with the novel idea of operating an array of bare HPGe detectors directly inside a sizable volume of cryogenic liquid as suggested in [Heu95]. This method combines the benefits of a scintillation-based active shielding and a radioactively ultra-pure passive shielding while also providing cryogenic cooling for the operation of the detectors. This rare decay search experiment is designed to investigate the nature of neutrinos and test the theory that they are their own antiparticles. Neutrinoless double beta decay is a rare nuclear process in which, within a nucleus, two neutrons decay into two protons, emitting two electrons and no neutrinos, violating the conservation of lepton number. If observed, this decay would provide evidence for the Majorana nature of neutrinos, which could have important implications for understanding the nature of dark matter and the evolution of the early universe.

The GERDA experiment began taking data in 2011 and has released several results, including the world's best limit on the half-life of neutrinoless double beta decay for the isotope ^{76}Ge. The experiment continued to take data with improved sensitivity and lower backgrounds and is expected to further constrain the possibility of observing neutrinoless double beta decay in the near future with LEGEND.

3.2: Experimental Setup

The GERDA experiment, situated at the INFN Laboratori Nazionali del Gran Sasso (LNGS), operates at a depth of 3500 meters water equivalent. This setup submerges high-purity germanium detectors enriched in ^{76}Ge within liquid argon (LAr) – a concept proposed in [Heu95]. The liquid argon serves a dual purpose, acting both as a passive shield against external radioactivity and as an efficient cryogenic medium for HPGe detectors. Background levels are quantified in terms of counts per keV per kilogram per year (cts/(keV kg yr)), given that the number of background events is roughly influenced by factors like detector mass, energy resolution, and operational time. Phase I of the experiment had an objective set to reach a sensitivity corresponding to a 15 kg.yr exposure with a background index (BI) of 10^{-2} cts/(keV kg yr) [Ack13].

This chapter provides a brief review of the GERDA experimental setup and design, encompassing various aspects such as experimental constraints, detector description, setup configuration, electronic readout, data acquisition (DAQ), and data processing. The ultimate objective is to achieve a near-background-free environment in the region of interest (ROI) surrounding the $Q_{\beta\beta}$. Central to the GERDA design is the utilization of bare germanium detectors constructed from ^{76}Ge-enriched material operated within liquid argon. This innovative approach facilitates a considerable reduction in cladding materials around the diodes, along with associated radiation sources, compared to conventional Ge-based experiments. Moreover, the background originating from cosmic ray interactions is reduced compared to traditional concepts of HdM, IGEX due to the lower atomic number (Z) of the shielding material. While natural Ge (natGe) possesses about 7.8% ^{76}Ge, which could potentially be used directly for 0νββ decay experiments, enriched detectors present a superior signal-to-background ratio and offer cost savings for a fixed mass of ^{76}Ge. This enhanced ratio results from factors like background sources scaling with detector mass and reduced cosmogenic production of ^{68}Ge and ^{60}Co in enriched Ge material compared to it's natural counterpart.

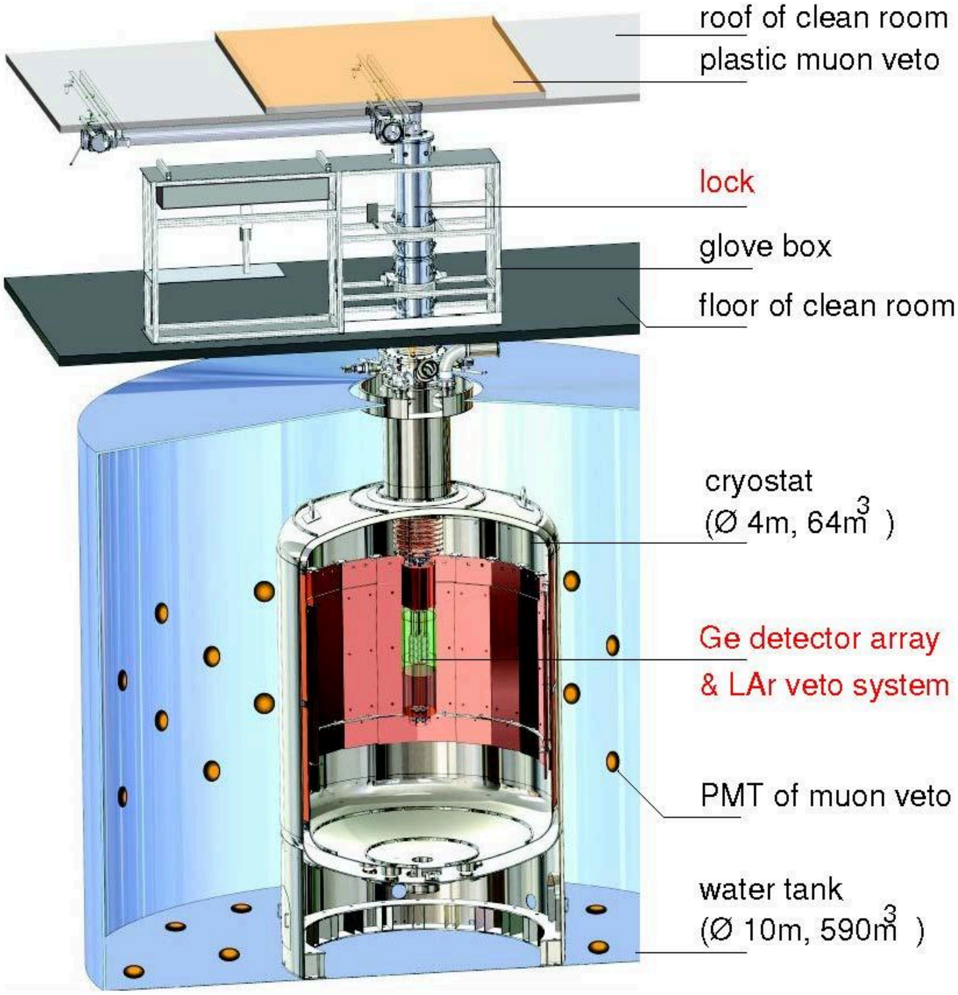

Figure 2: A schematic of experimental setup in GERDA Phase II with major components labled.

The GERDA experiment's realized setup in Phase I incorporates an array of germanium diodes suspended within a cryostat containing liquid argon, as depicted in figure 2. The cryostat is constructed from steel and is lined with copper from inside to minimize gamma radiation from the steel vessel. This cryostat resides within a water tank that acts as an additional passive shield and accommodates a muon veto system. The detectors are lowered into the liquid argon volume via a lock system situated in a clean room atop the water tank. To shield the cryostat's neck region, an additional muon veto system based on plastic scintillators is positioned above the clean room. This brief overview underscores the meticulous design choices made to minimize background sources and outlines the interconnected components in subsequent sections.

The Cryostat:

The cryostat configuration comprises two coaxial vessels encompassing torispherical domes, each with outer diameters of 4200 mm and 4000 mm respectively, in addition to corresponding cylindrical shells, towering approximately 4 meters in height. The cryostat spans a volume of 64 m^3 and is filled with liquid argon (LAr). It is built with stainless steel and is outfitted with an internal copper shield. The thickness of the copper shield, derived from considerations of the stainless steel's radioactivity characteristics, was fine-tuned to ensure that external sources of γ radiation, alongside the cryostat itself, contribute to the background index (BI) no more than 0.5×10^{-4} cts/(keV kg yr) [Bar09].

The Water Tank:

The water tank consists of a cylindrical body measuring 10 meters in diameter and standing 8.3 meters tall. An encompassing conical roof extends to a height of 8.9 meters, with the water level consistently maintained at 8.5 meters. The tank has a nominal capacity of 590 m^3 and envelops the cryostat with a protective 3-meter buffer of water. Functioning as a multifaceted barrier, it moderates and absorbs neutrons and reduces the influx of external γ radiation. Lastly, when filled with pure water, it acts as a Cherenkov medium, facilitating the identification of cosmic muons traversing through it.

Calibration System:

A crucial aspect of the GERDA experiment is its calibration system, which plays a key role in ensuring accurate and reliable measurements. To achieve this, biweekly calibration procedures are carried out using radioactive γ sources. These measurements are vital for establishing the energy calibrations and resolutions of the detectors and for tracking their stability over time. By monitoring specific γ lines, shifts in the energy scale can be detected, allowing for the identification of periods when individual detectors might exhibit degraded performance. Data from these periods can be either flagged for special treatment or excluded from the final analysis.

The calibration process is conducted by lowering three ^{228}Th calibration sources within the LAr cryostat in proximity to the detectors. Installed in June 2011, the calibration system forms an integral part of the GERDA cryostat setup. During the calibration run, the energy calibration of the diodes is computed using the distinct energy peaks of 7 prominent γ - lines in the ^{228}Th spectrum: 510.8 keV, 583.2 keV, 727.3 keV, 860.6 keV, 1620.5 keV, 2103.5 keV, and 2614.5 keV. The calibration function employs a second-order polynomial, designed to account for pulse-related ballistic defects and electronics non-linearities.

Muon veto:

Owing to the location of LNGS under the mountain, the rock overburden, equivalent to 3500 meters of water, results in a considerable reduction in the flux of cosmic muons to around ~1.25 per square meter per hour[Ger18]. Given that cosmic muons penetrating the experimental setup lose energy through both electromagnetic interactions and inelastic scattering with atomic nuclei, which may yield high-energy neutrons, the potential for indirect and direct background contribution from muons exists. These neutrons can initiate further inelastic interactions, generating additional radioactive isotopes and neutrons, thereby complicating the background scenario.

To effectively address these challenges, the experimental setup employs a muon veto system. This system capitalizes on the properties of Cherenkov light, emitted when particles travel through a medium faster than the speed of light in that medium. The water buffer enveloping the cryostat is instrumented with 66 photomultiplier tubes (PMTs) that detect the Cherenkov light produced by muons. This cost-efficient solution effectively identifies muons traversing the experimental environment. For muons entering the cryostat through its neck region, where they may only cross a limited water volume, an array of 36 plastic scintillator panels situated on the clean room's roof further augments the muon detection efficiency. The output signals from both the Cherenkov light detection system and the plastic scintillator array are amalgamated to form a muon veto, integrated into the germanium data acquisition (DAQ) framework. The muon veto system is designed to reduce the direct contribution of muon-related events to the background index (BI) as low as 10^{-5} counts per keV per kilogram per year (cts/(keV kg yr)) within the region of interest around $Q_{\beta\beta}$.

During Phase I, the detector array consisted of 4 strings housing 8 enriched semi-coaxial Ge detectors (15.6 kg total mass) and 3 natural Ge detectors. One string of natural Ge detectors was replaced with 5 BEGe detectors (3.6 kg total mass) in July 2012, serving as Phase II prototypes. During Phase I, an interpolated energy resolution at $Q_{\beta\beta}$ of 4.8(2) keV for enriched semi-coaxial detectors and 3.2(2) keV for BEGe detectors was observed and Background index of ~10^{-2}cts/(keV kg year) was achieved[Ago13]. No signal was detected for 0νββ decay, yielding a 90% CL limit of $T^{0\nu}_{1/2} > 2.1 \times 10^{25}$ years (median sensitivity 2.4×10^{25} years), disfavoring a prior claim [Kla04].

In the transition from Phase I to Phase II of the GERDA experiment, a significant advancement at mitigating background was achieved by integrating a comprehensive Liquid Argon (LAr) scintillation veto system. This upgrade yields substantial reductions in background index (BI) through notably improved discrimination between 0νββ signals and background events, primarily driven by their distinct energy deposition patterns. In 0νββ events, energy is deposited at a single location within the Germanium detector, whereas background events can deposit energy within the detector at multiple locations as well as the surrounding LAr. By capitalizing on this difference, background events are effectively identified and vetoed through the detection of scintillation light emitted by the LAr. Alongside, novel designs of enriched HPGe detectors of BEGe type were introduced, which showcase better energy resolutions and effective Pulse Shape Discrimination (PSD) performance.

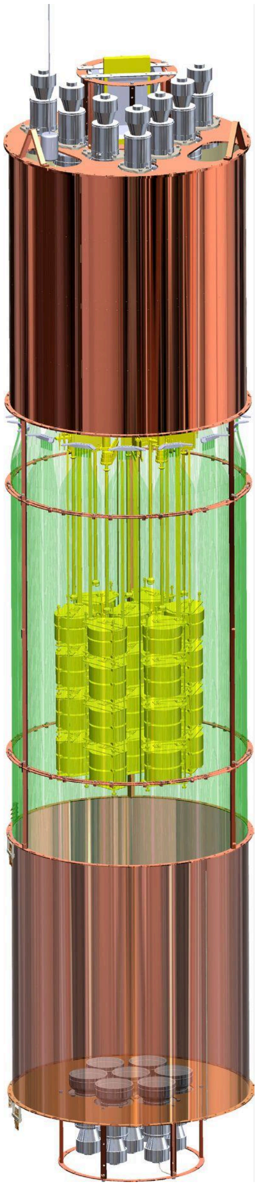

Nylon Mini-shroud:

During the commissioning of GERDA Phase I, a considerably higher than expected background index was observed along with a prominent presence of 1525 keV line from ^{42}K. This observation was due to radioactivity from the accumulation of charged ions including ^{42}K on the large n+ detector surface since these bare Germanium diodes have a high bias voltage of up to 4 kV. It was paramount to mitigate background due to ^{42}Ar which is a cosmogenic isotope of Argon and decays into ^{42}K with a half-life of ~33 years.Consequently, ^{42}K beta decays with half-life of 12.36 hours [Jan62] and a significant Q-value energy of 3.5 MeV. In Phase I, a copper cylinder so called “mini-shroud” was used around the detector array to mitigate the ^{42}K background. It screened the electric field of the detectors and acted as a physical barrier to prevent the drift and accumulation of charged ions on the detector's surface. This significantly reduced the level of the ^{42}K background by significantly reducing the volume from which ^{42}K ions could drift and accumulate on the detector surface. However, in Phase II, since a liquid argon (LAr) scintillation veto system was implemented to suppress various backgrounds, the copper MS couldn't be used. Scintillation light produced inside the copper MS wouldn't be detectable by the LAr instrumentation, drastically reducing the LAr veto system's effectiveness.

Figure 3: A schematic of a Nylon mini-shroud in Phase II to reduce ^{42}K background. Both the sides of nylon are coated with wavelength -shifting TBP to make it transparent for LAr veto system.

As an alternative to the copper mini-shroud, a new MS was developed for Phase II, made from ultra-pure nylon of 125 μm thickness. Unlike the copper MS, the nylon MS doesn't screen the electric field of the detectors but acts as a physical barrier, stopping the drift of ^{42}K ions toward the detectors. But Nylon is almost opaque to the ultraviolet scintillation light generated in liquid argon, therefore both sides of the nylon are coated with a wavelength shifter made of tetra-phenyl-butadiene (TPB). TPB shifts the 128nm scintillation light to around 450 nm, making it suitable for transmission through the nylon facilitating detection by the LAr veto system. Through this innovative approach, the combination of reducing ^{42}K collection on the Ge detector surface and employing the LAr scintillation veto led to a remarkable reduction of the ^{42}K background by over two orders of magnitude [Ack13].

Liquid Argon veto:

The Liquid Argon Veto system (LAr veto) in GERDA Phase II is designed to detect scintillation light produced by argon in the vicinity of the germanium detector array. This system was developed based on studies carried out in the low-background LArGe facility, where 8-inch photomultiplier tubes (PMTs) and silicon photomultipliers (SiPMs) coupled to wavelength-shifting fibers were utilized and demonstrated suppression of background by more than three orders of magnitude [Ago15]. In GERDA, the primary aim of the LAr veto is to identify and reject background events in the germanium detectors that deposit energy in the surrounding liquid argon (LAr) in coincidence, generating scintillation photons. These background events primarily include gamma-ray emissions from ^{228}Th decay chains in solid materials around the detectors. Additionally, it can effectively reject other types of background, such as muon events or decays from ^{42}Ar/^{42}K within liquid Argon volume.

The scintillation light around the detector array is detected using a PMT light readout system, comprising nine PMTs positioned at the top and seven PMTs at the bottom of the detector array. Within the central portion of the LAr veto setup, there is a curtain of wavelength shifting fibers, with coverage of ~50%. These fibers are linked to SiPMs for light detection and readout. The LAr light detection system in GERDA combines both PMTs and wavelength-shifting fibers with SiPM readout. This system is designed to be retractable, meaning it can be deployed alongside the germanium detector array into the cryostat through the lock system.

3.3. Background from β-decay of ^{42}K

The GERDA detector array is operated at cryogenic temperatures (87K) in liquid argon (LAr). Similar to other liquefied noble gases, argon exhibits a high scintillation light yield. It is transparent to its own scintillation light and can be relatively easily purified. Radioactively stable ^{40}Ar is the dominant isotope with >99% mole fraction [Bo14] in natural argon which originates from the electron capture of long-lived ^{40}K (^{40}K + e− → ^{40}Ar + ν) present in natural potassium within the Earth. Argon has two long-lived radioactive isotopes, 39Ar and ^{42}Ar, with half-lives of 269 years and 33 years, respectively [Chu99]. The 39Ar abundance in the atmosphere is sustained through cosmogenic production via reactions such as ^{40}Ar(n,2n)39Ar. Due to the relatively short half-life of 269 years of 39Ar, underground argon, shielded by rocks from cosmic radiation, experiences substantially lower levels of 39Ar contamination[Xu15]. The production of ^{42}Ar occurs through cosmic ray interactions in the upper atmosphere (^{40}Ar + α → ^{42}Ar + 2p). Both isotopes 39Ar and ^{42}Ar undergo β-decays with Q-values of 565 keV and 600 keV, respectively, which do not contribute to the background at Qββ of ^{76}Ge.

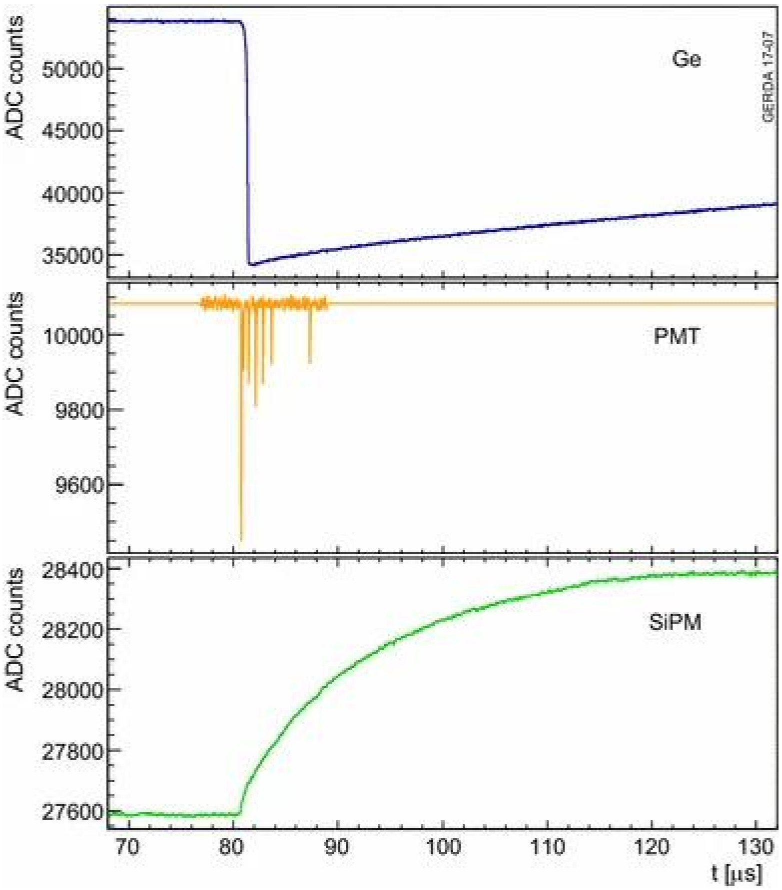

Figure 4: Sample traces of a background event with energy deposition in a Ge detector and the LAr veto system. Taken from [Ger18].

However, the daughter nuclide of ^{42}Ar beta decay, namely ^{42}K, has a significant Q-value of 3525 keV. As a β-emitting isotope, ^{42}K poses a substantial background source at Qββ. ^{42}K has a relatively short half-life of ~12 hours compared to 33 years that of ^{42}Ar. Thus, the concentration of ^{42}Ar in the LAr of the GERDA cryostat remains relatively constant. Approximately 18% of its decays involve β-particles accompanied by a 1525 keV γ-ray as shown in Figure 5. It's important to note that in the vicinity of the detector array, produced ^{42}K ions drift towards the detector due to the electric field generated by the applied bias voltage and get collected on the detector surface.

The n+ contact, covering nearly the entire detector surface, is insensitive ('dead') to ionizing radiation. In GERDA Phase II detectors, a typical dead layer is ~1.0 mm thick, providing partial shielding against background from β-decays on the detector surface. However, β-particles with energies up to 3.5 MeV have a range on the order of ~1 mm, allowing a small fraction of ^{42}K beta decays on the n+ surface to penetrate into the active volume of the detector.

Moreover, the transition between the dead and active detector volume is not sharply defined. Following the insensitive dead layer is a transition layer with incomplete charge collection, characterized by a zero electric field. Charges from energy deposition in this layer diffuse slowly until reaching the volume of non-zero electric field, where they drift towards the read-out contact. This incomplete charge collection results in energy loss, and due to the relatively slow process of diffusion, such events produce pulses with relatively slow rising-edge and are termed 'slow'pulses'. Consequently, β-decays from ^{42}K on the n+ surface typically generate slow pulses.

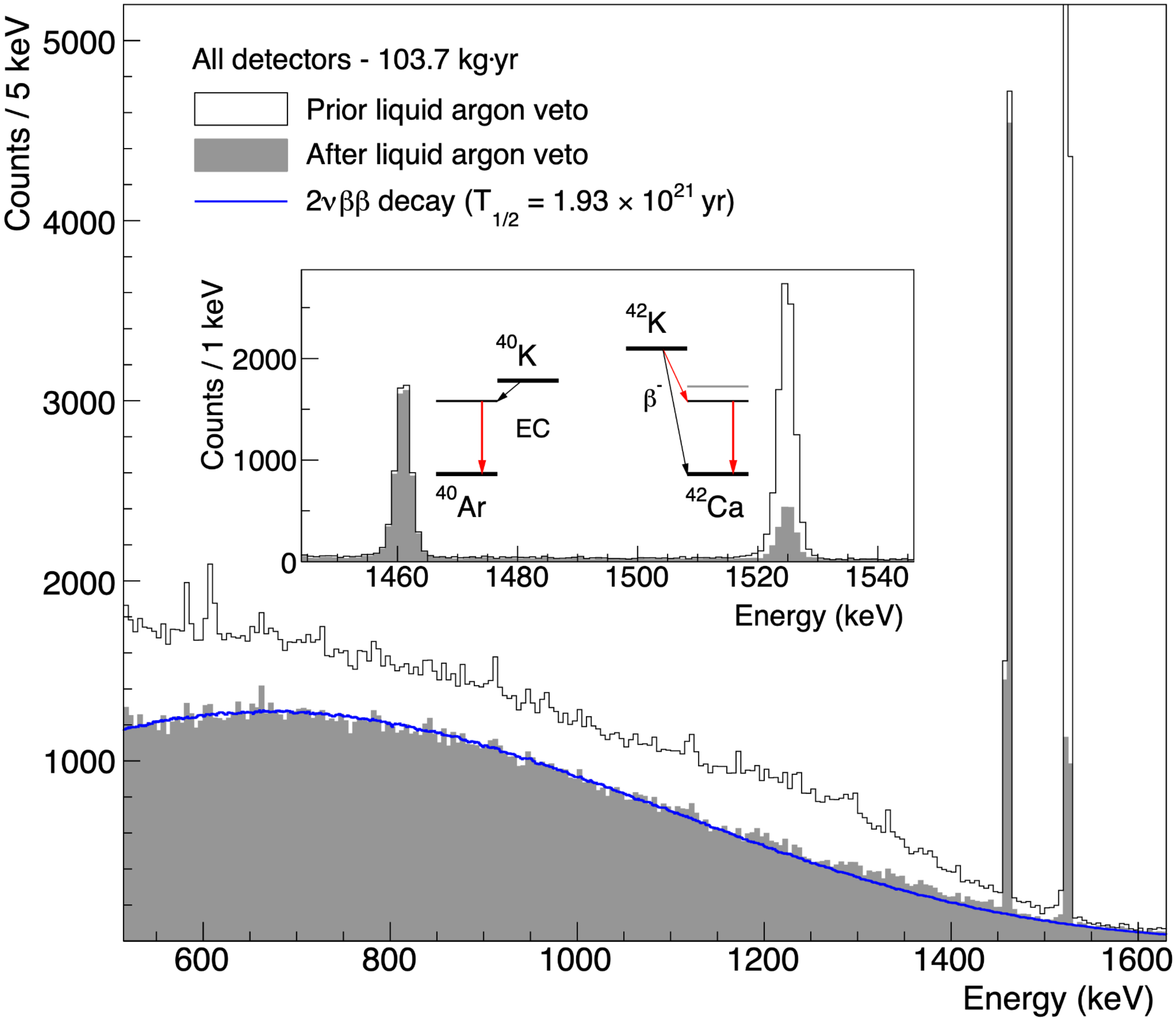

Figure 5: Energy spectrum of GERDA phase II events before and after applying liquid Argon (LAr) veto. The effectiveness of LAr veto is shown by suppression of ^{42}K peak compared with 40K peak.

The 1525 keV γ line stems from the decay of ^{42}K, which involves a β-γ cascade that can deposit up to 2 MeV in the LAr. The LAr veto system effectively reduces this line by a factor of about 5. In contrast, the 1461 keV γ line originating from ^{40}K, a single γ line, remains unaffected because it results from electron capture by 40K without any energy deposition in the LAr.

3.4. Radiation Detection : Interaction with matter

Semiconductor detectors are widely used in radiation detection applications due to their ability to convert the energy of radiation into measurable electrical signals. The working principle of semiconductor detectors is based on the band gap of the semiconductor material.

A semiconductor material, such as silicon or germanium, has a unique energy band structure with a small (~1 keV) energy gap between the valence band and the conduction band. In a pure semiconductor material, the valence band is completely filled with electrons, and the conduction band is completely empty. When an external energy, such as radiation, is absorbed by the semiconductor material, it can create electron-hole pairs in the conduction and valence bands, respectively.

The energy required to create an electron-hole pair in the semiconductor material is known as the band gap energy. The band gap energy is different for different semiconductor materials and determines the energy threshold for the detector to detect radiation. For example, silicon has a band gap energy of 1.1 electron volts (eV), while germanium has a band gap energy of 0.7 eV.

In a semiconductor radiation detector, the semiconductor material is doped with impurities to create a p-n junction. When a voltage is applied across the p-n junction, an electric field is established in the depletion region. As particles of high-energy radiation, such as gamma rays, enter the detector material, they interact with the atoms and generate electron-hole pairs through ionization. In the depletion region, the electric field separates electron-hole pairs and contributes to the electrical signal that may be measured.

The radiation detection by doped semiconductor detectors can be summarised in three steps:

Radiation absorption: When a high-energy radiation particle, such as a gamma ray, enters the detector material, it interacts with the atoms and creates electron-hole pairs via ionization. The number of electron-hole pairs created is proportional to the energy deposited by the radiation particle in the detector material.

Charge carriers drift: The electron-hole pairs generated by the ionization process are separated by the electric field in the depletion region. The electrons are attracted towards the p-type region of the detector, while the holes are attracted towards the n-type region of the detector.

Charge Collection: The separated charge carriers are collected by the contacts on the surface of the detector, which produce a measurable electrical signal. The signal is proportional to the number of electron-hole pairs generated and can be amplified and recorded by electronic circuits.

Many factors impact the performance of doped semiconductor detectors, including material parameters, doping level, detector size, and detector geometry.

3.4.1. Charged particles (alphas and betas)

Charged particles can interact with matter via a variety of mechanisms, including Coulomb scattering, energy loss via ionisation, and energy loss via radiation. When a charged particle travels through matter, it interacts with the electrons and can transfer energy to them.
The transfer of energy is affected by particle velocity and material density.
Coulomb scattering is the elastic scattering of charged particles caused by the electrostatic interaction of the charged particles with the material's atomic electrons. Although interaction of incident charged particles with atomic nuclei (as in Rutherford scattering or alpha particle induced nuclear reactions) are possible, they are rare and not significant in response of the typical radiation detectors. Instead, charged particle detectors must rely on the results of interactions with electrons for their response.

3.4.2. Photons (gamma rays)

When gamma rays interact with matter, it can do so through a variety of mechanisms, depending on the energy of the photon and the properties of the material it is interacting with. The main types of photonic interaction with matter are: photoelectric effect, Compton scattering, pair production.

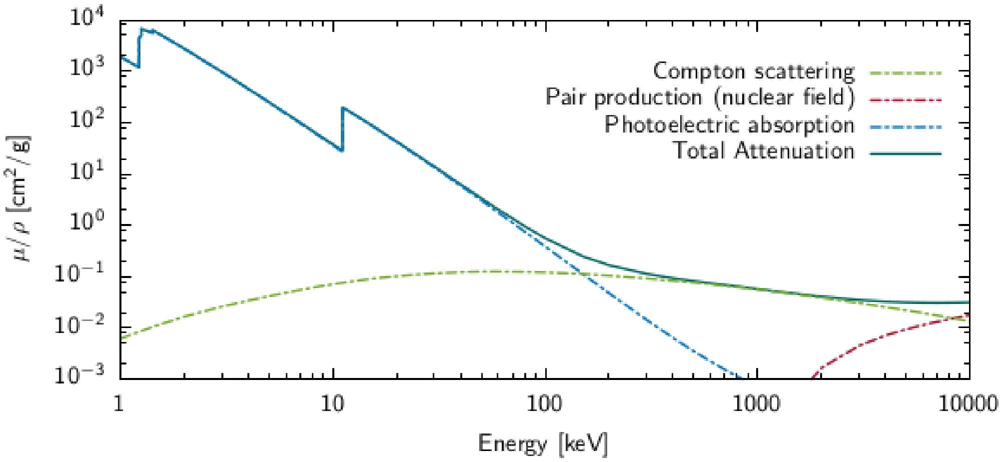

Figure 6: Attenuation coefficient as function of energy for different types of interactions of photons in germanium [Berg98].

Photoelectric effect:

In the photoelectric effect, a photon is absorbed by an atom, transferring all of its energy to an electron in the atom, which is then ejected from the atom. The electron is typically ejected from an inner shell of the atom, leaving behind a hole that can be filled by another electron from a higher energy level. The energy of the ejected electron is equal to the energy of the incident photon minus the binding energy of the electron, as described by the equation:

$$E_{e-} = h\nu - E_b$$

where h is Planck's constant, ν is the frequency of the incident photon, and E_b is the binding energy of the photoelectron.

The probability of the photoelectric effect occurring depends on the energy of the interacting photon and the atomic number of the material and can be expressed as [Knoll]:

$$P \propto \frac{Z^n}{E_\gamma^{3.5}}$$

where the exponent n is a function of photon energy E and varies between 4 and 5.

Compton scattering:

In Compton scattering, the incoming gamma-ray photon is deflected through an angle θ with respect to its original direction. The photon transfers a portion of its energy to the electron (assumed to be initially at rest), which is then known as a recoil electron.

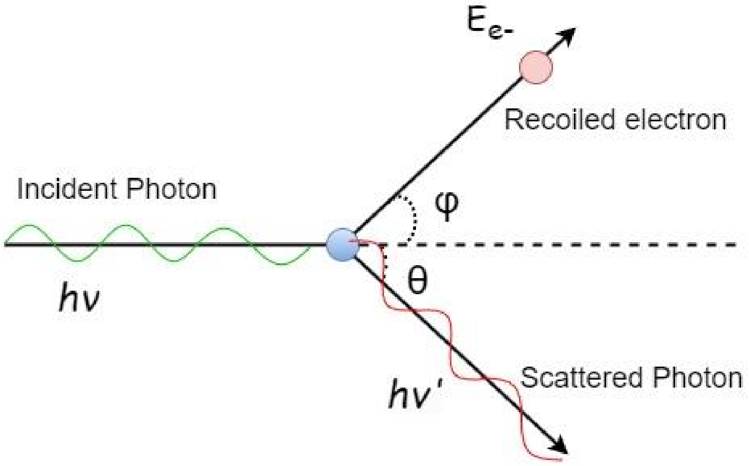

Figure 7: Schematic of Compton scattering

Because all angles of scattering are possible, the energy transferred to the electron can vary from zero to a large fraction of the gamma-ray energy and is expressed as:

$$E_{e-} = h\nu - hv'$$

where hv' is the energy of the scattered photon which is dependent on the scattering angle θ . By explicitly using conservation of energy and momentum, the energy of the scattered photon is expressed as:

$$hv' = \frac{hv}{1+\frac{hv}{m_e c^2}(1-cos\theta)}$$

The probability of Compton scattering depends on the energy of the photon and the atomic number of the material. In the intermediate energy range, the primary interaction mechanism involves Compton scattering, where a photon scatters off an electron, resulting in a partial transfer of energy. As the difference between the incoming and outgoing photon energies reaches its maximum when the scattering angle θ is π radians, the maximum possible energy of the recoiling electron is given by:

$$E_{e-,max} = h\nu - hv'(\theta = \pi) = \frac{2(hv)^2}{m_e c^2 + 2hv}$$

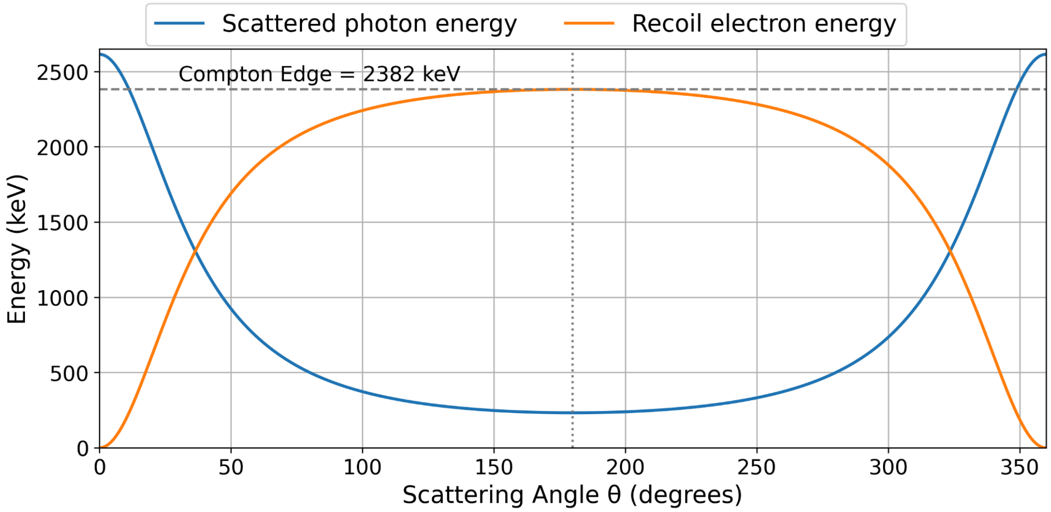

Figure 8: depicts the energy transferred to an electron as a function of scattering angle for the incoming 2614 keV photon from ^{208}Tl undergoing Compton scattering. The maximum energy transfer corresponds to 180^0 scattering angle and materializes as Compton edge around 2382 keV in the energy spectrum shown in the later section.

In radiation detectors, all scattering angles are typically encountered, leading to a continuous energy spectrum that ranges from zero up to this maximum, commonly referred to as Compton edge.

Pair production:

Pair production is energetically feasible if the gamma-ray energy is greater than twice the electron's rest-mass energy ($2m_ec^2$=1022 keV).The probability of pair production is low at gamma-ray energies that are only a few hundred keV over this threshold. Yet, as the energy rises into the many-MeV range, this interaction mechanism starts to dominate. The interaction transforms the gamma-ray photon into an electron-positron pair, which must happen in a nucleus' Coulomb field. The positron and the electron equally share all of the remaining energy carried in by the incident photon over the 1.022 MeV as kinetic energy.

$$E_{e-} + E_{e+} = h\nu - 2m_ec^2$$

The electron-positron pair deposits their kinetic energy within a small region (~few mm) in their immediate vicinity and can be treated as a single point deposition for all practical purposes.

Two annihilation photons are created as byproducts of the interaction because the positron will annihilate after slowing down in the absorbing medium. Conservation of momentum implies that the two annihilation photons each with energy $E\gamma = 511$ keV be emitted in opposite directions. Now, the annihilation photons can either escape the detector or interact with it further. These extra interactions may result in the partial or complete absorption of one or both photons of annihilation. The response of these annihilation gamma rays presents three possible scenarios depicted in figure 9:

a) Both ɣ-rays further interact and deposit all the energy within the detector, which would result in complete energy deposition from the radiation interaction and contribute to a Full Energy Peak (FEP) in the energy spectrum.

b) One of the two gamma rays deposits energy in active detector volume while the other escapes without interaction, which leads to deficiency of $511\,keV$ and appears as a Single Escape Peak in the energy spectrum.

c) Both the ɣ-rays escape the detector volume without interacting, leading to loss of $1022\,keV$ and results in Double Escape Peak (DEP) in the energy spectrum.

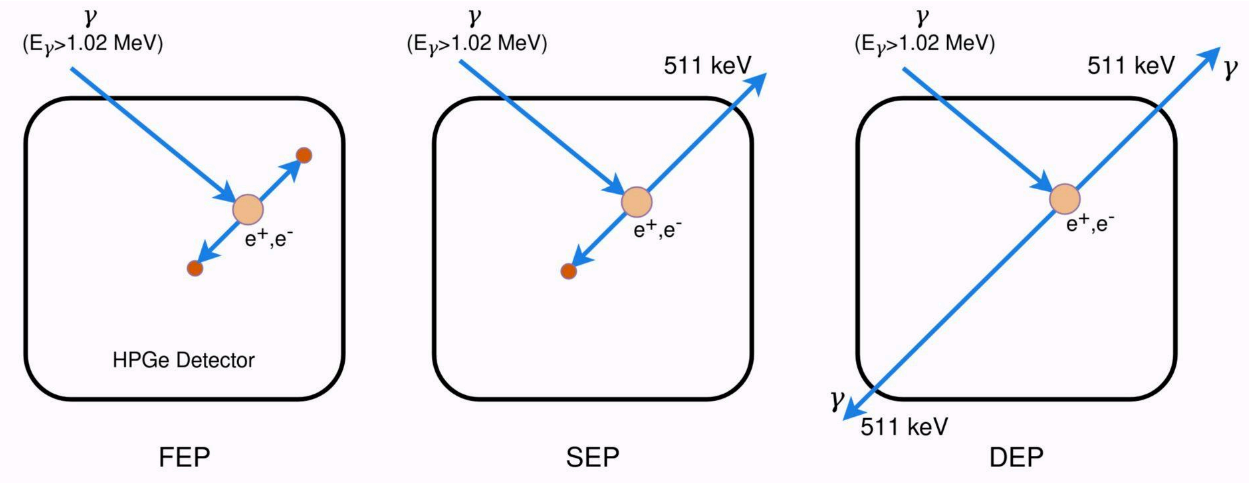

Figure 9: Possible realizations due to interaction of 2.614 MeV gamma ray from ^{228}Th via pair production

3.5. Detector Geometries in GERDA

In Phase II of the GERDA experiment, three different types of HPGe (High-Purity Germanium) detectors are employed, each possessing unique geometries and characteristics. These detectors have a lithium-diffused n+ contact of thickness 0.8-2.6 mm and a thin boron implanted p+ contact with thickness of ~300 nm. The HPGe detectors are used with a reverse bias voltage applied, effectively depleting the entire detector volume of free charge carriers. When an interaction occurs in the active volume, it generates electron-hole pairs based on the deposited energy. These charge carriers move in response to the electric field created by the applied positive bias voltage on the n + contact and the bulk impurity concentration. Electrons are gathered at the n + contact, while holes are collected at the p + contact, which serves as the readout.

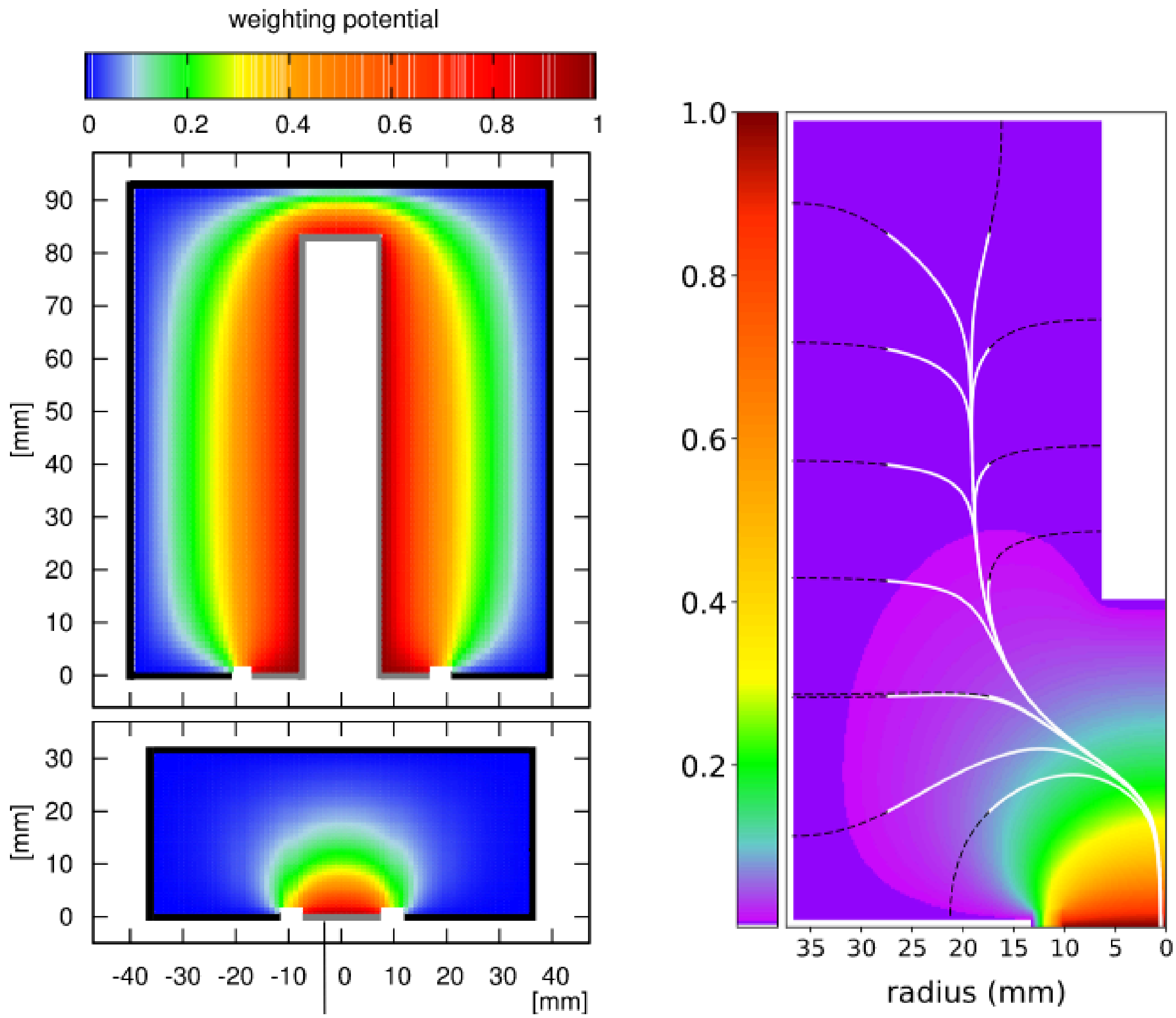

Figure 10: Detector geometry and weighting potential distribution for different detector geometries in GERDA: semi-coaxial (top left) , BEGe (bottom left) and Inverted coaxial (IC) on the right..

3.5.1. BEGe detectors

To improve the background index by an efficient pulse shape discrimination, GERDA collaboration incorporated 30 enriched HPGe detectors of BEGe design in Phase II. The BEGe detectors feature a cylindrical shape with a wrap-around lithium-diffused n+ layer and a flat boron-implanted p+ read-out contact. The p+ contact is centered on the high-impurity side of the crystal, separated by a passivated groove. The common drift-path of holes (h+) due to the high-weighting potential close to the p+ contact results in a standard response for energy deposition throughout most of the crystal volume irrespective of their spatial location, enabling high discrimination power for multi-site energy depositions with different drift times by Pulse Shape Analysis (PSA).

The BEGe detectors offer excellent energy resolution due to their reduced capacity of the small read-out contact, leading to low noise. Due to their characteristic weighting field distributions, they offer simple and efficient PSD techniques to discriminate between signal and background. All BEGe detectors in Phase II are custom-built using enriched Germanium with an average ^{76}Ge fraction of 88% and total mass of 20.02 kg.

3.5.2. Semi-coaxial detectors

Inherited from the former Heidelberg-Moscow and IGEX experiments, the seven semi-coaxial detectors contributed to most of the exposure during Phase I, and were included in Phase II.
The (semi-)coaxial detectors exhibit a coaxial geometric configuration characterized by a long concentric borehole, enabling the depletion of significantly larger diodes. The entire borehole surface is Boron-implanted and naked up the p+ contact. At the bottom, a passivated groove separates it from the remaining Li-diffused detector surface, which makes up the n+ contact. These detectors are the main ones used in GERDA Phase I and are redeployed for Phase II.
The signal contributions from both electrons (e-) and holes (h+) drift through a generally more homogenous weighting potential, leading to larger variation in response throughout the crystal and making PSD less efficient. The increased capacity of the large read-out contact offers poorer energy resolution compared to BEGe geometry. The average enrichment fraction of the enriched (semi-)coaxial detectors is 86.6% , with a total mass of 15.58 kg. Apart from these enriched semi-coaxial detectors, three semi-coaxial detectors with natural Germanium composition were used for coincident event studies for the initial part of Phase II and were later replaced by enriched detectors of inverted-coaxial geometry.

3.5.3. IC detectors

Inverted Coaxial (IC) detectors combine the benefits of a small readout contact of BEGe and a large detector mass of semi-coax geometry. They have a borehole opposite the p+ contact, which enables complete depletion of detector mass at a reasonable bias voltage.
Due to the similarity of weighting fields of IC detectors to their BEGe counterparts, the signal generation in IC detectors permits PSA performance comparable to that of BEGe. However, extended charge carrier drift effects, especially from the top part of the detectors, become significant and require drift-time corrections to account for it.
The IC detectors provide the baseline detector geometry for future use in LEGEND, as it brings the best of both other detector types by offering energy resolution improvement over semi-coaxial detectors and a much larger mass per detector compared to BEGe detectors.
During Phase II, the first five IC detectors with a total mass of 9.6 kg and ^{76}Ge enrichment of 88% were utilized.

Pulse Shape Analysis: Utilizing information derived from muon veto and the Liquid Argon (LAr) veto system, the GERDA experiment efficiently identifies background events and significantly reduce the background index. However, it's worth noting that certain background events may exclusively generate a signal within the germanium detectors with no energy deposition in LAr. In such scenarios, germanium detectors offer a unique capability to differentiate potential 0νββ events from background events by analyzing the topological characteristics of the corresponding charge and current pulses. Such an analysis is termed as pulse shape analysis (PSA). Since this analysis approach will be extensively employed throughout this dissertation, forthcoming sections will provide comprehensive information on signal generation in germanium detectors and the various PSA technique employed in the GERDA experiment for different detector geometries.

3.6. Signal formation in Germanium detectors

When ionizing radiation, such as gamma rays or charged particles interact with Germanium, they dissipate energy and generate electron-hole pairs. In germanium detectors being operated at liquid argon temperature of ~87K, around $3*10^5$ electron-hole pairs are generated per MeV of energy deposited [Eme65]. In p-type High Purity Germanium (HPGe) detectors, the p–n junction forms with the p-type bulk volume and the n+ contact, characterized by an ~1 mm thick donor-doped surface layer. Under operational bias voltages, the p-type bulk volume is completely depleted of free charges, constituting the active volume. Simultaneously, the n+ layer retains electrons in the conduction band, serving as the anode and forming a dead layer. The total electric field comprises contributions from both the bias voltage and the net space charge due to doped impurities.

The electric fields inside the detector can be computed by solving Poisson's equation by providing the potential of both contacts as boundary conditions.

$$\nabla^2\phi(r) = \frac{-\rho(r)}{\varepsilon} \quad , \quad \phi(p+) = 0 \ \ and \ \ \phi(n+) = V_{bias}$$

Where $\phi(r)$ is the electric potential, $\rho(r)$ is the space charge density and ε is the electrical permittivity of Germanium.

Under the influence of the applied electric field, the charge carriers (electrons and holes) created by the radiation drift towards the contacts. The speed and direction of their movement depend on the magnitude and direction of the instantaneous electric field within the detector.

The Shockley-Ramo theorem [Sho38] can be used to model the signal induced at the contacts due to movement of these charge carriers. Thus the charge and current induced on the contact are expressed as [He01]:

$$Q(t) = - q_0 . [\phi_w(r_h(t)) - \phi_w(r_e(t))]$$

$$I(t) = \frac{dQ(t)}{dt} = q_0 . [E_w(r_h(t)) . v_h(t) - E_w(r_e(t)) . v_e(t)]$$

where q_0 denotes total charge carried by charge carriers. $r_h(t)$, $r_e(t)$ and $v_h(t)$, $v_e(t)$ represent the instantaneous position and instantaneous drift velocity of holes and electrons respectively. The position dependent weighting potential and weighting field inside the detector is denoted by ϕ_w and E_w respectively. The weighting potential is dimensionless virtual quantity defined as electric potential within the detector with no space charge where the readout contact is at unit potential and other contacts are grounded. The weighting potential distribution within the detector satisfies the Laplace equation $\bigtriangledown^2\phi_w(r) = 0$ and can be calculated by setting boundary conditions $\phi_w(r)$=1 for readout contact and $\phi_w(r)$=0 for other contact. The weighting field represents the negative gradient of weighting potential inside the detector.

While the dynamics of the charge carriers is determined by the actual operating electric field, the current induced on the read-out contact can be calculated much easier with the help of the weighting field, as it involves solving the Laplace equation for weighting potential as no space charge is involved. The charge induced on the readout contact by moving charges is independent of the applied bias potentials and the space charge [[He01]. Evidently from equations above, the maximum induced charge on the readout contact by charge q is -q when the charge is infinitely close to the readout contact, and the minimum is 0 when the charge is infinitely close to the other contact.

Among GERDA HPGe detectors, the detectors with BEGe and IC design showcase a region of high weighting potential only around the p+ contact which results in the signal induced on readout contact being determined by the holes as they drift through this high weighting potential region and contribution from drifting electrons is negligible. Due to this inhomogeneous weighting potential distribution, the holes drifting toward the p+ contact follow similar paths irrespective of the spatial interaction position within the detector. As a result, events with similar energy deposition patterns such as single-site events exhibit a specific time structure of signal independent of interaction position. Only if the interaction position is very close to the p+ contact, the electrons' contributions are no longer negligible and contribute to the induced signal.

Contrary to this, due to the large size of p+ contact, the semi-coaxial detectors exhibit a relatively homogenous weighting potential across the detector volume and thus both electrons and holes contribute significantly to signal induced on the readout contact. Since the drift paths of the charge carriers within a semi-coax detector vary significantly depending on the interaction position, the topology of the charge signal is significantly dependent on the position of interaction. Thus events with specific energy deposition patterns such as single-site events exhibit varied time structure of signal making the pulse shape analysis a challenging task.

3.7. GERDA Data collection Phases and Data Partitioning:

To handle the variations arising from different setups and detector geometries, the dataset is partitioned into separate subsets. This allows each machine learning model to be tailored to the specific characteristics of the data, enhancing its adaptability and classification performance.

Phase I :

The commissioning phase of the GERDA experiment began in November 2009 and lasted until the beginning of Phase I in November 2011. During Phase I, the data collected was categorized based on the detector types used in the experiment, i.e., BEGe and semi-coaxial detectors. Semi-coaxial dataset was further subdivided into golden and silver datasets due to a brief rise in background level while installing the BEGe detectors in July 2012.

The BEGe and semi-coaxial detectors used in the Phase I datasets had a combined exposure of 23.5 kg.year.

Phase II:

Data collection for G ERDA Phase II started in December 2015 after a number of integration tests. Data collection lasted until November 11, 2019. Throughout Phase II, a total data lifetime of 3.4 years was accumulated, with an analysis-selected exposure of 103.7 kg yr. The GERDA Phase II data was divided into type-specific datasets due to the presence of various HPGe detector types and their varying performance in terms of energy resolution and Pulse Shape Discrimination (PSD). The detector array was upgraded in spring 2018 to accommodate 5 more HPGe detectors of inverted coaxial geometry.

Software for Data Processing and Simulation in GERDA :

Two specialised software frameworks, GELATIO and MaGe, are used by the GERDA experiment for data processing and Monte Carlo (MC) simulations.

GELATIO (GErda LAyouT for Input/Output) :

It serves as a powerful tool for the analysis and digital signal processing of the FADC (Flash Analog-to-Digital Converter) data acquired from the germanium detectors. It supports the entire analysis chain, from reading charge traces to calibration. The framework can accommodate a number of veto channels coming from the liquid argon (LAr) and muon veto systems. GELATIO offers a variety of waveform transformations and data containers and is based on MGDO (Majorana GERDA Data Objects), a collaborative development between the GERDA and Majorana collaborations.

MaGe (Majorana-GERDA):

The GERDA and Majorana collaborations worked together to create MaGe (MAjorana-GErda), which is based on the well-known simulation toolkit Geant4. MaGe specialises in offering specialised physics lists for low-energy process simulation. The software includes all of the experimental setups' geometries, including the complete GERDA geometry. Additionally, it provides useful tools like pre-built simulations of basic geometries without the need for hardcoded implementation, interfaces to widely used event generators (like Decay0), random sampling of events in bulk volumes or on surfaces and decay chain simulations to list a few.

3.7.1. Data acquisition:

GERDA Phase II initiated data collection in December 2015 and underwent a brief pause in the summer of 2018 for setup upgrades, and ended in November 2019. The data acquisition process was structured into sequentially numbered subsets called “runs”, with each run capturing data under a consistent hardware configuration, keeping the setup unchanged throughout the run.

As discussed earlier, Ionizing radiation in germanium detectors creates electron-hole pairs, generating a signal as they drift toward the contacts. The charge signals produced by the HPGe detectors consist of three components:

Baseline: This represents the signal recorded just before the particle interaction occurs.

Rising edge: The rising edge involves the signal rising from the baseline level to its peak amplitude, typically in less than 1 μs.

Exponential Decay Tail: An exponential decay tail is due to the RC preamplifier feedback with a typical time constant (τ) of around 150 μs.

Once the signal in one of the HPGe detectors exceeds a predefined threshold, it triggers the data acquisition system and signals from all HPGe detectors and PMTs and SiPMs of LAr veto system are digitized with 14-bit flash-ADCs (FADC) and stored for later analysis. The muon-veto system detectors, which encompass Cherenkov light PMTs and plastic scintillators, have an independent data acquisition system which provides a muon veto flag. All the recorded waveforms are centered in time around the event trigger position. Each waveform from an HPGe detector was digitized at a sampling rate of 25 MHz, with a trace length of 160 μs. This is referred to as the low-frequency (LF) trace. Additionally, a high-frequency (HF) trace was recorded at sampling frequency of 100 MHz and trace length of 10 μs. While the LF trace served as the primary basis for most Digital Signal Processing (DSP) tasks, the HF trace facilitated more precise analysis of the rising edge of the signal.

3.7.2. Monitoring stability of data acquisition system:

In addition to recording waveforms due to physical events, two types of artificial waveforms were injected into the preamplifier of each HPGe detector at regular intervals with an external trigger.

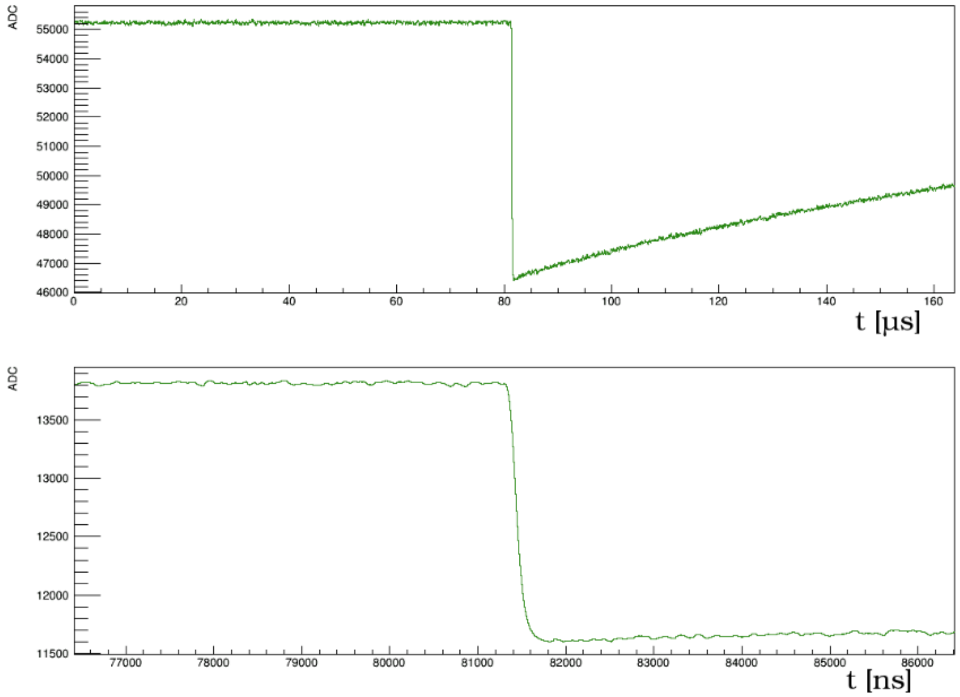

Figure 11: The two traces for an HPGe detector: a 160 μs LF trace at 25 MHz (top) and a 10 μs HF trace at 100 MHz (bottom)

Test Pulses (TP): At regular 20-second intervals, a pulse was introduced into the preamplifier of every HPGe channel simultaneously. While this pulse closely resembles a physical pulse, it has a slightly faster rising edge and an energy equivalent to about 3 MeV. Test pulses are used to evaluate the duty cycle and live-time of each HPGe detector and monitor preamplifier stability.

Baseline Events(BL): With an external trigger every 47 seconds (40s after upgrade in Nov’16), the empty traces featuring the baseline data from each HPGe channel were recorded. These events were used to monitor the stability of baseline over the period of corresponding data taking “run”.

These artificially induced waveforms were used to monitor the stability of data acquisition and estimate the efficiency of the quality cuts which will be discussed later.

3.7.3. Quality Cuts

Besides the genuine "physical" events originating from energy depositions in the detectors, there are parasitic events triggered by the DAQ system that do not correspond to actual physical interactions. To address this challenge, GERDA employs a set of stringent quality cuts to distinguish and eliminate such non-physical events, ensuring a higher level of data purity and accuracy in the analysis. During Phase I, a series of quality checks were applied to individual waveforms to identify those associated with genuine energy depositions. Moving on to Phase II, to effectively mitigate the impact of micro-discharges, quality cuts were refined from an individual waveform-based approach to an event-based approach. Thus the quality of all waveforms within a given event is evaluated and any event with at least one waveform failing the quality cuts would subsequently be discarded.

The quality cuts are designed to capture the full collective behavior of events, incorporating information from every single HPGe detector's waveform trace. The objective is to differentiate between proper signals, baseline fluctuations, pile-up traces and traces that saturate the dynamic range of the FADC channel. One typical example of a non-physical event is micro-discharges in the HV-lines, which generate strong signals of inverse polarity, often exceeding the dynamic range of the affected FADC channel. Additionally, electronic crosstalk may induce baseline fluctuations with features similar to a normal signal in neighboring channels.

Waveform Classification: Each waveform is subjected to a set of non-exclusive criteria based on waveform parameters extracted using Digital Signal Processing (DSP) algorithms.
Based on these criteria, an event is categorized into one of the four groups: baseline, physical, pile-up or saturated waveform.
Baseline waveforms: These waveforms have no signal in them, so they appear flat and without any distinctive features.
Physical waveforms: To be considered a physical waveform, it must contain a strictly singular pulse. The first half of the waveform should be flat, and the only trigger position must align with the center of the trace.
Pile-up waveforms:

Pre-trace pile-up: This is when a decay tail of a signal from a previous event overlaps with the current waveform and is determined by an exponential fit to the baseline.

In-trace pile-up: In certain instances, multiple pulses could be present within a single waveform and are identified by counting the number of the triggering pulses.

The probability of occurrence of pile-up during physics data taking is negligible due to the low count rate, which is not the case during calibration data taking.
Saturated waveforms: These waveforms saturate the dynamic range of corresponding FADC channel and are tagged by the FADC.

Quality cuts are applied in the standard tier2 calibration analysis to ensure data integrity. These cuts are meticulously tuned to eliminate signals reconstructed from waveforms with no physical origin. These quality cuts effectively tag almost all non-physical events improving the purity of the dataset. The physical events at $Q_{\beta\beta}$ are kept with efficiency larger than 99.9% [Ago20].

3.8. Energy Calibration with ^{228}Th sources

The main goals of the calibration analysis are to define and maintain a stable energy scale over years of data collection and to determine the resolution of the detectors. Given that the signature of 0νββ-decay in germanium detectors is a peak at a known energy of 2039 keV, precise energy calibration is crucial for this decay search. It is essential to accurately identify the peak region and reject all background events with different energies, combine data from various detectors over extended periods, and effectively leverage the excellent energy resolution of germanium detectors.

Germanium detectors are calibrated by exposing them to ^{228}Th sources with an activity of about 10 kBq. As illustrated in the decay scheme in Figure 12, ^{228}Th decays through multiple α and β decays to ^{208}Pb. The resulting energy spectrum, an example of which is shown in Figure 13 is recorded separately for each detector. The gamma line pattern in the spectrum is used to identify specific gamma lines and calibrate the detector's energy scale based on their known energy positions. Additionally, the resolution of a detector can be determined from the width of these gamma lines.

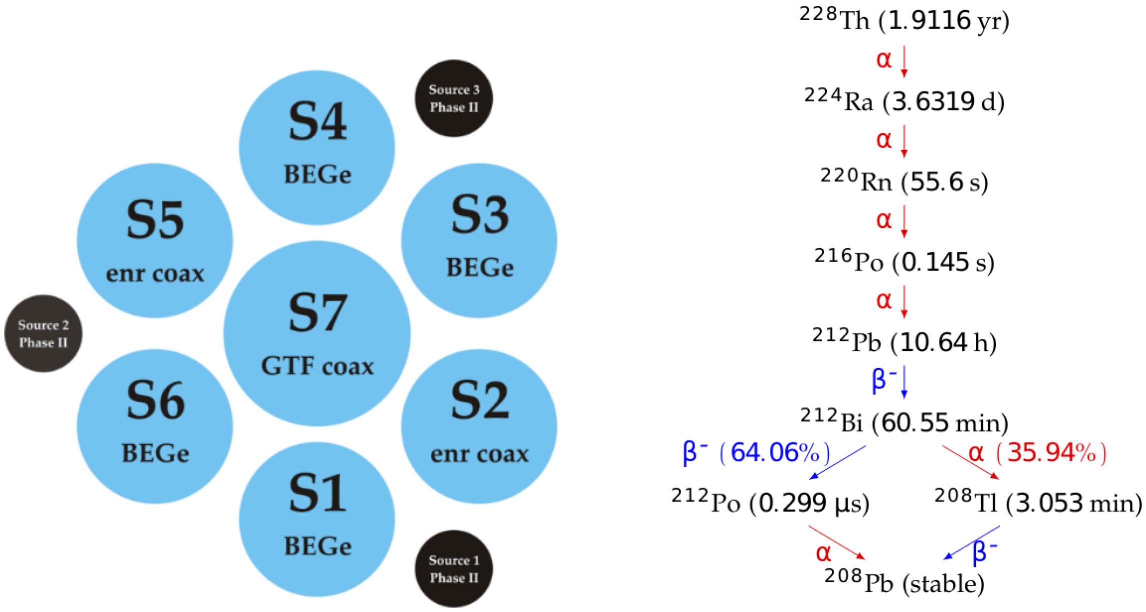

Figure 12: . a)Top view of the strings and calibration source positions in GERDA Phase II array b) Partial decay chain of ^{228}Th decay

The energy calibration process in GERDA Phase II involves exposing the germanium detectors to three ^{228}Th sources, each with an activity of ~10 kBq conducted at regular intervals. During regular operation, the ^{228}Th sources are placed approximately 8 meters above the detector array, enclosed in stainless steel capsules with tantalum shields. Three sources are used, positioned around the detector array as shown in Figure 12. For calibration, all three sources are simultaneously lowered to three specific heights, near the bottom, center, and top of the array, at depths of 8220 mm, 8405 mm and 8570 mm respectively below their initial storage position. Data is collected at each height for ~30 minutes to ensure enough statistics for calibration gamma lines, especially the double escape peak, while minimizing calibration time. During calibration, the photomultiplier tubes (PMTs) of the LAr veto system are turned off due to high event rates.

Energy Calibration and detector resolution:

The choice of ^{228}Th as the calibration isotope is based on practical considerations, including its half-life of 1.9 years. ^{228}Th decays through a series of α and β decays until it reaches the stable isotope ^{208}Pb, generating many monoenergetic γ rays during the decay-chain process. A representative decay scheme of ^{228}Th decay chain is shown in Appendix indicating major gamma lines. These γ rays span a wide energy range, forming a distinctive pattern in the resulting energy spectrum. Initially, energy spectra are analyzed to identify prominent peaks corresponding to known energy lines. Typically, between 5 to 8 peaks are identified in each detector. The most consistently identified peak is the strong 2615 keV line. If this peak is not identified, the peak identification process is considered to have failed. This calibration is done with upto 5 to 8 prominent gamma-lines of ^{228}Th decay-chain out of identified peaks at energies of 583 keV, 727 keV, 785 keV, 861 keV, 1592 keV, 1620 keV, 2103 keV, and 2614 keV. All of the gamma lines mentioned above can be traced back to beta-decays of ^{208}Tl and ^{212}Bi along the ^{228}Th decay chain. An illustrative calibration spectrum is provided in Figure 13 below highlighting major gamma lines used for energy calibration. Summation lines, resulting from simultaneous detection of two γ rays in coincidence with energies above 2.6 MeV, are identified by their high intensity in summed calibration spectra and reliably associated with the 2.6 MeV line but are ignored in energy calibration process as they are not statistically significant individually in a single calibration spectrum.

The centroids of the gamma-line peaks are estimated by fitting a Gaussian function for the peak, superimposed on a sigmoid function that accounts for background. The calibration curves are generated by fitting the calculated centroids of the gamma line peaks with a linear function.

$$E(x) = a + bx$$

where x represents the uncalibrated energy and E(x) is known literature value for the same gamma-line peak.

The estimation of energy resolution as a function of energy involves fitting the square root of the best values of gamma-line widths (σ) with the function $\sigma(E) = \sqrt{a + b \cdot E}$, where 'a' and 'b' are two fit parameters. As per convention, the energy resolutions of HPGe detectors are then quoted in terms of the Full Width at Half of Maximum of Gaussian(FWHM) fit where $FWHM(E) = 2.355 * \sigma(E)$

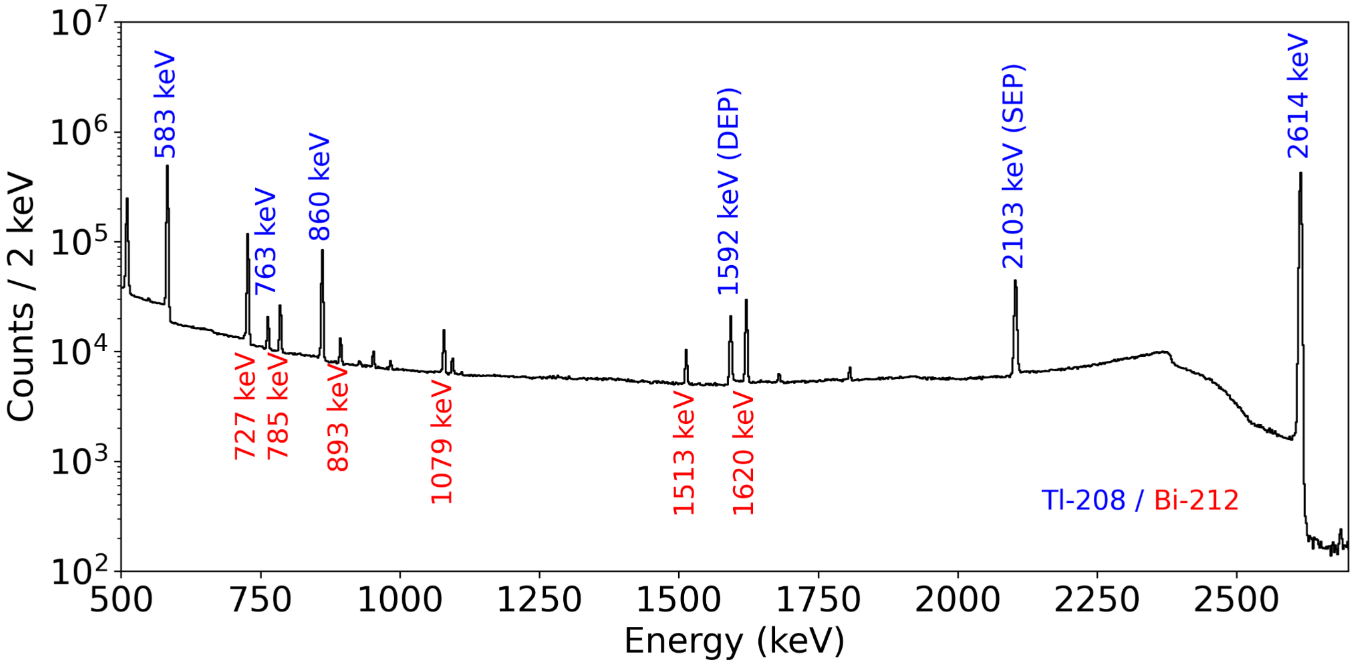

Figure 13: Energy spectrum of ^{228}Th source utilized for energy calibration in GERDA. The recorded spectrum is for ANG3 and is summed over all calibration data in Phase II (before upgrade). The major gamma peaks are highlighted along with their parent isotope (^{208}Tl/^{212}Bi).

Detector Type	Energy Resolutions at $Q_{\beta\beta}$ in terms of FWHM (keV)		
	Pre-upgrade	Post-upgrade	All Phase II
BEGe	2.9 ± 0.3	2.6 ± 0.2	2.8 ± 0.2
COAX	3.6 ± 0.3	4.9 ± 1.4	4.0 ± 0.9
IC	-	2.9 ± 0.1	2.9 ± 0.1

Table 4: A summary of the exposure-weighted average energy resolutions at Qββ for various detector types, further categorized into data partitions as pre-upgrade and post-upgrade[data taken from [GSTR20]. The uncertainties quoted arise from the spread of resolution among the detectors of each type from two partitions of the dataset.

The calibration data is stored on the DAQ machine and processed during data production to generate tier1 data containing waveforms in ROOT format and tier2 data containing processed waveform properties, such as different energy estimators. Energy calibration uses tier2 data with uncalibrated energy estimators. The resulting calibration curves describe the relationship between uncalibrated energy estimators and physical energies, applied in generating tier3 data, where only physical energies are stored. The two energy estimators used in higher-level data analysis are the Gauss energy and the ZAC energy. Both estimators take the maximum of a waveform after applying a digital filter.

3.8.1. Data of interest for Pulse Shape Analysis :

The calibration process also leverages the topologies of specific γ ray events. The highest energy and intensity γ ray in the decay chain is the 2.6 MeV γ ray emitted during the ^{208}Tl decay. When this γ ray interacts within the detector volume, it may undergo (e+,e-) pair production. The resulting electron deposits its energy in the detector, while the positron quickly thermalizes and subsequently annihilates with an atomic electron in the detector as described in earlier section in detail. This annihilation process generates two 511 keV γ rays, which may either be absorbed within the detector or escape. The energy spectrum shows specific peaks, such as the Full Energy Peak (FEP) at 2614.5 keV when all energy stays within the detector. The Single Escape Peak (SEP) at 2103.5 and Double Escape Peak (DEP) at 1592.5 keV occur when one or both γ rays escape respectively. DEP is particularly interesting as its energy deposition by the electron-positron pair resembles that of two electrons emitted in ββ decay depositing entire energy at one site and hence can be used as a proxy for potential 0νββ signal to perform pulse shape analysis. Conversely, the FEP at 1621 keV for ^{212}Bi dominantly undergoes multiple compton scatterings and produces energy depositions at multiple sites within the detector. behavior. These peaks are crucial for training and calibrating pulse shape discrimination methods, which will be discussed in detail in the next chapter.

3.9. Physics Data

After several integration test runs throughout 2015, GERDA Phase II data collection commenced in December 2015. The array was upgraded in spring 2018 to include additional HPGe detectors. The data taking was finished in November 2019. The total data collected over this period represents experiment lifetime of 3.4 years, yielding an exposure of 103.7 kg·yr.

The data was collected in runs, each representing a single unaltered hardware configuration without any setup changes including bias voltage adjustments. Each run varied in length since the hardware changes were aperiodic in nature. During the runtime, calibration sub-runs were carried out to monitor energy calibration stability. Pre-upgrade Phase II data includes runs 53 to 93, while post-upgrade data covers runs 95 to 114. Earlier runs pertain to Phase I and integration tests, including run 94.

For each run, a specific list describes the state of each HPGe detector and its usage in the analysis. The states are as follows:

ON: Detectors that show stable performance and are properly calibrated throughout the run are considered ON. Only these channels contribute to the analysis exposure.

OFF: Detectors that do not produce proper signals and would spoil the event-based quality cuts are set OFF and are ignored in the analysis.

Anti-Coincidence (AC) Mode: If a detector produces proper signals but has unstable calibration, such as due to gain instabilities, it is used for providing anti-coincidence information and is set to AC mode.

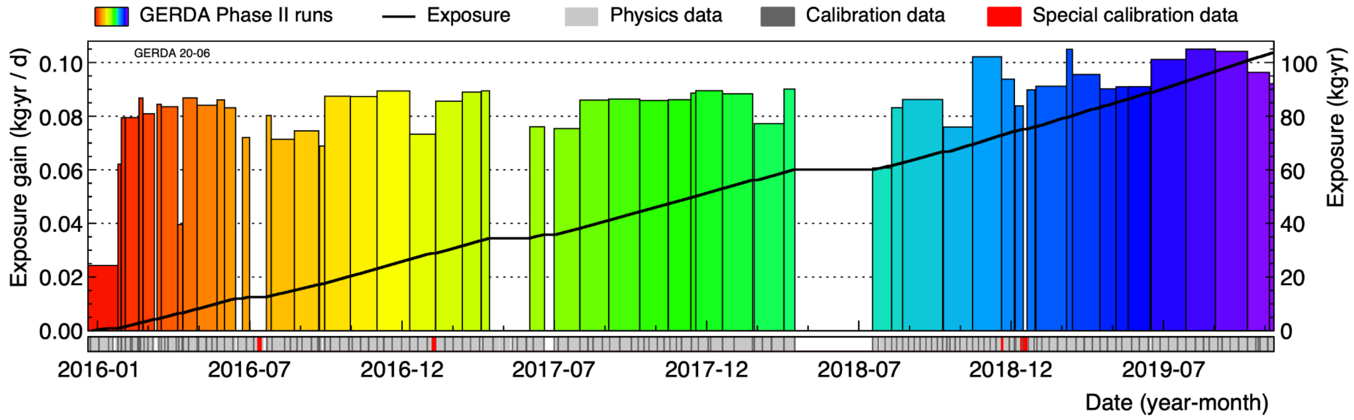

Figure 14: shows exposure accumulation, with each bar's area representing the analysis exposure for a specific run. The total exposure is 103.7 kg·yr. The type of data taken during each period is indicated on the bottom bar.

Figure 14 provides a detailed summary of the Phase II data-taking history. The bottom panel shows the data-taking profile, indicating which data type was collected during each period. The top section displays the accumulated valid analysis exposure rate per run. Initially, runs were short and had low exposure gain due to setup interactions and instabilities. After half a year, longer and higher exposure runs followed. The only significant gap in data collection corresponds to the upgrade period, while earlier gaps in exposure accumulation were due to problematic periods.

3.10. Overview of Background in GERDA Phase II

The GERDA experiment is designed to search for the extremely rare process of neutrinoless double beta decay ($0\nu\beta\beta$) in ^{76}Ge. Given the rarity of this decay, the experiment requires exceptionally low background. In GERDA Phase II, the background is meticulously analyzed and modeled in [Ger20]. The background sources can be categorized into several key components, each contributing to the observed spectra in the detectors.

1. Natural Radioactivity

1.1 ^{232}Th and ^{238}U Decay Chains

The natural decay chains of ^{232}Th and ^{238}U are significant sources of background in the GERDA experiment. These chains involve multiple isotopes that can emit high-energy gamma rays and beta particles, which may be detected by the germanium detectors.

Isotopes Considered:

From the ^{238}U decay chain: ^{234m}Pa, ^{214}Pb, ^{214}Bi

From the ^{232}Th decay chain: ^{228}Ac, ^{212}Bi, ^{208}Tl

These isotopes are assumed to be in secular equilibrium within their respective decay chains, meaning that the parent and daughter isotopes maintain a constant activity over time. The gamma and beta emissions from these isotopes do populate energies up to ~3MeV making them relevant for background considerations in the energy window around the 0νββ Q-value (2039 keV).

1.2 Alpha Emitters

Alpha particles present another significant background challenge, particularly those emitted by ^{210}Po and ^{226}Ra isotopes in ^{238}U the decay chain, which may contaminate the detector surfaces. The detectors have a thick lithium-diffused n+ surface that acts as a barrier against alpha particles. However, alpha particles can still penetrate the thin (~0.5 μm) boron-implanted p+ contact or the groove separating the contacts. If alpha particles are emitted directly at the surface or from a thin adjacent layer of liquid argon (LAr), they can deposit only part of their energy in the active detector volume, leading to characteristic low-energy tails in the spectra. Events originating from the detector grooves, where energy degradation occurs, contribute to a continuous background component. This is particularly challenging because it creates a spectral feature that overlaps with the region of interest for the 0νββ search.

2. Cosmogenic and Anthropogenic Isotopes

2.1 ^{60}Co Contaminations

^{60}Co is a cosmogenically produced isotope that can be introduced into the experimental setup through the activation of materials, particularly copper, by cosmic rays. ^{60}Co decays with a half-life of 5.27 years, emitting gamma rays with energies of 1173 keV and 1332 keV.

2.2 ^{40}K Contaminations

^{40}K is another common contaminant found in experimental setup materials. ^{40}K decays with a half-life of 1.248×10^9 years, producing a prominent gamma line at 1460 keV, often visible in the GERDA spectra, with typical accumulated statistics of around ~100 counts per detector. Since its decay energy is much below the Q-value of 0νββ, it does not contribute to the background in ROI.

2.3 ^{42}K and ^{39}Ar in Liquid Argon

The liquid argon (LAr) surrounding the detectors can contain cosmogenically produced isotopes, such as ^{42}Ar, which decays to ^{42}K with a half-life of 32.9(11) years [Sto65].

Subsequently, ^{42}K decays via beta decay with a half-life of 12.36 hours and a Q-value of 3525 keV. This decay is particularly problematic because the beta particles can be detected if the decay occurs close to the detector surfaces, contributing to the background in the ROI. The distribution of ^{42}K in LAr is likely inhomogeneous due to drift and convection of charged ^{42}K ions, potentially leading to significant background variations across the detector array.

^{39}Ar decays predominantly by beta emission with a maximum energy of about 565 keV. While it dominates the spectrum below this energy, it does not directly affect the ROI for 0νββ.

3. Detector Surface and Bulk Impurities

3.1 Surface Contaminants

This background component typically originates from alpha and beta-emitting isotopes on or near the detector surfaces. Contaminants like ^{210}Po and isotopes from the ^{226}Ra decay chain can emit alpha particles that penetrate the thin p+ contact and deposit partial energy in the detector, resulting in characteristic peaks with low-energy tails. Similarly, beta particles from ^{42}K decays can penetrate thin p+ contact and contribute to the overall background. These surface events can be mistaken for signal events unless effectively discriminated against.

3.2 Bulk Impurities in Germanium

While germanium crystals used in GERDA are of exceptionally high purity, there is still a possibility of cosmogenically produced long-lived isotopes like ^{68}Ge and ^{60}Co being present as bulk impurities. ^{68}Ge decays with a half-life of 271 days and due to the careful handling of detectors, which were mostly kept underground during their fabrication, the expected contribution from these isotopes is very low. For instance, contributions from ^{68}Ge and ^{60}Co around the Q-value of 0νββ are expected to be less than 10^{-4} counts/(keV·kg·yr), making them negligible.

4. External Sources

4.1 Muon-Induced Backgrounds

Cosmic muons and their secondary particles can introduce background events in the detectors. Although these are rare in the underground environment of the GERDA experiment, they can still pose a problem. The GERDA setup includes a water tank instrumented with Photo-multiplier tubes that acts as a Cherenkov detector to identify and veto events caused by muons passing through the experiment. This significantly reduces the muon-induced background, which is estimated to be around 3×10^{-5} counts/(keV·kg·yr)[Ger20].

Other potential background sources include neutron interactions with ^{76}Ge or contamination from external sources like the water tank and LAr cryostat. However, these contributions are generally very low and are considered negligible. For the 7 enriched semi-coaxial detectors, the combined data taken from December 2015 till April 2018 and it's corresponding background model fit is depicted in Figure 15 below. It is important to note that the distribution displayed in Figure 15 is the total unsuppressed background and was determined prior to the application of LAr veto or any of the pulse shape discrimination techniques.

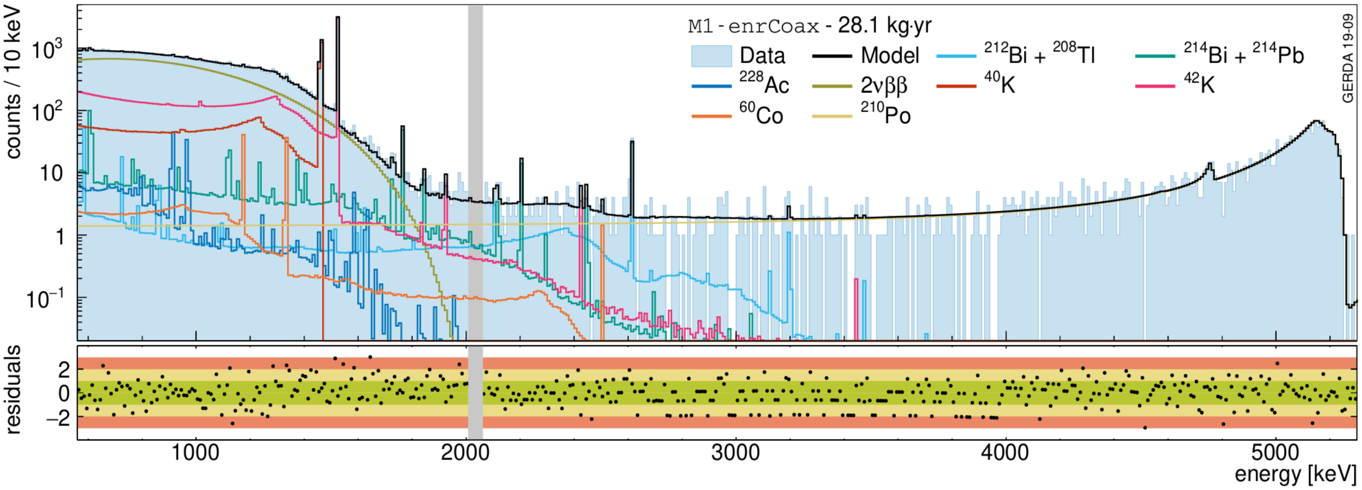

Figure 15: Background decomposition of the enriched semi-coaxial data set, showing the fit of different background components (taken from [Ger20]). The plot illustrates the energy distribution of events before any analysis cuts with contributions from various sources, including the surface alpha component (yellow) and the ^{42}K component (pink). The blinded region $Q_{\beta\beta}$±25 keV is highlighted in gray. The lower panels display normalized residuals with 1σ, 2σ, and 3σ bands marked in green, yellow, and red, respectively, indicating the fit's accuracy.

The gamma ray induced background at $Q_{\beta\beta}$ is predominantly due to the Compton scattered gamma ray depositions inside detector volume from decays of ^{212}Bi, ^{208}Tl , ^{214}Bi and ^{214}Pb isotopes from the ^{232}Th and ^{238}U decay chains. These Compton scattered gamma rays have different energy deposition patterns compared to the ββ decay. This is utilized to train a neural network based pulse shape discrimination technique to mitigate the gamma-induced background component, which is described in detail in subsequent sections.

For semi-coaxial detectors, ^{42}K is likely accumulated close to the p+ contact surfaces of the detectors. As evident from Figure 15 ,^{42}K component depicted with pink spectrum contributes notably to the background index (BI) around the Q-value of the 0νββ decay, with an estimated activity of 22±4 μBq, corresponding to a BI contribution of $(7\pm1)\times10^{-3}$ cts/(keV·kg·yr) [Ger20]. This result contrasts with the BEGe detectors, where the presence of ^{42}K on the p+ contact is not significant. The different behavior between the detector types may be attributed to the specific geometry of the semi-coaxial detectors, where the ^{42}K ions are more likely to be trapped near the p+ contact, unable to escape due to the bore-hole geometry

The analysis also examines alpha events in the energy spectrum, particularly focusing on the ^{210}Po peak at 5.2 MeV. The semi-coaxial data set includes a significant contribution from degraded-energy alpha events, which extend down to the Q-value of the 0νββ decay as depicted with yellow spectrum in Figure 15. This degraded alpha background is described by an empirical linear model that fits the data well. Note that ^{210}Po decays with a relatively short half-life of 138.3763(17) days [Be08] and the alpha component of the background decays exponentially over time.

The overall background index (BI) around the Q-value of the 0νββ decay was determined to be $15.4^{+1.8}_{-1.6} \times 10^{-3}$ cts/(keV · kg · yr) for the semi-coaxial data set. This value is consistent with previous measurements from Phase I of the experiment and shows improvement in the suppression of certain background components, particularly ^{42}K.

The contribution from these surface events remains an important consideration in the background model, given the challenges in discriminating them from other background sources. To mitigate this background due to surface contaminants, a dedicated pulse shape discrimination method is developed to discriminate the surface component of background from 0νββ signal and is discussed in detail later.

Bibliography (Chapter 3):

[Abt04] I. Abt et al., GERDA - Letter of Intent, tech. rep., 2004.

[Heu95] G. Heusser, “Low-radioactivity background techniques”, Annu. Rev. Nucl. Part. Sci. 45, 1 (1995), 543–590.

[Jan62] Janet S. Merritt and J. G. V. Taylor. 2011. THE HALF-LIVES OF K42 AND Br82. Canadian Journal of Physics. 40(8): 1044-1046

[Berg98] Berger, M. J. et al. XCOM: photon cross sections database. NIST Stand. Ref. Database 8, 87–3597 (1998).

[Hei10] T. Heindl et al., “The scintillation of liquid argon”, EPL ,vol. 91, no. 6, p. 62 002, 2010

[Ack13] Ackermann, KH., Agostini, M., Allardt, M. *et al.* The GERDA experiment for the search of 0*νββ* decay in ^{76}Ge. *Eur. Phys. J. C* 73, 2330 (2013).

[Bar09] I. Barabanov et al., Nucl. Instrum. Methods A 606, 790 (2009)

[Ger18] GERDA Collaboration., Agostini, M., Bakalyarov, A.M. *et al.* Upgrade for Phase II of the GERDA experiment. *Eur. Phys. J. C* 78, 388 (2018).

[Kla04] H.V. Klapdor-Kleingrothaus, I.V. Krishoveina, A. Dietz, O. Chkvorets, Phys. Lett. B 586, 198 (2004)

[Ago13] M. Agostini et al. [GERDA collaboration], Phys. Rev. Lett. 111, 122503 (2013)

[Eme65] F. E. Emery and T. A. Rabson, “Average Energy Expended Per Ionized Electron-Hole Pair in Silicon and Germanium as a Function of Temperature”, Phys. Rev. 140, A2089

[Sho38] W. Shockley, “Currents to Conductors Induced by a Moving Point Charge,” Journal of Applied Physics, vol. 9, no. 10, pp. 635–636, 1938.

[He01] Z. He, “Review of the Shockley-Ramo theorem and its application in semiconductor gamma-ray detectors” , Nucl. Instrum. Methods Phys. Res. A, 463 ,250-267 , 2001.

[Ago20] M. Agostini et al. (GERDA collaboration), Final results of GERDA on the search for neutrinoless double-β decay. Phys. Rev. Lett. 125, 252502 (2020)

[GSTR20] GERDA collaboration, GSTR-20-006: Parameters of final data release (analysis team)

[He01] He, Z. “Review of the Shockley–Ramo theorem and its application in semiconductor gamma-ray detectors”. In: Nuclear Instruments and Methods in Physics Research Section A: Accelerators, Spectrometers, Detectors and Associated Equipment 463.1 (2001)

[Xu15] J. Xu et al, A Study of the Residual 39Ar Content in Argon from Underground Sources, Astroparticle Physics, Volume 66 (2015) 53-60

[Bo14]Böhlke, J.K.. "Variation in the terrestrial isotopic composition and atomic weight of argon (IUPAC Technical Report)" *Pure and Applied Chemistry*, vol. 86, no. 9, 2014, pp. 1421-1432.

[Chu99] S.Y.F. Chu, L.P. Ekström and R.B. Firestone, WWW Table of Radioactive Isotopes, database version 1^{999}-02-28 from URL http://nucleardata.nuclear.lu.se/nucleardata/toi/

4. Pulse Shape Analysis

As detailed in Section 2.5.1, the sensitivity of the GERDA experiment scales linearly with the exposure (M.t) in the case of a background-free regime instead of $\sqrt{M.t}$ in the presence of a significant background at $Q_{\beta\beta}$. The sensitivity can be enhanced by increasing the source mass (M) and measurement time (t) and by minimizing the background (BI) at $Q_{\beta\beta}$. Given the other two factors are limited by monetary and time constraints, suppressing the background becomes the path forward. As detailed in Section 3.2, the GERDA setup is built with components with high radiopurity, and various passive shielding mechanisms effectively suppress the background levels. To further mitigate the background, the liquid argon and water tank are equipped with scintillation detectors to actively veto the non-signal events.

Even after such careful measures, the GERDA experiment still observed a significant background contribution around $Q_{\beta\beta}$ with a background index of ~ $5.4 \times 10^{-3}\ cts/kev.kg.yr$ after LAr veto for the semi-coaxial dataset in GERDA Phase II. The distinctive interaction topology of signal events (0νββ/2νββ) and background events within the germanium diode can be leveraged to distinguish them from each other.

In Figure 16, the energy deposition patterns of beta-beta events and those of various background components are depicted. In 0νββ decay, the resultant two electrons deposit their energy within a small volume (~ 1 mm^3) of a germanium detector [Abt07] . For all practical purposes, this can be considered a point-like energy deposition and is referred to as a single-site event (SSE). In contrast, background events, primarily caused by high-energy γ rays from natural radioactivity, typically undergo Compton scattering, leading to events with energy deposited in multiple separate locations (multi-site events, MSE). As a result of densely packed detector array geometry, such events with coincident energy depositions in multiple germanium detectors are considered background and are discarded by detector anti-coincidence cuts. Similarly, events such as gamma-ray accompanied beta-decay of ^{42}K, with coincident energy depositions within the liquid argon (LAr) volume surrounding the detector array are detected by scintillation detectors and discarded by LAr veto (detailed in Section 3.2). Note that a substantial fraction of interacting gamma ray background can Compton scatter but deposit their entire energies within the single detector volume, which would not be suppressed by either detector anti-coincidence or LAr veto. Additionally, due to the small thickness of the p+ and n+ contacts (~ 300 nm and ~1 mm, respectively), they are prone to α and β decays from surface contaminants, which contribute to background at $Q_{\beta\beta}$.

The SSE and MSE showcase a distinctive time structure of the measured charge/current pulses due to their characteristic energy deposition topology. To differentiate these MSEs within a single detector and surface events, GERDA employs pulse shape analysis (PSA) techniques, which rely on identifying specific features in the signal's time evolution. These PSA techniques are collectively employed to achieve a background-free operation of the experiment when combined with the LAr veto system.

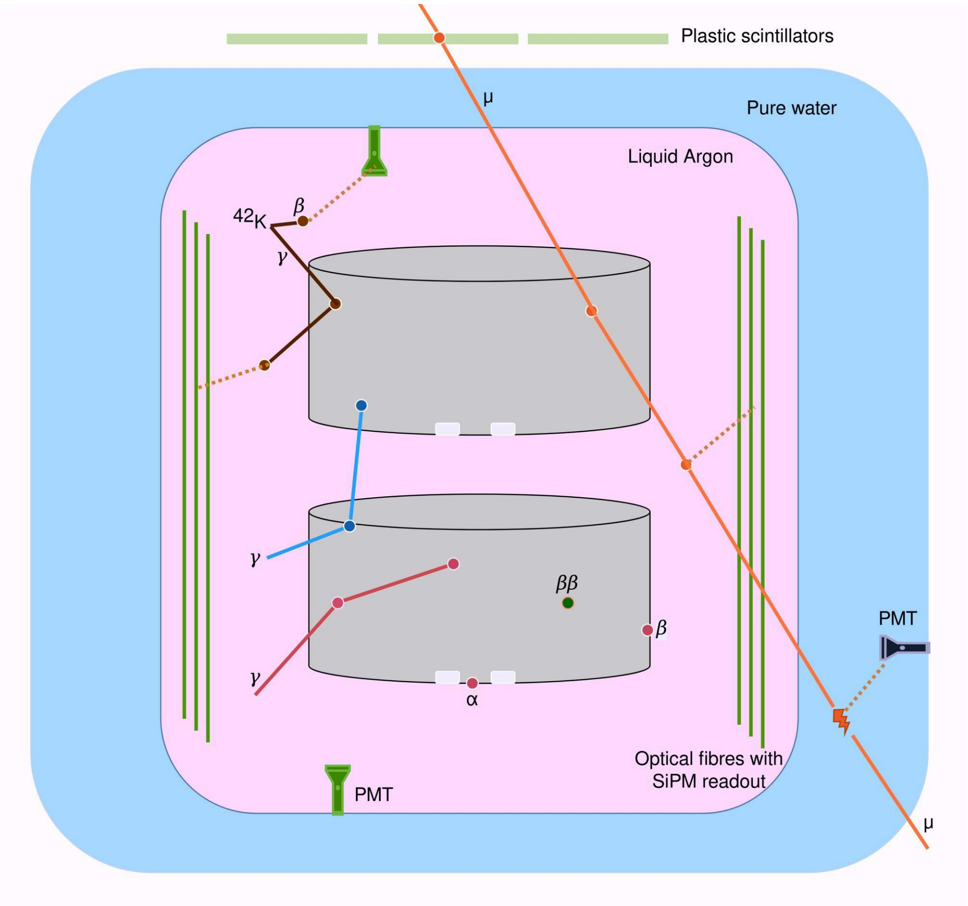

Figure 16: Energy deposition topology for various radiation interactions in the GERDA array. Beta-beta events (shown in green) have point-like energy deposition, whereas high energy gamma background Compton scatters lead to multiple spatially separated energy depositions. Background events such as ^{42}K β-decay (brown) and cosmic muons (orange) are discarded by scintillation detectors from LAr veto and muon veto. Events with coincident energy deposition in two or more Germanium detectors (shown in blue) are discarded by detector anti-coincidence cuts. The background from surface events from α and β decays and MSE within a single detector volume (shown in Magenta) warrants pulse shape discrimination techniques.

In previous analyses for the GERDA experiment's semi-coaxial detectors, pulse shape discrimination (PSD) techniques were primarily built on the work of A. Kirch [Kir14], who first implemented artificial neural networks for classification tasks using a Multilayer Perceptron (MLP) architecture through the TMVA package of ROOT. This framework was applied to data from both Phase I and Phase II of the experiment with little changes. These models were separately developed. and applied for Phase I and Phase II of the experiment. For Phase II, the data was further divided into pre-upgrade and post-upgrade subsets due to significant changes made to the GERDA array in 2018. For extracting the input features for these models, the data for each dataset collected over a timeframe of years was combined and normalized post-processing. This approach, however, overlooked potential temporal variations in pulse shapes that could arise from changes in DAQ electronics or detector bias voltage. Additionally, outliers in the data were not adequately addressed, which could have impacted the effectiveness of feature normalization. Additionally, the ROOT-based TMVA package, while functional, has significant limitations in terms of resources and transparency, especially when compared to more modern machine learning libraries like TensorFlow or PyTorch.

In this thesis, we have introduced several advancements to the PSD techniques used in GERDA. Specifically, we developed a new Convolutional Neural Network (CNN)-based model tailored to suppress the surface background component more effectively. This CNN-based approach not only surpasses the older risetime cut in terms of efficiency but also eliminates the energy dependence observed in the previous TMVA ROOT-based ANN models to suppress surface background. Furthermore, a thorough set of tests and procedures was implemented to ensure that the data is handled correctly throughout the analysis, minimizing any biases that could be introduced by improper selection of proxies for signal and background or potential outliers in data. A significant departure from previous work is the use of a different signal proxy, chosen specifically to mitigate biases introduced by the inhomogeneous distribution of ^{208}Th Double Escape Peak (TlDEP) events, which had been used as proxies in past analyses.

4.1. PSA for BEGE and IC detectors

For BEGe and IC detectors, pulse shape analysis (PSA) relies on a single parameter : the A-over-E (A/E) ratio, calculated as the maximum current amplitude (A) divided by the deposited energy (E) [Ago22]. For single-site events (SSEs), where energy deposition occurs at one point, the current signal exhibits a single peak structure with amplitude A. This peak corresponds to the moment when charge carriers reach the region of maximum weighting field at p+ contact.

In contrast, for events with energy depositions at multiple points, such as multi-site events (MSEs), the total signal is a superposition of signals generated by moving charge carriers from each energy deposition. These charge carriers from different locations reach the region of maximum weighting field at different times, resulting in a multiple peak structure in the current signal. Since the maximum amplitude of current pulse is proportional to the total charge of the moving charge cluster, events with multiple energy depositions produce current pulses with lower A values compared to SSEs.

For energy depositions at p+ contact such as those from alpha events, both the holes and electrons contribute significantly to signal formation, and due to high weighting fields, the resultant current pulses have a higher maximum amplitude and hence a higher A/E ratio compared to SSE. In contrast, β decays at n+ Li-diffused contact surface where the electric field is nearly non-existent can produce charges that slowly diffuse into active volume and then drift towards p+ contact over a timeframe of several μs . Thus, such events produce "slow-pulses" and exhibit a very low A/E ratio.

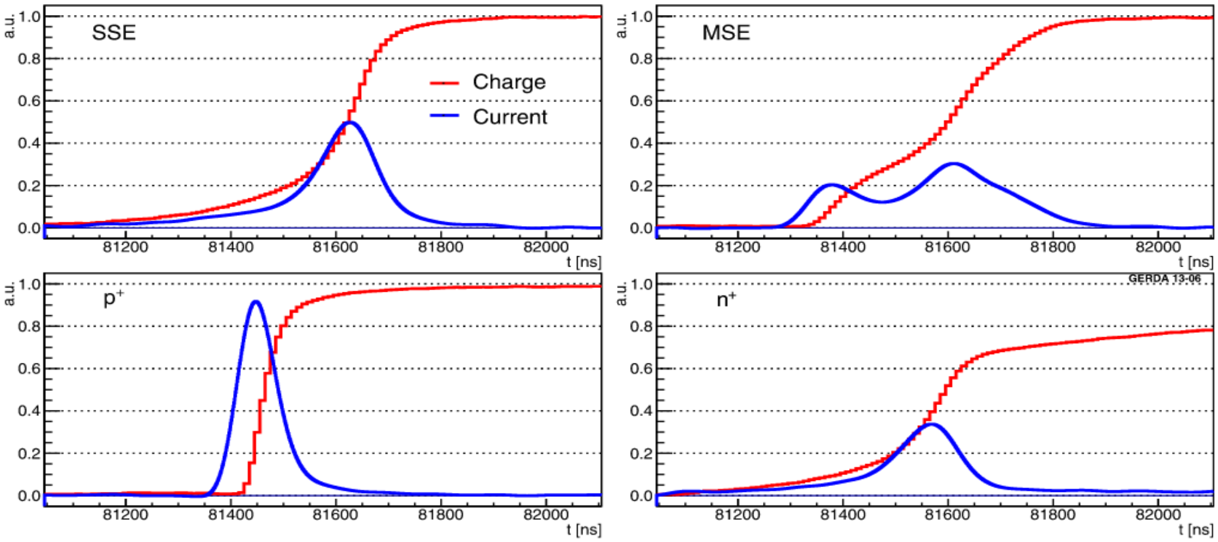

Figure 17: Typical pulse topology of SSE, MSE and energy depositions at p+ contact and n+ surface for BEGe & IC detectors. The charge pulses are normalized to a maximum amplitude of 1.

The amplitude of the current pulse (referred to as "A") is determined after applying a moving window average (MWA) filter three times, with a window length of 50 ns. Additionally, the pulse is interpolated to achieve a 1 nanosecond sampling time. MWA filter reduces the high-frequency noise while preserving the essential pulse shape characteristics. The energy estimator (referred to as "E") is computed using a pseudo Gaussian filter with a shaping time of 10 μs. To obtain the raw A/E value for each pulse, the computed A is divided by E, without calibration. The raw A/E values are then subjected to corrections for time stability and energy dependence before defining a cut value.

The raw A/E distribution of Single Site Events (SSEs) in the Compton continuum of the combined calibration data shows a slight linear dependence on energy, around a few percent per MeV. This effect is attributed to the fact that at higher energies, the charge cloud becomes larger, which in turn widens the current pulse. This energy dependence of raw A/E distribution is quantified by two functions: a linear one for the mean ,$\mu_{A/E}(E)$ and $a\sqrt{b + c/E}$ function for standard deviation $\sigma_{A/E}(E)$. Fitting these functions, A/E values are adjusted to account for energy dependence. Furthermore, the A/E values are normalized to the mean of the A/E distribution of the Double Escape Peak (DEP). Thus, the energy independent A/E classifier is defined as:

$$\zeta = (\frac{[A/E]}{\mu_{A/E}(E)} - 1)/\sigma_{A/E}(E)$$

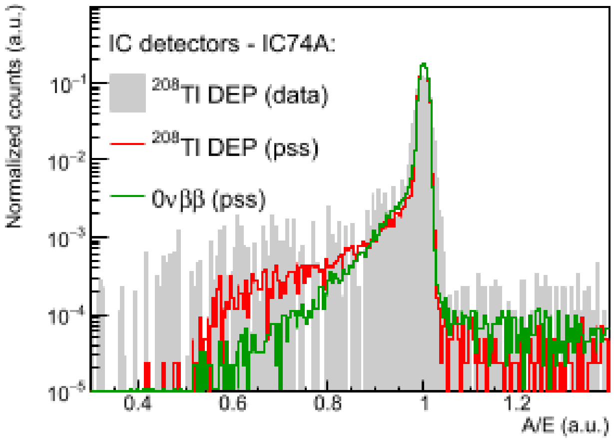

Figure 18: A/E distributions for DEP events from calibration data and simulated MC events are depicted. The distributions are normalized to have a unit integral.

The distribution of this energy-independent classifier ζ, is centered around zero and has a standard deviation of one for SSEs. To effectively discriminate against Multi-Site Events (MSEs) and n + surface events, a low-side A/E cut is chosen to maintain a 90% survival fraction for the DEP. On the other hand, a high-side A/E cut at ζ = 3.0 (equivalent to $3\sigma_{A/E}$ away from mean at zero) is applied to reject alpha (α) events in physics data above 3525 keV. It has been observed that the high-side A/E cut eliminates most events, including degraded alpha events, within a small region near the p + contact.

4.2. Need for multivariate PSA for semi-coaxial detectors

In the case of semi-coaxial detectors, the pulse shape can vary with the position of the energy deposition, making it more challenging to distinguish 0νββ events from background.

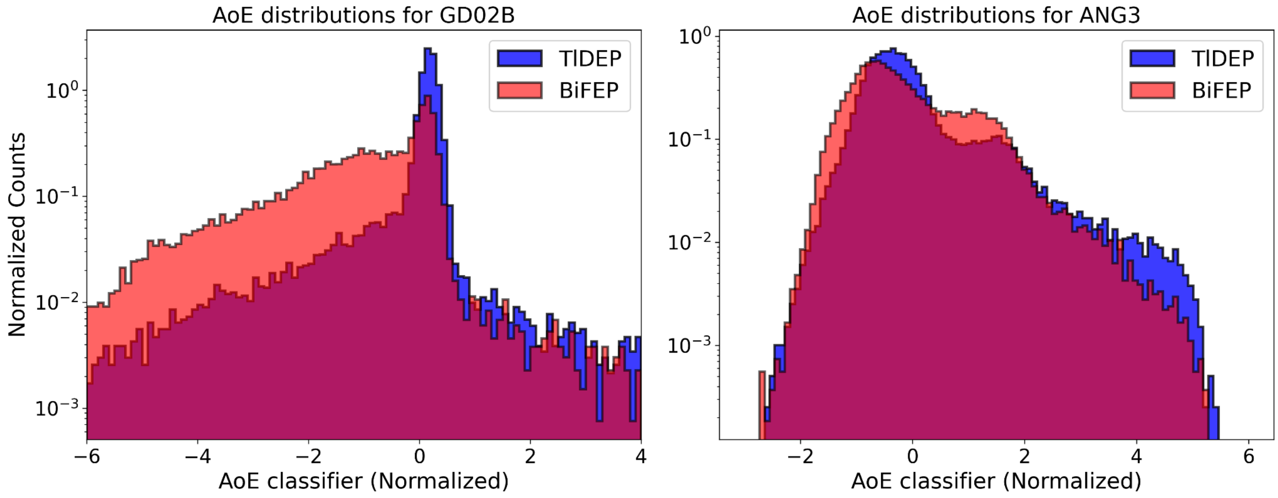

Figure 19: A/E parameter distribution of SSE (^{208}Tl DEP) and MSE (^{212}Bi FEP) for a typical BEGe detector (GD02B) and a typical semi-coaxial detector(ANG3).

Above Figure 19 shows the distribution of A/E parameter for SSE’s and MSE’s in a semi-coaxial detector in the right panel and it is evident that it offers no significant discrimination potential as compared to a BEGE or IC detector as depicted in the left panel.

Due to the homogeneous weighing potential distribution of semi-coaxial detectors, a single-parameter differentiator used for signal/background differentiation in Broad Energy Germanium (BEGE) detectors is ineffective as shown in Figure 19. Therefore, advanced multivariate pulse shape analysis techniques are required to distinguish between signal and background events based on the topological characteristics of charge and current pulses. Coaxial detectors, unlike BEGE detectors, have a significantly homogeneous weighing potential across their active volume. This uniformity makes distinguishing between signal and background pulses using a single-parameter approach difficult.The lack of discernible variations in the maximum amplitude of charge and current pulses limits the effectiveness of single-parameter discriminators, highlighting the need for more complex analysis techniques.

Multivariate pulse shape analysis appears to be a promising avenue for improving coaxial detector discrimination capabilities. A more comprehensive identification of the signals and background can be achieved by taking into consideration multiple features derived from the topology of charge and current pulses that carry information about energy deposition patterns. The multivariate approach allows for the investigation of complex correlations and interdependencies among these features, facilitating the extraction of discriminating information that might otherwise be obscured from single-parameter methods. Utilizing multivariate analysis techniques in coaxial detectors improves signal/background discrimination accuracy by capturing subtle variations in pulse shape, which may contain valuable information about the underlying physical processes.

4.3. Machine learning:

4.3.1. Introduction:

In recent years, scientific research in the field of rare decay searches has been fueled by the pursuit of understanding the intrinsic nature of fundamental particles and their intricate interactions. The sensitivity of these experiments is highly dependent on minimising background events that can obscure the desired rare decay signals. In this context, pulse shape discrimination (PSD) techniques have emerged as indispensable tools for reducing background levels and increasing the likelihood of detecting rare decays with unprecedented precision.

The previous chapter offered a glimpse into the pulse shape analysis of semi-coaxial detectors, where hardware and software advancements have successfully reduced background events by an order of magnitude compared to previous experiments. Nonetheless, additional enhancements are desired to achieve even greater sensitivity. This effort has resulted in the incorporation of multivariate analysis (MVA) techniques, specifically machine learning algorithms, in order to improve the pulse shape analysis.

The current experimental setup consists of a germanium detector array operating in a low-mass support structure immersed in liquid argon, protected by multiple layers of shielding, and strategically located underground to reduce cosmic ray interference. In addition, sophisticated software tools have been implemented for online data analysis, allowing for continuous monitoring of energy resolution and stability. Cross-talk, electromagnetic noise, discharges, and pile-ups are a few examples of the non-physical events that have been significantly reduced by the application of quality cuts. In addition, true physical events that coincide temporally with muon-veto signals or cause simultaneous energy depositions in multiple HPGe detectors are effectively removed from the analysis, further reducing background.

In spite of these remarkable accomplishments, after LAr veto, the residual background index of $\sim 5.4 \times 10^{-3}\, cts/kev.kg.yr$ for Phase II data indicate the possibility of further background reduction. Herein lies the significance of the current chapter, which examines the development and application of MVA techniques to the data collected during Phase II of the experiment.

4.3.2. Use of ML for PSA

The use of machine learning (ML) algorithms in coaxial detectors for pulse shape analysis provides a compelling solution to the difficult task of distinguishing between signal and background events. In this context, ML algorithms provide several advantages. For starters, they can effectively handle the high-dimensional and complex nature of pulse shape data, allowing the extraction of non-linear relationships and correlations that would otherwise be difficult to discern using traditional analytical methods. Second, ML algorithms can adapt and learn from data, allowing for the creation of robust models capable of generalizing well to previously unseen pulse shapes. Third, through iterative training and feedback procedures, ML algorithms offer the potential for continual enhancement and refinement. ML models can be retrained and optimized to improve performance and adjust to changing detection scenarios as more labeled data becomes available.

Furthermore, ML techniques can accommodate a wide range of algorithms, including decision trees, recurrent neural networks, deep neural networks, and ensemble methods, providing flexibility and the ability to experiment with different modeling approaches.

4.3.3. TensorFlow: A Versatile Platform for Machine Learning Models in Multivariate Data Analysis

TensorFlow, developed by Google's Brain Team, stands as one of the most versatile and powerful open-source platforms for machine learning and deep learning applications. Owing to its robustness and adaptability, it has become the standard for machine learning model development, particularly multivariate data analysis. With its extensive library of readily available algorithms and frameworks, TensorFlow provides researchers and data scientists with a vast array of tools for training, evaluating, and testing sophisticated classification techniques in parallel. This feature enables meaningful comparisons between various methods, thereby facilitating the selection of the most appropriate strategy for a given problem or application scope. The foundation of TensorFlow lies in its computation graph paradigm, where mathematical operations are represented as nodes in a graph, and data flow between these nodes as tensors. This approach allows for efficient parallelization and optimization of computations, making TensorFlow ideal for large-scale and computationally intensive tasks.

The present work is utilizing various ML models built with TensorFlow to analyze and scrutinize the elusive neutrinoless double β-decay. A primary objective of the analysis is the selective rejection of events stemming from sources other than the signal of interest. Consequently, the classification process aims to categorize events into the distinct classes of "signal" and "background."

TensorFlow possesses a plethora of implemented classifiers that accommodate a variety of data characteristics and different linear and nonlinear correlation responses. These classifiers include:

- Multilayer Perceptron (MLP): These versatile feedforward neural networks consist of multiple layers of interconnected nodes (neurons). MLP models are ideally suited for a vast array of multivariate classification and regression tasks, making them a fundamental option in numerous data analysis scenarios.
- Convolutional Neural Networks (CNN): CNNs excel at extracting meaningful features via convolutional layers and are primarily used for image and spatial data analysis. These models have revolutionized computer vision tasks and are proficient at identifying patterns in images and spatial datasets.
- Long Short-Term Memory (LSTM): LSTM models are specialised recurrent neural networks (RNNs) designed to process sequential and time-series data. These networks are suitable for time-series analysis and sequential data prediction because they can capture long-term dependencies in the data.
- Decision Trees: decision trees partition the data based on various features to create a hierarchical decision-making structure. Decision trees are valuable for understanding feature importance and handling both numerical and categorical data.
- Random Forest: Random forests are an ensemble learning technique that combines multiple decision trees to improve predictive accuracy and prevent overfitting. They are robust models that can manage complex datasets.

Each of these classifiers thrives on a shift from traditional one-dimensional cut-based discrimination patterns to the paradigm of multivariate supervised learning. By leveraging user-supplied data sets with pre-classified events, these techniques are capable of extracting meaningful patterns and improving classification performance significantly.

The availability of pre-implemented models within TensorFlow simplifies the model-building process, allowing researchers to focus on preprocessing and training procedures to optimize classifier performance for their unique data sets. In addition, TensorFlow's seamless integration with GPU and TPU accelerators enables researchers to harness the power of parallel processing, which further improves the performance of machine learning models on large datasets.

4.3.4. Multilayer Perceptron (MLP)

The Multilayer Perceptron (MLP) model is a feedforward neural network that is frequently employed in classification tasks. The architectural structure consists of numerous layers of interconnected neurons. In this discourse, we shall delve into the intricacies of a Multilayer Perceptron (MLP) model as applied to classification tasks.

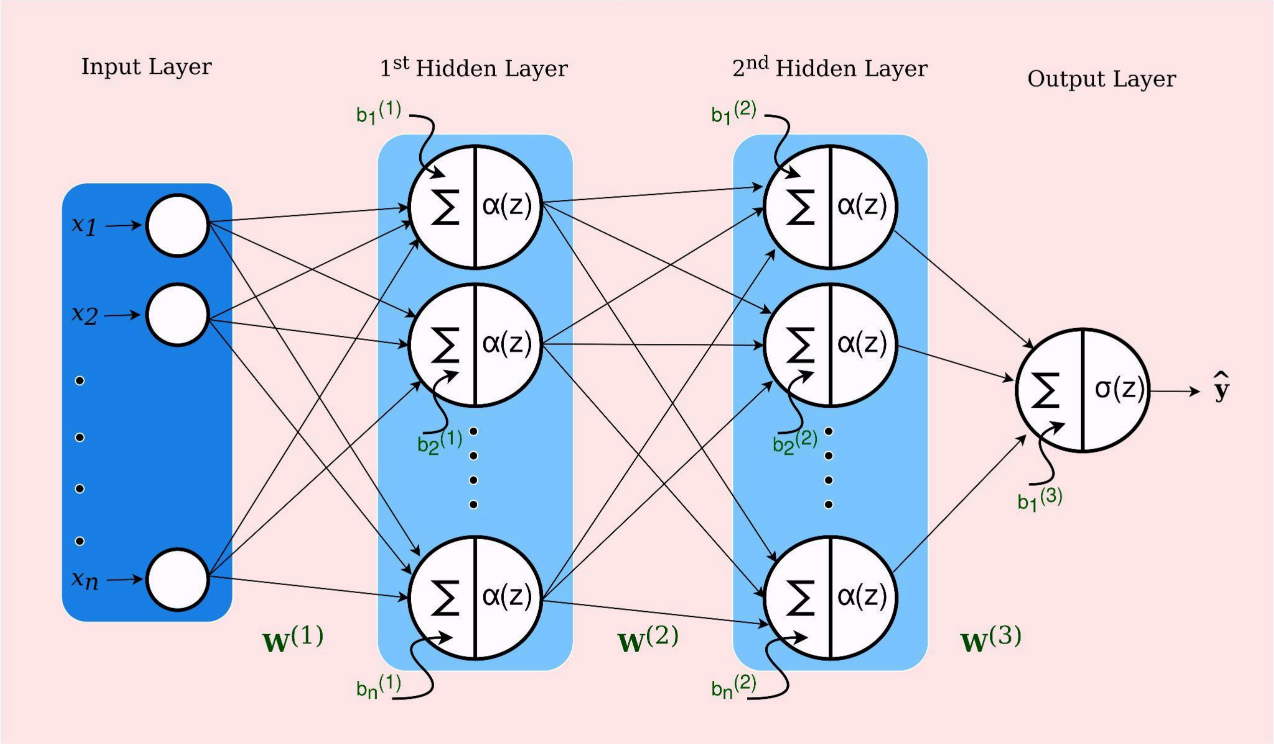

Figure 20: A schematic of a typical multilayer perceptron model with two hidden layers and an output layer with a single neuron is shown.

1. Input Layer: The initial layer of the Multilayer Perceptron (MLP) is referred to as the input layer. This layer is responsible for receiving the feature vectors that represent the input data. Every element within the feature vector is associated with a corresponding neuron within the input layer. The number of neurons in the input layer equals the total number of input features present in the dataset.

2. Hidden Layers: Subsequent to the input layer, there exist one or more hidden layers. The aforementioned layers function as intermediary stages of processing that acquire hierarchical representations of the input data. Every individual neuron within a hidden layer establishes connections with all neurons present in the preceding layer, whereby each connection is assigned a specific weight. In addition, it is noteworthy that every neuron possesses an associated bias term.

3. Activation Function: An activation function is employed within each neuron of the hidden layers (and occasionally the output layer) to introduce non-linearity which enable network to learn non-linear patterns within the data. Without activation functions, a neural network would be equivalent to a linear model, incapable of representing non-linear patterns.

The activation functions that are frequently employed in various machine learning models include Rectified Linear Unit (ReLU), sigmoid, and hyperbolic tangent (tanh). The activation function plays a crucial role in determining the activation state of a neuron, either by triggering a "firing" response or maintaining an inactive state. This decision is made by evaluating the weighted sum of the input data along with the bias term.

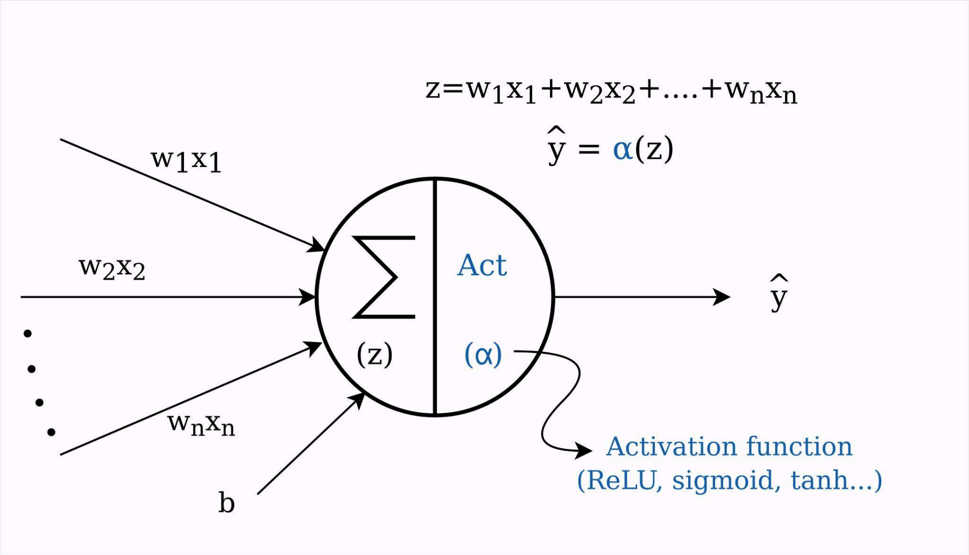

Figure 21: Working of activation function within a neural network.

The summation of the inputs (x_1, x_2,..., x_n) from the previous layer, each weighted by corresponding weights (w_1, w_2,..., w_n) and including bias represents “z”. The non-linear activation function α takes this summation as input.

The output of the activation function is the transformed value of the input "z" and is used as the output of the neuron in a neural network, conveying information to subsequent layers or for making predictions in the case of output layer.

4. Weights and biases: These are essential components of the multilayer perceptron (MLP) as they represent the learnable parameters that govern the connections between neurons. Throughout the training procedure, the model iteratively modifies its parameters in

order to minimize the discrepancy between its predicted outputs and the actual labels present in the training dataset. The optimization process is commonly accomplished through the utilization of methods such as gradient descent and backpropagation.

5. Output layer: The output layer, situated at the end of the multi-layer perceptron (MLP), is responsible for generating the classification outcomes. The choice of activation function for this layer is task-dependent. The sigmoid activation function is frequently employed in binary classification tasks, as it yields probabilities within the range of 0 to 1.

6. Loss function: The loss function quantifies the disparity between the predicted outputs and the actual labels. For binary classification tasks, we utilize binary cross-entropy loss (also called logloss), which is calculated as:

$$L = \frac{-1}{N}\sum_{i=1}^{N} y_i \,.\, log\,\widehat{y}_i + (1 - y_i)\,.\,log(1 - \widehat{y}_i)$$

where N is the number of events , y_i is the label value (0 or 1) for ith event, and $\widehat{y}_i$ is a classifier value by the ML model. Evidently, for a positive class sample where the true label "$y_i = 1$", the loss penalizes the model more as "$\widehat{y}_i$" deviates from 1. Similarly, for samples from the negative class with the true label "$y_i = 0$", loss value increases in a logarithmic manner as it deviates more and more from 0.

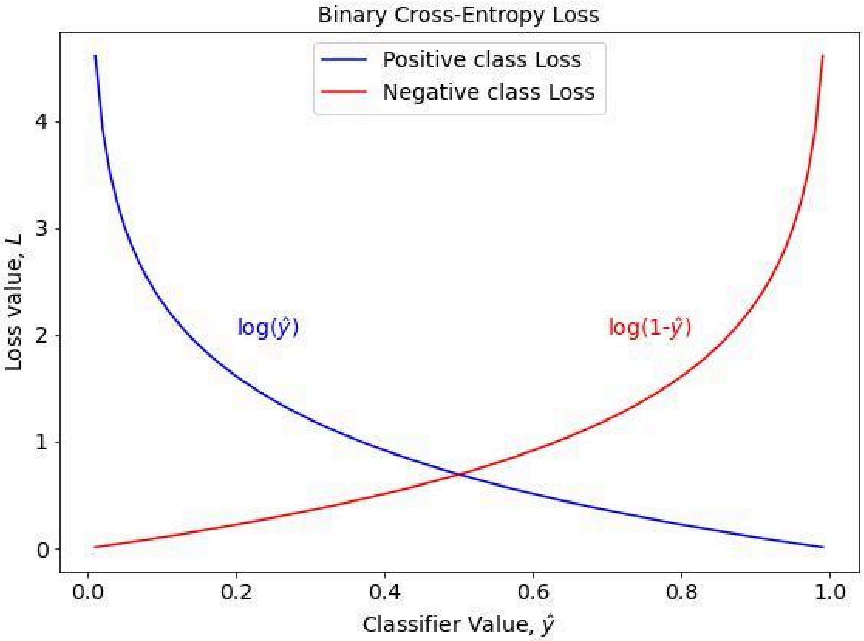

Figure 22: Two terms from binary cross-entropy loss function are plotted here for different possible classifier outcomes. For each sample from data, one of the terms contributes to loss depending on its true label.

The objective during the training process is to minimize the value of the loss function by iteratively adjusting the weights and biases of the model.

7. Training: The training procedure encompasses the presentation of input data to the multilayer perceptron (MLP), the computation of the model's predicted outputs, the comparison of these outputs to the true labels through the utilization of a loss function, and the subsequent adjustment of the model's parameters via optimization algorithms such as stochastic gradient descent (SGD), Adam etc. The iterative process persists until the model attains a satisfactory level of performance on the training data. This iterative process is explained in brief below:

Forward Pass : Given an input vector $\bar{x}$ = (x_1, x_2,..., x_n), the forward pass operations at a neuron *j* in the hidden layer *l* can be expressed as:

$$z_j^{(l)} = \sum_{i=1}^{n^{(l-1)}} w_{ij}^{(l-1)} a_i^{(l-1)} + b_j^{(l)}$$

$$a_j^{(l)} = \sigma(z_j^{(l)})$$

where $z_j^{(l)}$ is the weighted sum for neuron *j* in layer *l*. $w_{ij}^{(l-1)}$ are the weights connecting neuron *i* in layer $l-1$ to neuron *j* in layer *l*. $b_j^{(l)}$ is the bias term for neuron *j* in layer *l*. σ is the activation function (e.g., ReLU, sigmoid) and $a_j^{(l)}$ is the activation output of neuron *j* in layer *l*, which serves as input for the next layer. At the output layer, we use sigmoid activation for binary classification tasks, and the predicted classifier can be expressed as:

$$\hat{y} = \sigma(z^L) = 1/(1 + e^{-z^L}) \quad \epsilon\, [0, 1]$$

where $\hat{y}$ is the predicted probability that the input belongs to the positive class.

Backpropagation and parameter updates : To minimize the loss function, we compute the gradients of the loss with respect to the model's parameters (weights and biases). This is done through backpropagation, which applies the chain rule to compute the gradients layer by layer, starting from the output layer and moving backward.

The gradient of the loss function with respect to the weight w_{ij}^l connecting the nodes *i* and *j* of layer *l-1* and layer *l* respectively, can be expressed with the chain rule.

$$\frac{\partial L}{\partial w_{ij}^l} = \frac{\partial L}{\partial a_j^l} \times \frac{\partial a_j^l}{\partial z_j^l} \times \frac{\partial z_j^l}{\partial w_{ij}^l}$$

Substituting a_j^l and z_j^l from above, we get,

$$\frac{\partial L}{\partial w_{ij}^{l}} = \frac{\partial L}{\partial a_{j}^{l}} \times \sigma'(z_{j}^{l}) \times a_{i}^{(l-1)}$$

$$\text{where } \frac{\partial L}{\partial a_{j}^{l}} = \sum_{i=1}^{n^{(l+1)}} w_{ij}^{(l+1)} \times \sigma'(z_{j}^{l+1}) \times \frac{\partial L}{\partial a_{j}^{l+1}}$$

Similarly, the gradient of loss with respect to bias can be described as ,

$$\frac{\partial L}{\partial b_{j}^{l}} = \frac{\partial L}{\partial a_{j}^{l}} \times \frac{\partial a_{j}^{l}}{\partial z_{j}^{l}} \times \frac{\partial z_{j}^{l}}{\partial b_{j}^{l}}$$

Based on these calculated gradients, model parameters such as weights and biases are updated after each backward pass. In the simplest case of a gradient descent optimizer, the weights and bias are updated in the opposite direction as that of the respective gradient with loss by a factor termed “learning rate” in each iteration:

$$w_{ij}^{l}(t+1) = w_{ij}^{l}(t) - \alpha \times \frac{\partial L}{\partial w_{ij}^{l}} \quad and \quad b_{j}^{l}(t+1) = b_{j}^{l}(t) - \alpha \times \frac{\partial L}{\partial b_{j}^{l}}$$

In this analysis, we use the Adam optimizer, which is an adaptive learning rate optimization algorithm. It maintains per-parameter learning rates, which are adapted based on estimates of first and second moments of the gradients. The parameter updates with Adam Optimizer are explained in brief as below assuming the gradient at time step t to be g_t :

$m_0 = 0,\ v_0 = 0\ , t = 0$: *initialization at t=0*
$m_t = \beta_1 m_{t-1} + (1 - \beta_1) g_t$: *biased first moment estimate*
$v_t = \beta_2 v_{t-1} + (1 - \beta_2) g_t^2$: *biased second moment estimate*

Both m_t and v_t are initially set to 0. The bias toward 0 is more pronounced in both, as β_1 and β_2 are both equal to ~1. To correct for this bias,

$\widehat{m_t} = m_t / (1 - \beta_1^t)$ *and* $\widehat{v_t} = v_t / (1 - \beta_2^t)$: *bias corrected first and second moments*

$\theta_{t+1} = \theta_t - \alpha \times \dfrac{\widehat{m_t}}{\sqrt{\widehat{v_t}} + \epsilon}$: *Update weights and biases*

Here $\theta_t = \{w_t, b_t\}$ are model parameters in step t, and ϵ is a small constant to prevent division by zero (commonly set to 10^{-8}).

After undergoing training, the Multilayer Perceptron (MLP) can be utilized to generate predictions on novel and unobserved data. This is achieved by feeding the input through the trained network and extracting the output from the output layer.

Hyperparameters:

A model parameter, which encompasses weights and biases associated with neurons and their connections, is an internal configuration variable that can be estimated based on the input data. In contrast, a model hyperparameter is defined as a configuration variable that is external to the model. They influence the behavior and performance of the machine learning model, but their values are not learned during training. Properly tuning hyperparameters is crucial for optimizing model performance and preventing overfitting. In the context of MLP, hyperparameters include the number of hidden layers, the number of neurons within each layer, the learning rate, the activation functions, the loss optimizer, and the batch size.

4.3.5. Convolutional Neural Network (CNN)

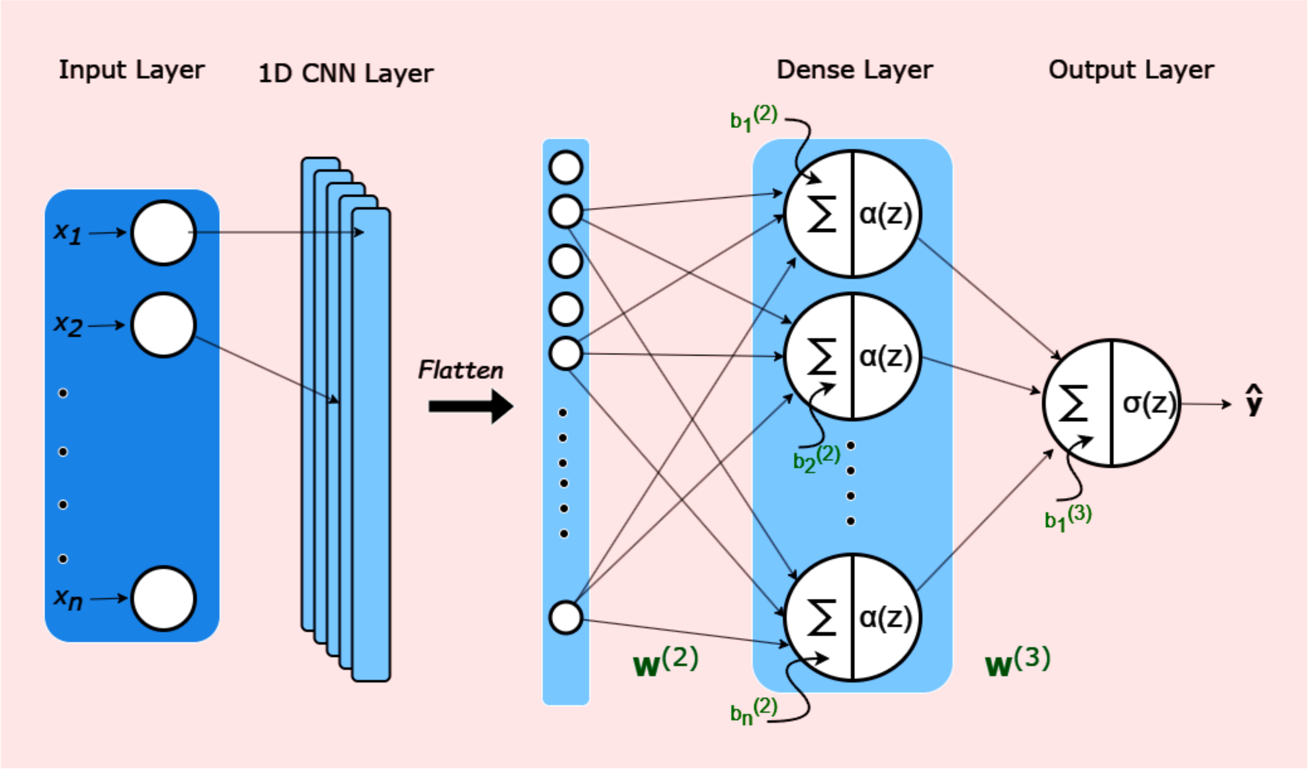

Figure 23: A schematic of a typical Convolutional Neural Network with single 1-dimensional convolutional layer followed by a fully-connected layer and output layer with a single neuron is shown.

The Convolutional Neural Network (CNN) is a specialised deep learning model that has been specifically developed for the purpose of processing and analysing visual data, including but not limited to images and videos. Most popular Convolutional Neural Networks (CNNs) are designed as 2D CNNs, which are commonly used for processing visual inputs such as images and videos. These models excel at capturing spatial patterns and hierarchical features within

2D data. However, when the input data is a one-dimensional sequence—such as time-series data, waveforms, or signal data—a 1D CNN is more appropriate.

In the context of this study, where the input is a 1D sequence, we employ a 1D CNN model. The 1D CNN is a specialized deep learning architecture tailored for analyzing sequential data. Unlike 2D CNNs that work on pixel grids, 1D CNNs apply convolutional filters across the sequence to detect local patterns, such as trends or periodic signals. The input layer receives the sequential data, with each point representing a feature at a specific time step or position. Convolutional layers then apply filters along the sequence, performing element-wise operations to extract relevant features. As with 2D CNNs, activation functions like Rectified Linear Unit (ReLU) are used to introduce non-linearity, enabling the network to learn complex, non-linear patterns. The output from these layers is fed into fully connected layers, which further process the features and map them to output classes. In binary classification tasks, such as distinguishing between signal and background events, the output layer typically consists of a single neuron with a sigmoid activation function to produce a probability score for classification.

1D CNNs are particularly effective in detecting local patterns within sequences, providing a powerful tool for analyzing one-dimensional data. Their ability to recognize patterns regardless of their position in the sequence makes them highly robust for tasks like signal processing, where the timing of features may vary. Moreover, CNNs are capable of effectively processing translation-invariant features.

Convolution Operation: For an input sequence $\bar{x}$ = (x_1, x_2,..., x_n) and a filter **w**=(w_1, w_2,..., w_k), the convolution operation produces an output sequence (also called feature map) **z**=(z_1, z_2,..., z_m) which can be expressed as:

$$z_j = \sum_{i=1}^{k} w_i x_{j+i-1} + b$$

where k is the length of the filter and b is the bias term. Also, *m=n−k+1* (assuming no padding and a stride of 1) where n is the length of the input sequence. In the case of multiple filters, the operation is repeated for each filter, and each filter produces a different feature map.

After the convolution operation, an activation function (e.g., ReLU, sigmoid) is applied element-wise to the feature map:

$$a_j = \sigma(z_j)$$

Subsequently, the fully connected (dense) layer is used to combine the features extracted by the convolutional layer to make classification. The operations in fully connected layers follow the same principles as described in the case of MLP architecture.

4.3.6. Recurrent Neural Network (RNN) :

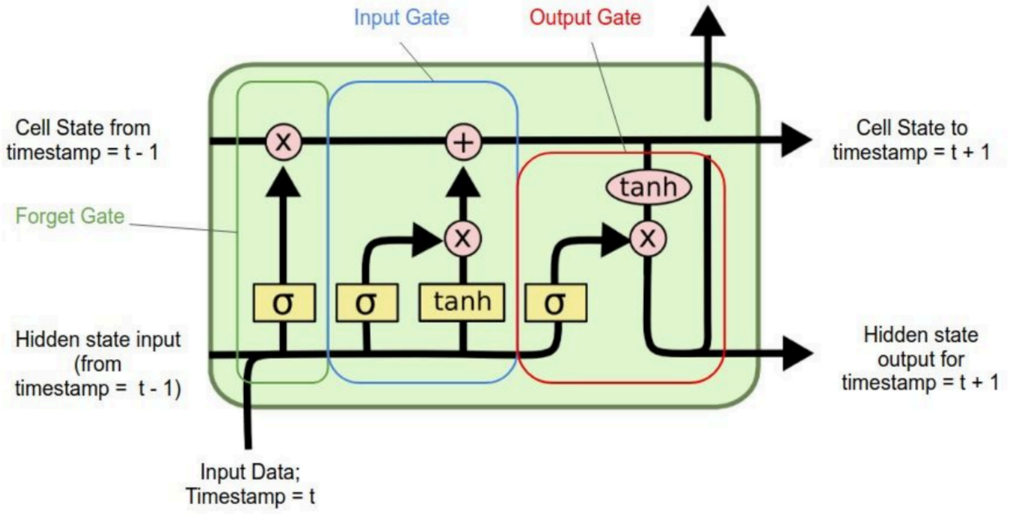

Figure 24: Schematic of a LSTM cell

Recurrent Neural Network (RNN) is a type of artificial neural network designed to process sequential data, making it ideal for time series analysis, natural language processing, and speech recognition. Long Short-Term Memory (LSTM) is a specialised type of RNN that effectively captures long-term dependencies and maintains memory over extended sequences by addressing the vanishing gradient problem faced by conventional RNN.

An LSTM network is composed of memory cells, each responsible for storing and updating information over time. The key components of an LSTM cell include:

Cell State (Ct): The cell state functions as the LSTM's long-term memory. It traverses the entire input data sequence, allowing the network to retain relevant information over time. To control the flow of information, the cell state is updated by using specific gating mechanisms.

Input Gate (i): The input gate determines the amount of new information added to the cell state during the current time step. It controls the flow of incoming data and enables the network to selectively update the cell state.

Forget Gate (f): The forget gate determines which cell state information to discard at the current time step. It ensures that irrelevant information is not propagated throughout the sequence, thereby resolving the gradient-vanishing issue experienced by conventional RNNs.

Output Gate (o): The output gate controls how much information from the updated cell state is made available to the subsequent layer or the final prediction. It controls the output of the LSTM cell, influencing the final classification decision.

Due to its unique architecture and memory retention abilities, LSTM excels at capturing long-term dependencies in sequential data. This is essential for tasks where data from distant time steps is necessary for accurate predictions.

4.3.7. Training, Validation, and Testing Model Performance

Training machine learning models to accurately recognise and classify signal-like and background-like events requires realistic training and validation samples. This entails preparing representative datasets with a balanced distribution of events from each class to expose models to a variety of scenarios. Appropriate sampling and validation techniques are employed to prevent overfitting and ensure model generalizability. Our goal is to identify and evaluate suitable models for classifying a given event as signal or background based on its pulse topology. Data partitioning is a critical aspect in the field of machine learning as it significantly contributes to the creation of resilient and dependable models. The preprocessing and feature extraction steps are crucial in converting the raw signals obtained from germanium detectors, which are in the form of charge pulses, into meaningful input representations. It is crucial to partition the dataset into separate subsets, specifically the training, validation, and testing sets, in order to attain optimal model performance and prevent overfitting.

The purpose of data partitioning is to ensure that machine learning models are trained and evaluated on distinct datasets that do not overlap with each other. Every partition within the model development pipeline fulfills a distinct function, thereby playing a crucial role in the construction of a robust and generalized machine learning model. This subsection aims to delve into the importance and methodology involved in the creation of these datasets.

Training Dataset: The training dataset serves as the basis for creating and tuning a machine learning model. It makes up the bulk of the data and is used to train the model to identify underlying patterns and connections between input features and corresponding target labels (signal or background). The model effectively learns from the underlying patterns in the data by tuning its internal parameters based on the supplied input-output pairs during the training process.

Validation Dataset: This dataset is utilized to evaluate the performance of models across different hyperparameter choices. Also, it is used to assess how well the model performed during training on an unseen validation dataset and helps identify any possible overfitting problems. Overfitting occurs when a model becomes too specialized on the training data, leading to a continuous decrease in loss on the training set. However, the loss on a separate validation set eventually starts increasing. This indicates that the model is essentially memorizing the training data instead of learning, resulting in poor performance on new, unseen data. To combat overfitting, we monitor the models ability to generalize on validation data and avoid overfitting by “early stopping” the training. “Early stopping” is a regularization technique in machine learning aimed at preventing overfitting. It involves monitoring the model's performance on a validation dataset during training. If the performance ceases to improve or starts degrading, indicating overfitting, training is halted early. The model parameters from the epoch with the best performance on the validation set are saved. This is the model that generalizes well to new data. By stopping the training early, before the model has had a chance to overfit, we can prevent it from becoming too specialized to the training data.

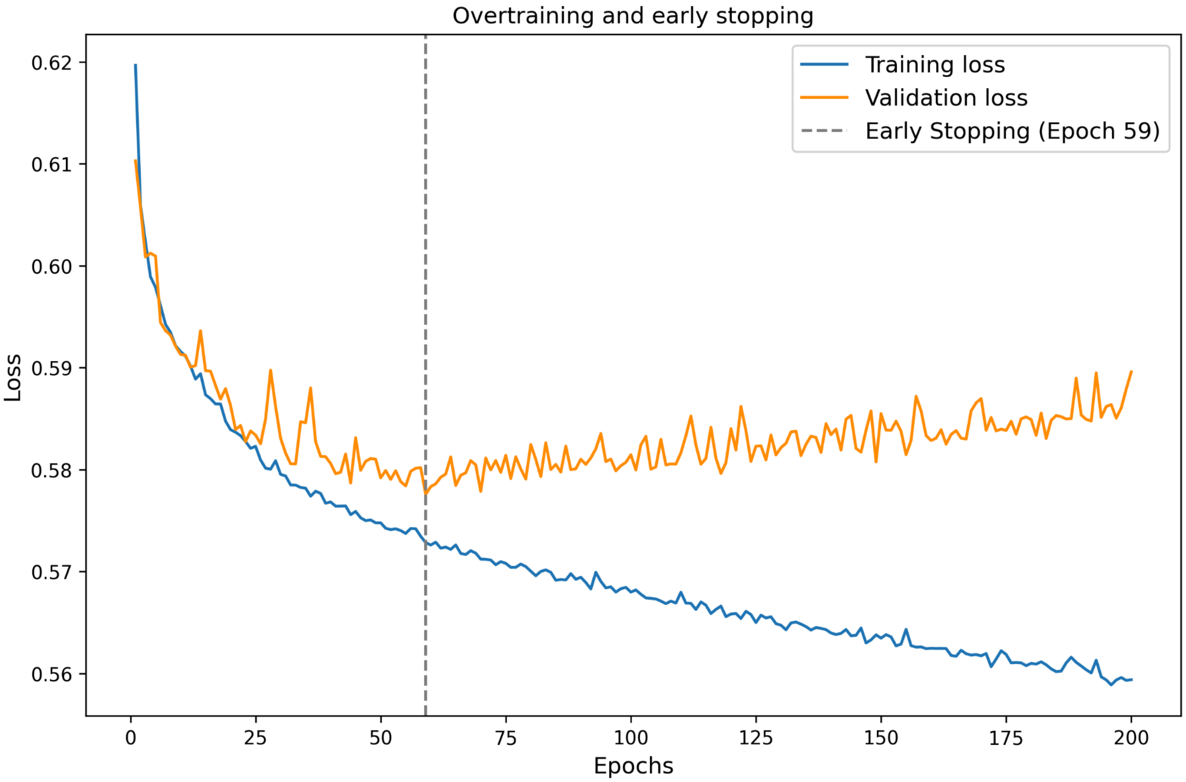

Figure 25: The plot illustrates the evolution of training and validation loss as a function of epochs as the training progresses. Initially, both training and validation loss decline as the model learns from the data. However, overtraining becomes evident as the training loss continues to decrease while the validation loss stagnates or rises. This divergence indicates the model's tendency to overfit the training data, compromising its generalization ability. Early stopping, represented by a dashed grey line, suggests halting training early to prevent overfitting. Model weights from this "early stopped" epoch are utilized for subsequent analysis.

Since the validation dataset is used for hyperparameter optimization and 'early stopping' and thus can lead to data leakage, we use a different independent dataset termed 'test dataset' to measure the model's true performance on unseen data.

Test Dataset: The model's performance and generalization abilities are evaluated using the testing dataset as the last yardstick. It is used to evaluate how well the trained model performs when applied to fresh, untested data. Due to the testing set's independence from the training and validation data, it is possible to evaluate the model's accuracy in classifying new events as either background or signal based on charge pulse topology.

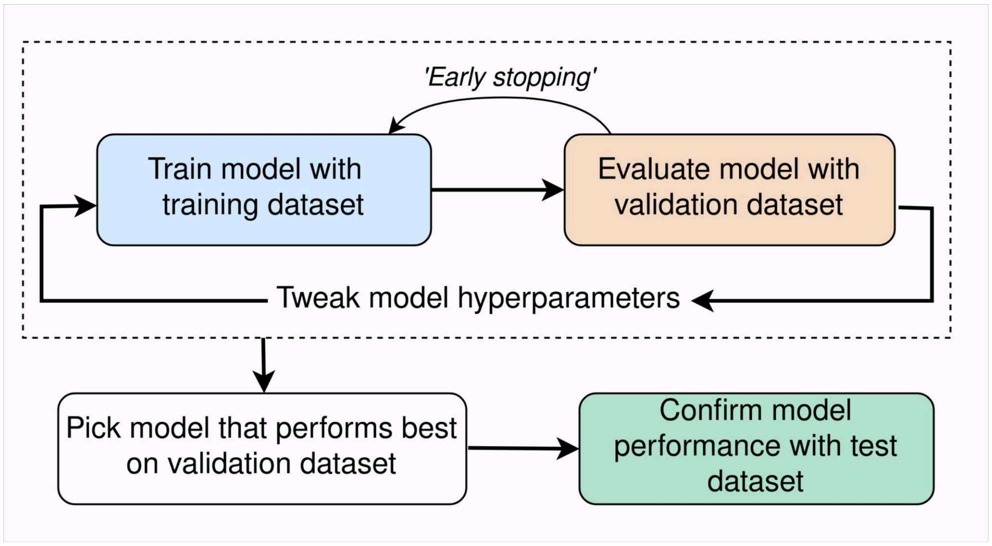

Figure 26: Schematic workflow of model optimization with data splitting.

The choice of the optimal split percentage is subjective and depends on the data composition and model complexity. While there is no universally ideal split percentage, two key considerations are taken into account:

i) A low amount of training data can result in a high variance in training for the machine learning model.

ii) Inadequate testing and validation data can lead to greater variance in model evaluation and performance statistics.

In current analysis, we maintain a ratio of 60:20:20 events for training, validation, and test datasets, respectively.

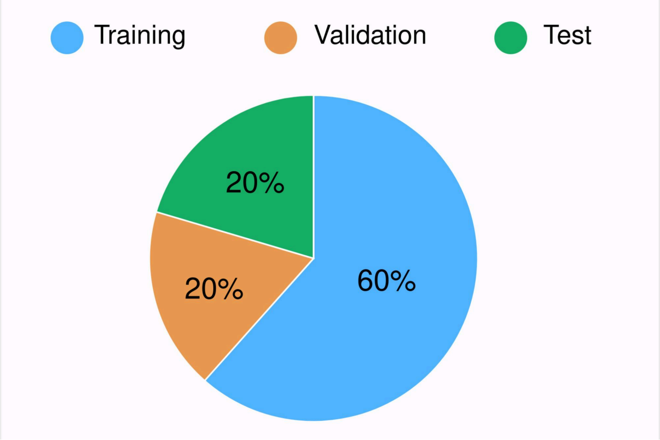

Figure 27: A pie chart showing division of data in training, validation and test dataset in ratio 60:20:20 respectively.

Random sampling, a common method for dataset division, involves shuffling and randomly selecting samples for the training, validation, or test sets based on user-defined percentage ratios. However, its drawback is evident in class-imbalanced datasets, where target classes have unequal representation. This can introduce bias. To address this issue, we employ stratified sampling. Unlike random sampling, stratified sampling preserves class distribution in each set—train, validation, and test. This approach ensures a more fair and balanced data splitting, allowing the machine learning model to be trained and validated on representative data distributions.

4.4. Input features

The successful adaptation of multiple machine learning models for pulse shape analysis within the context of the GERDA experiment necessitates the careful consideration of crucial factors. Important to this process is the careful selection of input variables that possess significant discriminatory capability, enabling the models to distinguish between signal-like and background-like events. In addition, it is essential to provide training and testing samples that accurately reflect the characteristics of these events. In addition, since the experiment involves various setups and detector geometries, such as BEGe and semi-coaxial detectors, the dataset must be partitioned into distinct subsets to account for these differences. The purpose of this section is to provide a comprehensive and detailed explanation of the methodology used to construct input features for the adaptation of data for multiple machine learning models.

The core of the feature building is the preprocessing of the data obtained from the germanium detectors in form of as charge pulses. This initial step involves cleaning the data, neutralizing high frequency noise, and addressing any missing or corrupted data. Subsequently, feature extraction is performed to transform the digitized charge pulses into meaningful representations suitable for machine learning models.

In the case of semi-coaxial detector geometries, where both electrons and holes contribute to charge collection, variations in the weighting potential distribution can lead to significant differences between the early and late stages of the pulse. Therefore, limiting the analysis to particular portions of the leading edge, such as the bottom, middle, or top, may result in a loss of discrimination power. For multivariate analysis, the entire pulse, specifically the entire rising portion of the sampled trace, is utilized to ensure maximum discrimination capabilities. To facilitate this, a series of preprocessing steps are carried out to prepare the corresponding samples of the trace as input parameters for subsequent analysis.

To prepare the trace samples for subsequent analysis, a series of preprocessing steps are implemented:

Interpolation: Interpolating the high frequency charge pulse from 10 ns binning to 1 ns binning enhances precision in determining when the charge amplitude crosses 50% of its maximum. This finer resolution ensures a more accurate reference point for aligning pulses and establishing a consistent time reference across samples.

Reduce High-Frequency Noise: A 50 ns Moving Window Average (MWA) is applied using the output of the GEMDMWAverageRT module. This smoothing technique helps in reducing high-frequency noise, resulting in a cleaner waveform that facilitates the identification of relevant features.

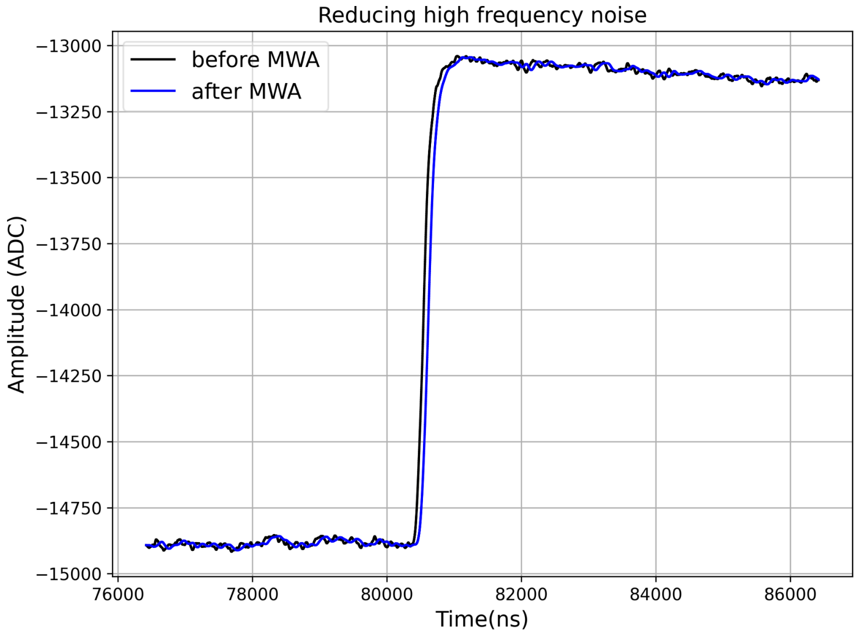

Figure 28: shows a visual comparison of the charge pulse before and after smoothening with MWA filters.

Baseline Subtraction: The average baseline value for the first 2 microseconds of the waveform is calculated and subtracted from the entire pulse. This step helps in removing any possible baseline drift, ensuring accurate measurement of pulse characteristics.

Calculate Maximum Amplitude: The trapezoidal filter from the GEMDEnergyGast module is utilized to determine the maximum amplitude of the waveform. This filter identifies the peak value of the pulse, which is indicative of its energy content.

Amplitude Normalization: The waveform is normalized to have a maximum amplitude of 1. This scaling process aligns all pulses to a common reference amplitude, facilitating energy-independent feature extraction and comparison.

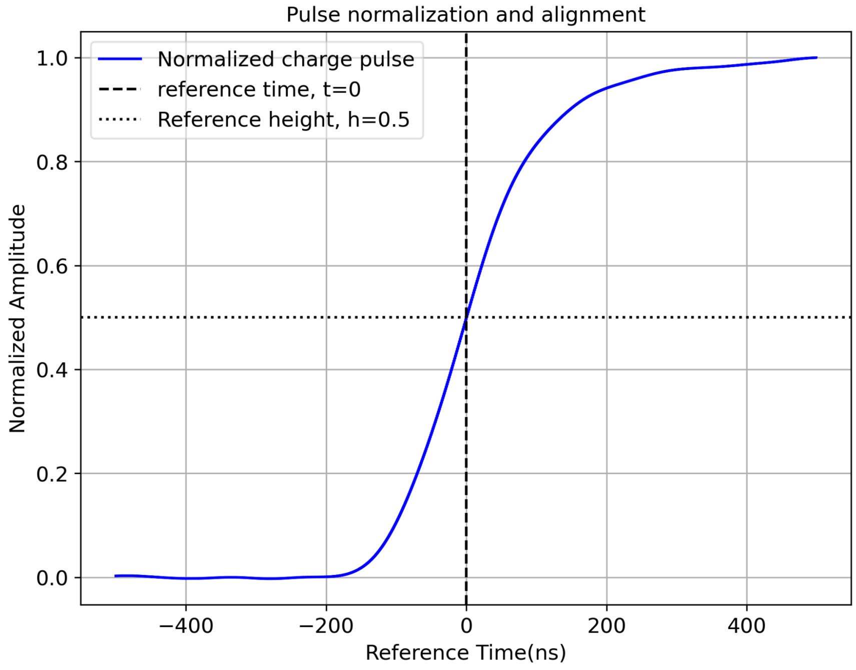

Figure 29: illustrates pulse height normalization with maximum pulse amplitude. The reference time is set to 0 when the pulse reaches half the maximum amplitude (shown with a dashed line).

Set Reference Time: The time at which the waveform reaches 50% of its maximum normalized amplitude is identified, and this time is set to 0 as the reference point. This alignment ensures that all pulses are referenced based on their respective 50% amplitude crossing time, establishing a consistent time reference across samples.

Calculate Input Variables: Finally, 50 input variables are calculated, representing the times when the pulse reaches various percentages (1%, 3%, ..., 99%) of its maximum amplitude. These time values serve as input features, capturing the intricate pulse shape characteristics and providing valuable information for subsequent classification tasks.

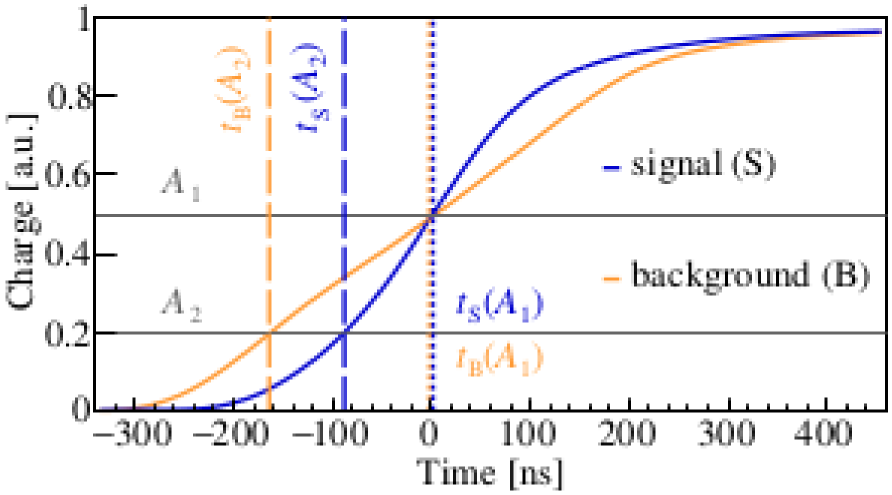

Figure 30: *illustrates the extraction of 50 features from the preprocessed charge pulse. The reference time is set at the 50% of maximum amplitude crossing point, and 50 input variables are computed, representing specific time points capturing the pulse shape for subsequent analysis. (adapted from [Kir14])*

4.4.1. Input feature Scaling

Feature scaling is a standard preprocessing step in machine learning, aimed at enhancing the efficiency and stability of the training process. The goal of feature scaling is to transform various numerical features to be on a similar scale. Scaling ensures that all features are on a comparable scale and have comparable ranges. By scaling the input features, we ensure that certain features do not dominate the learning process solely because of their larger scale producing skewed results. Also, since activation functions like sigmoid are more sensitive around 0, scaling the features helps the optimization algorithm converge more rapidly during training and promotes overall stability.

Normalizing features helps maintain numerical stability during the training process. Large input values can result in exploding gradients, which might cause instability and slower convergence of model weights. Without normalization, features with larger scales might have a disproportionate impact on the learning process, and the model might give more importance to features with larger magnitudes. Normalization ensures that all features contribute equally to the learning process. Feature normalization can act as a form of regularization. It can help prevent overfitting by limiting the impact of outliers and ensuring that the model generalizes well to unseen data.

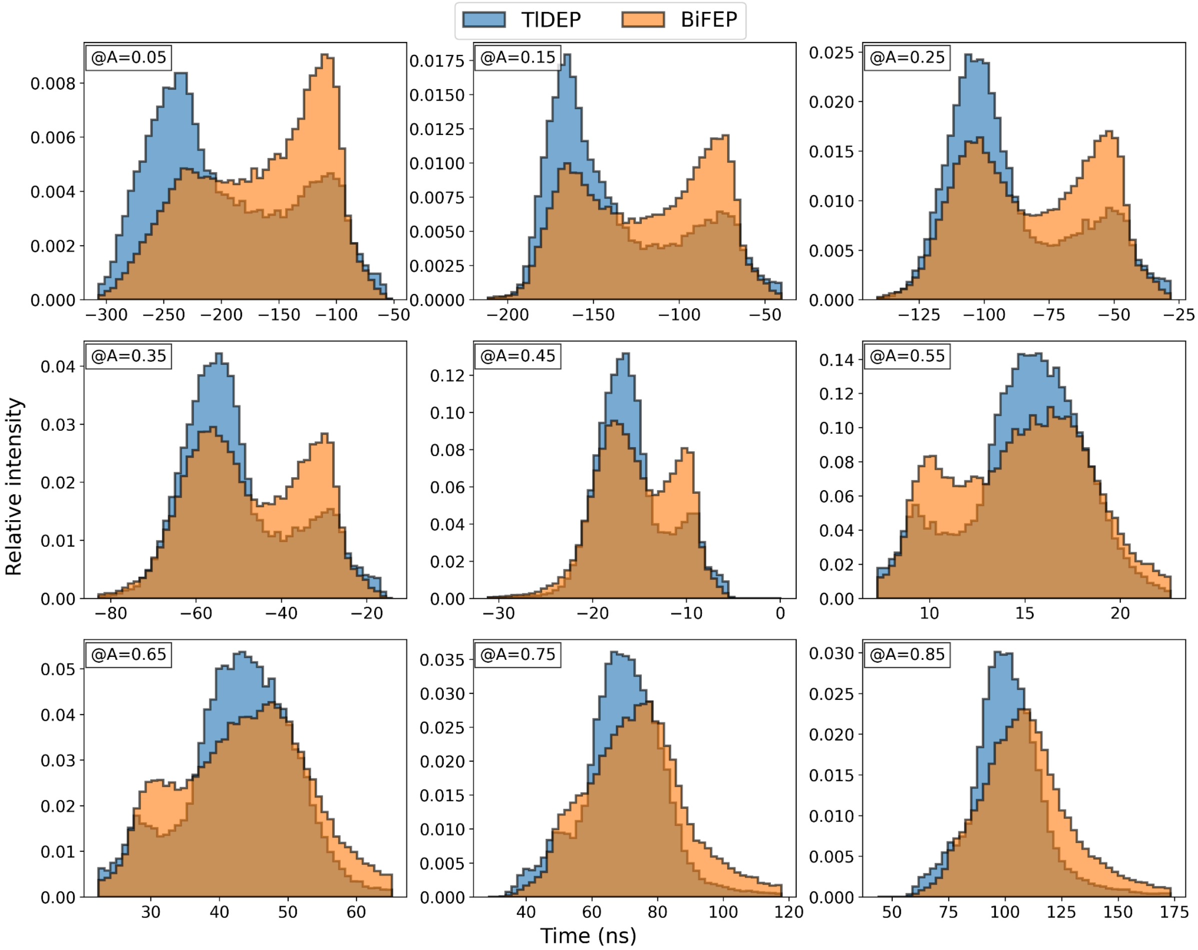

Figure 31: For ANG3, time distribution for signal-like and background-like events at different pulse amplitudes with maximum pulse amplitude normalized to 1. The plot shows ^{228}Th calibration events with energies within ±1 FWHM of the 1593 keV DEP of ^{208}Tl (in blue) and the 1621 keV FEP of ^{212}Bi (in red). These time distributions represent the individual input variable distributions for the signal and background proxies used in training the ANN-MSE model.

Two common normalization techniques that are often used are Min-Max scaling (scaling feature values to a specific range, e.g., [0, 1]) and Z-score normalization (scaling to have a mean of 0 and a standard deviation of 1).

Min-Max normalization scales the features to a specific range (commonly [0, 1]), which can be beneficial if the neural network's activation functions or architecture benefit from inputs within a specific interval.

$$X_{normalized} = \frac{X - X_{min}}{X_{max} - X_{min}}$$

where X_{max} and X_{min} are the minimum and maximum values for the particular feature. Since it is Sensitive to minimum and maximum values of a feature across the samples in a dataset, the outliers in data can adversely affect the effectiveness of such scaling. In case of outliers, an extreme value of X_{max} or X_{min} would result in most of the distribution being squeezed in a small part of the scale.

Z-score Normalization (also called Standardization) centers the feature distribution with a mean of 0 and a standard deviation of 1, making it suitable when features have different scales. It is calculated by subtracting the mean of the feature distribution and dividing by the standard deviation.

$$X_{standardized} = \frac{X - \mu}{\sigma}$$

where μ and σ are the mean and standard deviation of the feature distribution.

Z-score normalization is robust to outliers because it considers the mean and standard deviation, which are less affected by outliers compared to the range of values in Min-Max Scaling.

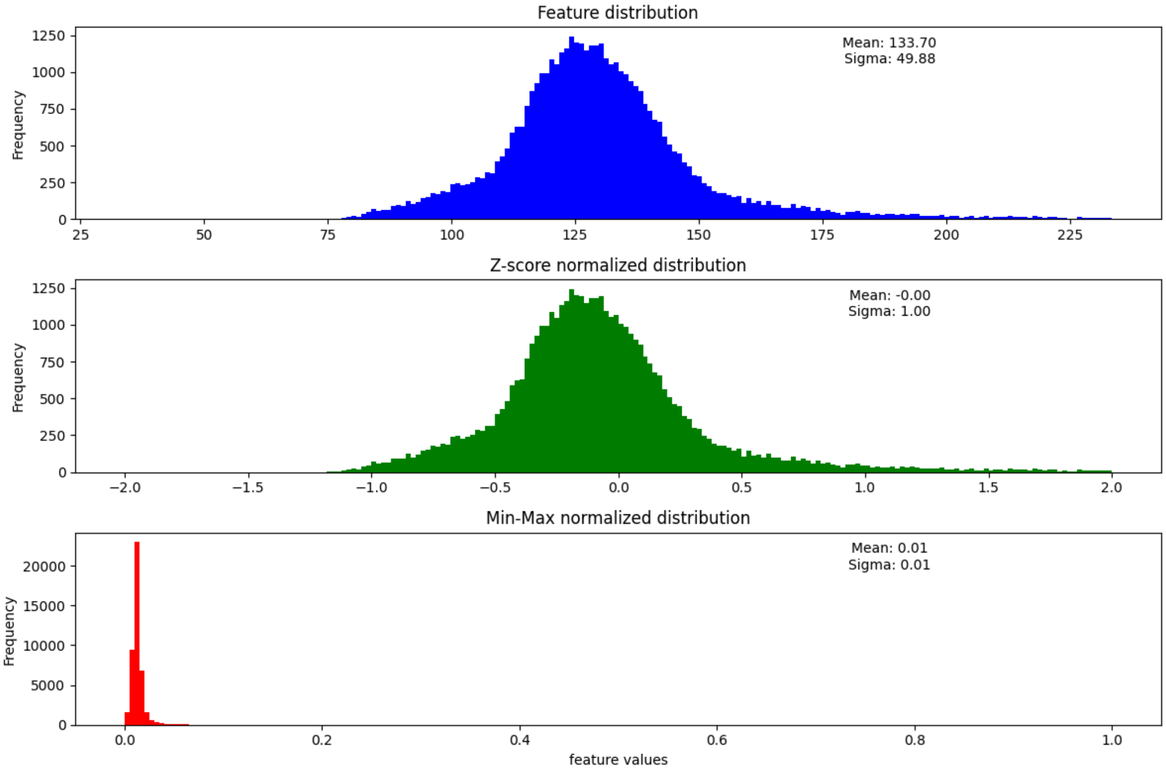

Figure 32: The distribution of normalized values (top panel) for a particular feature (IV45) and its counterparts after applying z-score normalization (middle panel) and Min-Max scaling (bottom panel), respectively.

For our analysis, Z-score normalization would be more suitable due to its resistance to outliers. Since our dataset may contain variations and outliers, Z-score normalization ensures that these outliers do not unduly influence the scaling process, leading to a more robust and reliable analysis.

4.4.2. Accounting for temporal variations in pulse shape in the dataset

As discussed in section 3, the data acquisition process was structured into sequentially numbered subsets called “runs”, with each run capturing data under a consistent hardware configuration, keeping the setup unchanged throughout the runtime. But across the different runs, the charge pulse shapes may vary due to potential changes in electronics or detector bias voltage. This variability can lead to different feature distributions for samples collected in different runs. Scaling the features from all the data from all runs by combining them would not appropriately account for these variations, potentially resulting in suboptimal normalization and impacting the performance of machine learning models.

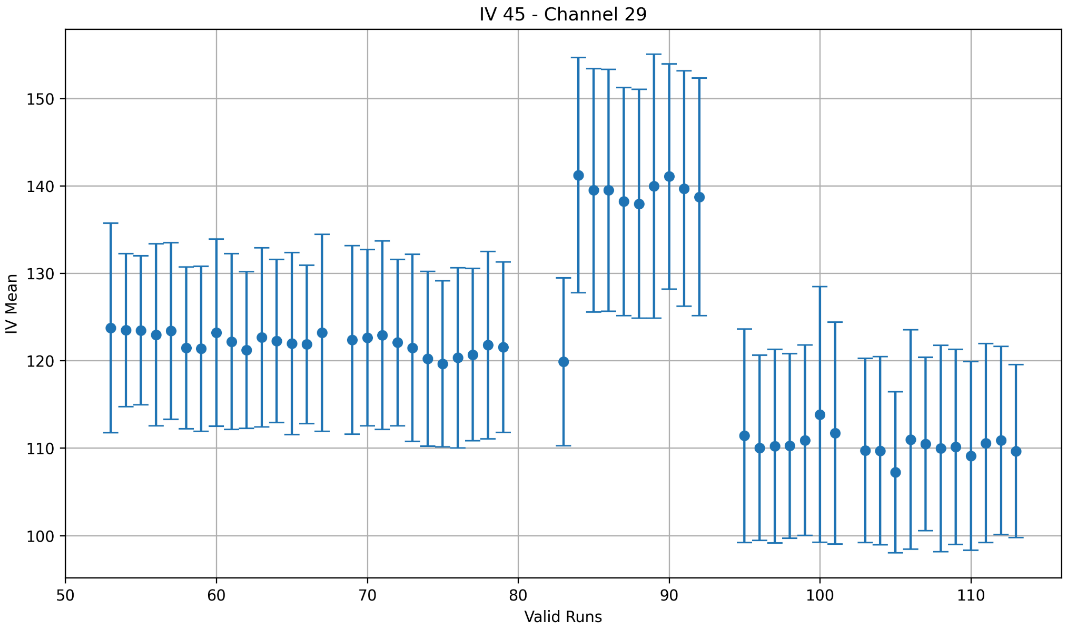

Figure 33: The variability in feature distributions across different runs is illustrated in the accompanying figure for detector ANG4. The figure plots the mean of one of the features (IV45) as a function of run number, highlighting a significant change after run 84. According to the data-taking logs, the bias voltage of this detector was reduced from 3500V to 2750V due to high leakage current encountered during Run 84, and it was maintained at this lower voltage until Run 93.

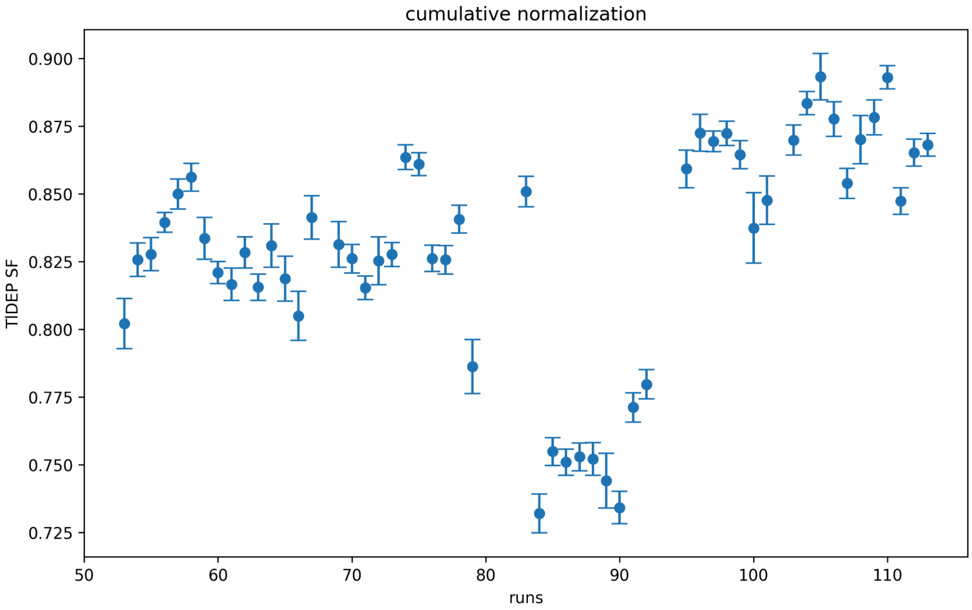

Figure 34: The figure illustrates the signal efficiency of a Multi-Layer Perceptron (MLP) model trained with feature scaling using cumulative data for ANG4, plotted as a function of run number. The model's performance significantly deteriorates for data from runs 84 to 93. This decline in performance can be attributed to the different pulse shapes resulting from the reduced bias voltage during these runs.

The model underperforms for runs 84 to 93 due to the changes in pulse shapes caused by the reduced bias voltage. The altered voltage affects the weighting potential and the overall shape of the pulses, leading to a shift in the feature distribution. Since the feature scaling was performed on cumulative data without accounting for these run-specific variations, the model fails to generalize well to the data from runs 84 to 93, where the pulse characteristics deviate from those in other runs. To mitigate this issue, it is essential to normalize the features within each run independently. Thus, batch-wise scaling is implemented, with each batch consisting of data from a specific run.

Group Data by Runs: Organize your dataset into groups based on the runs. Each group represents data collected during a specific run.

Feature scaling: For each group (Run), independently calculate the mean and standard deviation of each feature across the samples collected during that Run period and scale the features within that group (Run). This ensures that the scaling process considers the variations in charge pulse shapes across different runs.

Combine Scaled Data: Once each run's data is scaled independently, the scaled data from all runs is combined for subsequent analysis.

By applying Z-score normalization on a per-run basis, the normalization process can better account for the temporal variations in pulse shapes, leading to more consistent feature scaling and improved model performance across all runs. This approach ensures that the differences in hardware configuration and operating conditions are appropriately reflected in the normalized feature distributions, enhancing the robustness of the machine learning models.

4.5. Selection of proxy samples for training ANN models

To train machine learning (ML) models for this purpose, carefully selected training data is essential, consisting of calibration and physics data from other peaks that share similar pulse characteristics as the signal and background events.

For the ML model aimed at discriminating between signal and multi-site events, the ^{208}Tl Double Escape Peak at 1592.5 keV energy is used as a proxy for the signal. The 0νββ events exhibit a characteristic single-point energy deposition within the germanium detector, similar to the single-point energy deposition resulting from the annihilation of an electron-positron pair in the Double Escape Peak. One drawback of using DEP events as proxy for signal is difference in the spatial distribution of these events within the detector. Since DEP events are accompanied by escape of two annihilation gamma rays, these events are predominantly situated at detector edges whereas 0νββ events are expected to be distributed homogeneously across the detector volume.

As a proxy for the multi-site event background, events from the Full-Energy Peak (FEP) of ^{212}Bi at 1620.5 keV are selected. The FEP predominantly consists of multi-site energy depositions caused by Compton scattering within the detector, closely resembling the multi-site background events.

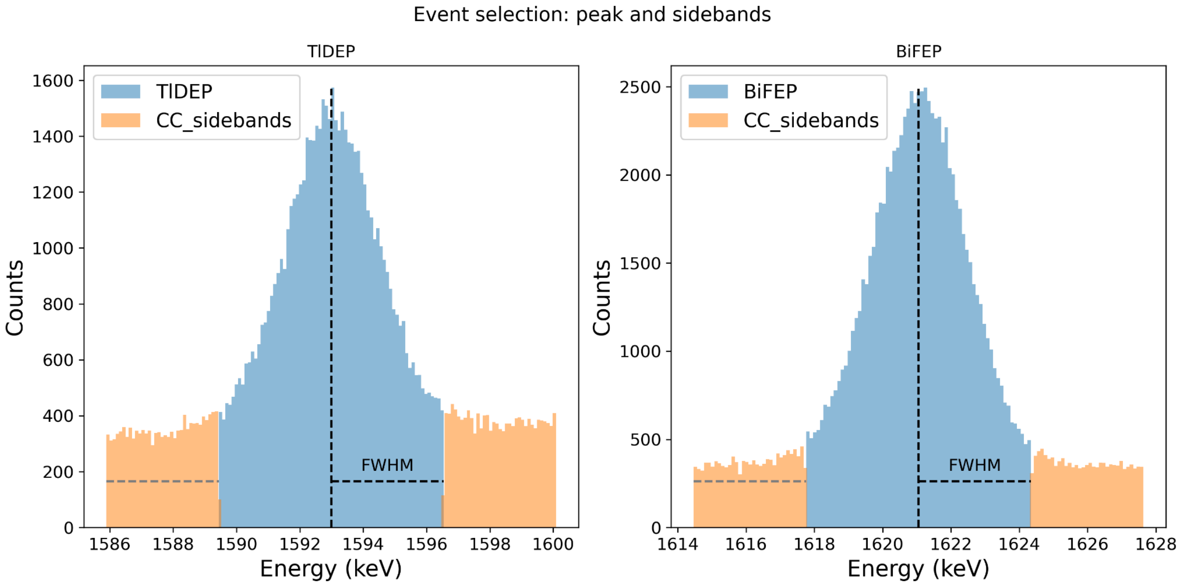

Figure 35: Selection of signal and background proxy data for SSE/MSE differentiating models. The left panel indicates events for signal proxy in blue and Compton sidebands in orange used to account for Compton events underlying the DEP. Similarly, the right panel shows events chosen as proxy for multi-site background from the full-energy peak of ^{212}Bi in blue and underlying Compton events in orange.

To select these proxy events, energy intervals centered at the Double Escape Peak of ^{208}Tl and Full-energy peak of ^{212}Bi are created, with a width of ±1 Full Width at Half Maximum (FWHM) of the respective peaks in the energy spectrum. The choice of energy intervals with similar signal-to-noise ratios prevents any energy dependence in the classification output of the ML model.

Although events from Double Escape Peak of ^{208}Tl have similar energy deposition pattern as that of ββ decay, it needs to be noted that the distribution of these DEP events is not homogenous across the detector volume unlike that of ββ events. This inhomogeneity is a result of a prerequisite that both 511 keV annihilation photons need to escape detector volume and thus the double-escape peak events are predominantly situated at the corners and edges of the detector.

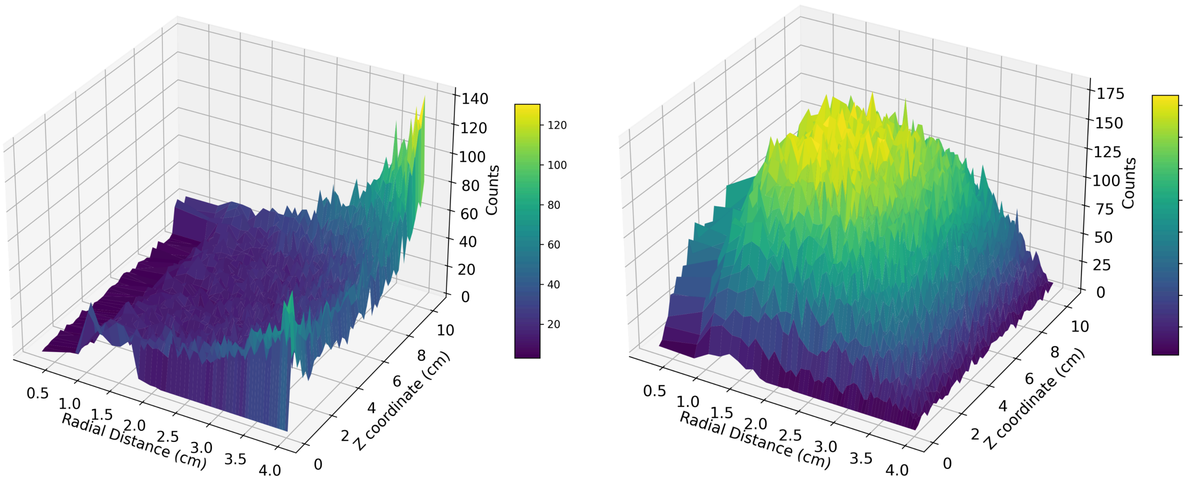

Figure 36: Simulated spatial distribution of TlDEP and BiFEP events in the ANG2 detector volume, presented as a function of radial distance and z-coordinate along the detector height. The bin sizes along the radial axis are scaled by the square root of the radial distance to ensure that each bin represents an equal volume within the detector. A position of a given event is represented here by its barycenter calculated as energy weighted average of all corresponding interaction points as detailed in later subsection.

Another issue with the choice of signal and background event classes from calibration data is that both samples are not perfectly pure but rather a mixture of SSE and MSE due to the Compton events under the energy lines. In order to suppress this underlying Compton background, a coincidence cut with 511 keV energy deposition in any of the other detectors can be applied which retains events involving escape of one or more annihilation photons escaping the detector volume like DEP and SEP of ^{208}Tl. The resulting energy spectrum, plotted in Figure 37, shows that events in the double and single escape peaks are retained while suppressing all other γ-lines and the Compton continuum. This approach effectively improves the purity of SSE sample at DEP and MSE sample at SEP. However, Since these two peaks from ^{208}Tl are 511keV apart, using signal and background samples from distant peaks for training introduces an energy dependency in the multivariate analysis, and the 511 keV coincidence cut results in much smaller training sample sizes and hence is not an ideal solution due to performance and overtraining concerns.

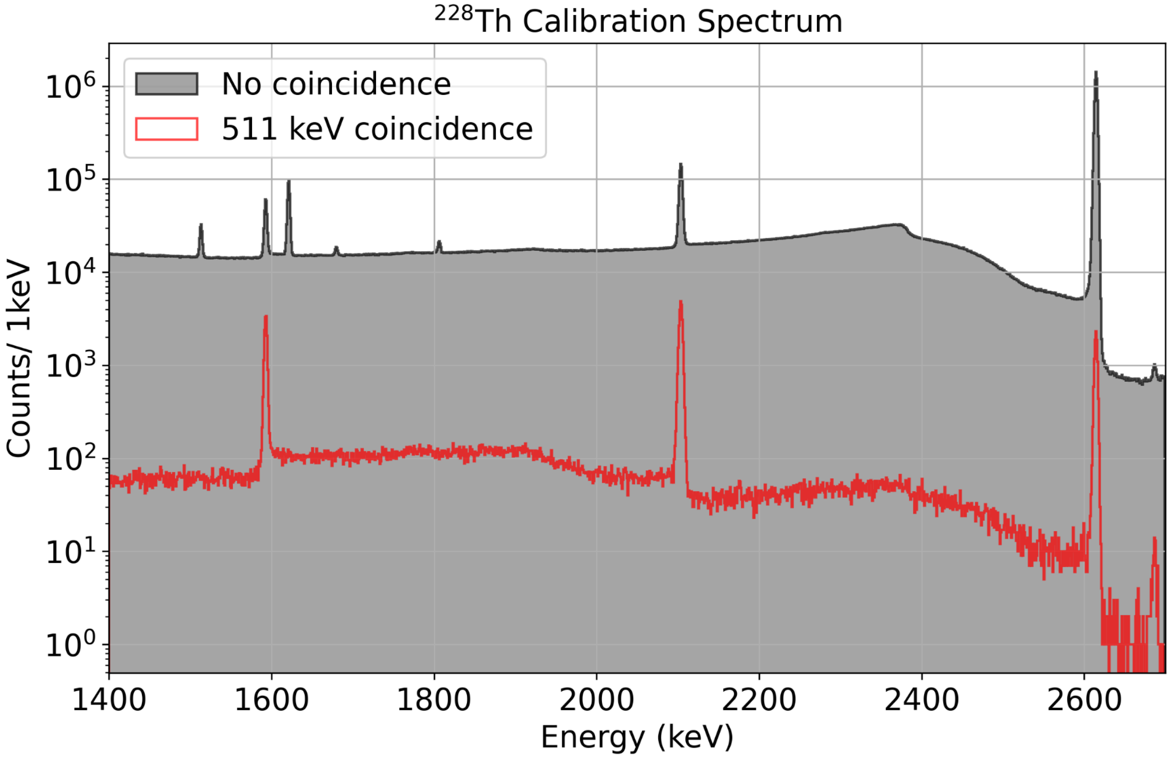

Figure 37: . Calibration spectra before and after 511 keV cut coincidence for semi-coaxial detectors in Phase II.

4.6. Model Performance Comparison

In this analysis, we implemented and compared three distinct machine learning models for the binary classification task: Convolutional Neural Network (CNN), Multi-Layer Perceptron (MLP), and Recurrent Neural Network (RNN). Each of these models was trained using the TensorFlow framework and evaluated using ROC curves to assess their performance in distinguishing signal-like events from background.

The Receiver Operating Characteristic (ROC) curve is a graphical representation used to evaluate the performance of binary classification models. It plots the True Positive Rate (TPR) against the False Positive Rate (FPR) at various threshold settings. The TPR, also known as sensitivity or recall, is the ratio of correctly predicted positive observations to all actual positives which in this case is equal to signal efficiency. The FPR, on the other hand, is the ratio of incorrectly predicted positive observations to all actual negatives and represents survival fraction of the background. By visualizing the trade-offs between TPR and FPR, the ROC curve provides insight into the performance of a model across different cut thresholds on the binary classifier value. One key metric derived from the ROC curve is the Area Under the Curve (AUC). The AUC provides a single scalar value that summarizes the overall ability of the model to discriminate between the positive and negative classes. An AUC of 0.5 suggests no discriminative power, equivalent to random guessing, while an AUC of 1.0 indicates perfect discrimination.

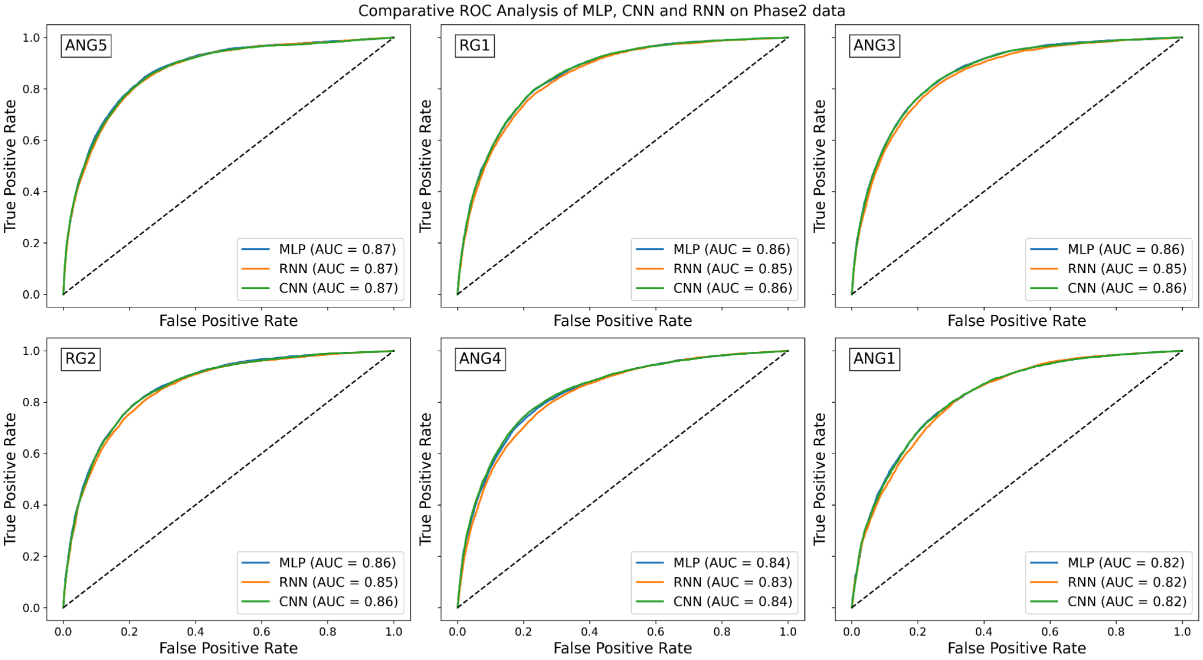

Figure 38: For each of the semi-coaxial detectors, the ROC curves for the CNN, MLP, and RNN models evaluated on Phase II data are plotted for comparison. The AUC values are listed next to corresponding algorithms.

Upon examining the ROC curves for each model shown in Figure 38 above, we observed that they all exhibit similar shapes, indicating comparable performance. Additionally, the AUC values for the CNN, MLP, and RNN models were found to be very close to each other, further corroborating their similar discrimination power. Given the comparable performance of the CNN, MLP, and RNN models as indicated by their ROC curves and AUC values, any of these models could potentially be chosen for our final analysis.However, we have decided to proceed with the CNN model.

In our specific context, the input data consists of pulse shapes from high purity germanium detectors. These pulse shapes can be thought of as one-dimensional signals where the objective is to capture and distinguish any subtle spatial patterns that differentiate signal pulses from background pulses. CNNs are inherently designed to detect such patterns through their convolutional layers, which apply filters to local regions of the input data. Additionally, CNNs are known for their robustness to translational variance, meaning they can recognize patterns regardless of their position within the input. This property is especially beneficial for our analysis, as it ensures that the model can accurately detect relevant features of pulse shapes even if they are shifted or slightly altered in time. Thus, despite the similar ROC curves and AUC values observed across the models, CNN is used as the architecture of choice for further analysis.

4.7. Overtraining check: Model performance on test dataset

In order to develop reliable and generalizable models, it is important to check for their robustness to make sure they are not overtrained. Overtraining, or overfitting, occurs when a model performs exceptionally well on the training data but fails to generalize to unseen data, leading to poor performance on the test dataset. This typically happens when the model learns to memorize the training data, including its noise and outliers, instead of capturing the underlying patterns that apply to new data. As discussed in section 4.3.7, we implemented “Early Stopping” where the validation loss is monitored during training and the training process is stopped once the validation loss stops decreasing, indicating that the model is no longer improving its generalization performance and may start overfitting.

The whole dataset is split into training, validation, and test subsets in a 60:20:20 ratio while maintaining balanced distribution of signal and background events in each subset. This partitioning allows the model to be trained on one portion of the data, validated on another to tune hyperparameters and employ “early stopping”, and tested on a separate set to evaluate its generalization performance.

In this analysis, events from the ^{208}Tl Double Escape Peak at 1592.5 keV represent signal and background is sampled from the Full-Energy Peak (FEP) of ^{212}Bi at 1620.5 keV. In order to check for possible overtraining, a comparison of model response on training subset and testing subset is evaluated. Below Figure 39 showcases density histograms of the predicted classifier outputs for both the training and test subsets for individual semi-coaxial detectors in Phase II. These responses are overlaid to visually assess the similarity between the distributions of predicted classifiers for signal and background events in both training and test subsets.

From Figure 39, it is evident that the classifier distributions for signal events from the training subset closely overlap with those from the test dataset for all semi-coaxial detectors in this study. Similarly, the classifier distributions for background events from the training subset and the test subset align closely. This high degree of overlap indicates that the model has learned to generalize well from the training data to the test data, effectively capturing the underlying patterns without overfitting. To quantify this, the table 5 summarizes the binary cross-entropy loss and accuracy metrics for both the training and test datasets for each semi-coaxial detector. Here, the accuracy is calculated using a standard cut-off threshold of 0.5, which is common practice for binary classification tasks.

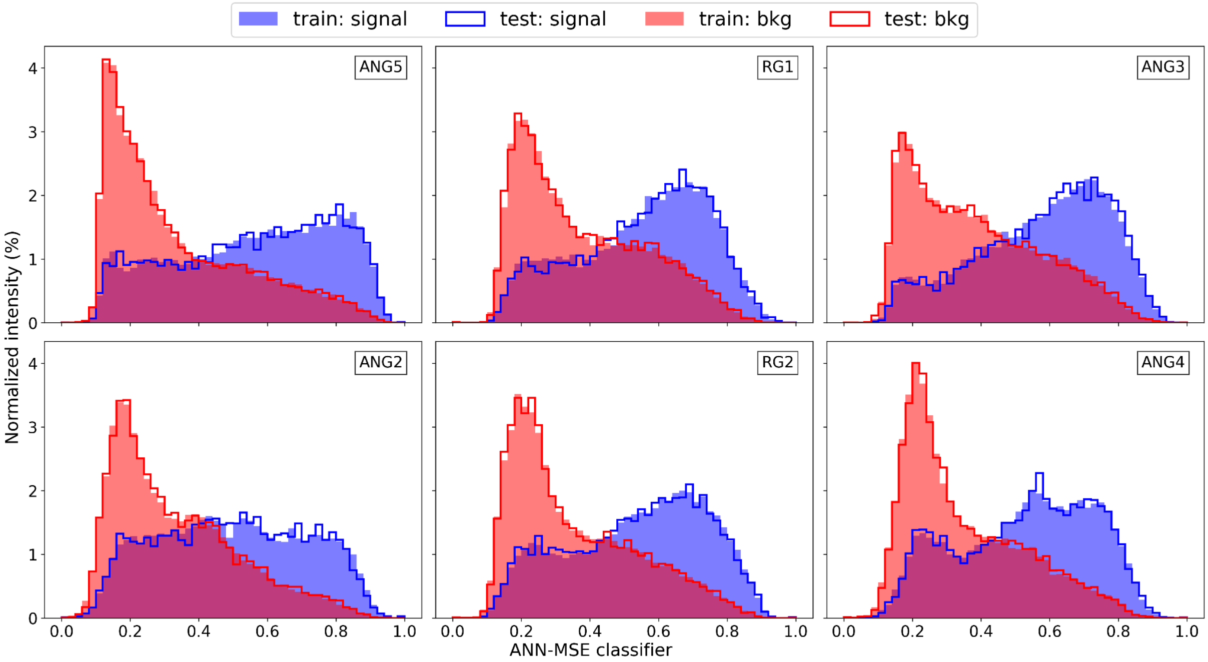

Figure 39: The figure illustrates predicted classifier distributions for the signal (in blue) and background (in red) across training and test subsets for individual semi-coax detectors in Phase II. The filled histograms represent the training data, while the step histograms depict the classifier distributions for the test subsets.

Detector		ANG5	RG1	ANG3	ANG2	RG2	ANG4
Loss	Training	0.568	0.596	0.585	0.586	0.582	0.582
	Validation	0.568	0.590	0.586	0.587	0.583	0.589
	Testing	0.565	0.592	0.581	0.588	0.586	0.582
Accuracy	Training	0.713	0.686	0.697	0.698	0.702	0.704
	Validation	0.714	0.693	0.699	0.692	0.702	0.695
	Testing	0.713	0.688	0.703	0.697	0.696	0.702

Table 5: The table displays binary cross-entropy loss and accuracy metrics for training, validation, and testing subsets across various semi-coaxial detectors in Phase II. The loss and accuracy values are consistent across subsets for all detectors which indicates robust model performance without overtraining. The accuracy values are calculated using 0.5 as the cut off threshold for classifiers and account for both signal and background events in respective datasets.

The classifier distributions for signal and background events are nearly identical between the training and test datasets, and the similar loss and accuracy metrics further support this conclusion. The combined evidence from the classifier distributions in Figure 39 and evaluation metrics listed in table 5 confirms that the models are not overtrained and will be used for further analysis.

After verifying that our models are both robust and free from overtraining, events from several peaks of interest in calibration data are utilized to assess their practical performance. As described in Section 3.2, throughout the experimental runtime, multiple calibration runs were performed with ^{228}Th as a calibration source with a distinctive energy spectrum that is useful for calibration and multiple gamma peaks originating from ^{208}Tl and ^{212}Bi decays. Out of these prominent gamma peaks, the ^{208}Tl Double Escape Peak (TlDEP) at 1592.5 keV is primarily associated with single-site events, while the Full-Energy Peak (FEP) ^{212}Bi (BiFEP) at 1620.7 keV, and the Thallium-^{208} Single Escape Peak (TlSEP) at 2103.5 keV, and Full-Energy Peak (TlFEP) at 2614.5 keV are predominantly multi-site in nature.

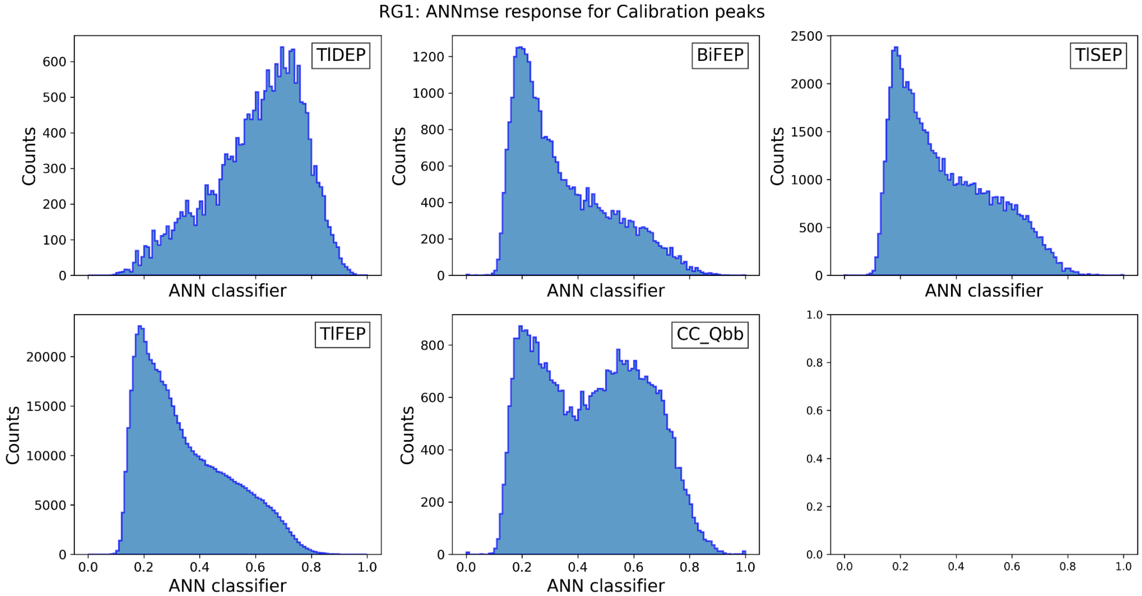

Figure 40: The predicted classifier distributions for events from various energy ranges corresponding to these above mentioned peaks from the RG1 detector. The last panel titled “CC_Qbb” represent events from Compton continuum in the ∓25 keV window centered at $Q_{\beta\beta}$-value of 2039 keV and constitutes of a mixture of both single-site and multi-site events.

It is evident that events from the TlDEP peak are primarily classified as signal, with classifier values close to 1, whereas events from the other peaks, which are predominantly multi-site, have comparatively lower classifier values. Notably, the shape of the classifier distributions for all multi-site event peaks which include BiFEP, TlSEP, and TlFEP are very similar, as anticipated.

4.8. ANN-MSE classifier Threshold selection

In this study for binary classification with a machine learning model, a sigmoid layer is utilized in the final layer to generate classifiers with values ranging from 0 to 1. Here, the proximity of a classifier value to 0 signifies an event resembling background, while proximity to 1 indicates an event resembling a signal.

To optimize the classification and retain a high signal efficiency, a specific threshold on classifier value is set. In case of ANN-MSE, this threshold is configured in such a way that approximately 90% of ^{208}Tl DEP events, which are signal-like, possess classifier values exceeding this designated threshold and pass the ANN-MSE-cut. Note that the efficiency or survival fraction of a particular peak is determined as the fraction of events that pass the cut where the side-bands from below and above the peak are subtracted assuming a linear scaling of underlying Compton-events.

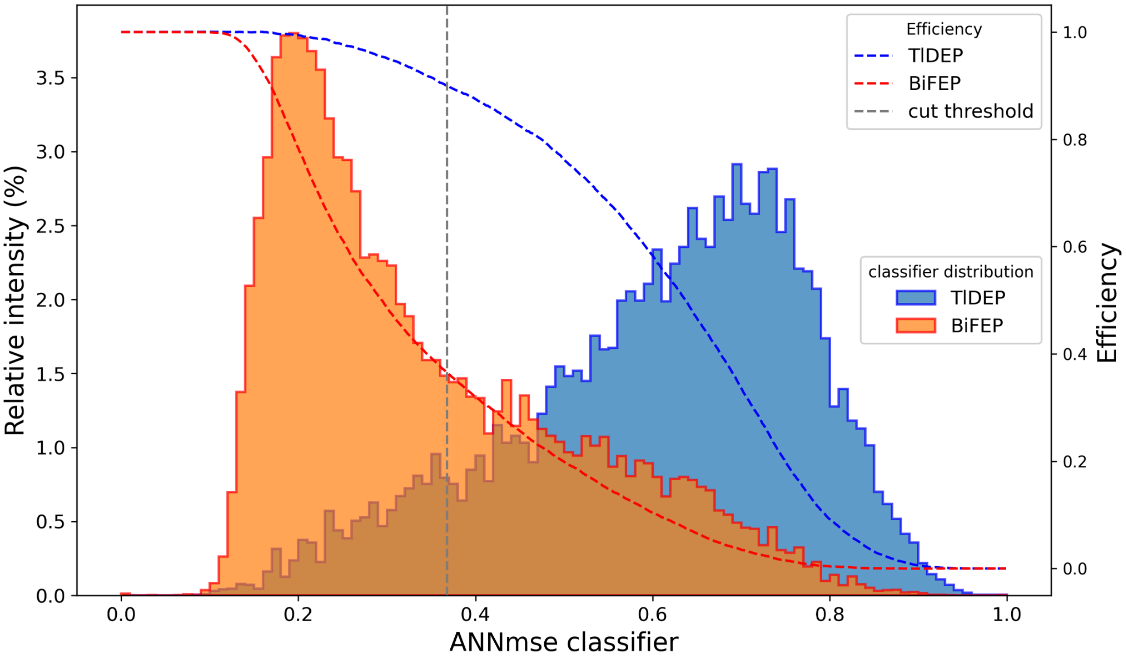

Figure 41: illustrates the ANN-MSE classifier distributions for both TlDEP (signal-like) and ^{212}Bi Full-Energy Peak (BiFEP, background-like) events from the RG1 detector. The efficiency of these events as a function of the classifier threshold is also plotted with dashed lines. The calibrated ANN-MSE cut threshold is marked by a grey line, set to achieve 90% efficiency for the TlDEP peak. The same calibration procedure is applied to other semi-coaxial detectors to determine their respective ANN-MSE cut thresholds. A detailed plot showing the calibration results for all detectors can be found in the appendix.

To visualize the suppression of background-like events and retained efficiencies for signal-like events along with the derived classifier cut threshold is drawn in Figure 42 below. Below the efficiencies, for several peaks of interest from the calibration data, including TlDEP, BiFEP, TlSEP, TlFEP, as well as 2νββ events from physics data, are plotted as a function of the classifier cut threshold for each of the semi-coaxial detector in Phase II.

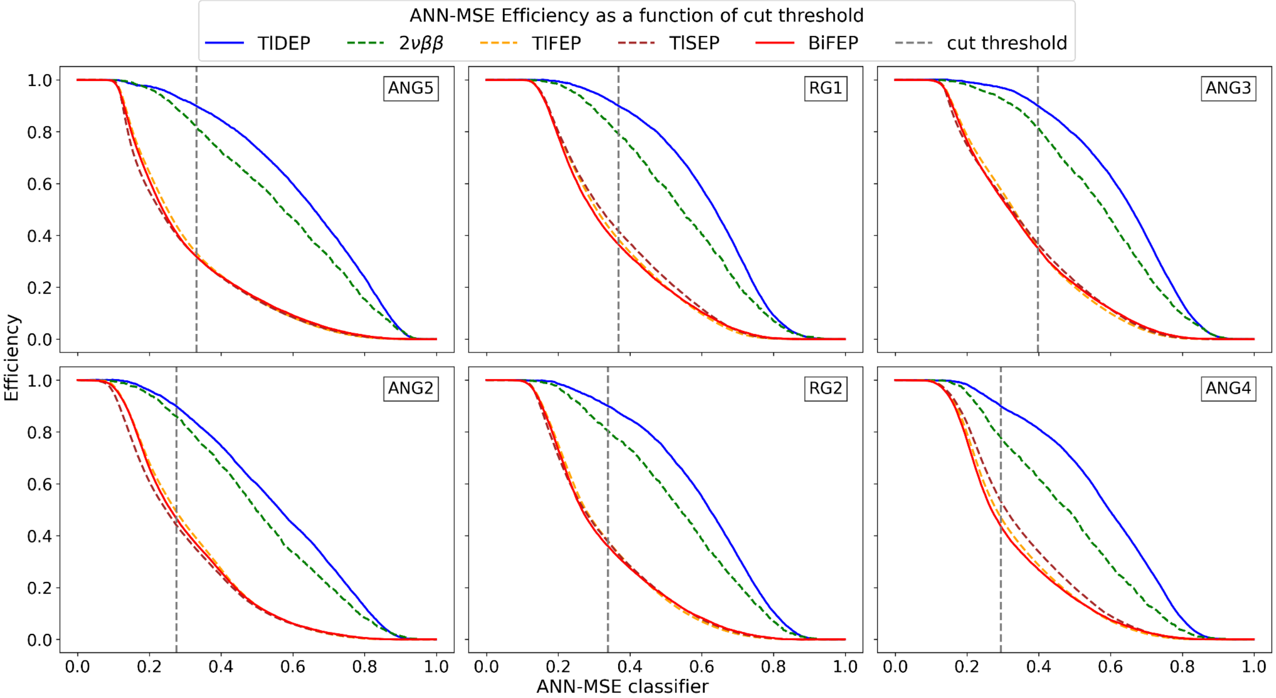

Figure 42: Survival fractions of different energy ranges from calibration and physics data as a function of the classifier cut threshold is shown. The grey line indicates position of calibrated ANN-MSE-cut parameter set at 90% of TlDEP survival. Note that for survival fractions for gamma peaks from calibration data, underlying Compton contributions are subtracted statistically using ANN-response on Compton sidebands of respective peaks assuming linear scaling of Compton continuum.

The Figure 42 demonstrates that TlDEP and 2νββ events exhibit much higher efficiencies compared to BiFEP, TlSEP, and TlFEP events, which are significantly suppressed across all semi-coaxial detectors. Notably, the efficiency for 2νββ events is still considerably lower (~10%) than that for TlDEP events, despite TlDEP being chosen as the proxy for signal-like events.

In developing the ANN-MSE model to differentiate between single-site and multi-site events, we initially used TlDEP events as a proxy for the signal as detailed in the earlier section. However, due to the inhomogeneity of TlDEP events, they do not closely represent the 0νββ signal. As depicted in the Figure 36, TlDEP events are distributed unevenly across the detector volume and are predominantly located at the edges of the detector, whereas 0νββ decay events are expected to be distributed uniformly across the detector volume. Semi-coaxial detectors showcase a more homogeneous weighting potential compared to BEGe/IC detectors, as depicted in Figure 10. This homogeneity influences the pulse shapes, leading to position-dependent variations. Consequently, models trained with TlDEP events may learn to exploit these positional dependencies of pulse shapes to distinguish between single-site and multi-site events, as shown in Figure 43. This figure illustrates the position dependence of the ANN-MSE efficiency for simulated 0νββ events in semi-coaxial detectors.

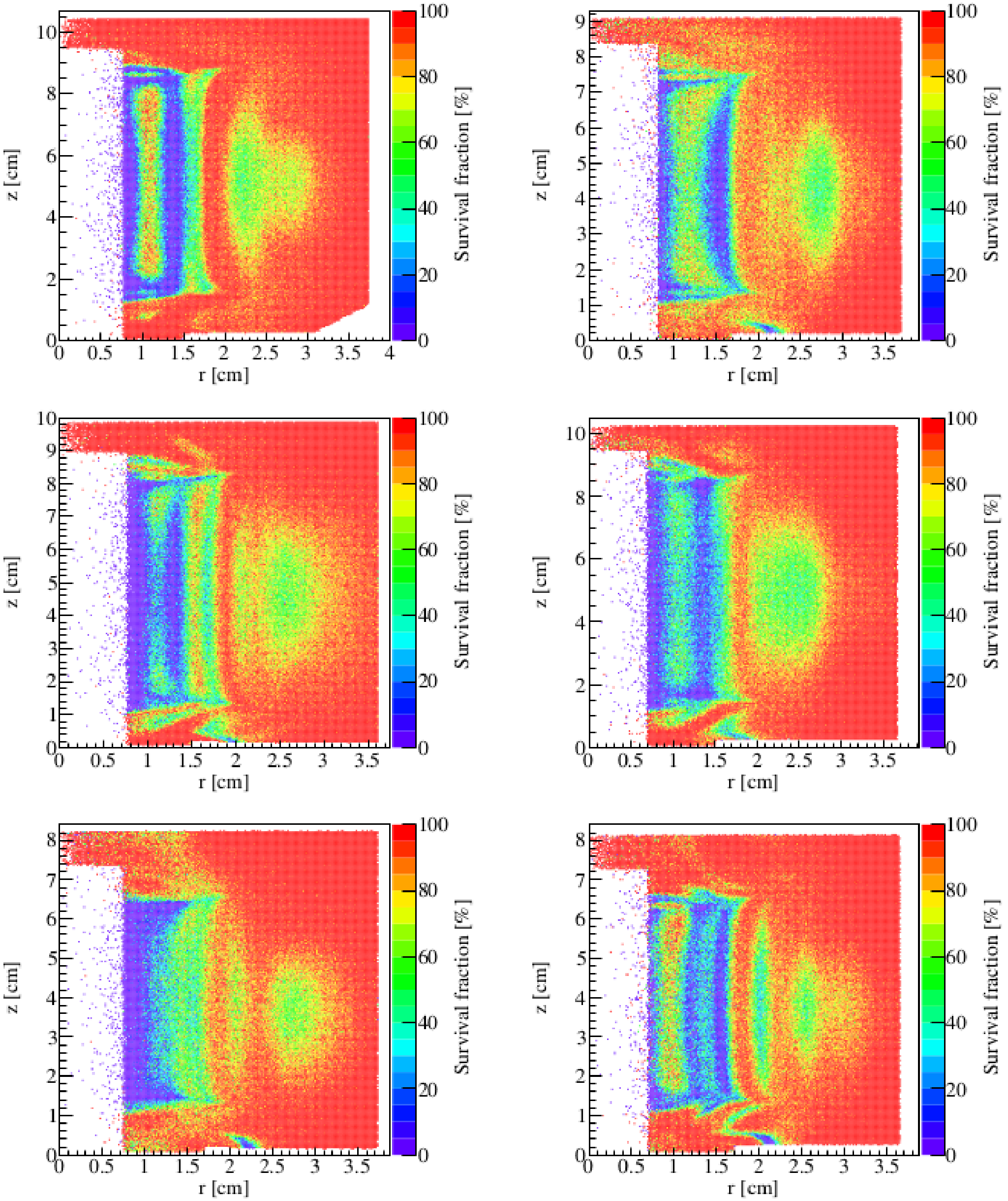

Figure 43: Spatial distribution of ANN-MSE efficiency for homogeneously simulated 0νββ events inside detector volume for each of the semi-coaxial detectors is shown as a function of radial distance (r) and height (z). (taken from [Kir14]). Similar behavior was observed in the current analysis with TlDEP as a signal proxy, although with less statistics of simulated events, and relevant figures can be found in the Appendix A.

To mitigate this positional dependence and better approximate the 0νββ decay signal, we selected a different proxy: events from the Physics dataset after LAr (liquid argon) veto in the energy range of 1.0-1.3 MeV. These events are primarily from the neutrino-accompanied double beta decay of ^{76}Ge and are expected to be uniformly distributed across the detector volume assuming homogeneous enrichment. Although the statistics for these events are lower compared to TlDEP events from calibration data, they provide a more accurate representation of single-site events due to their higher purity of SSE samples due to significant suppression of Compton background due to LAr veto which is not operational during calibration data taking. With proper measures to prevent overtraining, we train reliable ANN-MSE models effectively to differentiate between single-site and multi-site events using this proxy.

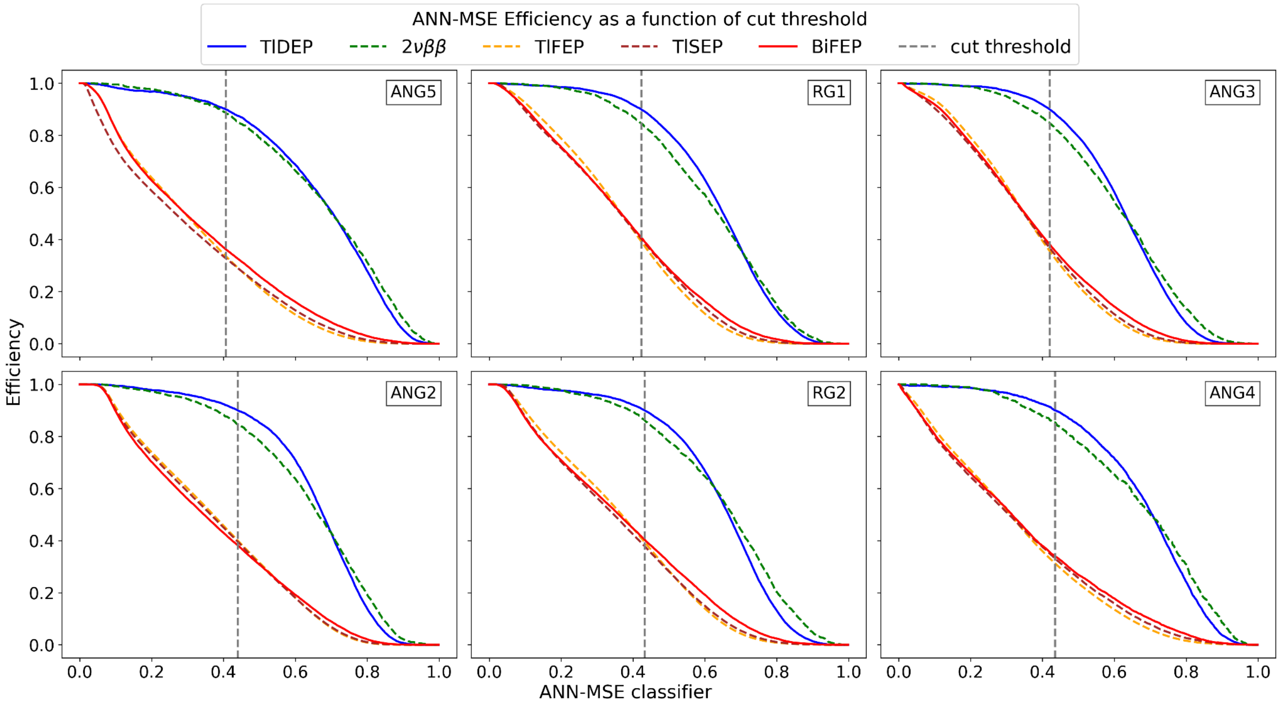

Figure 44: Survival fractions of different energy ranges from calibration and physics data as a function of the classifier cut threshold is shown. The grey line indicates position of calibrated ANN-MSE-cut parameter set at 90% of TlDEP survival.

After incorporating the 2νββ samples for training ANNmse models, the efficiency for 2νββ events improves and approaches that of TlDEP events as evident from above Figure 44. TlDEP events continue to be used for setting the ANN-MSE cut threshold, ensuring that the models are both accurate and reliable.

From the Figure 45, it is evident that the classifier values for single-site events, such as those from TlDEP, cluster at higher values above the cut threshold. Conversely, predominantly multi-site peaks like BiFEP, TlSEP, and TlFEP have a much higher fraction of events below the classifier threshold, indicating that these events would be effectively removed by the ANN-MSE cut. Additionally, note the higher classifier values for the Compton edge at energies just below 2382 keV in the calibration spectra.

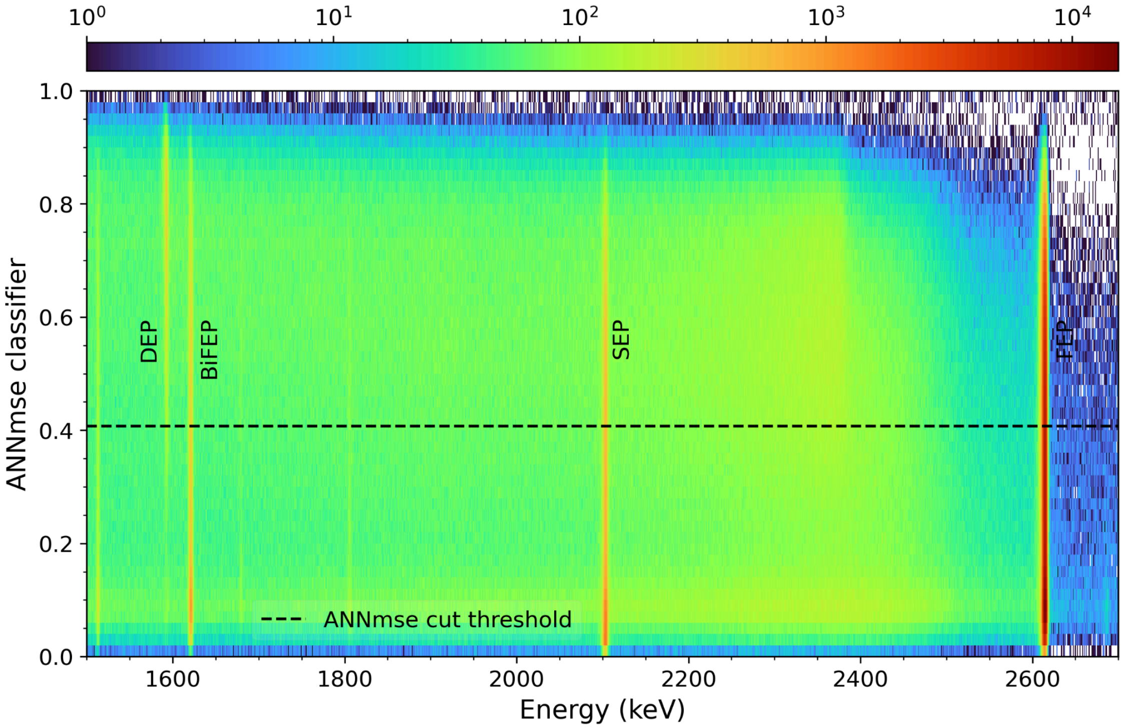

Figure 45: For ANG5, a 2-dimensional heatmap of ANN-MSE classifiers from the ^{228}Th calibration data as a function of energy with prominent gamma lines is presented. The dashed black line represents the ANN-MSE cut threshold for the given detector set, calibrated to preserve 90% of TlDEP events.

As depicted in the bottom panel of Figure 46 below, apart from TlDEP at 1592 keV , all other gamma peaks are highly suppressed owing to their predominantly multi-site nature. The efficiency remains almost flat over the complete range of the Compton continuum, indicating robustness of model performance. Any possible energy dependence has been accounted for and it is illustrated in detail at the end of this chapter.

A detailed quantitative assessment of the ANN-MSE performance for each of the semi-coaxial detectors used in Phase II is provided in the table 6 below. As depicted in Figure 41, for each semi-coaxial detector, the MSE cut thresholds are optimized to maintain 90% efficiency for TlDEP events, which are primarily single-site. In contrast, BiFEP, TlSEP, and TlFEP events from the 228228Th calibration spectra, which are mostly multi-site, experience significant suppression, with ~65% of these events being rejected by the ANN-MSE. The "2νββ" column represents events from the Physics data within the 1.0-1.3 MeV energy range, primarily attributed to neutrino-accompanied double beta decay, and these are predominantly single-site events. The statistical errors shown are calculated as binomial errors on the efficiencies.

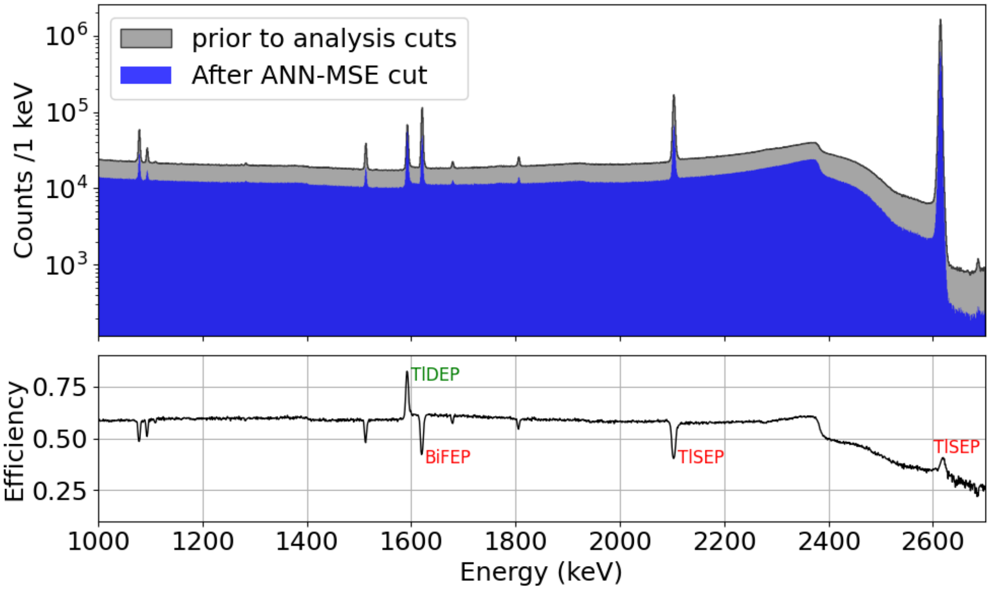

Figure 46: Combined 228Th calibration spectrum for all semi-coaxial detectors in phase II before and after the ANN-MSE cut is presented in the top panel. The bottom panel depicts ANN-MSE efficiency as a function of energy with major peaks of interest indicated with labels.

Detector	ANN-MSE threshold	ANN-MSE efficiency (%)				
		BiFEP	TlSEP	TlFEP	CC@$Q_{\beta\beta}$	2νββ
ANG5	0.407	36.1 ± 0.2	32.7 ± 0.1	33.5 ± 0.1	55.5 ± 0.2	88.5 ± 0.8
RG1	0.423	40.7 ± 0.2	40.3 ± 0.1	39.2 ± 0.1	59.4 ± 0.2	84.6 ± 0.8
ANG3	0.420	38.1 ± 0.2	36.8 ± 0.1	35.5 ± 0.1	55.6 ± 0.2	84.8 ± 0.7
ANG2	0.440	38.2 ± 0.2	39.5 ± 0.1	40.0 ± 0.1	58.6 ± 0.2	84.7 ± 0.7
RG2	0.433	40.3 ± 0.2	37.8 ± 0.1	39.3 ± 0.1	59.2 ± 0.2	86.2 ± 0.7
ANG4	0.435	34.1 ± 0.3	33.2 ± 0.2	31.3 ± 0.1	53.4 ± 0.3	85.3 ± 1.1
ANG1	0.430	42.5 ± 0.3	42.2 ± 0.2	43.7 ± 0.1	63.8 ± 0.3	82.0 ± 1.5

Table 6: For each of the semi-coaxial detectors in Phase II, the ANN-MSE cut thresholds and corresponding ANN-MSE efficiency in units of % for various peaks in the ^{228}Th calibration spectra are presented. The CC@$Q_{\beta\beta}$ column represents events from the Compton continuum within a ±25 keV window around $Q_{\beta\beta}$. The last column lists the observed ANN-MSE efficiency for events after LAr veto in the Physics data within the 1.0-1.3 MeV energy range, attributed to 2νββ decays.

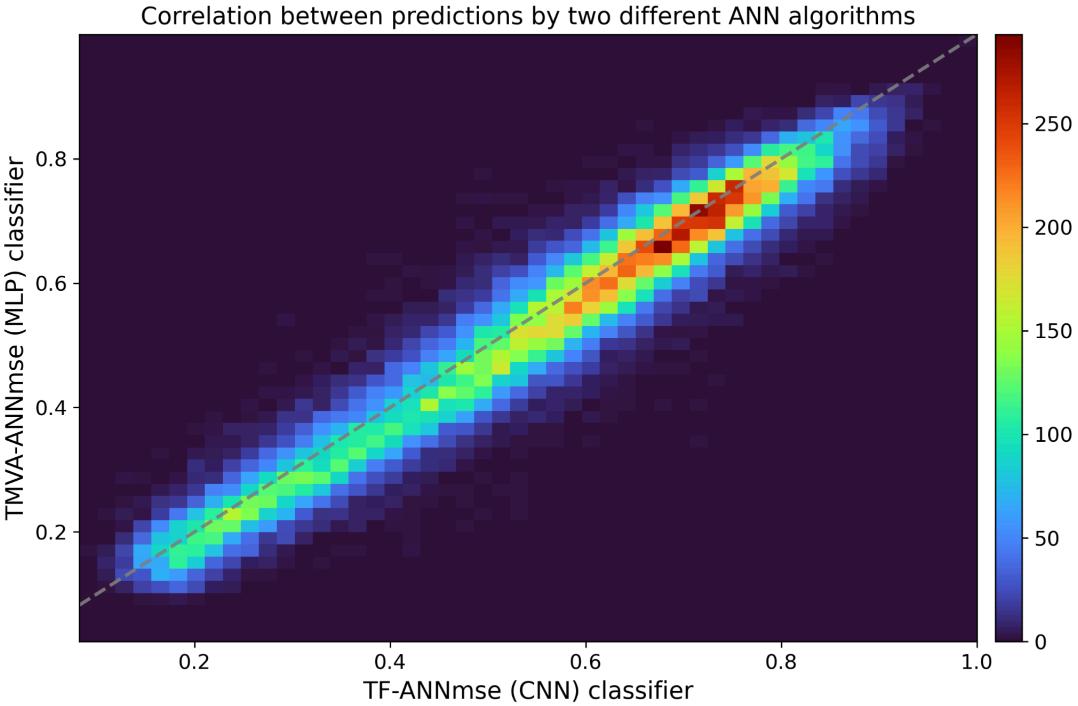

Figure 47: Predictions on TlDEP events from detector RG2 by two different algorithms with different architecture and optimizer functions are visualized as a 2-d histogram. The dashed line indicates x=y and the strong correlation in predictions is indicative of robustness of the model performance for a given dataset.

Noteworthy agreement between models is highlighted by the strong correlation between classifiers, emphasizing their shared understanding and reliable predictions.

4.8.1.Effect of ANN-MSE on alpha background

Given the significance of the α component in the semi-coaxial background of the Region of Interest (ROI), we explore ways to reduce this background and enhance sensitivity using rise time-based pulse shape discrimination (PSD). Since Phase I, the Artificial Neural Network for Multi-Site Events (ANN MSE) has been a well-established PSD technique to discriminate between single site and multi- site events.

A complementary PSD technique tailored to discriminate alpha background would be more effective if it were anti-correlated with the ANN MSE. This means that removing a class of background events already cut by ANN-MSE could potentially reduce the neutrinoless double beta decay (0νββ) efficiency without effectively reducing the potential background. The ANN-MSE is designed to remove MSE, which typically have longer rise times compared to single-site events (SSE). Therefore, a cut based on rise time that targets fast α events with smaller rise times should indeed be anti-correlated to some degree with the ANN MSE which is observed by plotting correlation between these two PSD methods as shown in Figure 62 in later section.

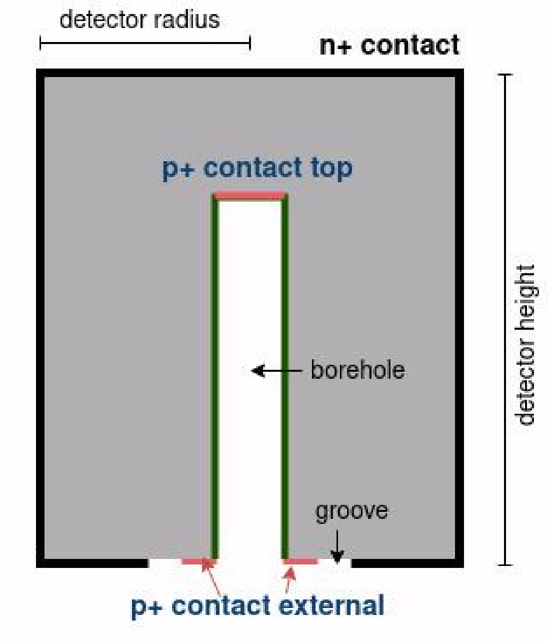

Figure 48: shows the alpha-sensitive surfaces on a typical semi-coaxial detector geometry. The whole p+ contact and the groove are sensitive to alpha contamination. The lateral surface of p+ contact is shown in green and top and external part are shown in red. The p+ and n+ contacts are separated by a groove for passivation.

Figure 48 illustrates all the possible alpha-sensitive surfaces in a typical semi-coaxial detector geometry. The distribution of these surface contaminants on the detector surface is unknown and could vary significantly between individual detectors. Form the Monte Carlo simulations and pulse shape studies in [Laz19], the alpha background on the sides of the bore hole (shown in green) showcase relatively longer rise times as charge carrier electrons need to traverse bulk volume of detector to reach n+ contact whereas for top and external part of p+ contact and groove , the rise times are much smaller.

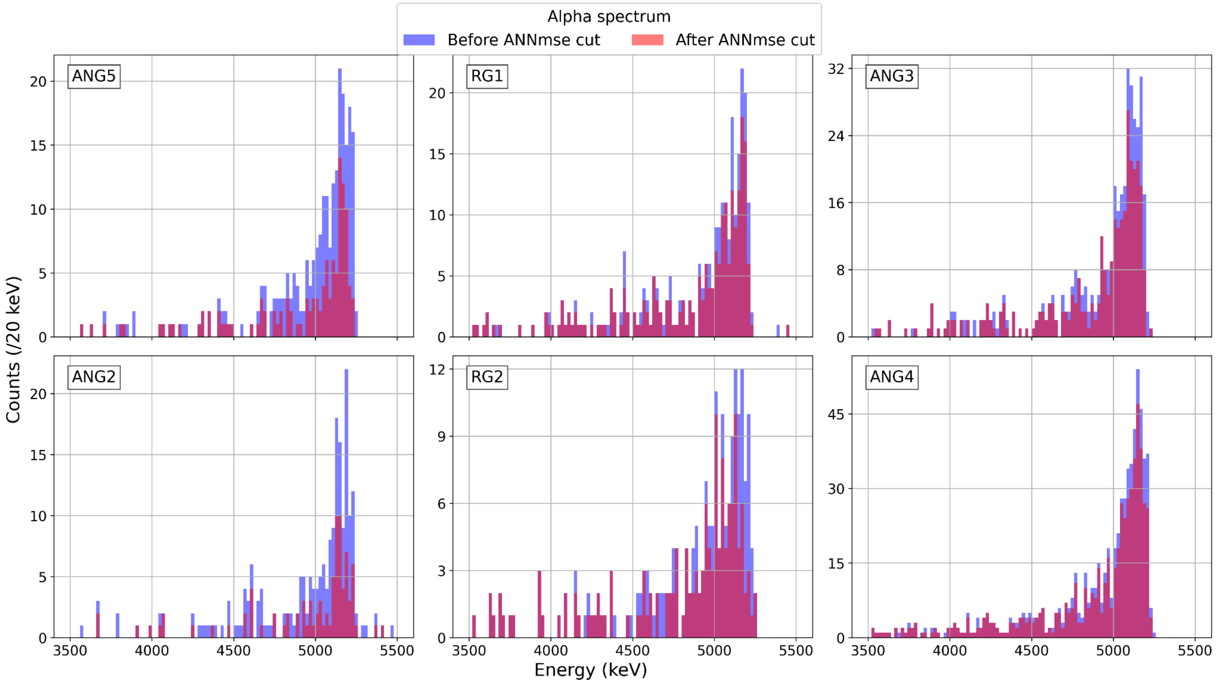

Figure 49: Energy spectrum for energies above 3.5 MeV in GERDA Phase II data before (in blue) and after (in red) applying the ANN-MSE cut. The fraction the alpha events removed by ANN-MSE cut are expected to be from surface contamination from the sides of borehole.

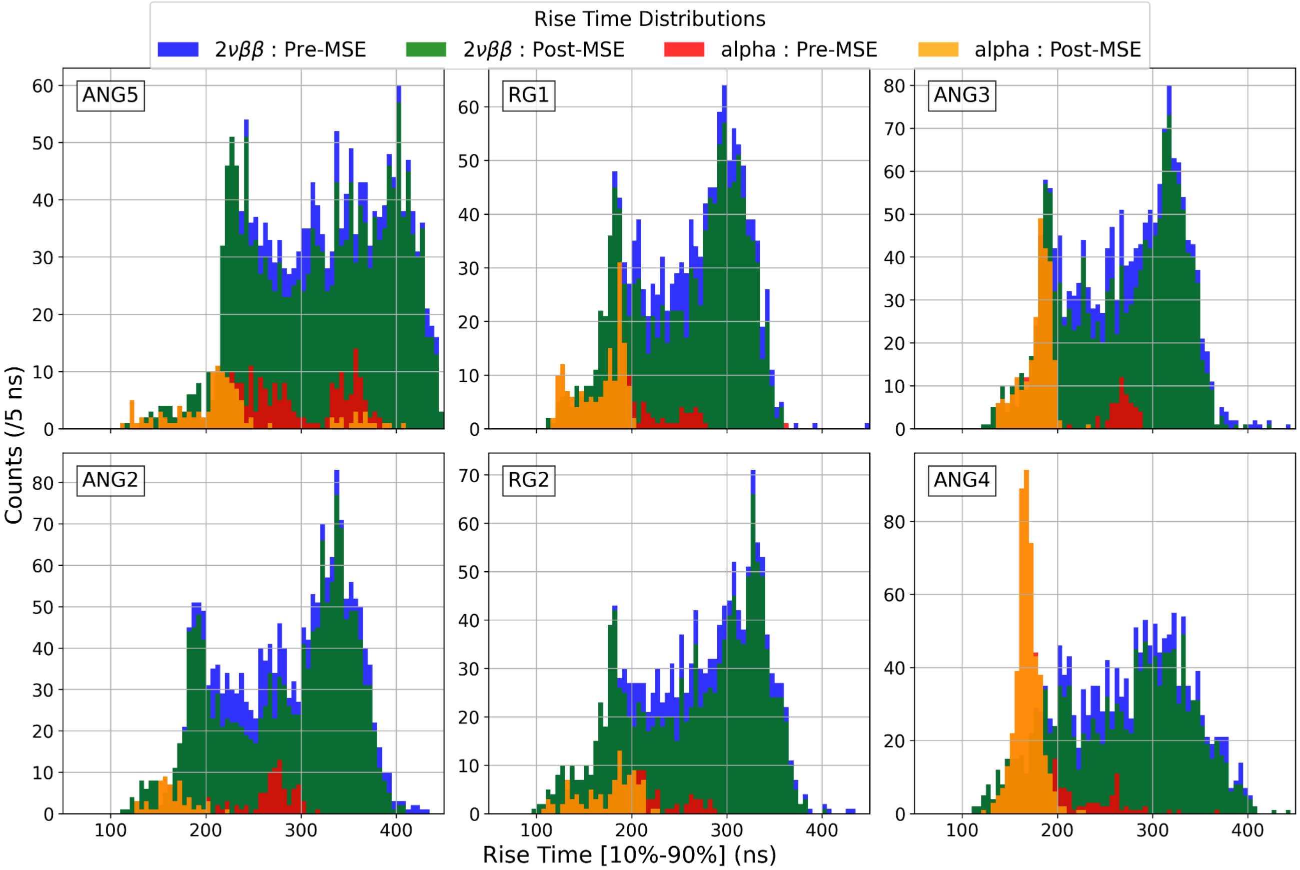

Figure 50: For six coaxial detectors in Phase IIS, the rise time distributions for 2**ν**bb and alpha events are overlaid to compare the distributions before and after applyingthe ANN-MSEE cut. For all detectors, almost all alpha events with higher rise times are removed by ANN-MSE cut leaving behind alphas with relatively shorter rise times.

Figure 50 shows that almost all alpha background with relatively higher rise times supposedly due to surface contaminants on lateral sides of p+ contact are effectively removed by ANN-MSE cut while maintaining high signal efficiency for 2**ν**bb events. This enables us to formulate a discrimination technique based on the rise time parameter to effectively remove these remaining alpha background.

As observed in figure 49, The energy spectrum of alpha background before and after the ANN-MSE cut shows a varying fraction of all alpha background removed by the respective ANN-MSE cuts for individual coax detectors, which would point to differing surface contaminant distributions among the different semi-coaxial detectors.

4.9. ANN-alpha

The Pulse Shape Discrimination (PSD) with ANN-MSE for semi-coaxial detectors, as described earlier in this chapter, performs excellent separation of gamma induced multi-site background from the single-site events . In addition to previously considered multi-site events (MSE) contributions originating from gamma radiation, alpha surface events (i.e., those occurring on the p+ contact and detector groove) have been identified as a significant background source for the GERDA experiment, particularly at the onset of data collection in December 2015.

It's worth noting that while the alpha background includes major contributions from the decay of ^{210}Po with a half-life of 138.4 days [Eic54], which tends to diminish over time, addressing this source of background remained vital as the GERDA experiment advanced into Phase II. Phase II aims to achieve a substantial reduction in the background index (BI) by an additional order of magnitude, down to 10^{-3} cts/(kg·keV·yr) compared to Phase I. To meet this ambitious objective and maintain the highest possible efficiency for detecting the $0\nu\beta\beta$-signal, a second neural network algorithm, referred to as ANN-α, has been developed. This neural network is tailored to address the unique requirements posed by the presence of alpha-induced background components. In Phase II, an alternative method was previously implemented to suppress surface background. The relevant analysis was utilized for publication. This method was based on a monoparametric "risetime cut." This method has been elaborated upon in the subsequent section, 4.10.

4.9.1. Input for ANN-alpha

For the training of ANN-α in Phase II, events within the energy range of 1000 keV to 1300 keV, primarily associated with $2\nu\beta\beta$-decay, have been selected as the signal-like sample. This specific range is chosen to avoid any contaminating gamma-ray background peaks in the physics energy spectrum. In contrast, alpha events within the energy interval of 3.5-5.5 MeV from physics data are designated as the background-like sample, as these events exhibit different topological characteristics due to alpha contamination at the p+ contact and the groove, resulting in a faster rising edge in the charge pulse. Since the ANN-α classification is designed to complement the ANN-MSE based pulse shape discrimination, the signal and background samples are chosen such that only those events not vetoed by the LAr veto and that also survive the ANN-MSE cut are used for further ANN-α analysis. This focused approach allows ANN-α to effectively discriminate between alpha-induced background events and signal-like events, contributing to the overarching goal of reducing background in the GERDA experiment during its Phase II operation.

Despite the smaller training dataset compared to the MSE-based training, an efficient—if not superior—separation from the signal event class is achieved. The comparison between training and test datasets indicate negligible overtraining effects . Alpha decay pulse shapes significantly differ from those generated by ββ or gamma-induced energy deposition in the germanium crystal bulk, facilitating easier event classification. Figure 51 illustrates the input variable distribution at 5% and 95% pulse height for alpha event samples for the 2vββ and α events.

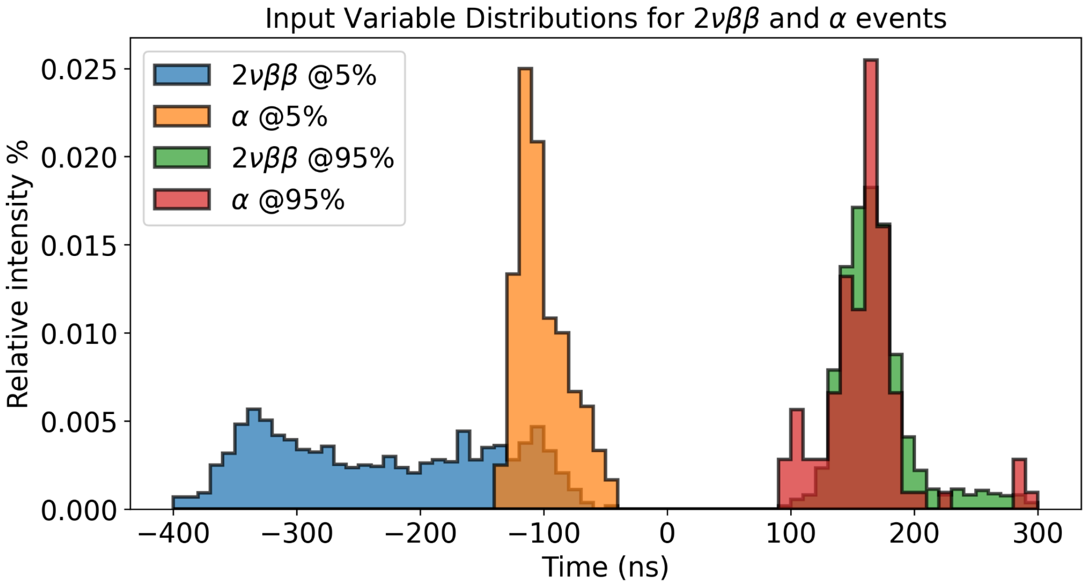

Figure 51: Time distribution of different input variables when reaching 5% and 95% pulse height for 2vββ and α events.

4.9.2. Feature Selection for ANN-α

The selection of input features for training ANN-α is based on the observed dissimilarities between signal and background distributions. Specifically, the first 15 input features, corresponding to the rising edge up to 39% of the maximum amplitude, are chosen. This partial rising edge selection is driven by several key considerations:

1. Dissimilarity Between Signal and Background: The chosen features show significant differences between the signal (primarily 2vββ-decay events) and background (alpha-induced events) as shown in figure 52. This dissimilarity enhances the neural network's ability to distinguish between the two types of events effectively.

2. Resistance to Electronics Variations: The lower part of the rising edge is more resistant to changes in electronics. Pulse shape simulations with ADL4, as described in Chapter 5, have demonstrated that this portion of the pulse shape is less affected by variations in the electronic setup. This stability ensures that the features used for training are consistent and reliable across different experimental conditions.

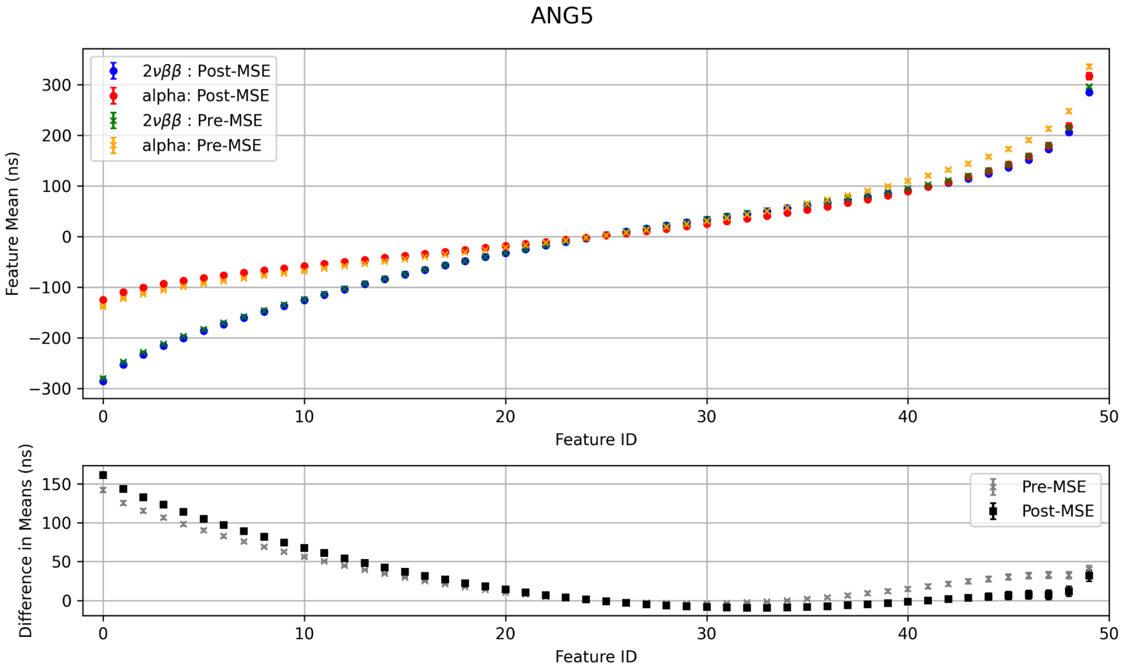

Figure 52: The top panel illustrates the plot of the mean values of each input feature distribution of 2vββ (in blue) and alpha (in red) events, highlighting the differences in their pulse topology. The bottom panel displays the absolute differences in the means of the respective 2vββ and alpha features, providing a straightforward measure of their dissimilarity.

By focusing on these specific features, the model can leverage the most distinguishing characteristics of the pulse shapes while minimizing the impact of potential electronic fluctuations, thus improving the robustness and accuracy of the event classification.

4.9.3. Overtraining Check for ANN-α: Model Performance on Test Dataset

To ensure the robustness and generalizability of ANN-α, it is important to check for overtraining, similar to the process employed for the ANN-MSE model discussed earlier. Overtraining occurs when a model performs exceedingly well on the training data but fails to generalize to unseen data, leading to poor performance on the test dataset. As detailed in the Figure 25, "Early Stopping" is implemented, where the validation loss is monitored during training. Training is halted once the validation loss stops decreasing, indicating that the model is no longer improving its generalization performance and may start overfitting.

For ANN-α, the dataset is similarly partitioned into training, validation, and test subsets in a 60:20:20 ratio, ensuring a balanced distribution of signal and background events in each subset. This partitioning allows for training on one portion of the data, validating to tune hyperparameters and employ “early stopping,” and testing on a separate set to evaluate generalization performance. To quantify the overtraining check for ANN-α, Table 7 summarizes the binary cross-entropy loss and accuracy metrics for both the training and test datasets.

across various semi-coaxial detectors. The accuracy is calculated using a standard cut-off threshold of 0.5, which is common practice for binary classification tasks.

Detector		ANG5	RG1	ANG3	ANG2	RG2	ANG4
Loss	Training	0.290	0.267	0.204	0.240	0.254	0.261
	Validation	0.304	0.262	0.196	0.230	0.268	0.268
	Testing	0.307	0.275	0.220	0.232	0.250	0.251
Accuracy	Training	0.842	0.826	0.892	0.875	0.831	0.851
	Validation	0.835	0.833	0.906	0.877	0.811	0.859
	Testing	0.837	0.810	0.890	0.865	0.837	0.863

Table 7: The table displays binary cross-entropy loss and accuracy metrics for training, validation, and testing subsets across various semi-coaxial detectors in Phase II. The loss and accuracy values are consistent across subsets for all detectors which indicates robust model performance without overtraining. The accuracy values are calculated using 0.5 as the cut off threshold for classifiers and account for both signal and background events in respective datasets.

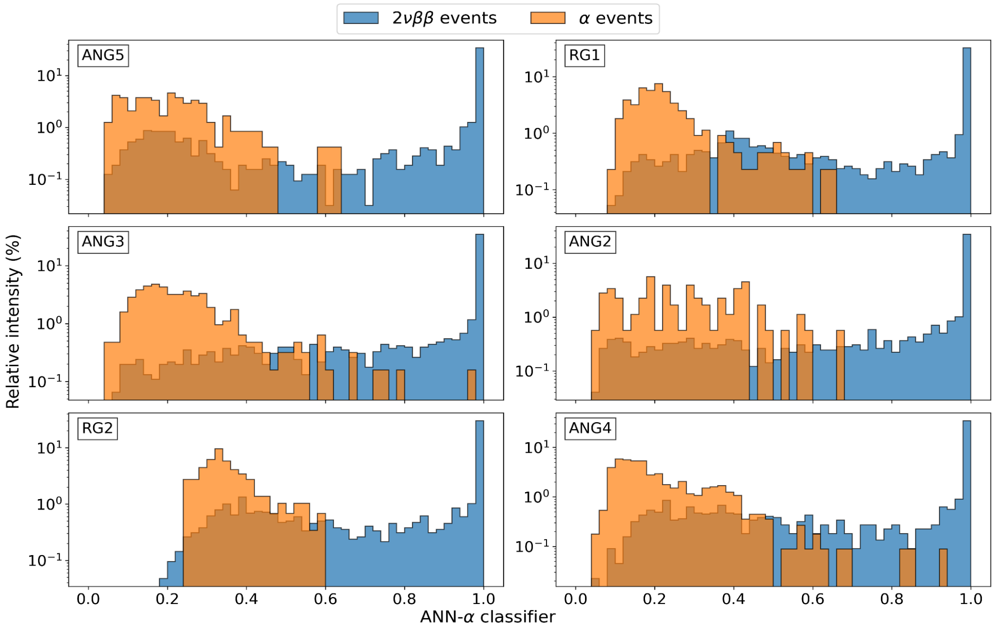

Figure 53: shows the predicted ANN-α classifier distributions for 2νββ (1.0-1.3 MeV) and α events (>3.5 MeV) after applying the ANN-MSE cut, for each semi-coaxial detector in Phase II. The 2νββ events (in blue) are centered around a classifier value of 1, while the α events are concentrated closer to zero.

Even though the sample sizes in the dataset were much smaller compared to ones for ANN-MSE, the use of proper early stopping measures and selection of relevant features ensures that there is no significant overtraining, as evidenced from Table 7.

After verifying that our models are both robust and free from overtraining, the models are applied to physics data to make predictions and standardize a cut threshold for classification.

4.9.4. Standardizing ANN-α cut threshold

The ANN-α models are designed to complement the ANN-MSE Pulse Shape Discrimination (PSD). Unlike the ANN-MSE cut, which is set to ensure approximately 90% of ^{208}Tl DEP events (signal-like) exceed the threshold, the ANN-α cut is determined using a figure of merit (FoM) derived from physics data. This method accounts for the variability in ANN-MSE's effectiveness at suppressing alpha background across different detectors.

The survival fraction of 2νββ events ($\varepsilon_{2\nu\beta\beta}(x)$) and alpha events ($\varepsilon_{\alpha}(x)$) is determined for varying thresholds (x) of the ANN-α classifier as fraction of events that have classifier values greater than x. The FoM is defined as a function of the ANN-α classifier threshold (x):

$$Figure\ of\ merit,\ f(x) = \varepsilon^{2}_{2\nu\beta\beta}(x)\ .\ (1 - \varepsilon_{\alpha}(x))$$

The optimal cut threshold is determined by maximizing the “Figure of Merit”. Events with ANN-α classifier values greater than this threshold are classified as signal-like while events with classifier values less than the threshold are classified as background-like.

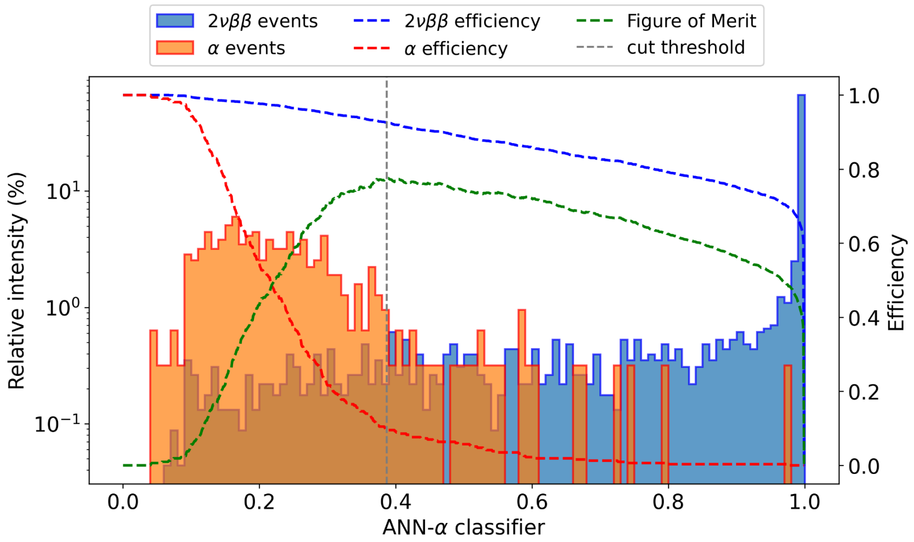

Figure 54: Calibration of the ANN-alpha cut threshold for the ANG3 detector. The ANN-alpha classifier distributions are shown for 2νββ (signal-like) events in blue and alpha (background-like) events in orange. The efficiency of these events as a function of the classifier threshold is plotted with dashed lines, with blue representing 2νββ and red representing alpha events. The figure of merit (FoM) is indicated by the dashed green line. The calibrated ANN-alpha cut threshold, determined by the maximum of the FoM, is marked by a grey vertical line.

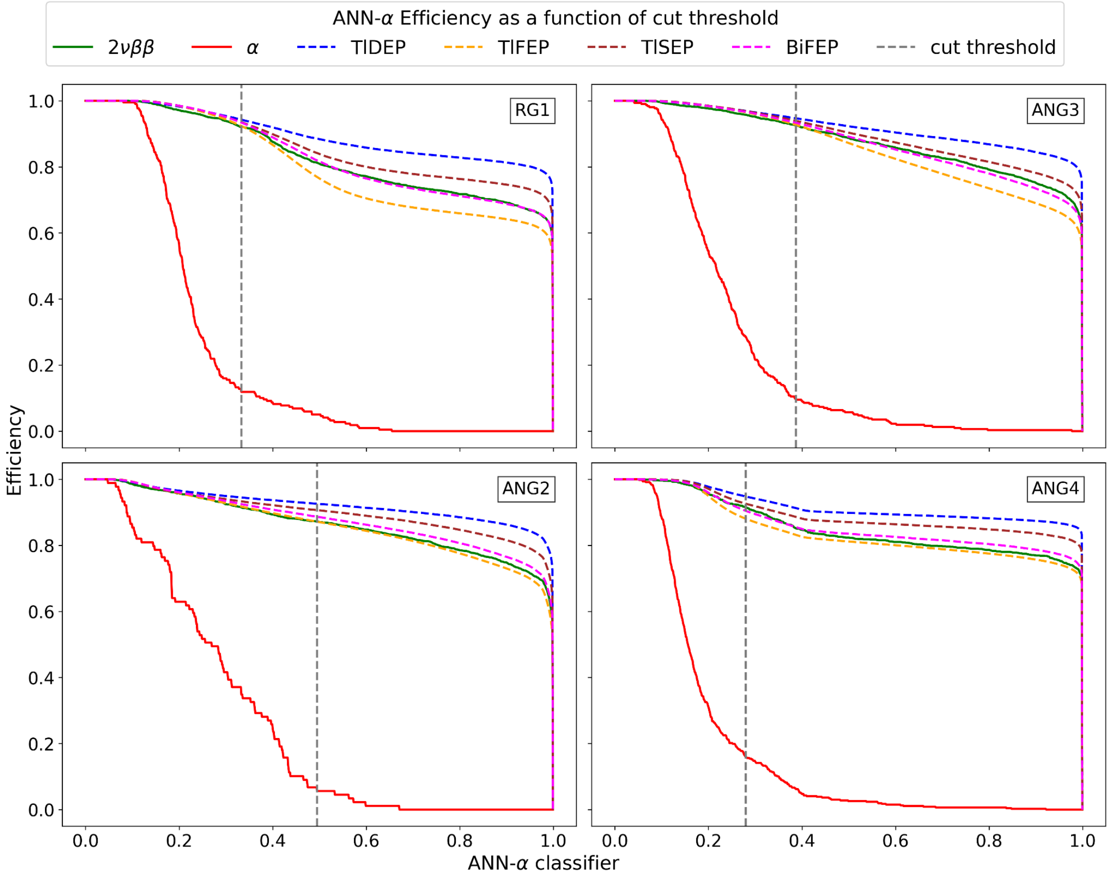

Figure 55: Survival fractions of different energy ranges from calibration and physics data as a function of the ANN-α classifier cut threshold is shown. The grey line indicates the position of the calibrated ANN-α cut parameter set at the maximum of the figure of merit.

4.10. An Alternative : Risetime Cut

It is evident from the simulations in coax detectors that the pulse shapes are strongly dependent on the spatial position of the event in the detector geometry. In energy spectra, we observe significant background contribution at higher energies (>3.5 MeV) which can be attributed to alpha decays mainly from ^{210}Po and partially from ^{226}Ra(4.7MeV). Alpha particles, being highly ionizing in nature, have a short range in germanium and LAr of the order of a few tens of μm. Thus the n+ surface with a dead-layer thickness of ~1mm is not sensitive to alpha radiation. The p + surface has a dead layer thickness of roughly 0.3μm and alpha decays occurring on or very close to the p+ surface will contribute to the measured background. In addition, the alpha decays on the groove of the detector can deposit energy in the active volume of the detector.

Due to their particular location in detector geometry as depicted in Figure 48, pulse shapes of remaining alpha events have a characteristic fast charge collection time and this results in signals with fast rise-time. The Rise Time based pulse shape discrimination utilises this to perform a volume cut which in essence excludes the relevant surfaces with the alpha background. The rise time parameter is extracted from the 100 MHz trace with the following subsequent steps:

1. Computing baseline by averaging the trace between 76.6-78.6 μs.
2. Filtering with Moving Window Average
3. Linear interpolation to achieve 1ns binning
4. Determination of 10% and 90% quantiles of waveform

A Gelatio module, GEMDRiseTime is implemented with all the above mentioned digital filters. The module computes the rise time parameter by determining the first time bin above the higher threshold of 90% pulse amplitude and the last time bin above the lower threshold of 10% while scanning from maximum amplitude to minimum and computing the time difference. To compute this, we need to know the values of baseline and the amplitude of charge signal. The baseline is computed using the HF (100 MHz) trace by averaging 2 μs of trace before the rising edge of charge pulse. To extract the amplitude, a Gast Trapezoidal filter is used for energy reconstruction because by design, the Gast filter measures the amplitude in terms of ADC channels which removes the need for any further conversion unlike in Gaussian filter.

To achieve our goal of removing the alpha events while maximising the 2νββ signal survival, we define a mono-parametric cut based on the rise time of the signals. The rise time cut is designed to complement the ANN-MSE PSD. Since ANN-MSE is more effective in suppressing alpha background for some detectors than others, an optimal cut threshold for the rise time cannot be defined apriori. Instead, we define it from physics data by comparing the survival efficiency of 2**ν**bb and α events. As a proxy for signal, 2**ν**bb events between 1.0 MeV and 1.3 MeV that survive LAr veto are used. This energy window doesn't have any major peaks from the background and LAr efficiently suppresses the gamma component of the background. The high energy events above 3.5 MeV that constitute the alpha events are used as proxy for background. We define a figure of merit as a function of the rise time as a product of the square of signal acceptance and background rejection efficiency:

$$Figure\ of\ merit,\ f(t) = \varepsilon^2_{2\nu\beta\beta}(t)\ .\ (1 - \varepsilon_{\alpha}(t))$$

Where $\varepsilon_{2\nu\beta\beta}(t)$ and $\varepsilon_{\alpha}(t)$ are the survival fraction of $2\nu\beta\beta$ and α events respectively for a cut threshold set at rise time t. The cut threshold is set as the rise time t which maximises the defined figure of merit. Any event with risetime lower than the theshould is classified as part of the background-like and all events that have risetime value higher than the threshold are classified as signal-like.

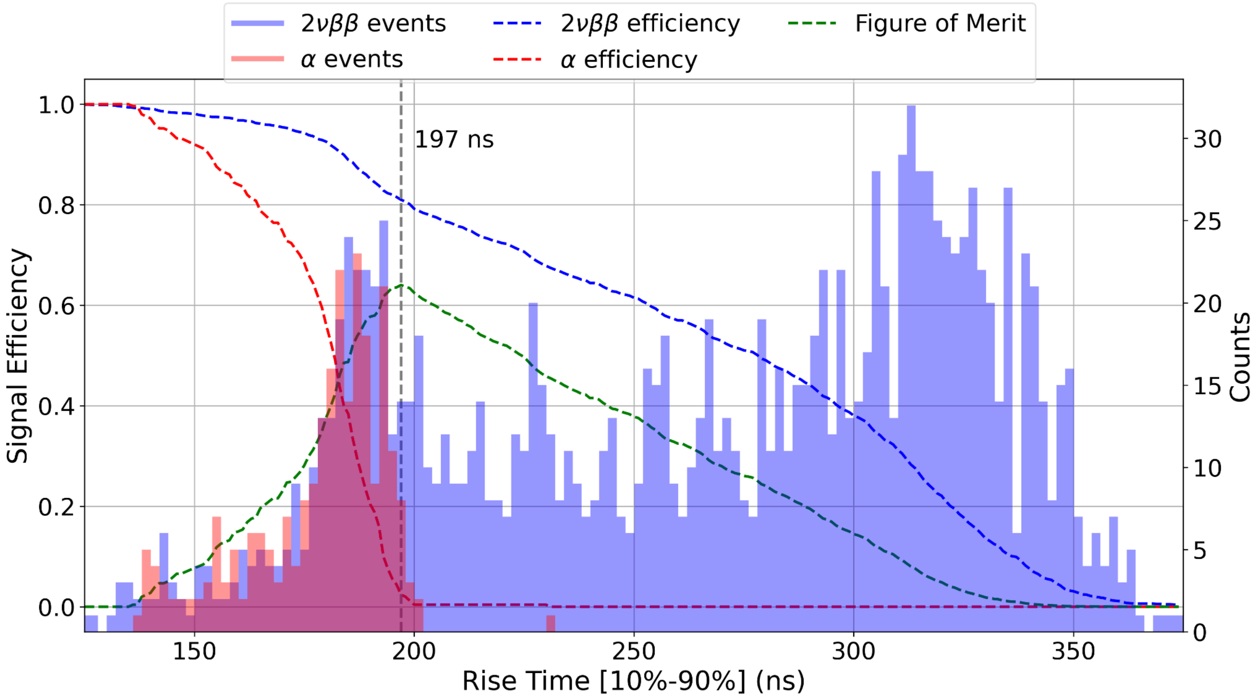

Figure 56: The risetime distributions of $2\nu\beta\beta$ and alpha events that survive the LAr veto and ANN-MSE cut, along with their survival fraction as a function of risetime is plotted for pre-upgrade data from ANG3 detector. The risetime cut threshold is determined at maximum value of designed figure of merit depicted in green.

By design, the choice of figure of merit is not unique and different variations of it are tested to check for stability and robustness of cut threshold. In the following table, risetime cut positions for different variations of figure of merit are listed for coax detectors in Phase II.

	Risetime cut thresholds for different coax detectors						
Figure of merit	ANG1	ANG2	ANG3	ANG4	ANG5	RG1	RG2
$\varepsilon^3_{2\nu\beta\beta} \cdot (1-\varepsilon_\alpha)$	200	181	195	184	231	191	205
$\varepsilon^2_{2\nu\beta\beta} \cdot (1-\varepsilon_\alpha)$	200	182	197	184	231	196	214
$\varepsilon_{2\nu\beta\beta} \cdot (1-\varepsilon_\alpha)$	200	204	199	195	239	199	214

Table 8: Risetime cut positions determined using different figures of merit for semi-coaxial detectors in Phase II . Evidently, the different figures of merit lead to similar cut positions which can be attributed to steep fall in alpha events survival fraction compared to more gradual decline in survival fraction of 2**ν**bb event.

For different coax detectors in Phase II, the survival fractions of signal and background and chosen figure of merit are showcased in Figure 58. Different detectors have different geometries and different pulse shapes which leads to different cut thresholds. Hence cut position for each coax detector is calibrated independently.

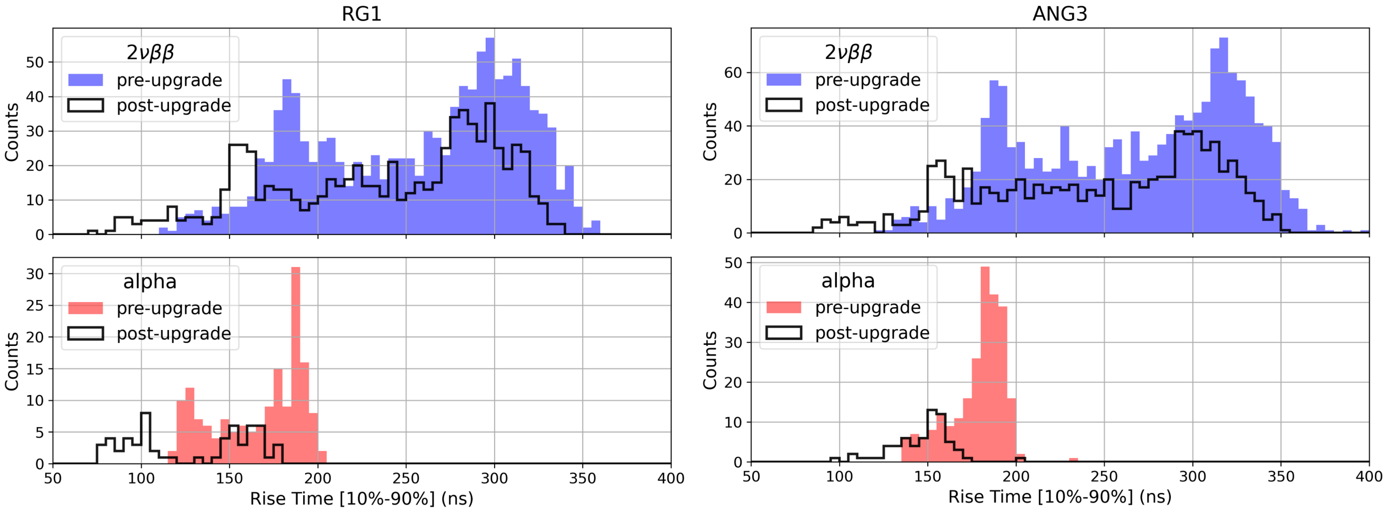

Figure 57: shows the distribution of the rise time parameter for 2νββ events (top panels) and alpha events (bottom panels) from pre-upgrade runs (filled) and post-upgrade runs (step). Note that the rise time distributions are shifted due to changes in the DAQ electronics after the upgrade.

The electronic response of the data acquisition system significantly impacts pulse shape evolution, making rise time parameters sensitive to any major changes in the electronics. The GERDA Phase II array underwent an upgrade in 2018, with changes to the readout electronics affecting the rise time distributions. For the RG1 and ANG3 detectors, Figure 57 depicts the rise time distributions of 2νββ and alpha events from both the pre-upgrade and post-upgrade periods. It shows that the rise time distributions are shifted to lower values after the upgrade.

Combining data from these two periods to calibrate a rise time cut would not be effective due to these shifts. Therefore, the data is split into pre-upgrade and post-upgrade Phases and analyzed independently for each of the semi-coaxial detectors.

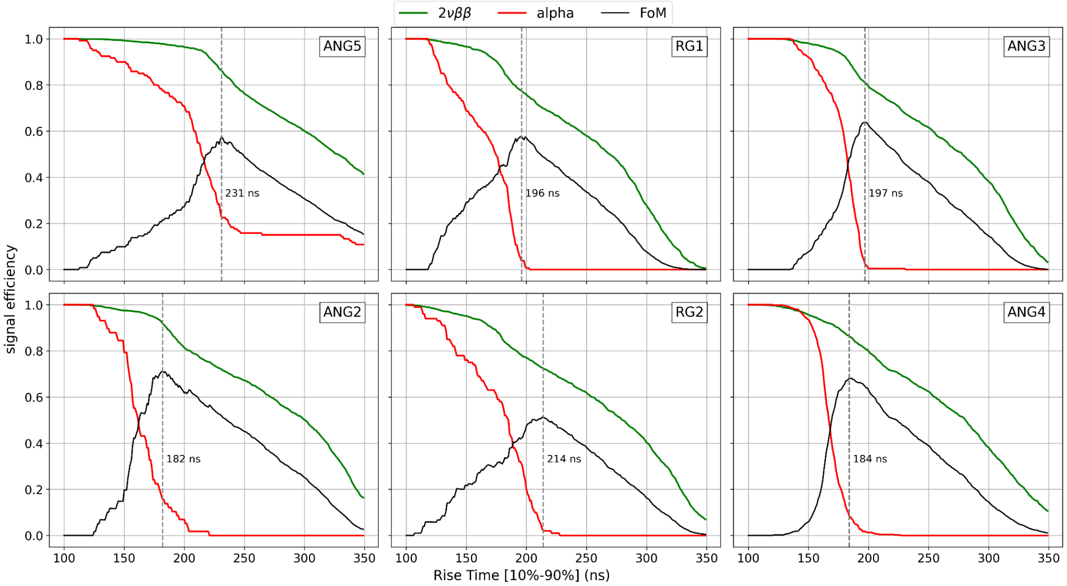

Figure 58: Risetime response of signal and background samples and figure of merit is depicted for different coax detectors for runs 53-93. The cut position determined at the maximum of the figure of merit, is indicated by a dotted line.

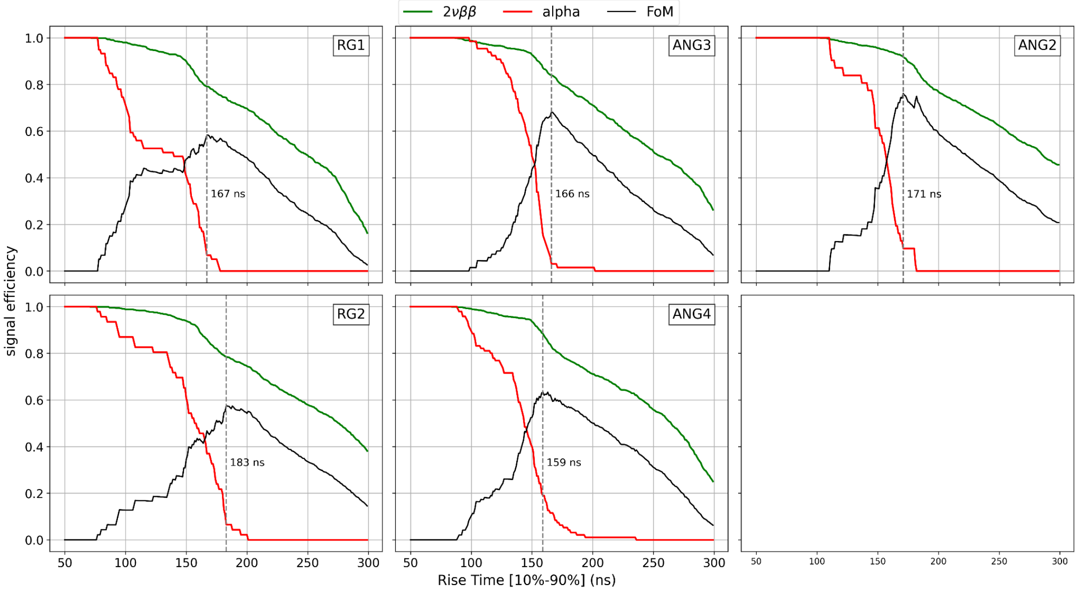

Figure 59: Risetime response of signal and background samples and figure of merit is depicted for different coax detectors for runs 95-114. The cut position determined at the maximum of the figure of merit is indicated by a dotted line.

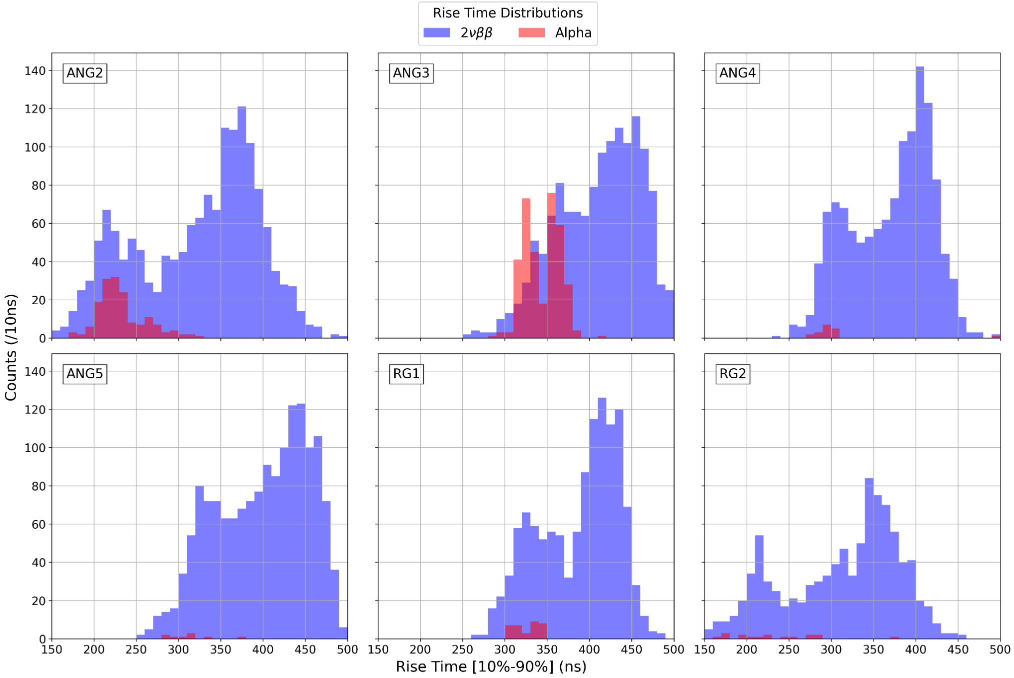

Figure 60: illustrates the distribution of the risetime parameter for 2νββ events (in blue) and alpha events (in red) in semi-coaxial detectors during Phase I. The two distributions show considerable overlap and extend over a higher range. Notably, except for ANG2 and ANG3, the other semi-coaxial detectors exhibit minimal alpha event populations after applying the ANN-MSE cut.

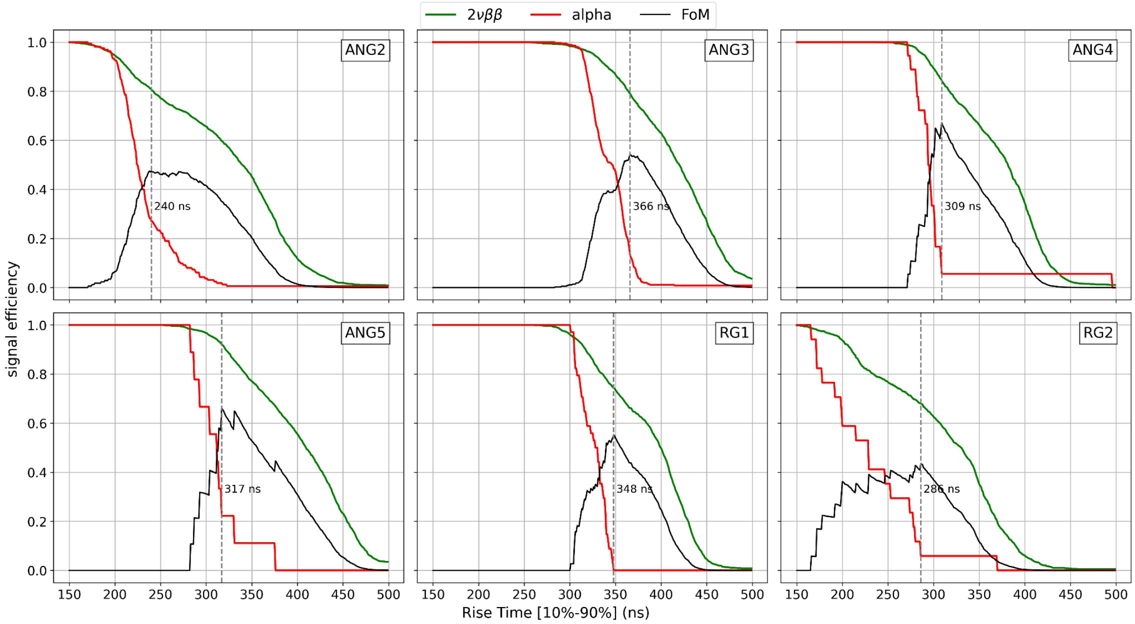

Figure 61: risetime response of signal and background samples and figure of merit is depicted for different coax detectors for runs 25-49 from Phase I. The cut position determined at maximum of figure of merit, is indicated by dotted line.

Clearly, the cut threshold is significantly dependent on the alpha events response due to limited alpha statistics. It's important to note that Risetime based alpha-cut works in conjunction with ANN-based MSE cut to remove almost all alpha background. Figure 58 depicts excellent suppression of alpha background while maintaining high signal efficiency for 2νββ events.

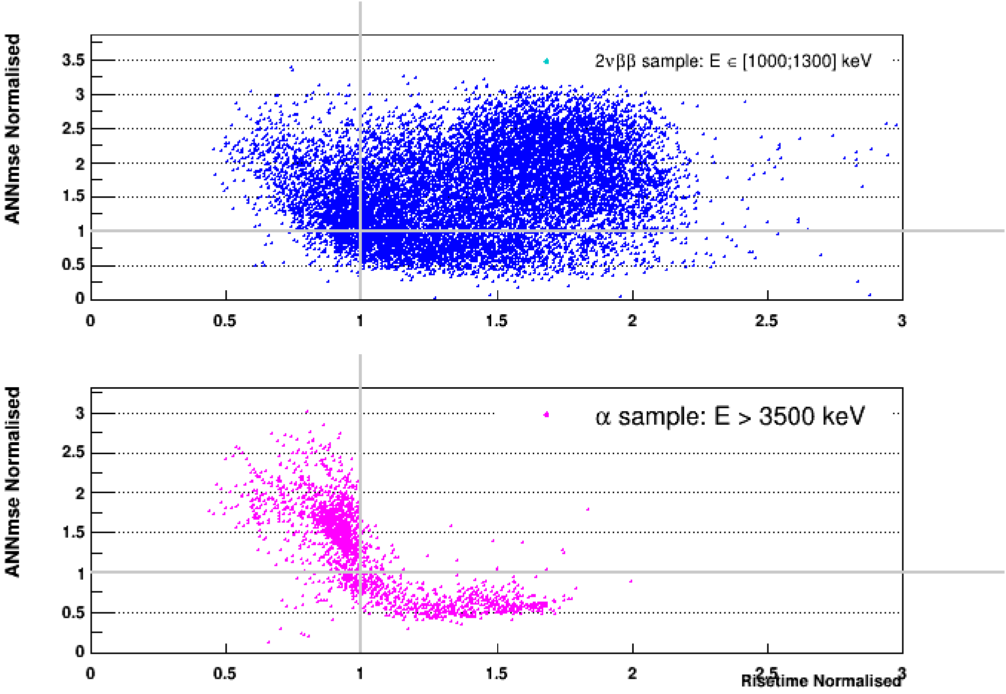

Figure 62: Observed correlation between ANN-based MSE cut and risetime-based cut for 2νββ events (top panel) and alpha events (bottom panel). The values of the ANN-MSE classifier and risetime are normalized by the respective cut thresholds, so only the events in the top right quadrant survive both PSD cuts.

4.11. Comparison of ANN-α and Risetime PSD for mitigating surface background

In the analysis of pulse shape discrimination (PSD) techniques for mitigating surface background in semi-coaxial detectors, two distinct methods have been evaluated: ANN-α, a multivariate approach which is based on a neural network, and a mono-parametric Risetime Cut. The objective was to enhance surface background rejection while maintaining high efficiency for the signal of interest, specifically the neutrino-accompanied double beta decay (2νββ) events. To compare the performance of these two methods, an exposure weighted efficiency for the 2νββ events and α events (both surviving the the LAr veto and ANN-MSE cut) is calculated accounting for different accumulated exposures of individual semi-coaxial detectors. The ANN-α cut achieves 87.7% efficiency for 2νββ events compared to 82.5% of that of risetime cut. Both the methods achieve similar surface background reduction with efficiency of 9.7% for the α events. Based on the comparison, the ANN-α method is favored due to its higher efficiency in preserving 2νββ events while achieving excellent α background rejection.

4.12. DeltaE cut: Events with incomplete charge collection

The events stemming from the n+ layer or the passivation groove exhibit incomplete charge collection, which introduces a large difference between the ZAC and Gauss energy reconstructions. This uncertainty in energy reconstruction is due to the relatively short integration time of the ZAC filter [Ago15], which is optimized for FEP (at 2614.5 keV) resolution. Some of these specific events, particularly in the case of coaxial detectors, may survive other PSA cuts employed.

To address these events with uncertain energy reconstruction, an additional classification method is employed based on energies reconstructed using pseudo Gaussian filters with varying integration times. Energy is reconstructed twice: once with a 4 μs integration time (referred to as E_{short}) and again with a 20 μs integration time (E_{long}). The ratio E_{short}/E_{long} is then normalized to the mean of E_{short}/E_{long} distribution of events from the 2614.5 keV calibration line which is calculated by fitting a Gaussian to the distribution. This normalization results in the classifier δE, which is defined as:

$$\delta E = \left(\frac{E_{short}/E_{long}}{<E_{short}/E_{long}>_{FEP}} - 1 \right) . E$$

Where E is the ZAC-reconstructed energy of the corresponding event. As per definition, the classifier δE has mean centered at zero.

The normalization $< E_{short}/E_{long} >_{FEP}$ is conducted in a time-dependent manner to account for any potential instabilities in the readout electronics. For each calibration run, the mean of the fitted Gaussian distribution for the FEP is used as the normalization factor for subsequent physics runs. Notably, events in the Compton continuum display a higher proportion of large negative δE values. This can be attributed to the greater occurrence of pulses with incomplete charge collection, which is absent in energy peaks where the entire energy has been collected. In the 2νββ region of physics data, a Gaussian distribution similar to that of calibration data is observed, with no significant energy dependence.

A cut value is applied to the lower side of the δE distribution, and this value is set separately for each detector at a distance of 3σ away from zero. This cut value is sufficiently lenient, ensuring that over 99% of signal events are retained while effectively removing events with uncertain energy (i.e., cases where there is a significant difference between energies reconstructed using the ZAC and Gauss filters).

4.13. Energy dependence corrections

In this analysis, we employ multiple pulse shape discrimination (PSD) methods to differentiate potential 0νββ signals from background events. To tackle the problem of non-reliable pulse shape simulations of the GERDA detectors, the analysis for signal efficiency of the Pulse Shape Discrimination (PSD) methods relies on Single Site Event (SSE) proxies derived from data.

Two key proxies are considered:

a) ^{208}Tl Double Escape Peak (DEP) events at 1592 keV from calibration data.

b) 2νββ events within the energy range 1000-1300 keV from physics data.

These proxies are invaluable for their ability to closely emulate the characteristics of 0νββ decay signals. However, their energies are significantly lower than the 0νββ signal's energy, by ~450 keV for ^{208}Tl DEP events and ~1000 keV for 2νββ events. This discrepancy necessitates a thorough investigation into the potential energy dependence of the PSD methods employed in this analysis and to correct for it. Understanding and correcting for any energy-dependent variations is crucial to ensuring the accuracy and reliability of the final signal efficiency calculations.

To investigate the energy dependence of the PSD methods, we utilize waveform rescaling to generate new waveforms that mimic events at target energies, with each set rescaled at 25 keV intervals. The rescaling of the pulses, added on top of bare baselines, has been first implemented by A. Lazzaro [GSTR18]. This rescaling is achieved by adjusting the waveform by the ratio of the target energy to the original energy of the waveform, and additionally, to account for the energy-dependent signal-to-noise ratio, a scaled baseline extracted from a library of baselines obtained from the same detector is superimposed.

The operation to transform an original waveform w0 at energy E0 into a rescaled waveform w at apparent energy E can be expressed as:

$$w = w_0 \frac{E}{E_0} + b\sqrt{1 - (\frac{E}{E_0})^2}$$

where b is the baseline waveform from the same detector chosen at random.

To obtain a corrected PSD signal efficiency estimate for 0νββ decay, we quantify this energy dependence by extrapolation of PSD efficiencies from the ^{208}Tl DEP events and use the correction term to extrapolate PSD efficiency for 2νββ events, which are the closest proxy to that of 0νββ signal. Compared to the ~4 keV wide peak for ^{208}Tl DEP, the 2νββ events are extracted from a much wider energy range of 300 keV, and hence it's not suitable for energy dependent efficiency analysis. Thus, the PSD efficiencies of the rescaled ^{208}Tl DEP samples over a range of energies from 0.5 MeV to 1.55 MeV are calculated . These calculated efficiencies are then plotted as a function of energy, and a fitting function is applied to these data points to model the relationship between PSD efficiency and energy.

The fit function is defined as:

$$\epsilon(E) \;=\; a \,+\, b\,(1 - e^{-c\cdot(E-d)})$$

where $\epsilon(E)$ represents efficiency at energy E and a, b, c, d are fit parameters. The fit function was chosen to fit the energy dependent efficiency due to its ability to capture the observed non-linear behavior at lower energies and the saturation at higher energies. This function accurately models the initial rapid decrease/increase in efficiency and the subsequent plateau, reflecting the characteristics of the data across multiple detectors. Such a fit for each individual semi-coaxial detector for both ANN-MSE and ANN-α implementations is depicted in figure 63 and figure 64 respectively.

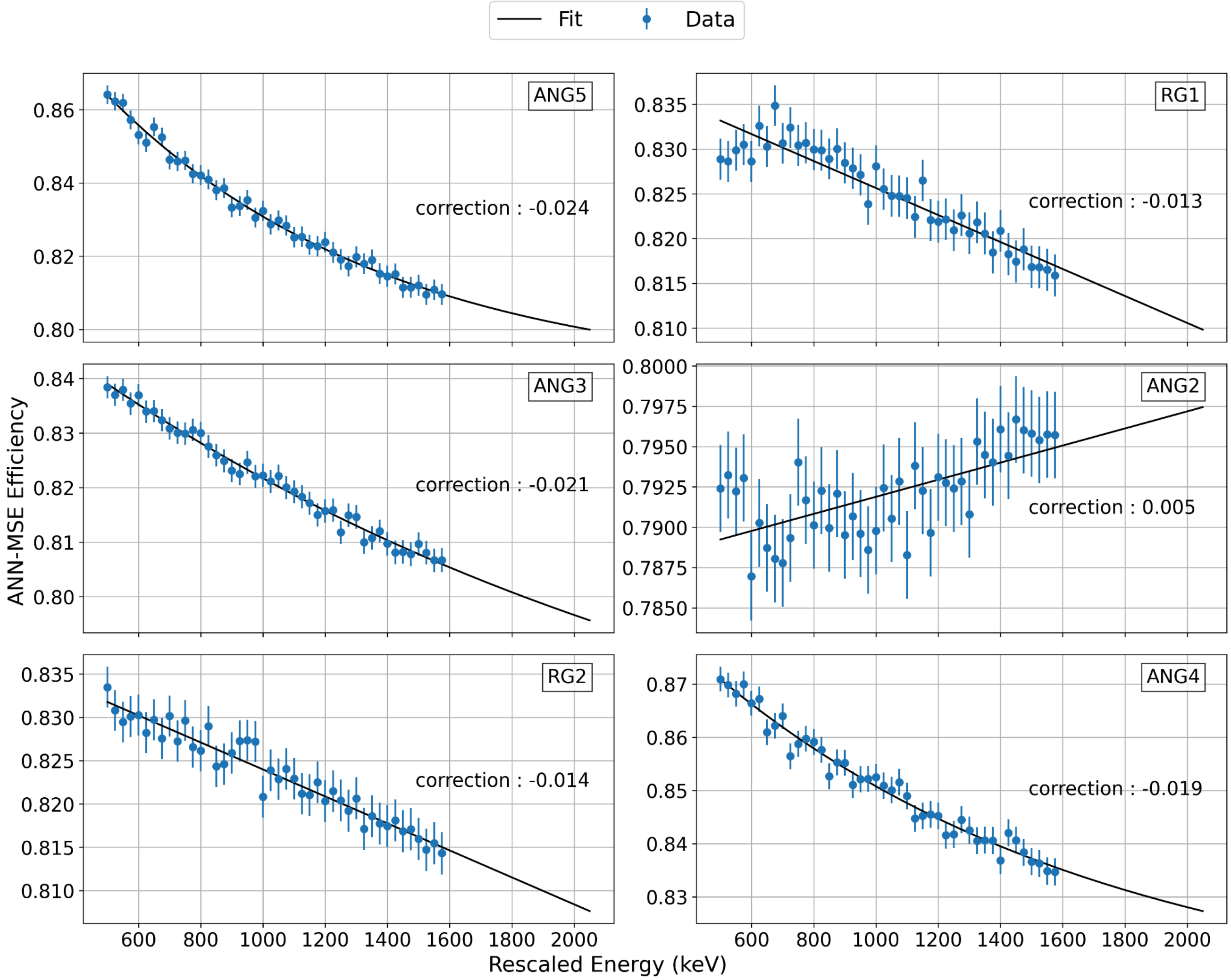

Figure 63: The figure illustrates the ANN-MSE efficiencies for rescaled ^{208}Tl Double Escape Peak (DEP) samples across an energy range from 0.5 MeV to 1.55 MeV at 25 keV

intervals. The blue points represent the calculated ANN-MSE efficiencies at various energy scales. The black line denotes the best fit to the data using the fit function defined earlier.

Using the best fit values, the PSD efficiencies for ^{208}Tl DEP are extrapolated to the $Q_{\beta\beta}$ value of 2040 keV. The energy correction term is calculated as the difference between PSD efficiency at 2040 keV, and that at 1150 keV. This energy correction term is subsequently added to the 2νββ PSD efficiency to derive the PSD efficiency for 0νββ events at $Q_{\beta\beta}$. This corrected efficiency accounts for the energy dependence observed in the ^{208}Tl DEP rescaled samples and is adjusted with the 2νββ efficiency accordingly.

$$correction\ term\ =\ \epsilon_{DEP}(2040\ keV)\ -\ \epsilon_{DEP}(1050\ keV)$$

$$\epsilon_{0\nu\beta\beta} = \epsilon_{2\nu\beta\beta} +\ correction\ term$$

The respective correction terms are also mentioned on the plots with the fitting function below for both the PSD techniques employed in this analysis.

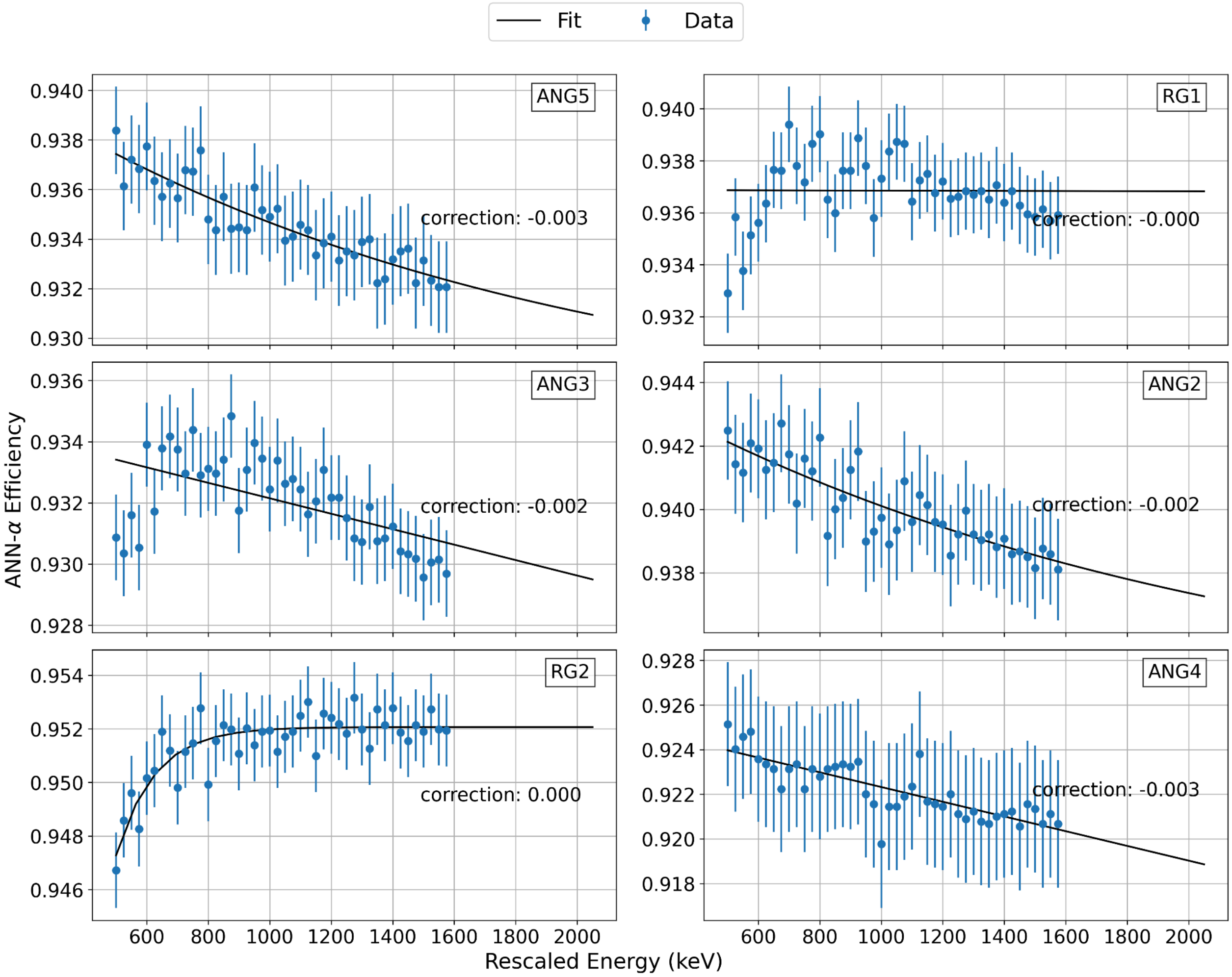

Figure 64: The figure illustrates the ANN-α efficiencies for rescaled ^{208}Tl Double Escape Peak (DEP) samples across an energy range from 0.5 MeV to 1.55 MeV at 25 keV intervals.

The blue points represent the calculated ANN-α efficiencies at various energy scales. The black line denotes the best fit to the data using the fit function defined earlier.

The analysis of energy dependence corrections in our Pulse Shape Discrimination (PSD) methods, illustrated in Figure 63 above, shows that the rescaled samples do not exhibit a significant energy dependence. Our results indicate a consistent performance of the Artificial Neural Network (ANN) across the investigated energy range. This stability is essential for the reliability of our final signal efficiency calculations. While minor variations in signal efficiency were observed, these fluctuations were minimal, generally within a couple of percentage points between 1MeV and $Q_{\beta\beta}$. For a more detailed examination of these plots and further discussion, please refer to the appendix of this thesis. We don't observe any significant energy dependence of the ANN-α cut.

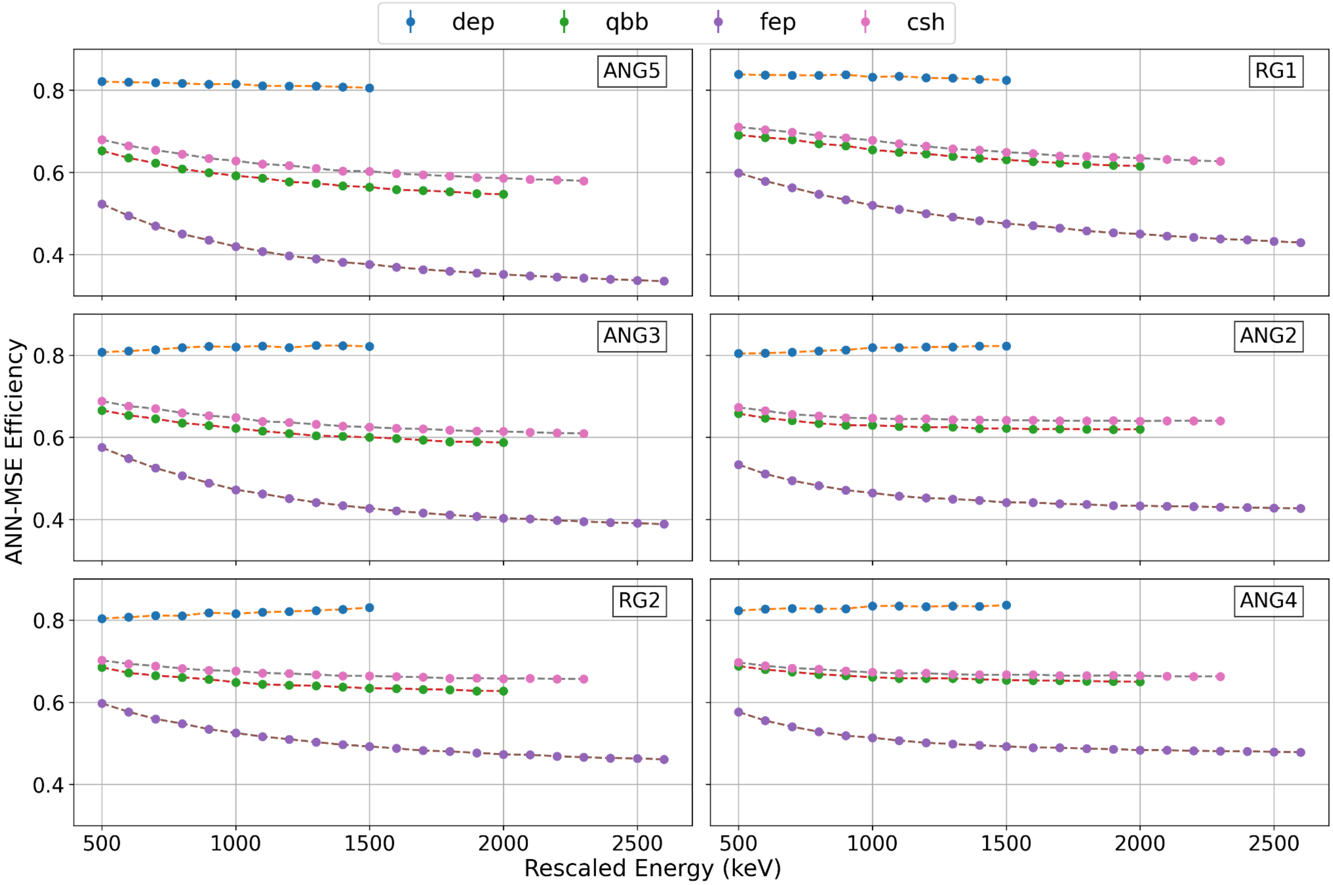

Figure 65: The figure illustrates the trend in ANN-MSE efficiencies for various peaks of interest from calibration data recorded before the upgrade in Summer 2018. Note that the underlying Compton contribution is not subtracted here thus ^{208}Tl DEP events shown in blue indicate efficiency little less than 90%. The Compton continuum at $Q_{\beta\beta}$ is shown in green with pink plot showcasing events from Compton shoulder at 2380 keV with higher SSE content

than the Compton continuum. The ^{208}Tl Full energy peak is shown in purple and is mostly MSE in nature and shows gradual increase in survival fraction at energies below ~1.5 MeV possibly due to a lower signal-to-noise ratio at lower energies.

Bibliography (Chapter 4) :

[Eic54] J. F. Eichelberger, K. C. Jordan, S. R. Orr, and J. R. Parks, “Calorimetric Determination of the Half-Life of Polonium-210”,Phys. Rev. 96, 719

[Ago22] Agostini, M., Araujo, G., Bakalyarov, A.M. et al., “Pulse shape analysis in GERDA Phase II”, Eur. Phys. J. C 82, 284 (2022).

[Abt07] I. Abt et al., Background reduction in neutrinoless double beta decay experiments using segmented detectors: a Monte Carlo study for the GERDA setup. Nucl. Instrum. Methods A 570, 479–486 (2007)

[Ago15] M. Agostini et al. (GERDA collaboration), “Improvement of the energy resolution via an optimized digital signal processing in GERDA Phase I.”, Eur. Phys. J. C 75(6), 255 (2015)

[Laz19] A. Lazzaro, “Signal processing and event classification for a background free neutrinoless double beta decay search with the GERDA experiment” , PhD thesis, Technische Universität München, 2019

[GSTR18] A. Lazzaro, GSTR-18-002 (2018)

[Ger20] The GERDA collaboration., Agostini, M., Bakalyarov, A.M. *et al*. Modeling of GERDA Phase II data. *J. High Energ. Phys.* 2020, 139 (2020).

[Sto65] R. W. Stoenner *et al.*, Half-Lives of Argon-37, Argon-39, and Argon-42.*Science***148**,1325-1328(1965).DOI:10.1126/science.148.3675.1325

[Be08] 48] M.-M. Bé et al., Table of Radionuclides, vol. 4 of Monographie BIPM-5, Bureau International des Poids et Mesures, Pavillon de Breteuil, F-92310 Sèvres, France (2008).

[Kir14] A. Kirch, “Search for the neutrinoless double β -decay in GERDA Phase I using a Pulse Shape Discrimination technique”, PhD thesis, University of Heidelberg, 2014

5. Half-life and sensitivity evaluation

GERDA aimed to detect neutrinoless double-beta ($0\nu\beta\beta$) decay using high-purity germanium (HPGe) detectors with enriched ^{76}Ge. This method maximizes detection efficiency by combining the source and detector, benefiting from the superior energy resolution of germanium detectors, which provides a clear signal for $0\nu\beta\beta$ decay. To minimize thermal noise, the detectors were operated in liquid argon (LAr), serving both as a cooling medium and a shield against radioactive decays from surrounding materials.

The Phase I of GERDA, from November 2011 to September 2013, achieved an exposure of 23.5 kg·yr with an average background inde BI of 11×10^{-3} counts/(keV·kg·yr) at $Q_{\beta\beta}$. Phase II began data taking in December 2015 after significant upgrades, targeting a background index BI of 10^{-3} counts/(keV·kg·yr) and a "background-free" regime with 100 kg·yr of exposure. This regime, where the expected number of background events in the signal region is zero, allows the sensitivity to scale linearly with exposure. These goals were met by adding 20 kg of broad energy germanium (BEGe) detectors to the existing coaxial detectors and enhancing the LAr volume around the detector array with photo-sensors to serve as an active veto. In 2018, an additional 9 kg of inverted coaxial (IC) detectors were installed, and the LAr instrumentation was further upgraded.

Since Phase I, GERDA has implemented a strict blinded analysis. Events within ±25 keV of $Q_{\beta\beta}$=2039 keV are excluded from the data stream and only analyzed after finalizing all procedures and parameters. The energy of events is reconstructed using a zero-area cusp filter, optimized for each detector and calibration run. Weekly calibrations with ^{228}Th sources determine the energy scale, resolution, and monitor analysis cuts. The energy resolution (FWHM) at $Q_{\beta\beta}$ is specific to each detector type, as shown in Table 4. Stability parameters, such as gain, leakage current, and noise, are monitored by injecting test pulses at 0.05 Hz into the front-end electronics. Approximately 80% of the data corresponds to stable conditions and is suitable for physics analysis. Quality cuts based on baseline flatness, pulse polarity, and pulse time structure reject signals from electrical discharges or noise bursts, with physical event acceptance efficiency at $Q_{\beta\beta}$ exceeding 99.9%. Events with multiplicity more than one i.e energy depositions in more than one germanium detector are classified as background. Phase II's unique feature is the LAr veto, rejecting events depositing energy in the LAr volume surrounding the detectors. Events are classified as background if a photosensor in LAr detects a signal within about 6 μs of the germanium detector trigger. This results in a dead time of (2.3±0.1)% before and (1.8±0.1)% after the upgrade. Events preceded by a muon-veto signal within 10 μs are also discarded, inducing a negligible dead time of less than 0.01%.

As discussed in chapter 3, LAr instrumentation as a veto was a major upgrade from Phase I to Phase II, significantly reducing the gamma background around $Q_{\beta\beta}$. Events showcasing coincident energy depositions in LAr volume are removed by this veto.

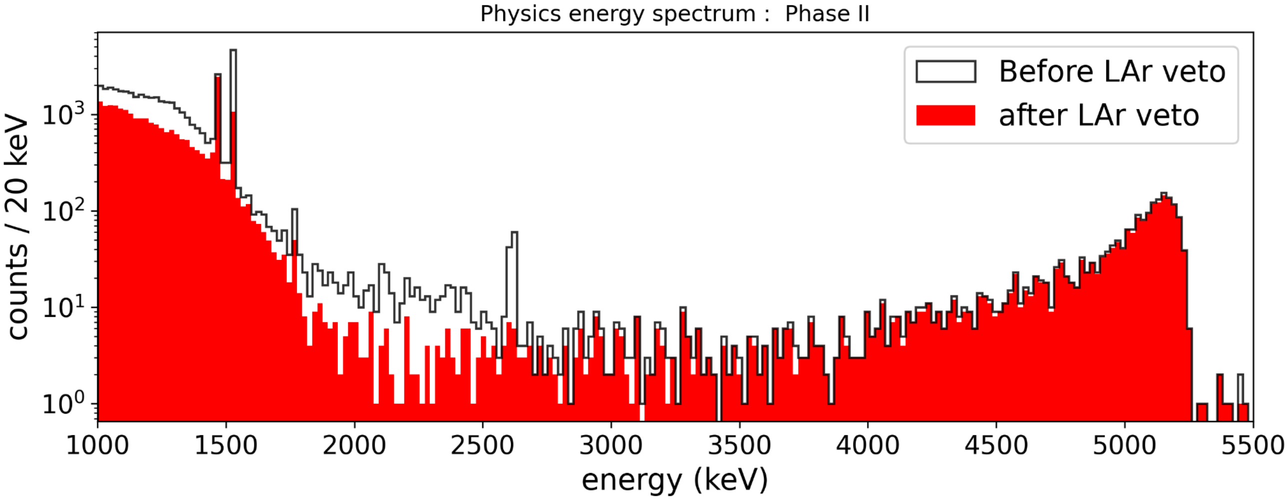

Figure 66: Events before (step histogram) and after (in red) applying LAr veto for Phase II semi-coaxial data.

As shown in Figure 66, the 1525 keV γ line that stems from the decay of ^{42}K which involves a β-γ cascade is highly suppressed while the 1461 keV γ line originating from ^{40}K remains unaffected which results from electron capture by ^{40}K without any energy deposition in the LAr. It is noteworthy that although LAr veto significantly suppressed the gamma background, the high energy background due the surface events (alpha and beta contaminants) show negligible reduction. This surface component of background at $Q_{\beta\beta}$ is mitigated by high level pulse shape discrimination cuts as shown in Figure 67 below.

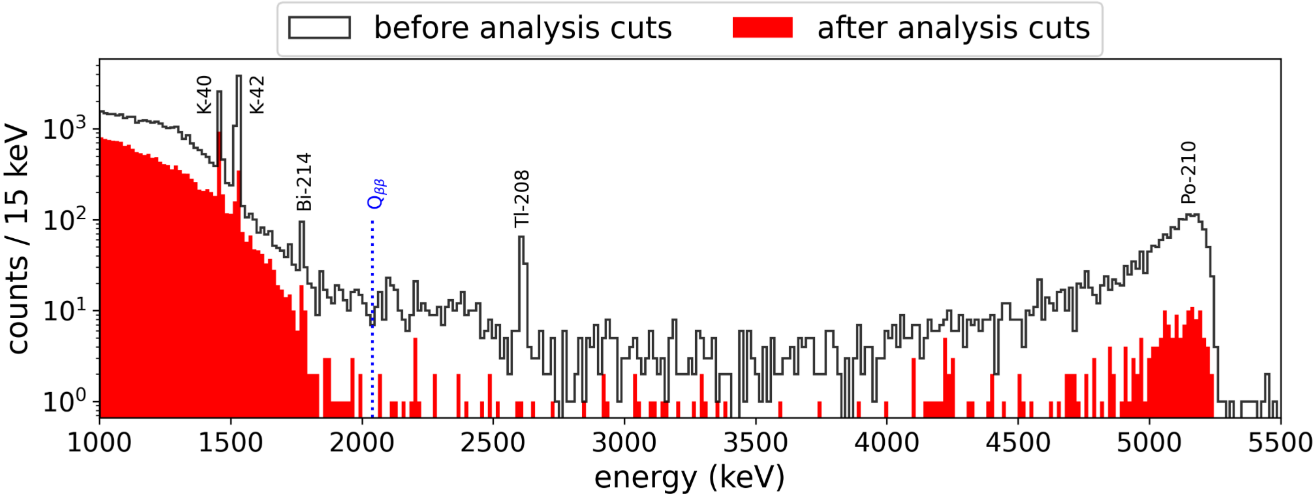

Figure 67: Energy spectrum of GERDA Phase II data from all semi-coaxial detectors under study is shown before and after applying analysis cuts. Apart from the prominent 2νββ continuum , gamma peaks from ^{40}K and ^{42}K, and ^{208}Tl FEP are visible and alpha events populate higher energies.

Figure 67 presents the background spectrum (from all semi-coaxial detectors) for Phase II of the GERDA experiment. This spectrum encompasses all data selected for analysis, gathered using 7 high-purity germanium (HPGe) detectors of semi-coaxial geometry over two distinct data collection periods. Detailed information regarding the data collection processes and selection criteria is provided in Chapter 3.

Before applying high-level pulse shape discrimination (PSD) and liquid argon (LAr) veto cuts, the spectrum displays typical GERDA background features, including:

a) At low energies, the $2\nu\beta\beta$ continuum is dominant.
b) Surface alpha particles, primarily from ^{210}Po, detected with degraded energy.
c) Surface beta particles from ^{42}K, with energies below 3.5 MeV.
d) Various gamma contributions from ^{42}K in the LAr, as well as isotopes from the ^{40}K and ^{232}Th decay chains present in the materials surrounding the detector array.

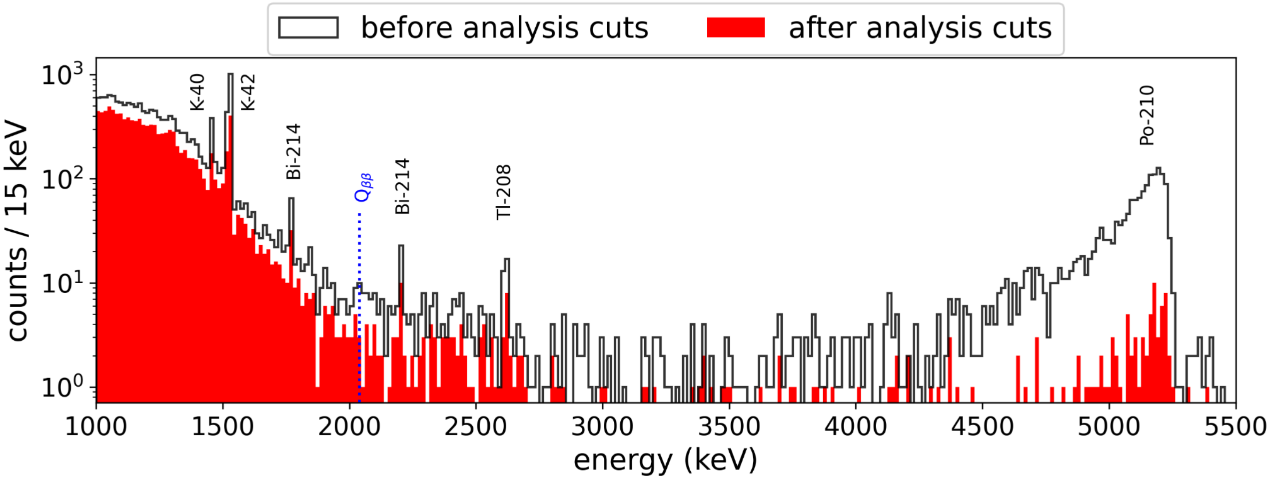

Figure 68: Energy spectrum of GERDA Phase I data from all semi-coaxial detectors under study is shown before and after applying analysis cuts.

The efficiency of detecting $0\nu\beta\beta$ events is determined by the product of the following factors:

i) Enrichment Fraction: fraction of ^{76}Ge in the detector material.

ii) Active Volume Fraction: fraction of the detector's total volume that is active and capable of detecting energy depositions.

iii) Probability of $0\nu\beta\beta$ energy at $Q_{\beta\beta}$: probability that a $0\nu\beta\beta$ decay occurring will result in a detectable signal within the region of interest (ROI), accounting for factors like bremsstrahlung.

iv) PSD Efficiency: The probability that a $0\nu\beta\beta$ event will be correctly classified as a signal.

v) Liquid Argon (LAr) accidental coincidence: Estimated through the test pulse acceptance, this accounts for the accidental coincidence with the LAr veto.

Each parameter calculated separately for each detector is taken from [GSTR06] and combined as an exposure-weighted average. The table below presents the individual components of these efficiencies for each dataset, with the total efficiency for $0\nu\beta\beta$ decay shown in the final column.

dataset		Energy Resolution @$Q_{\beta\beta}$ (keV)	^{76}Ge Enrichment fraction	Active volume fraction	Probability of 0νββ energy at $Q_{\beta\beta}$	LAr veto efficiency	PSD efficiency	Total efficiency
Phase I	golden	4.3	0.866	0.866	0.917	-	0.787	0.544
	Silver	4.3	0.866	0.866	0.917	-	0.787	0.544
	BEGe	2.7	0.880	0.887	0.897	-	0.873	0.663
Phase II	coax	4.0	0.867	0.866	0.917	0.980	0.732	0.507
	BEGe	2.8	0.880	0.887	0.895		0.886	0.608
	IC	2.9	0.878	0.927	0.918		0.900	0.660

Table 9: Summary of the efficiency parameters for different datasets from the GERDA experiment. The individual components of the total efficiency for 0νββ signal are reported along with total efficiency and acquired exposure.

5.1. Region of Interest

For the 0νββ decay analysis, the energy range considered is 1930 keV to 2190 keV. This energy window is constrained by the presence of potential gamma peaks at 1921 keV from ^{42}K and at 2204 keV from ^{214}Bi. The energy intervals 2103 ± 5 keV and 2119 ± 5 keV are excluded due to known SEP from ^{208}Tl at 2104 keV and FEP from ^{214}Bi at 2119 keV. No other gamma lines or structures are expected in this range according to the background model.

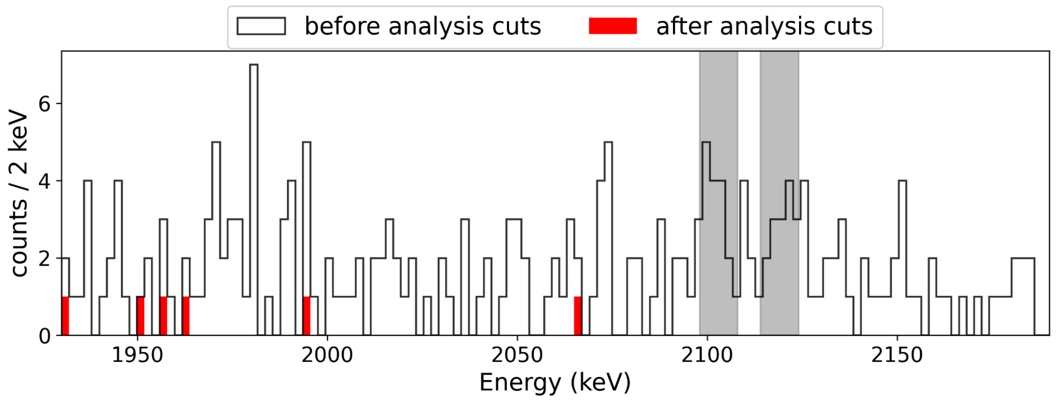

Figure 69: For semi-coaxial detectors in phase II, the events in the analysis window are shown before (step histogram) and after (in red) all the analysis cuts are applied.

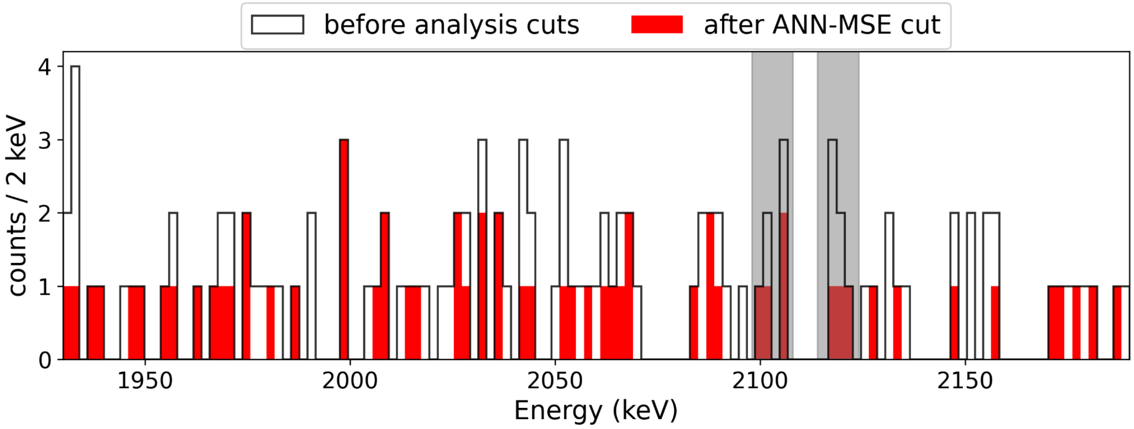

Figure 70: For semi-coaxial detectors in phase I, the events in the analysis window are shown before (step histogram) and after (in red) all the ANN-MSE cuts are applied.

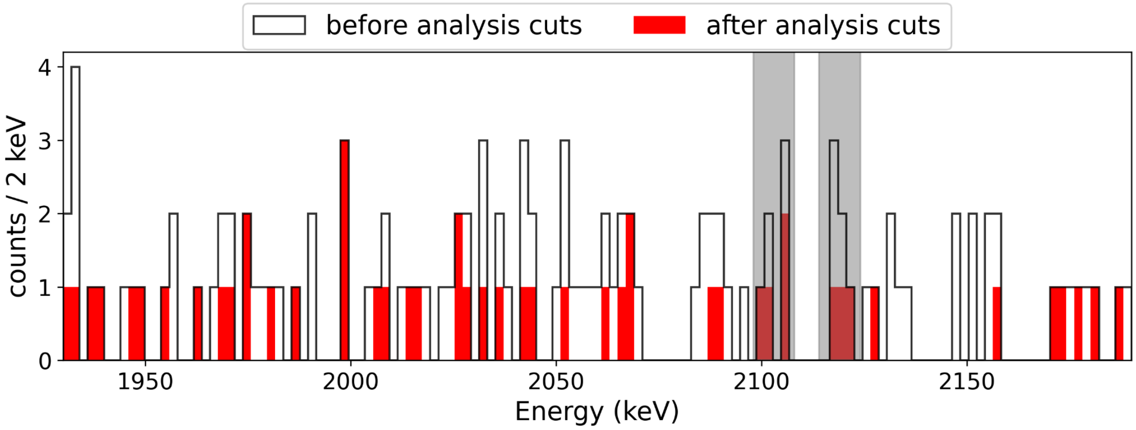

Figure 71: For semi-coaxial detectors in phase I, the events in the analysis window are shown before (step histogram) and after (in red) all the analysis cuts are applied.

Dataset		Exposure (kg.yr)	Total Events	After LAr veto	After PSD (ANN-)		After all analysis cuts
					MSE	alpha	
Phase I	golden	19.8	84	-	45	72	34
	silver	1.3	20	-	9	19	8
Phase II	pre-upgrade	28.6	104	43	61	78	5
	post-upgrade	13.2	29	11	11	21	1

Table 10: For semi-coaxial detectors, the total number of events in the 240 keV window around $Q_{\beta\beta}$ surviving after different analysis cuts are listed for individual datasets.

dataset		Exposure (kg.yr)	Background Index ($\times 10^{-3}$ $cts/(keV.\, kg.\, yr)$)			
			Before cuts	After LAr only	After PSD only	After Analysis cuts
Phase I	golden	19.8	17.6	-	7.1	7.1
	Silver	1.3	64.1	-	25.6	25.6
Phase II	coax	41.8	13.3	5.4	4.6	0.59
	BEGe	53.3	14.3	6.2	2.7	0.55
	IC	8.6	19.9	5.3	2.4	0.49

Table 11: Summary of the background indices for different datasets and their significant reduction with different analysis cuts is reported.

The analysis was performed with all the GERDA data, including the unblinded data. In Phase II of GERDA, a total of 14 events were found in the analysis window:

- 6 events in coaxial detectors
- 7 events in BEGe detectors
- 1 event in IC detectors

These events are likely attributed to α decays, ^{42}K β decays, or γ decays from the ^{238}U and ^{232}Th decay chains.

5.2. Evaluation of the limit on the half-life $T^{0\nu}_{1/2}$

This section is dedicated to detailed discussion regarding the statistical analysis of GERDA data to derive the limit on the half-life of neutrinoless double-beta decay ($T^{0\nu}_{1/2}$) and the median sensitivity of the experiment. A combined analysis is performed using data from both Phase I and Phase II by fitting all the partitioned data sets simultaneously. The key parameter is the signal strength (S), which is the inverse of the half-life for potential 0νββ decay.

$$S = 1/T^{0\nu}_{1/2}$$

As a function of this signal strength S_i , the number of expected 0νββ events in the *i*-th dataset D_i can be expressed as:

$$\mu_i^S = \frac{N_A ln2}{m_a}\epsilon_i \mathcal{E}_i S$$

where N_A is Avogadro's number, m_a is the molar mass of the *⁷⁶Ge* isotope, ϵ_i is the global signal efficiency, and $\mathcal{E}_i$ is the exposure from the *i*-th dataset. The exposure $\mathcal{E}_i$ is calculated as a product of total detector mass and data taking time and is represented in units of *kg.yr*. The global signal efficiency ϵ_i represents the overall efficiency of detecting *0νββ* decay events under operational conditions. It accounts for the ^{76}Ge enrichment fraction in detector mass, the active volume fraction of the detectors, the signal efficiency of all analysis cuts, the fractional live time of the detector and the probability that *0νββ* decay events in the active detector volume have a reconstructed energy at $Q_{\beta\beta}$.

As a function of the background index (BI_i), the number of expected background events in the *i*-th dataset D_i can be expressed as:

$$\mu_i^B = \mathcal{E}_i BI_i \Delta E$$

where ΔE is the width of the energy window around $Q_{\beta\beta}$.

An unbinned likelihood function is used to fit each dataset D_i assuming a flat distribution for the background (one free parameter per data set) and a Gaussian distribution for a possible *0νββ* signal centered at $Q_{\beta\beta}$ with a width based on the energy resolution σ_i. The likelihood function for the *i-th* data set is expressed as:

$$L_i(D_i|S,\ BI_i,\theta_i) \ = \ \prod_{j=1}^{N_i^{obs}} \frac{1}{\mu_i^S+\mu_i^B}\left[\frac{\mu_i^S}{\sqrt{2\pi}\sigma_i} exp\left(\frac{-(E_j-Q_{\beta\beta}-\delta_i)^2}{2\sigma_i^2}\right) + \frac{\mu_i^B}{\Delta E}\right]$$

where E_j are individual event energies and N_i^{obs} is the total number of events observed in the *i-th* data set. σ_i is the energy resolution at $Q_{\beta\beta}$ of the *i-th* data set and δ_i is possible systematic offset in energy. θ_i represents set of parameters with systematic uncertainties on signal efficiency, energy resolution and energy offset $\theta_i=\{\epsilon_i,\sigma_i,\delta_i\}$. Allowing only physically allowed regions, the parameters signal strength S and background index BI_i are bound to non-negative values. The combined likelihood L is the product of the individual likelihoods L_i for each data set D_i, weighted by the Poisson terms for the corresponding number of observed events:

$$L(D|S,\ BI,\theta) \ = \ \prod_i \left[\frac{exp(-(\mu_i^S+\mu_i^B)) \times (\mu_i^S+\mu_i^B)^{N_i^{obs}}}{N_i^{obs}!} \times L_i(D_i|S,\ BI_i,\theta_i)\right]$$

where $D = \{D_1,..., D_i,...\}$, $BI = \{BI_1,..., BI_i,...\}$ and $\theta = \{\theta_1,..., \theta_i,...\}$ represent all data sets, their background indices, and corresponding set of parameters with systematic uncertainties, respectively.

A profile likelihood ratio is used to assess the signal strength, comparing the likelihood of the model with and without a signal. For Frequentist analysis, a two-sided test statistic based on the profile likelihood ratio $\lambda(S)$ is expressed as:

$$t_S = -\ 2\ ln\lambda(S)\ \ = -\ 2\ ln\frac{L(S,\hat{\hat{BI}},\hat{\hat{\theta}})}{L(\hat{S},\hat{BI},\hat{\theta})}$$

In the numerator, $\hat{\hat{BI}}, \hat{\hat{\theta}}$ are the parameters that maximize the likelihood L for a fixed S whereas In the denominator: $\hat{S},\ \hat{BI}$ and $\hat{\theta}$ are the values that correspond to the absolute maximum likelihood (i.e., the best fit for all parameters).

Monte Carlo simulations are used to generate possible experimental outcomes for a range of values for signal strength S based on the parameters listed in table 9 and table 11. Confidence intervals are constructed for a discrete set of signal strength values $S = \{S_j\}$. For each simulated outcome, the test statistic t_{S_j} is evaluated. The probability distribution $f(t_S|S_j)$ of the test statistic for each S_j is calculated from the entire set of simulated outcomes. Further, the *P-value* of the data for a specific S_j is calculated as:

$$p(S_j) = \int_{t_{obs}}^{\infty} f(t_S|S_j)\, dt_{S_j}$$

where t_{obs} is the value of the test statistic for the GERDA data for signal strength S_j.

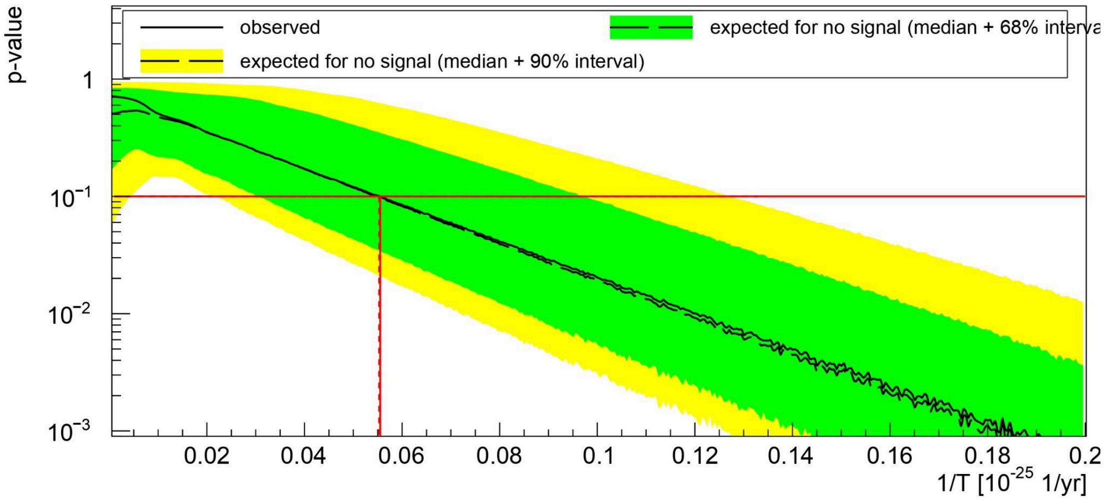

Figure 72: . p-value distribution for the frequentist hypothesis test on the inverse half-life $1/T^{0\upsilon}_{1/2}$. The green and yellow bands represent the 68% and 90% probability intervals from Monte Carlo simulations without signal. The dashed black line indicates the median P-value, while the solid black line shows the p-value for GERDA data. The results at 90% C.L. which corresponds to p-value of 0.1 are shown by red arrows.

The 90% confidence level (CL) interval is given by all S_j values with $p(S_j) > 0.1$. The values of $p(S_j)$ are plotted as a solid line in figure 72.

The current analysis yields a one-sided interval, indicating a limit of:

$$T^{0\upsilon}_{1/2} = 1/S > 1.8 \times 10^{26}\, yr$$

The experimental sensitivity, which is a measure of the experiment's capability to detect 0νββ decay if it exists, is evaluated using the distribution of $p(S_j)$ from Monte Carlo generated outcomes with no injected signal (S =0). In figure 72, the dashed line represents the median and the color bands indicate the 68% and 90% probability central intervals. The experimental sensitivity corresponds to the S value where the median of $p(S_j)$ crosses the P-value threshold of 0.1. The current analysis yields an experimental sensitivity of:

$$T^{0\upsilon}_{1/2} = 1/S > 1.8 \times 10^{26}\, yr$$

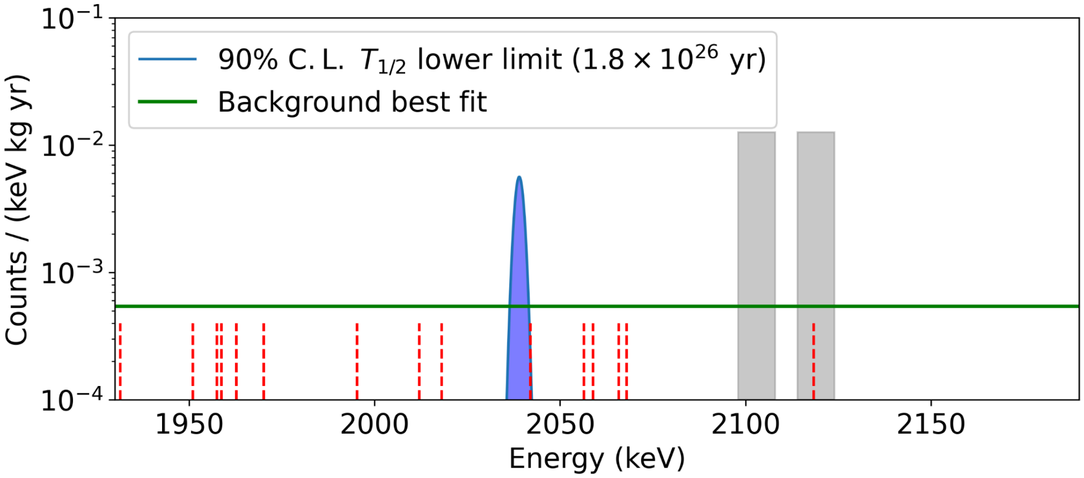

Figure 73: The expected 0νββ decay signal for $T^{0\upsilon}_{1/2}$ equal to the lower limit is shown as the blue peak. Its width is the energy resolution of the partition that contains the event closest to $Q_{\beta\beta}$. The energies of events from Phase II in the region of interest surviving all analysis cuts are marked by dashed vertical lines.

In the analysis, systematic uncertainties, including those related to energy reconstruction, energy resolution, and efficiencies, are incorporated through additional nuisance parameters, each constrained by a Gaussian probability distribution. Systematic uncertainties are included in the likelihood by varying the parameters $\theta_i=\{\epsilon_i,\sigma_i,\delta_i\}$ in the fits. This is done by adding multiplicative Gaussian penalty terms to the likelihood. For efficiency ϵ_i and energy resolution σ_i, the central values and standard deviations are taken from Table 9 while for energy offset δ_i, the central value is zero and the standard deviation is 0.2 keV. The overall effect of these systematic errors leads to a slight worsening of the limit at the percent level.

6. Summary and Outlook

In 2005, the GERmanium Detector Array (GERDA) experiment was initiated at the Laboratori Nazionali del Gran Sasso (LNGS) in Italy with the ambitious objective of either confirming or refuting the controversial claim of neutrinoless double beta decay (0νββ) in ^{76}Ge [Kla04]. The confirmation of the Majorana nature of neutrinos, which entails that they are their own antiparticles, and the provision of critical insights into the absolute mass scale and hierarchy of neutrinos would be profoundly impacted by the detection of this ultra-rare process. The GERDA experiment employed high-purity germanium (HPGe) detectors enriched with ^{76}Ge operated bare in liquid argon to minimize background..

The GERDA experiment was divided into two phases: Phase I (before 2013) and Phase II (after 2015), during which the experimental setup and data analysis tools were progressively enhanced. These upgrades led to a remarkable reduction in background. In Phase II, the background index was reduced to 5.6×10^{-4} cts/(keV·kg·yr), making GERDA the most sensitive ^{76}Ge double beta decay experiment at that time. Despite these advancements, no evidence for 0νββ decay was observed, leading to a lower limit on the half-life of 1.8×10^{26} years at 90% confidence level, and setting the corresponding limit range for the effective Majorana neutrino mass (m_{ee}) to 79–180 meV.

This thesis builds upon the advancements made in GERDA by focusing on the development and optimization of robust artificial neural networks (ANNs) for pulse shape discrimination (PSD), specifically tailored for the semi-coaxial geometry of HPGe detectors. Previous efforts in GERDA utilized a Multilayer Perceptron (MLP) architecture through the ROOT-TMVA package for PSD, but these methods had limitations, including potential biases introduced by improper data handling and the use of inappropriate signal proxies. To address these challenges, my work introduced a new Convolutional Neural Network (CNN)-based model that outperformed previous methods in terms of higher signal efficiency while suppressing background, especially surface background from alpha and beta decays mainly from ^{210}Po and ^{42}K respectively. Importantly, the new ANN-α based pulse shape discrimination for surface background improves upon the previously used mono-parametric risetime cut method, more efficiently suppressing surface background events without introducing the energy dependence seen in earlier approaches.

Additionally, this thesis provides a comprehensive analysis of a variety of ANN architectures with GERDA data to ensure that the inputs are handled appropriately to prevent training bias. Additionally, this thesis introduces the utilization of a distinct signal proxy, the 2νββ samples, which were specifically selected to reduce the biases that were introduced by the inhomogeneous distribution of ^{208}Th Double Escape Peak (TlDEP) events, which had been employed in previous analyses. The use of TensorFlow for model development enhanced the accessibility and transparency of the model building and training procedure, representing a significant improvement over legacy methods. Additionally, Geant4-based Monte Carlo simulations were conducted to validate the performance of the PSD techniques, providing valuable insights despite certain limitations in detector modeling.

The GERDA experiment's success paved the way for its successor, the LEGEND experiment, which is designed to further expand the boundaries of 0νββ decay detection in ^{76}Ge. The first phase, LEGEND-200, will involve up to 200 kg of ^{76}Ge-enriched detectors with the goal of exploring the Inverted Hierarchy region of neutrino mass ordering. Subsequently, the LEGEND-1000 phase, with 1 ton of ^{76}Ge-enriched detectors, will probe the Normal Hierarchy. My contributions to PSD techniques for semi-coaxial detectors in GERDA are expected to provide useful insights for the analysis campaign in LEGEND-200. The advancements and solutions developed in this thesis, particularly those addressing issues like input feature normalization, have directly informed the ongoing analysis efforts in the LEGEND-200 experiment, which aims to further improve upon the achievements of GERDA and explore new frontiers in the search for neutrinoless double beta decay.

Appendix A: Pulse Shape Simulations

To investigate neutrinoless double beta decay (0νββ) in the GERDA experiment, it is crucial to have a thorough comprehension of pulse characteristics in Germanium detectors. This chapter explores the realm of Monte Carlo (MC) simulations and pulse shape simulations, which are crucial tools in our attempt to validate and refine pulse shape discrimination (PSD) techniques.

Our simulations serve a dual purpose. Firstly, they offer a thorough understanding of the pulse characteristics displayed by various events in Germanium detectors, revealing insights into the spatial distribution of energy deposition. Using machine learning, we utilize different PSD techniques such as multilayer perceptrons (MLP), decision forests, convolutional neural networks (CNN), and recurrent neural networks (RNN). For the GERDA experiment to be sensitive enough to detect the faint signatures of neutrinoless double beta decay, these methods are essential for efficiently suppressing background events.

The calibration data and Physics data offers a crucial training set for pulse shape discrimination (PSD) methods. However, accurately assessing the signal efficiency of 0νββ events which would have homogenous distribution across the detector volume presents a nuanced challenge. The double escape peak (DEP) from calibration data offers a proxy for SSEs but these events are found primarily along the detector's edges due to the higher likelihood of 511 keV γ-rays escaping. To calculate signal efficiency accurately, a sample reflecting the homogeneous distribution of 0νββ decay events across the detector is essential. The 2νββ decay region, typically within 1.0 – 1.3 MeV is a potential candidate which comes closest with similar energy deposition characteristics. It should however be noted that 2νββ decay events in this region possess roughly half the energy of $Q_{\beta\beta}$. Therefore the possible energy dependence needs to be taken into account to correct for a lower signal-to-noise ratio for these pulses. In order to test the efficiency of PSD methods for the expected 0νββ signal, we use MC simulated pulses that mimic the event topology and have similar noise levels.

Monte Carlo simulations play a pivotal role in bridging the gap between theoretical expectations and experimental reality. We use these simulated data to extract insights into how the spatial position of energy deposition in a Germanium detector influences pulse characteristics. This understanding is pivotal for validating pulse shape discrimination (PSD) techniques on simulated data, enabling robust scrutiny of experimental results from GERDA data. These simulations uniquely allow us to assess the efficiency of PSD techniques, especially on 0νββ events, where experimental substitutes are unavailable.

By connecting these simulations to the wider framework of neutrinoless double beta decay, our goal is to improve our understanding of the characteristics of signal and background events. The multivariate PSD techniques refined with insights from these simulations help improve the signal efficiency and evaluate expected survival fraction of 0νββ signal.

Simulation Overview:

The simulation outlined in this chapter seeks to reproduce the entire sequence of physical processes involved in signal generation in High-Purity Germanium (HPGe) detectors. It is structured into three sequential parts, as illustrated in Figure 74.

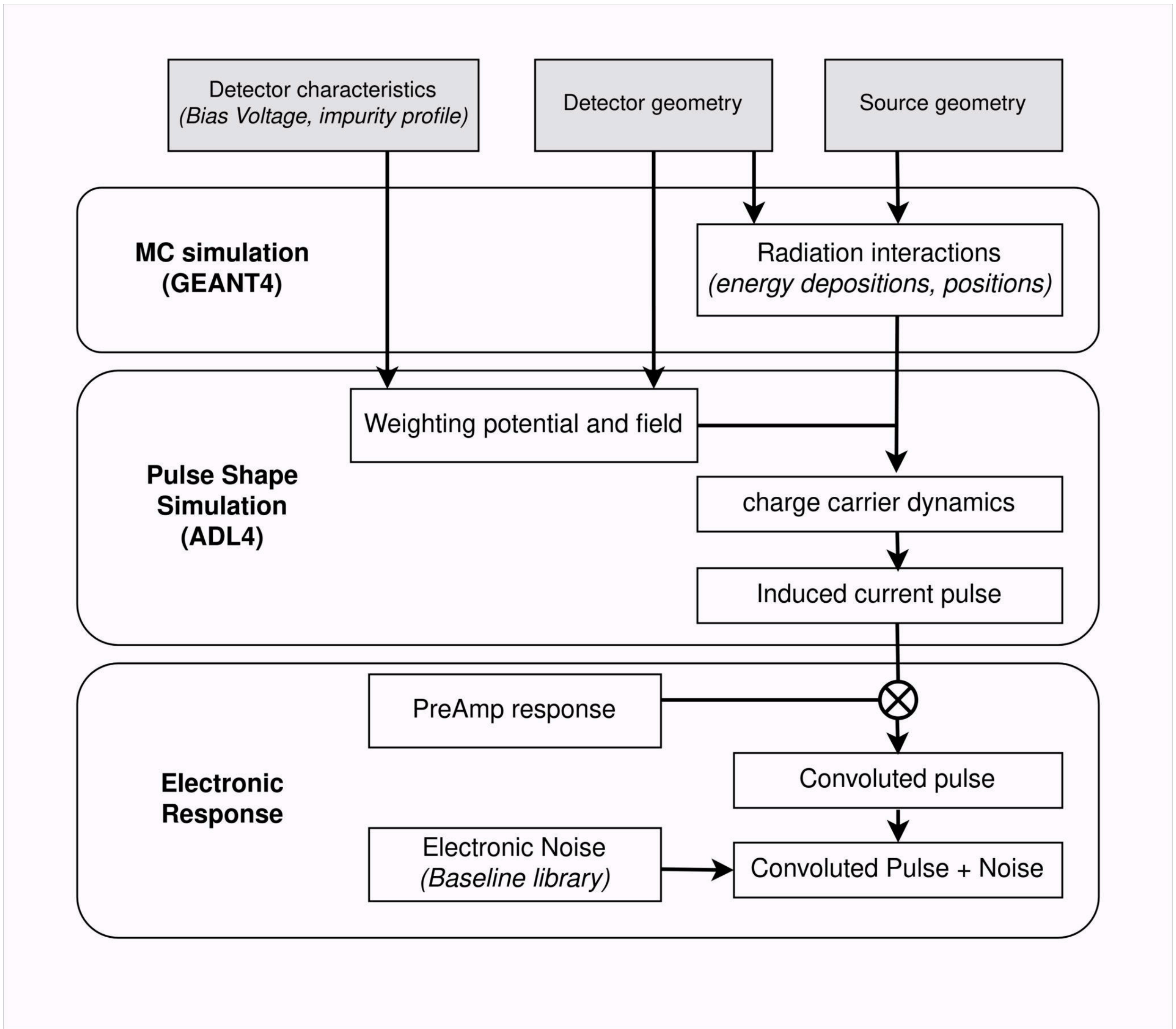

Figure 74: The simulation workflow is divided into three sequential parts. The workflow includes a)simulation of energy depositions inside detector volume, b) simulation of charge carrier drift and induced signal on p+ contact and c) incorporation of electronic response within the generated pulse.

Monte Carlo Simulation (MaGe Framework):

The initial block employs a Monte Carlo simulation conducted with the MaGe (MAjorana-GErda) framework [74]. This simulation leverages the Geant4 simulation package to model the transportation and interaction of gamma-rays and charged particles through the detector material. The outcome includes the determination of interaction points and corresponding energy depositions within the Germanium crystal.

Charge Carrier Dynamics (ADL4):

The second part delves into the dynamics of charge carriers generated at the interaction sites within the detector. It details the calculation of the signal induced on the read-out contact as a result of the drift of charge carriers towards the contacts. This computation is executed using ADL4 package..

Electronic response and Noise:

The final part of the simulation addresses the signal shaping process of the read-out electronics, incorporating considerations for electronic noise. The signals generated in this stage are directly comparable to the measured signals, providing a comprehensive representation of the experimental outcomes.

The subsequent subsections elaborate on the intricacies of the simulation, offering a detailed insight into the charge carrier dynamics and the final steps of signal processing, respectively.

Energy deposition simulation with MAGE:

MaGe (MAjorana-GErda) is a collaborative effort between the GERDA and Majorana collaborations, built upon Geant4. Geant4 provides specialized physics lists tailored for simulating low-energy processes. MaGe encompasses the geometries of diverse experimental setups, including the comprehensive GERDA geometry. It also offers tools such as interfaces to popular event generators (e.g., Decay0), random event sampling in bulk volumes or on surfaces, decay chain simulation.

In the simulation of the ^{228}Th decay chain, only the decays of ^{208}Tl and ^{212}Bi are considered. These particular decays are emphasized due to their significant contribution to the observed high-energy calibration spectrum. Additionally, all pertinent high-energy events in the calibration data employed for Pulse Shape Analysis (PSA) stem from these specific decays.

Pulse Shape Simulation with ADL (Agata Data Library):

The initial step involves utilizing the identified interaction locations within the germanium detectors and corresponding energy depositions, as depicted in Figure 74, as input for subsequent pulse shape simulations with ADL. The MaGe source code uses coordinates in the GERDA array frame of reference to output energy depositions in the detectors whereas

ADL source code expects the positions of energy deposition coordinates to be utilized with the detector at origin. Therefore a supplementary transformation of the 3-dimensional vector positions is carried out to ensure compatibility.

The explicit computation of the electric field within the germanium crystal, the dynamics of electron/hole charge carriers generated in the active detector volume, and the resulting signals induced on the read-out contact due to charge movement is performed using the AGATA Data Library (ADL4) simulation package. It is made available through the courtesy of the AGATA Collaboration, with the version 4.0, being employed for this study.

The ADL software facilitates the simulation of position-sensitive detector response to radiation interactions. The source code for simulating the electric field inside the detector volume relies on the Finite Element Method (FEM) to solve Poisson's equation for electric potential with a defined set of boundary conditions [Bru16]. The versatility of the ADL software allows adaptation to any user-specified HPGe detector geometry mapped by a variable 3D grid. The pulse shape simulations with ADL are performed in two steps: First, the electric and weighting potential and their respective field distribution within a Germanium detector are computed and stored in file for subsequent use. Later, the signal shape based on specified potentials and a particular interaction location are simulated. This partitioning is maintained since calculating the potentials is computationally time-consuming and assessing the potential distribution alone is adequate for exploring certain detector characteristics, such as the depletion voltage.

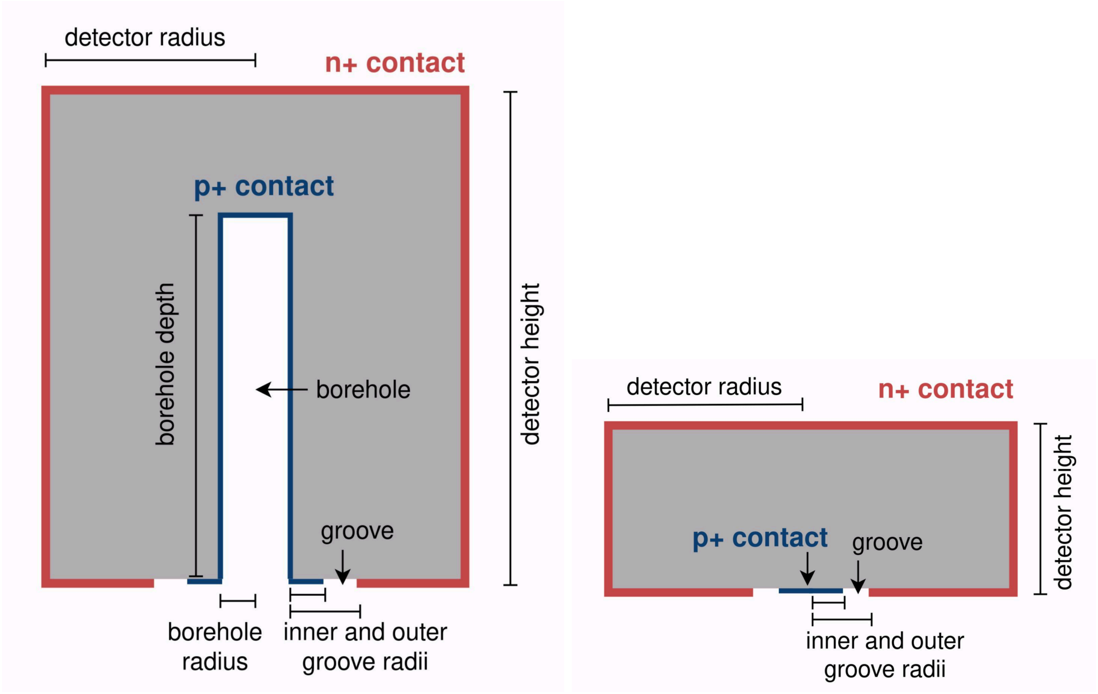

Figure 75: Schematic cross-sectional view of a) semi-coaxial detector and b) BEGe detector with labeled parameters utilized to simulate the detector.

In GERDA semiconducting germanium detectors, specifically of p-type, the p-n junction is established at the border of the approximately 1mm thick donor-doped surface mantle, referred to as the n+ layer. Operational bias voltages, typically higher than the detector-specific depletion voltages, lead to the full depletion of free charges in the inner bulk material, rendering it the active volume. In contrast, the outer n+ layer or dead-layer predominantly retains electrons in the conduction band, acting as the anode. On the other hand, the very thin Boron-doped p+ layer, covering the entire surface of the inner bore hole in semi-coaxial detectors, serves as the read-out contact or cathode. The p+ contact and n+ contact are electrically separated with a small groove surrounding p+ contact on the surface of the detector .This distinctive detector configuration is fundamental to understanding the intricacies of pulse shape simulation within the ADL framework. The ADL source code has been updated to incorporate each of the six enriched semi-coaxial germanium detectors individually, adhering to their respective geometries and dimensions shown in Figure 75. These include specifications such as detector height, radius, dead layer thicknesses, borehole depth and parameters related to the radius of the bore hole or grooves. The detector geometry and electrical and weighting field calculations are defined and executed over user-supplied three-dimensional mesh with grid size of 0.1 mm. The chosen grid size is a balanced compromise between computational efficiency and the accuracy of the implemented pulse shape simulation.

Signal formation:

The electric fields inside the detector can be computed by solving Poisson's equation by providing the potential of both contacts as boundary conditions.

$$\nabla^2 \phi(r) = \frac{-\rho(r)}{\varepsilon} \quad , \ \phi(p+) = V_{cathode} \ and \ \phi(n+) = V_{anode}$$

Where $\phi(r)$ is the electric potential, $\rho(r)$ is the space charge density and ε is the electrical permittivity of Germanium.

Under the influence of the applied electric field, the charge carriers (electrons and holes) created by the radiation drift towards the contacts. The speed and direction of their movement depend on the magnitude and direction of the instantaneous electric field within the detector.

The moving charge carriers through the detector induce the measured current on the contact and not the actual charges arriving at the contacts. The Shockley-Ramo theorem [Sho38] can be used to model the signal induced at the contacts due to movement of these charge carriers. Thus the charge and current induced on the contact are expressed as [He01]:

$$Q(t) = - q_0 . [\phi_w(r_h(t)) - \phi_w(r_e(t))]$$

$$I(t) = \frac{dQ(t)}{dt} = q_0 . [E_w(r_h(t)). v_h(t) - E_w(r_e(t)). v_e(t)]$$

where q_0 denotes total charge carried by charge carriers. $r_h(t)$, $r_e(t)$ and $v_h(t)$, $v_e(t)$ represent the instantaneous position and instantaneous drift velocity of holes and electrons respectively. The position dependent weighting potential and weighting field inside the detector is denoted by ϕ_w and E_w respectively. The weighting potential is dimensionless virtual quantity defined as electric potential within the detector with no space charge where the readout contact is at unit potential and other contacts are grounded. The weighting potential distribution within the detector satisfies the Laplace equation $\nabla^2\phi_w(r) = 0$ and can be calculated by setting boundary conditions $\phi_w(r)$=1 for readout contact and $\phi_w(r)$=0 for other contact. The weighting field represents the negative gradient of weighting potential inside the detector.

While the dynamics of the charge carriers is determined by the actual operating electric field, the current induced on the read-out contact can be calculated much easier with the help of the weighting field, as it involves solving the Laplace equation for weighting potential as no space charge is involved. The charge induced on the readout contact by moving charges is independent of the applied bias potentials and the space charge [[He01]. Evidently from earlier equation, the maximum induced charge on the readout contact by charge q is -q when the charge is infinitely close to the readout contact, and the minimum is 0 when the charge is infinitely close to the other contact.

Impurity profile: The total electric field comprises contributions from both the bias voltage and the net space charge. The ADL software, tailored for the specific requirements of the GERDA experiment, had been previously adjusted, validated, and effectively employed in prior works, as outlined in [Sal15] and [Kir14]. In the present simulation study, the impurity profile parameters were adopted from [Kir14], where they were derived through simulations for the optimization of depletion voltage. The net impurity charge field is computed assuming a uniform impurity distribution throughout detector volume. Homogeneous impurity distribution is assumed due to the inability to deduce impurity gradients from the depletion voltage. This assumption, while necessary, is an approximation, and a gradient in net impurity may affect the accuracy of the pulse shape simulation.

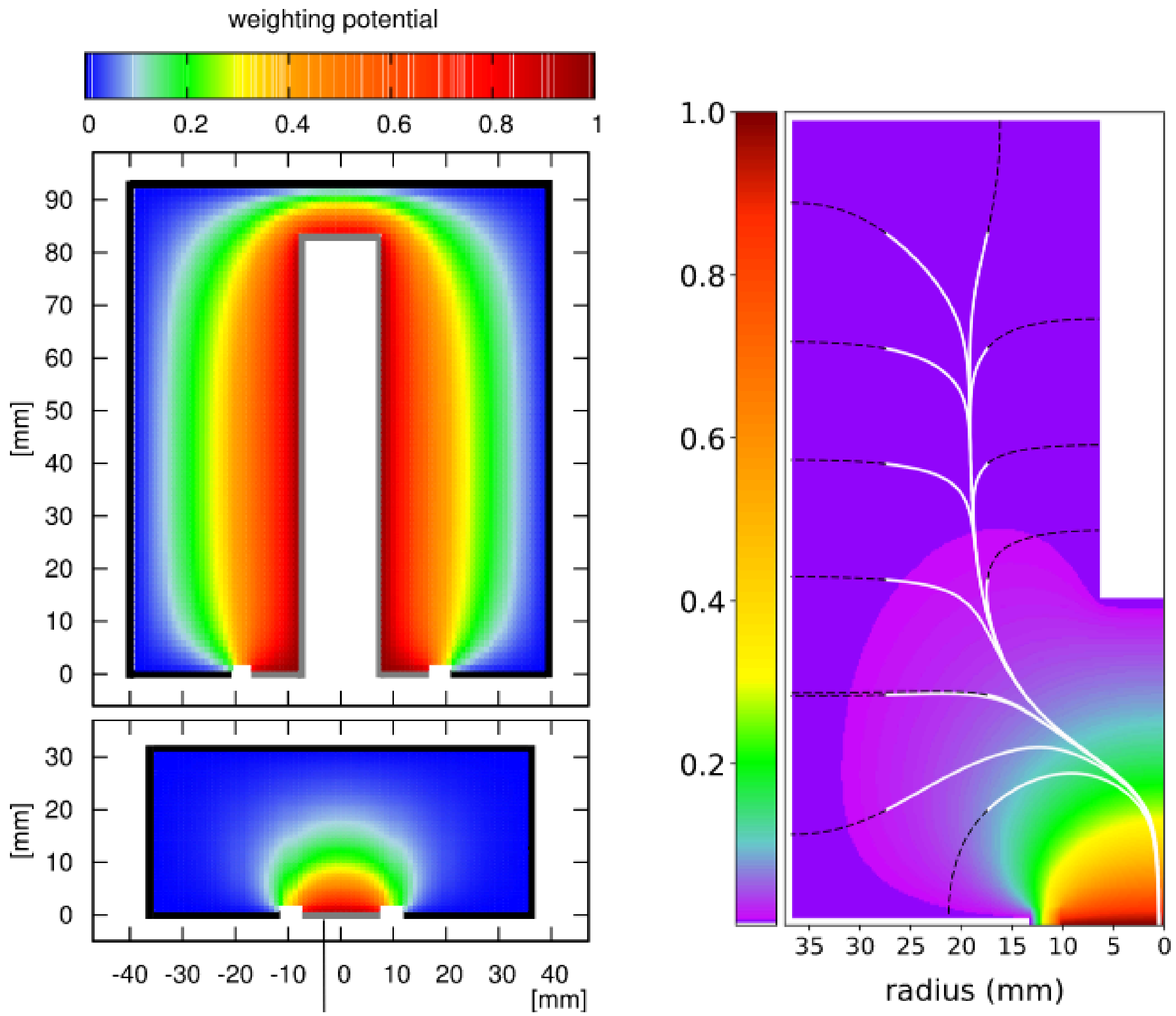

Figure 76: Cross sectional view of the three detector geometries and their weighting potential distribution.

As illustrated in Figure 76, for coaxial detectors, the weighting potential exhibits greater homogeneity throughout the bulk volume compared to BEGe/IC detectors. As a result, both electrons and holes actively contribute to the induced signal, and the trajectories of the generated charge carriers are significantly influenced by their starting positions within the detector.

The BEGe/IC detectors exhibits a distinctive electric field configuration that initially consolidates charges from various locations into the center of the detector. Subsequently, these charges follow a shared trajectory path towards the p+ contact. The weighting potential, illustrated in Figure 76 for a typical BEGe/IC detector, remains nearly zero throughout the detector volume, with significant values concentrated around the p+ contact. Consequently, when incident radiation generates electron-hole pairs in the bulk volume, there is an immediate but minimal current induced in the contacts. This current becomes substantial only when the holes have drifted into the extensive weighting potential surrounding the p+ contact. The resemblance in trajectories within this significant weighting potential explains the similarity in pulse shapes for bulk events irrespective of their starting positions.

If electron-hole pairs are generated in proximity to the p+ contact, the induced current is immediately substantial, leading to what is termed "fast pulses." The maximum current is also elevated since both holes and electrons move simultaneously within the weighting potential, potentially inducing up to twice the current produced by holes alone in the case of bulk events.

Electronic response:

The pulse shape simulation with ADL does not take into consideration the effect of read-out electronics on the shape of the signal. Despite the comprehensive electric field simulation and subsequent computations of detector traces, the influence of the read-out electronic hardware, including the charge-sensitive preamplifier, digital sampling device, and cabling to the FADC-input channels, remains unaccounted for. To enable a meaningful comparison between simulated and measured charge pulses, it is imperative to determine and incorporate the missing electronics response function into the signal modeling.

The fist stage of a readout system of a HPGe detector is a combination of a charge-sensitive preamplifier and a feedback circuit as illustrated in Figure 77. The induced signal is amplified by the preamplifier (A) which in turn charges the feedback capacitor (C_f). The capacitor is then discharged through a feedback resistor (R_f). This results in a fast rising edge of charge pulse followed by a slow decay tail. The preamplifier modifies the pulse shape and it is important that the preamplifier response is taken into account to generate pulse shape simulations comparable to measured pulse shapes in GERDA. A model of the electronic response of a preamplifier has been developed by K. Panas [Pan18] . In current work, this model was applied, and it's parameters were optimized for each of the semi-coaxial detectors individually.

Owing to very small band gap of 0.7 eV for Germanium, Germanium detector at cryogenic temperature of liquid nitrogen (~87K) produces ~$3*10^5$ electron-hole pairs per MeV of energy [Eme65] deposited by interacting radiation. These electron-hole pairs drift along the electric field in opposite directions inside the detector and induce current on the readout contact. The time integral of the induced current is directly proportional to the total charge generated inside the detector. The output signal from the detectors is characterized by very low amplitude and requires effective amplification. As a first step to measure this induced signal, a charge sensitive preamplifier is instrumented at the readout contact. A Charge Sensitive Preamplifier (CSP) transforms a current signal at its input to output a voltage signal with an amplified amplitude that is directly proportional to the time integral of input current pulse. The diagram below outlines a basic representation of a charge sensitive preamplifier:

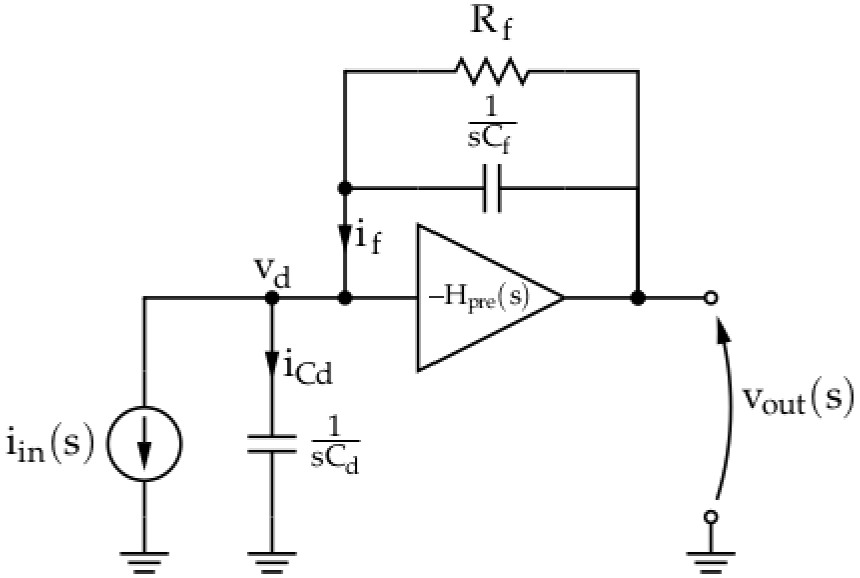

Figure 77: Schematic of a generic preamplifier-detector system utilized to model electronic response.

$$V_{out}(t) \propto \int^{t} i_d(\tau)d\tau = Q(t)$$

A feedback capacitor (C_f) positioned between the input and output accumulates charge from the detector, with the preamplifier's gain defined by $1/C_f$. The CSP generates output voltage proportional to the time integral of input current, which in turn is directly proportional to the total energy deposited in the detector by radiation interaction. Hence the amplitude of the output voltage serves as an effective measure of energy deposited by radiation interaction.

To reset the charge-sensitive preamplifier circuit involves incorporating a high-value feedback resistor (R_f) in parallel with the feedback capacitor. This discharge of feedback capacitor via feedback resistor creates exponential decay to output voltage with time constant defined by the product R_fC_f.

Although the actual electronics in GERDA is more complicated, the model based on the simplified preamplifier-detector system in Figure 77 is able to reproduce the impact of electronics on pulse shapes. The main effects of the electronics include:

a) The limited speed of the charge-sensitive preamplifier limits the bandwidth.
b) The discharge of capacitor via feedback resistor results in exponential tail.
c) The detector capacitance further limits the bandwidth.

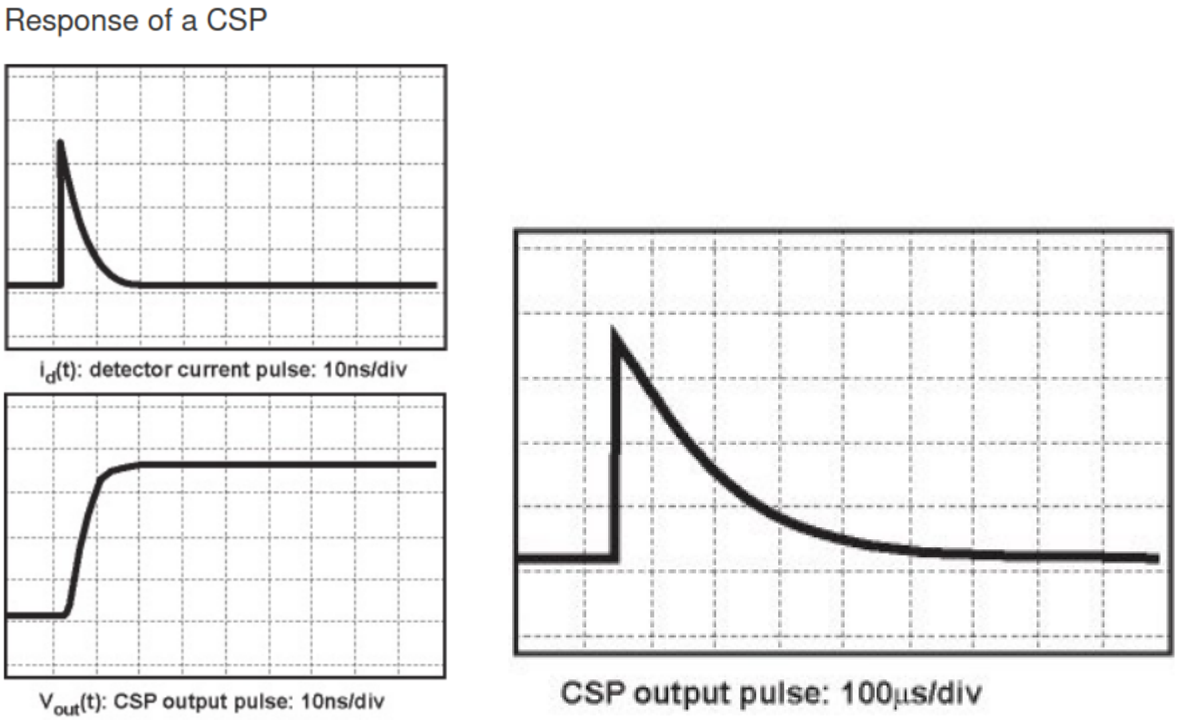
Response of a CSP

$i_d(t)$: detector current pulse: 10ns/div

$V_{out}(t)$: CSP output pulse: 10ns/div

CSP output pulse: 100µs/div

Figure 78: Response of CSP at lower and higher timeframes. Note the charge pulse has opposite polarity to that of the current pulse.

By conducting a Laplace analysis of the above circuit, the transfer function of the preamplifier can be derived. The response of the preamplifier (T(s)), expressed in terms of the complex frequency (s = i · ω), is characterized by the following equation:

$$T(s) = \frac{1}{C_f}\left[\alpha s^2 + s + s\alpha(\omega_{sum} + \omega_{pre}) + \alpha\omega_{sum}\omega_{pre} + \omega_f\right]^{-1}$$

Where,

$$C_{sum} = C_f + C_d \quad ; \quad \omega_{sum} = \frac{1}{R_f C_{sum}} \; ; \; \alpha = \frac{C_{sum}}{C_f.GBP}$$

$$\omega_f = \frac{1}{R_f C_f} \quad ; \quad \omega_{pre} = \frac{GBP}{K_{pre}}$$

K_{pre} is the gain of the preamplifier and GBP refers to Gain-Bandwidth-Product which expresses the bandwidth of the preamplifier for a given gain.

The impulse response is obtained by calculating the inverse Laplace transform of transfer function T(s):

$$h(t) = \mathcal{L}^{-1}[T(s)]$$

In order to obtain the impulse response in discrete time domain, a bilinear transformation of the transfer function is necessary which is shown in detail in appendix. Note that the calculation of the transfer function involves using the current signal as an input, while the output from the ADL simulation is presented in the form of a charge pulse. To accommodate this disparity, the impulse response is differentiated and is subsequently convolved with the simulated charge pulse as illustrated in Figure 79.

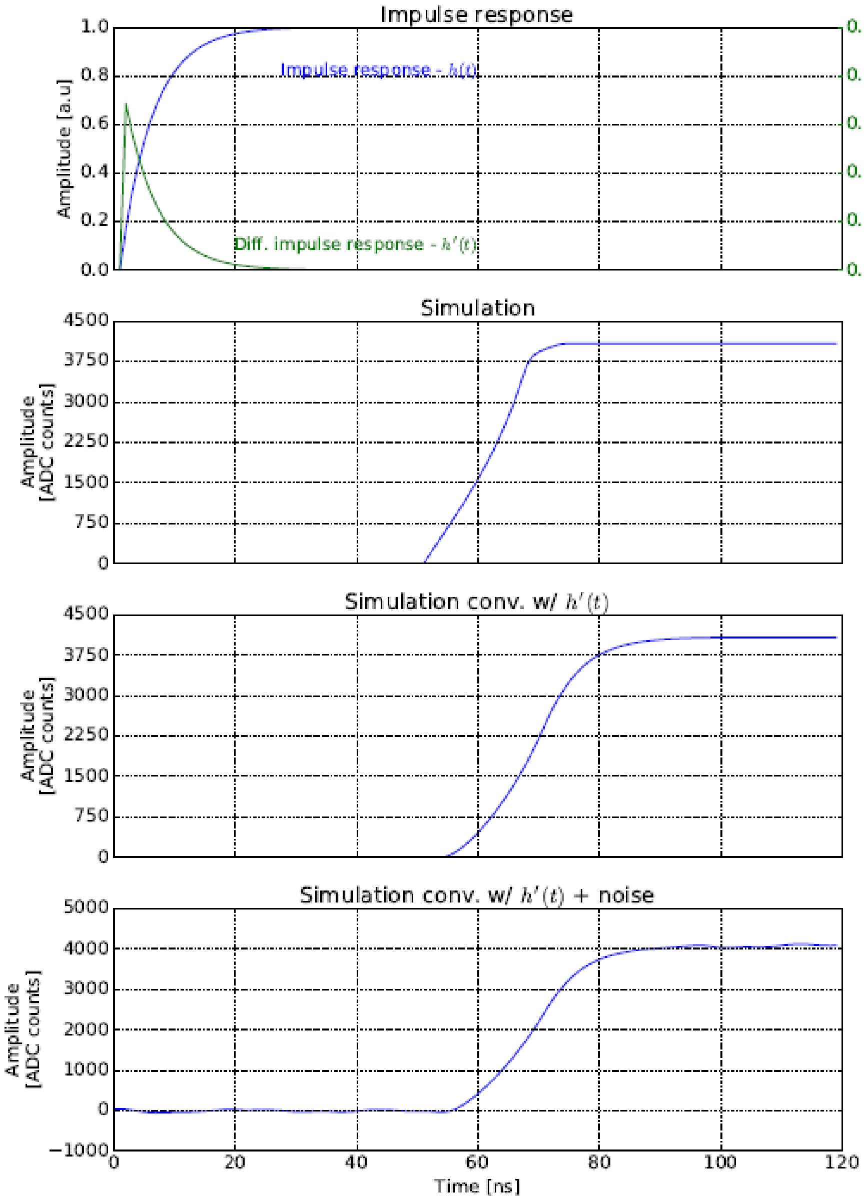

Figure 79: Electronic response convolution with simulated charge pulse and addition of noise. (adapted from [Pan18])

The gain of the amplifier is set to $K_{pre} = 150 * 10^3$. The remaining four free parameters that include feedback resistance (R_f), feedback capacitance (C_f), detector capacitance (C_d) and gain-bandwidth product (GBP) are optimized individually for each semi-coaxial detector.

To refine the model parameters of electronic response, a comprehensive analysis is conducted by comparing GERDA's measured pulses with simulated pulses incorporating electronic response. The model parameters are systematically adjusted during this comparison. As pulse shapes can vary based on the position of energy depositions and event topology (SSE/MSE), it is essential to derive a representative charge pulse. This is achieved by selectively using pulses from predominantly single-site events (SSE) with fixed energy, and subsequently averaging numerous individual pulses to obtain a representative pulse profile.

The optimization process focuses on comparing average charge traces derived from predominantly single-site events within the double escape peak (DEP) energy region, specifically within ±1·FWHM centered around 1592.5 keV. The individual charge pulses are normalized and aligned based on their reference time at 50% height of the maximal amplitude. Averaging these aligned traces yields a representative signal profile, as illustrated in Figure 80. For each detector under examination, these averaged traces from measured data are systematically compared with various iterations of averaged simulated traces to deduce optimal parameter values.

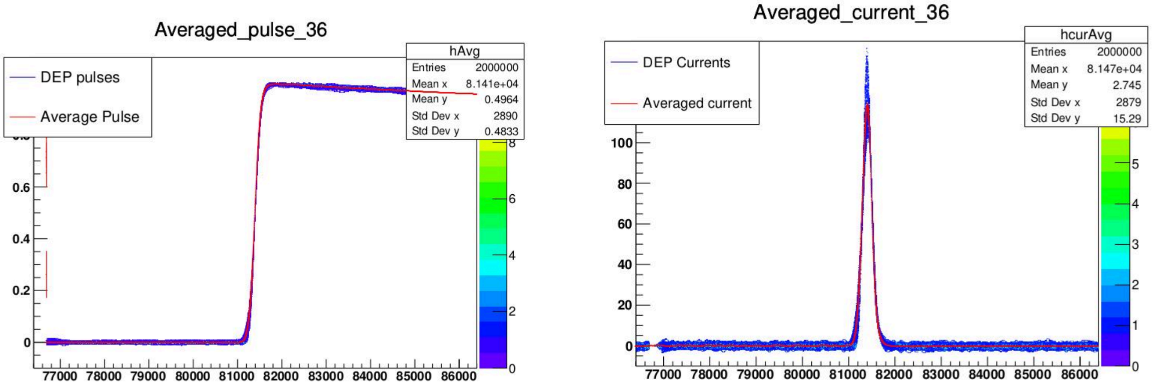

Figure 80: Aligning of normalized individual charge and current pulses to generate a representative signal profile. Shown here are SSE traces from ANG1 in blue and averaged profile in red.

The product $R_f. C_f$ corresponds to the decay constant of the charge signal, representing the discharge of the charged feedback capacitor through the feedback resistor. Consequently, the values of the feedback capacitance (C_f) are tuned by fitting the decay tail of averaged charge pulses from experimentally measured data, while feedback resistor (R_f) is kept at 500 MΩ. A fit to such a decay tail is illustrated in Figure 81.

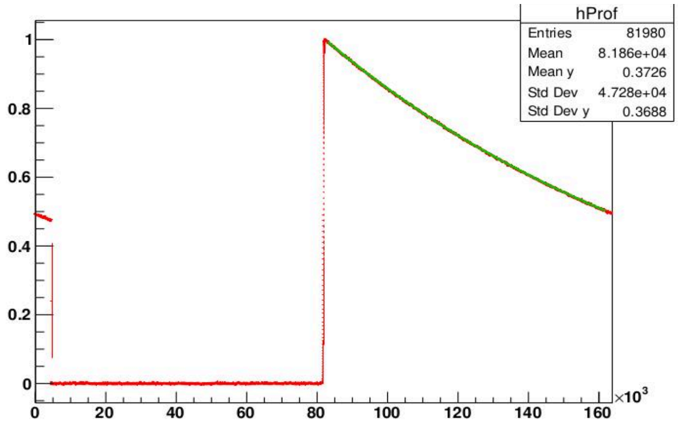

Figure 81: Optimization of R_f and C_f model parameters by fitting the decay tail of the averaged charge profile from GERDA data. Here, an averaged charge profile from ANG1 is shown in red and an exponential fit to the decay tail in green.

The gain-bandwidth product (GBP) and detector capacitance both have bandwidth limiting effect and thus are tuned concurrently by varying both the parameters in a wide range and evaluating how well the resultant simulated pulses match the observed experimental pulses.

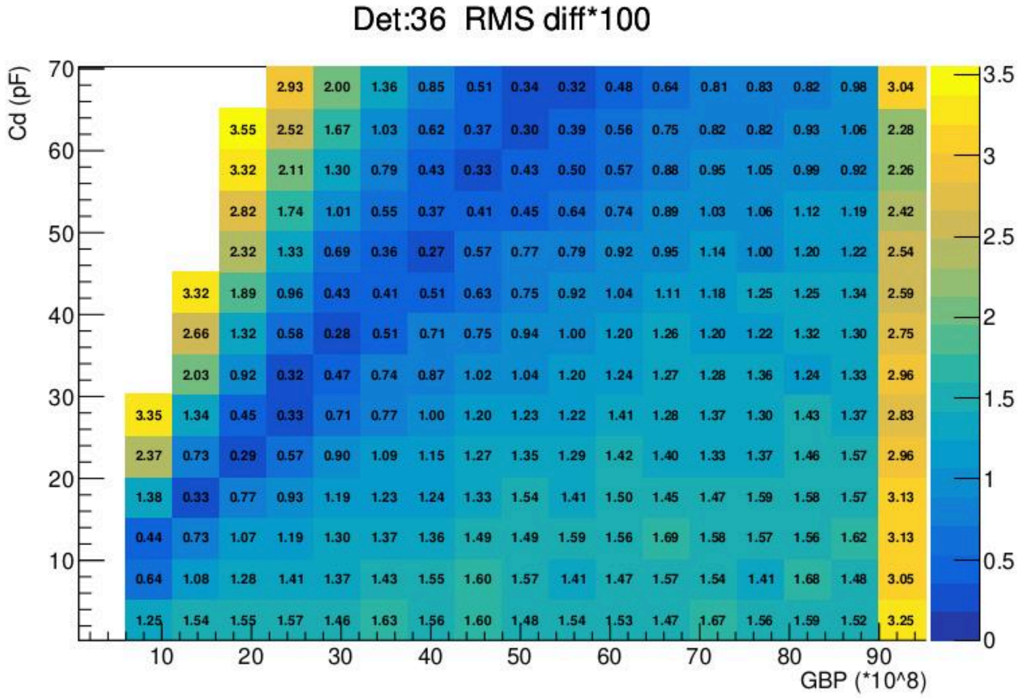

Figure 82: Root mean squared difference between averaged charge pulse from measured data and averaged simulated pulse is shown for systematic iterations over gain

bandwidth product (GBP) and detector capacitance (C_d) parameters. The plot shows correlation between simulated pulses for a given GBP/C_d ratio as expected (refer to Appendix B).

Electronic Noise Implementation:

To replicate electronic noise in the simulated pulses, flat pulses are extracted from recorded baselines—non-triggered charge pulses with a 100 MHz sampling frequency. The similarity in noise behavior between observed data and pulse shape simulation is essential to avoid any bias in further analysis.

A dedicated library of baseline traces from physics runs for each germanium detector is created from which a baseline trace is picked at random and added to a simulated pulse. The noise amplitude is normalized based on the experimental signal-to-noise ratio before being added to the simulated event signal with the convolved electronics response. As depicted in Figure 83 below, the resulting pulses resemble experimentally obtained pulses, enabling the application of identical analysis tools and ANN modeling for a meaningful comparison and estimation of the 0νββ efficiency.

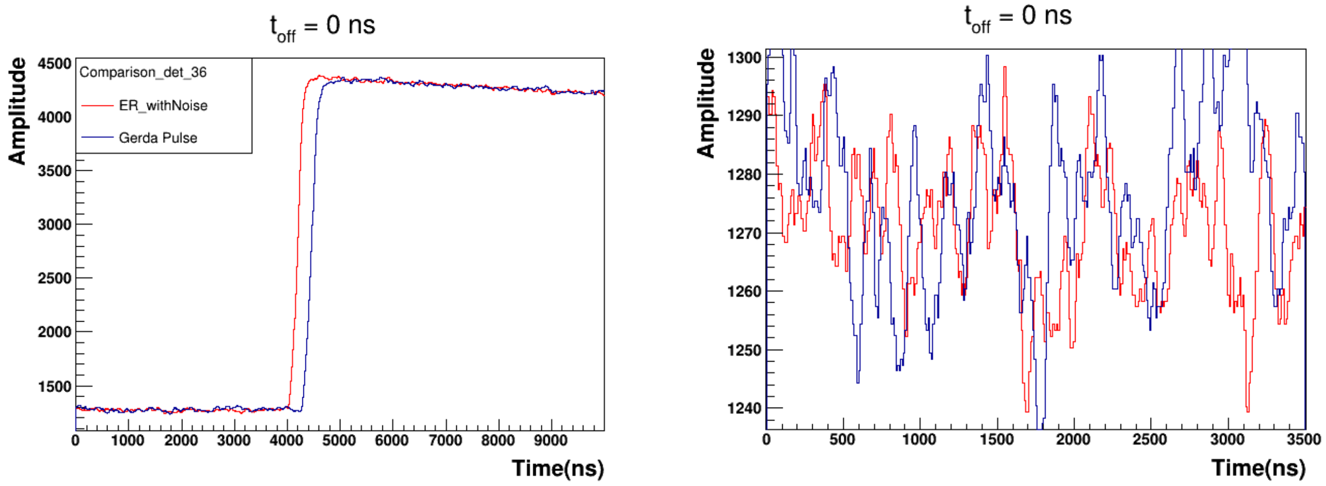

Figure 83: A representative charge pulse from GERDA data (blue) and pulse shape simulation (red) is overlaid, and the inset shows zoom-in of the partial baseline, highlighting the similar noise levels for both.

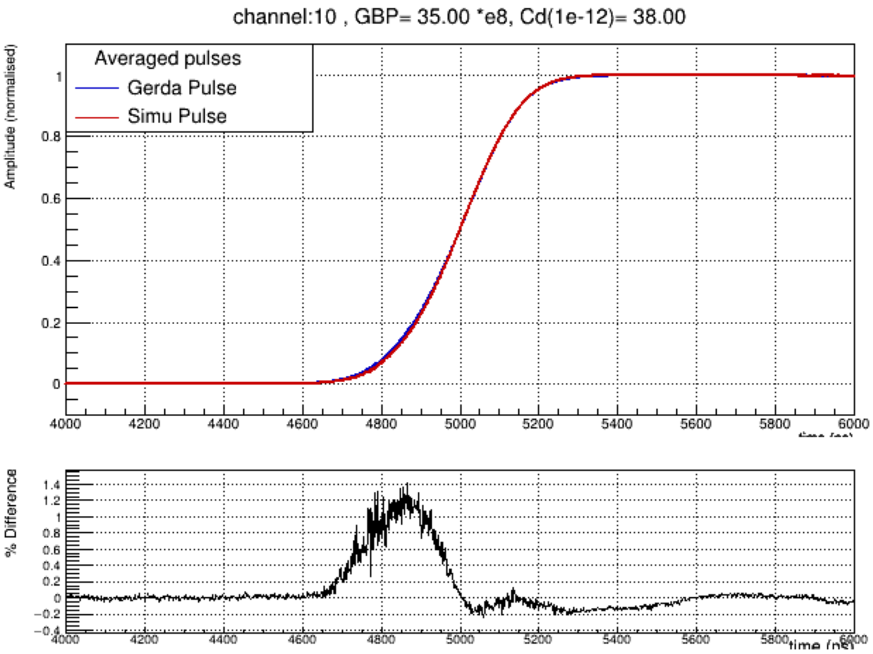

Figure 84: Comparison of an averaged charge pulse from DEP events from observed GERDA data and that from pulse shape simulations with optimized ER-model parameters. Bottom panel shows disparity between simulated pulse and measured pulse as percentage of amplitude.

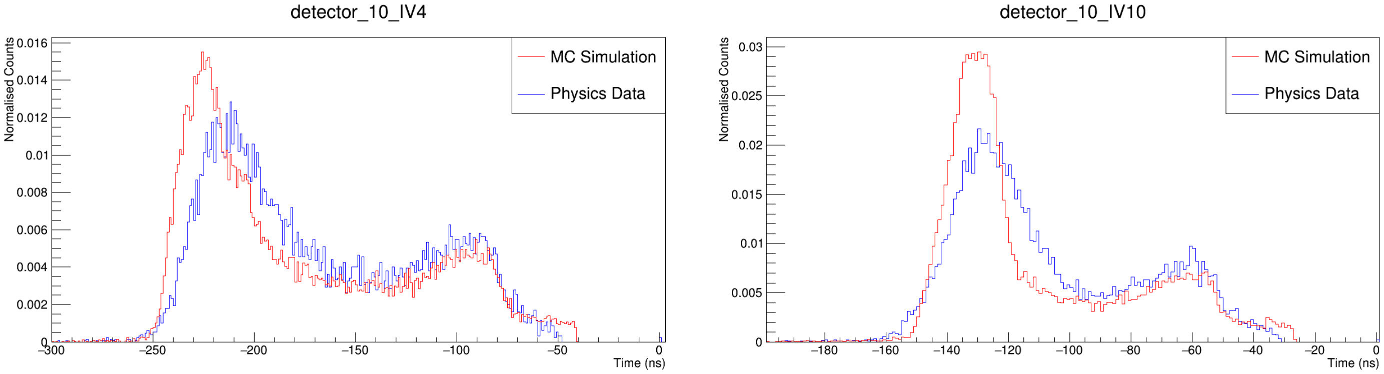

Figure 85: Input variable distribution for DEP events from the GERDA data (Blue) and simulation (red) are shown for 9% (left) and 21% (right) of maximum pulse amplitude. These are the inputs for ANN-based model and show good match.

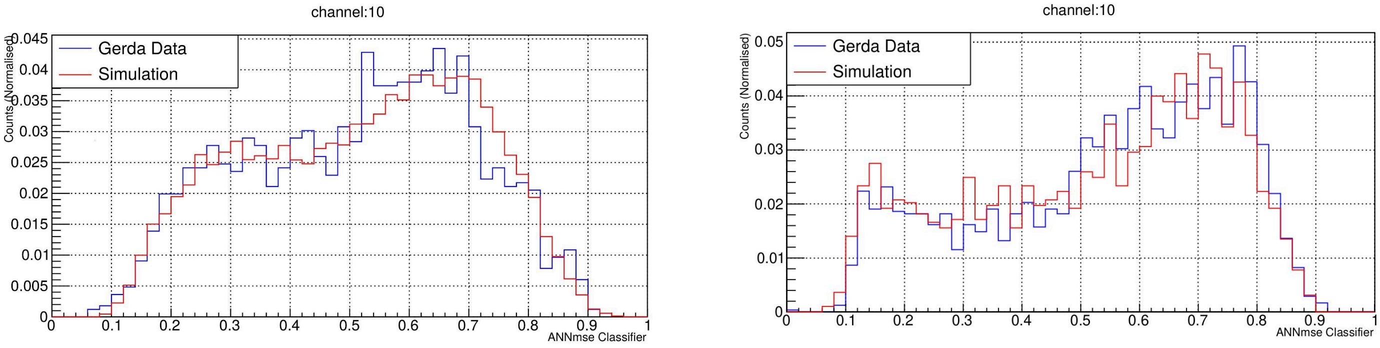

Figure 86: Comparison of classifier response of MLP based ANN-MSE model on GERDA data (blue) and simulation (red) shows excellent match for 2νββ events (left) and ^{208}Tl DEP events (right). The model is trained with GERDA calibration data.

In this appendix, we discuss the Monte Carlo (MC) simulations conducted using Geant4 for simulating energy depositions and ADL4 for subsequent pulse shape simulations. These simulations were aimed at creating a synthetic GERDA dataset that could be used to train neural network models following the same procedures and techniques applied in GERDA data analysis. The models trained on this simulated data demonstrated excellent performance in discriminating between signal and background events, closely mirroring the classifications observed in actual GERDA data. A simple comparison of the classifier distributions from GERDA data and the simulation data is presented in the figure 87 below.

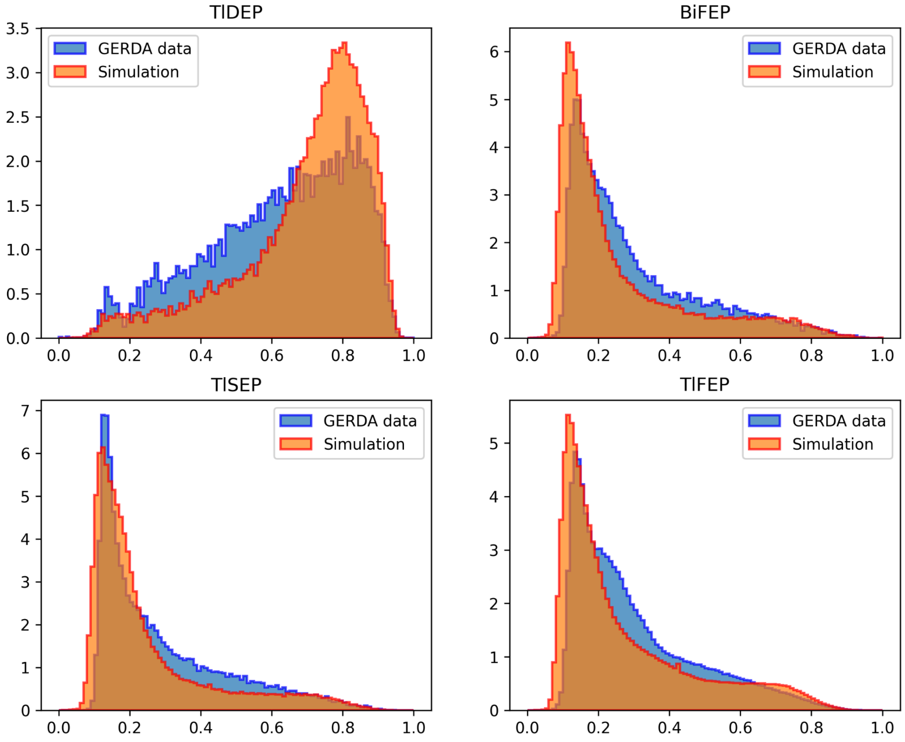

Figure 87: ANN-MSE classifier distributions for peaks of interest from ^{228}Th calibration data from GERDA (in blue) and from simulations (in orange) are shown.

However, when these simulation-trained models were applied to GERDA data, their performance was sub-optimal, as shown in the subsequent figure 88. This discrepancy likely arises from the model's reliance on specific features unique to the simulation data, which do not generalize well to GERDA data.

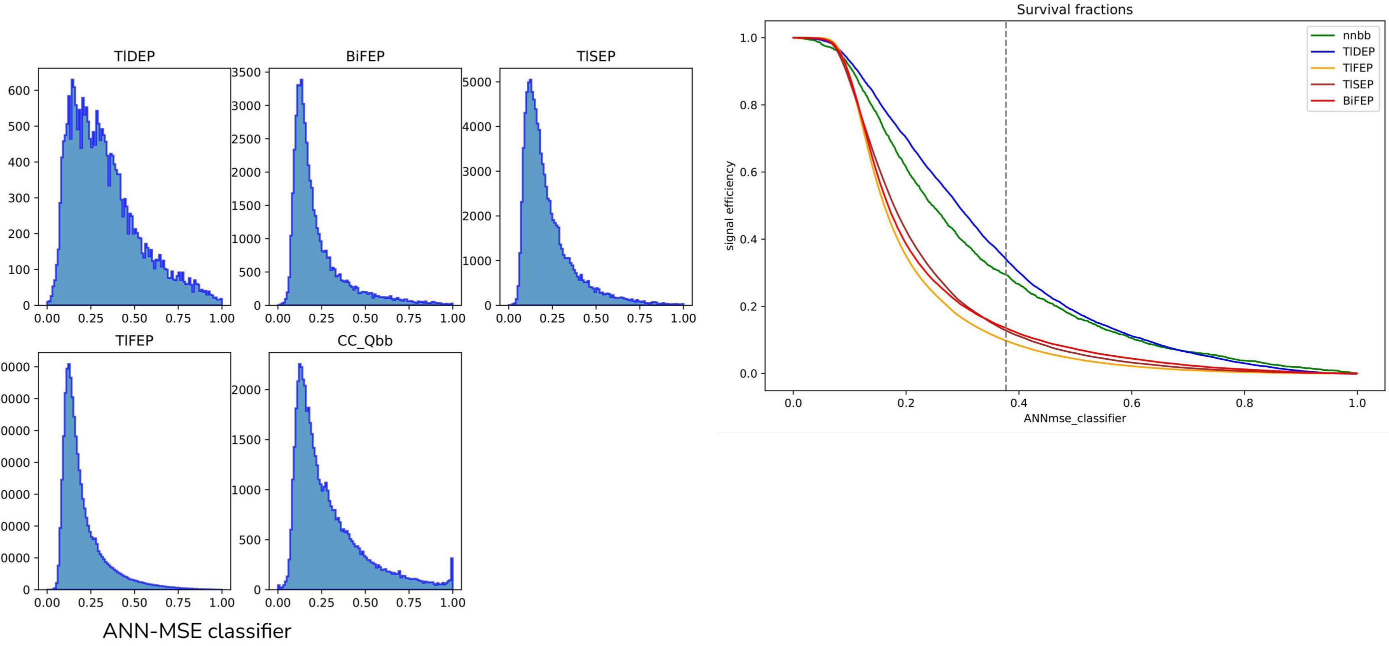

Figure 88: The predicted classifier distributions by ANN-MSE model trained on simulated data for GERDA calibration data from various energy ranges corresponding to these above mentioned peaks from the ANG2 detector. The last panel titled “CC_Qbb” represent events from Compton continuum in the ∓25 keV window centered at $Q_{\beta\beta}$-value of 2039 keV and constitutes of a mixture of both single-site and multi-site events. The right panel shows efficiency as function of classifier threshold which clearly indicates the model shows no significant discrimination power between signal and background.

In contrast, models trained directly on GERDA data maintained comparatively higher performance when applied to the simulated data. This indicates that the models trained on GERDA data have effectively learned generalized patterns in the signal and background pulse shapes, allowing them to distinguish these patterns even in simulated data, as evidenced in figure 89 below.

These findings highlight the importance of using real experimental data for training to ensure the robustness and generalizability of machine learning models in high-stakes physics experiments.

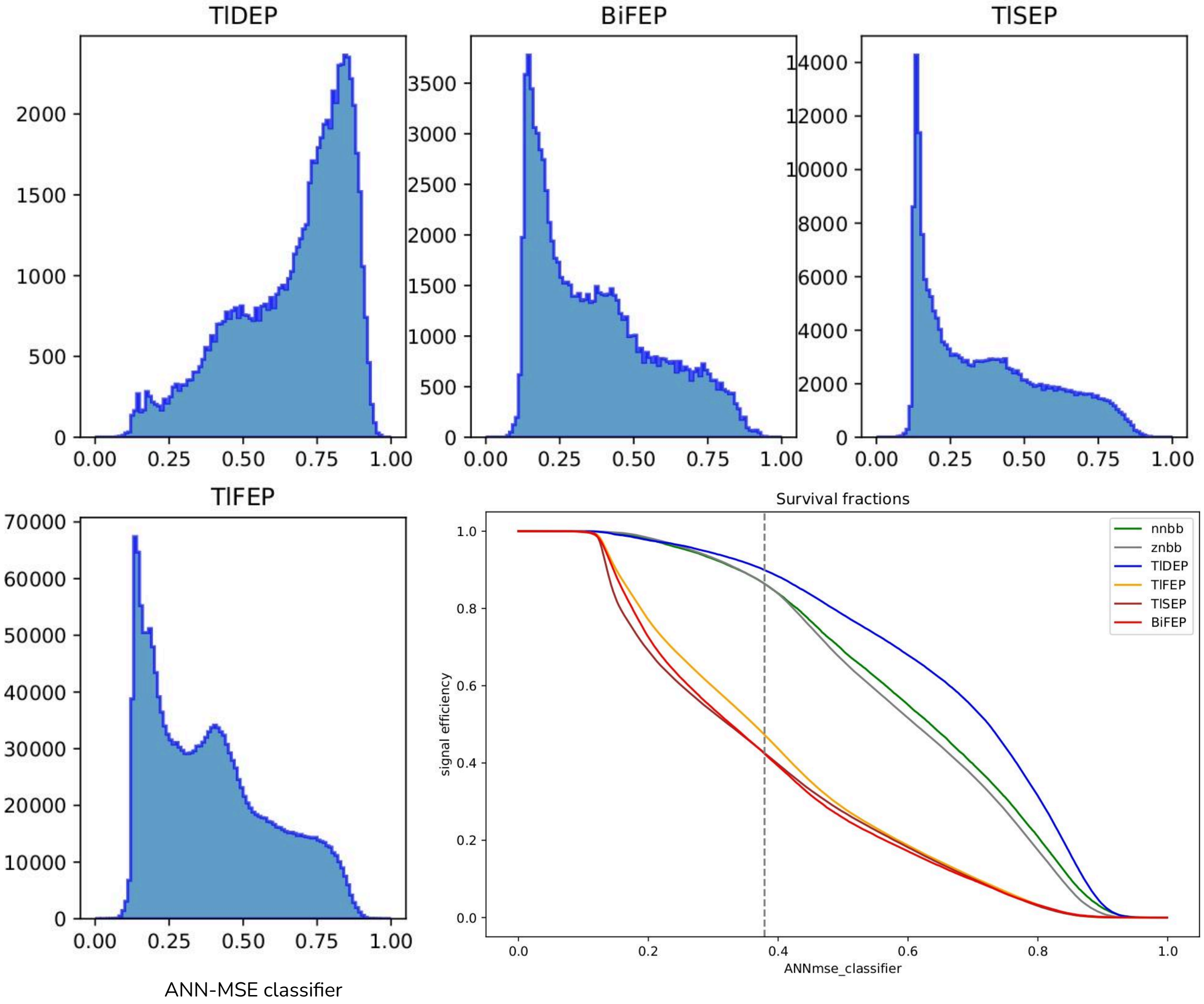

Figure 89: The predicted classifier distributions by ANN-MSE model trained on GERDA data for Simulated calibration data from various energy ranges corresponding to these above-mentioned peaks from the ANG3 detector. The bottom right panel shows efficiency as a function of classifier threshold, which clearly indicates the models trained on physical data retain similar discrimination power between signal and background when applied to simulated data.

Simulating energy deposition topology for SSE vs MSE :

In 0νββ decay, two electrons generated during the process deposit their energy in a confined volume of approximately 1 mm^3 within a germanium detector [Abt07]. This energy deposition is effectively treated as a point-like occurrence, referred to as a single-site event (SSE). Conversely, background events, predominantly induced by high-energy γ rays from natural radioactivity, typically undergo Compton scattering. This leads to events with energy deposited in multiple distinct locations, termed multi-site events (MSE). The distinct drift paths and time-dependent movements of electron/hole charge carriers in the two event topologies lead to differences in their final pulse shapes. The characteristic time structures of the charge signals can be directly utilized by the ANN-based classifier for an efficient pulse shape discrimination.

To effectively train and calibrate pulse shape discrimination techniques, it is imperative that the utilized data accurately represents the signal and background being distinguished. The 2νββ events serve as the closest approximation to the 0νββ signal, comprising predominantly pure single-site events (SSE) with a small MSE component due to the emission of bremsstrahlung photons. The fraction of kinetic energy of primary electron converted into bremsstrahlung is ~3% [Ber05] for electrons with 1-2 MeV energy and most of these low energy bremsstrahlung photons will be absorbed very close to interaction position due to their short mean free path at energies of few tens of KeVs. Thus 2νββ events can be considered pure SSE. However, due to the very low decay rate of 2νββ decays, the statistics of 2νββ events are limited. To address this limitation, we aim to identify a proxy for the signal using calibration data from a ^{228}Th source, which provides more substantial statistics. A representative energy spectrum for a calibration run from GERDA Phase II is shown in Figure 90.

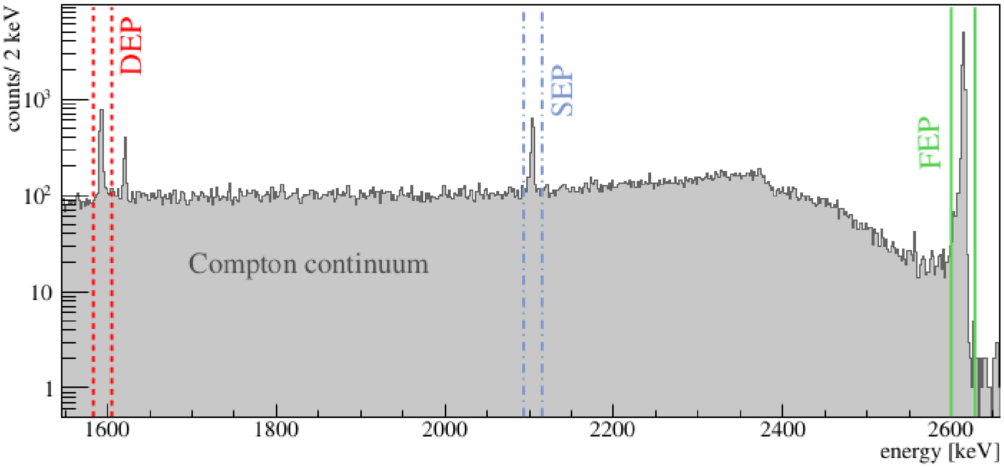

Figure 90: ^{228}Th energy spectrum observed in GERDA Phase II calibration runs using a representative COAX detector. The spectrum is predominantly characterized by γ-rays originating from the decay of ^{208}Tl, featuring a full energy peak (FEP) at 2614 keV, along with a distinct double escape peak (DEP) at 1592 keV and single escape peak (SEP) at 2103, as well as a broad Compton continuum. A full energy peak at 1620 keV originates from decay of ^{212}Bi from the ^{228}Th decay chain.

When ionizing radiation such as high energy photons or charged particles interact with Germanium, they dissipate energy creating a large number of electron-hole pairs Drifting in the electric field; these charges induce signals on the contact, as detailed in Section 5.2. At cryogenic temperature of liquid nitrogen (~87K), interacting radiation produces ~$3*10^5$ electron-hole pairs per MeV of energy irrespective of the nature of radiation. Therefore discriminating 0νββ events from high energy γ-induced background relies on distinct interactions of electrons and high energy photons with the detector material and the resulting spatial energy deposition pattern. In germanium, a ~1 MeV electron dissipates all of its energy within 1-2 mm [Ber05] which is determined by the material's stopping power. In contrast, the range for photons is expressed as the mean free path, representing the average distance a photon travels before interacting with the germanium detector material which is on the order of centimeter. Events with multiple energy depositions within the active volume of the detector are termed multi-site events (MSE), distinguishing them from 0νββ events characterized by single, localized energy deposition, referred to as single-site events (SSE).

Three primary mechanisms through which high energy photons interact with matter are as follow:

Photoelectric absorption: The photon imparts its complete energy to an electron in the detector material, ejecting it from the atom. This dominates at low energies, up to a few hundred keV.

Compton scattering: The incident γ-ray undergoes elastic scattering off an electron in the detector material, losing a portion of its energy.

Pair production: At energies ≥ 1022 keV, the incident γ-ray can convert into an electron-positron pair in the Coulomb field of a nucleus in the detector material.

The cross-section for each mechanism is dependent on the energy of the incident photon and at energies above ~1MeV, Compton scattering is dominant.

When 2614 keV MeV gamma rays from ^{208}Tl interact with germanium via pair production, two annihilation photons are generated as byproducts when a positron annihilation occurs after slowing down in the absorbing medium. Momentum conservation dictates that the two annihilation photons, each with energy E_{γ}=511 keV, are emitted in opposite directions. Subsequently, these annihilation photons can either escape the detector or undergo additional interactions within it.

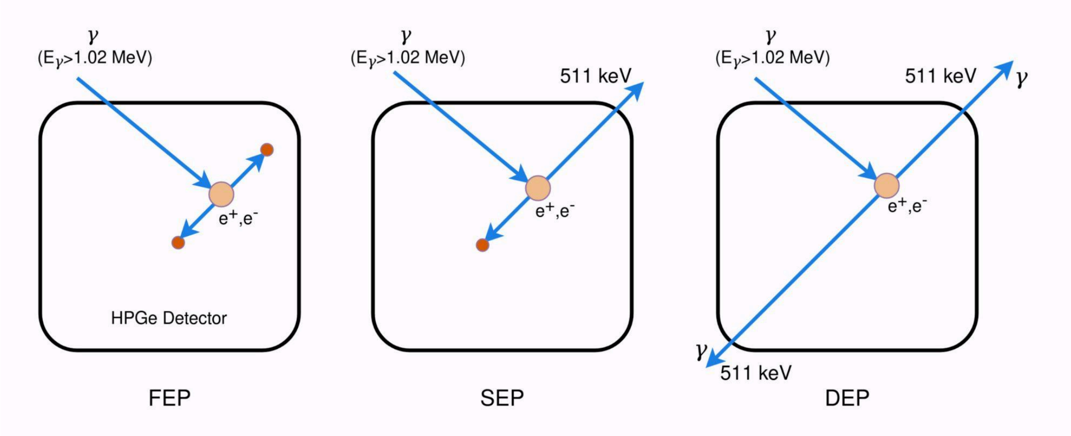

Figure 91: possible realizations due to interaction of 2.614 MeV gamma ray from ^{228}Th via pair production leading to observed Full energy peak(FEP). Single escape peak(SEP) and Double escape peak(DEP) in ^{228}Th energy spectrum

The outcomes of these interactions can be summarized in three scenarios depicted in Figure 91 above:

a) Both 511 keV γ-rays interact further, depositing all their energy within the detector. This results in complete energy deposition, contributing to a Full Energy Peak (FEP) at 2614 keV in the energy spectrum.

b) One of the two gamma rays deposits energy in the active detector volume, while the other escapes without interaction. This leads to a deficiency of 511 keV and appears as a Single Escape Peak (SEP) at 2103 keV in the energy spectrum.

c) Both γ-rays escape the detector volume without interacting, resulting in a loss of 1022 keV and appearing as a Double Escape Peak (DEP) at 1592 keV in the energy spectrum.

Therefore events involving the ^{208}Tl double escape peak at 1592.5 keV result from a 2.6 MeV gamma interacting via pair production. Subsequently, two 511 keV annihilation photons escape the detector, resulting in double escape peak (DEP) events that exhibit event topology very similar to 0νββ events, with highly localized single-site energy deposition. A fraction of DEP events may display MSE behavior if the 2.6 MeV photon undergoes Compton scattering before pair production.

The Compton edge around 2380 keV represents the maximum energy deposited in a single Compton event by a full-back scattering of the incident γ-ray. Overall, γ-rays often interact multiple times with the detector material until full absorption or escape detection. The ratio of Compton to FEP events depends on detector size, geometry, and source position.

Finding a proxy for SSE and MSE in calibration data: calculating SSE fractions:

To find a proper proxy that genuinely represent signal-like single-site events (SSEs) and background-like multi-site events (MSEs), the position information derived from the MaGe simulation of the ^{228}Th calibration spectrum can be utilized.

As a proxy for high-energy gamma background interactions involving multiple Compton scatterings leading to MSE, peaks from high-energy gamma emissions in the ^{228}Th calibration data, such as 2.6 MeV full energy peak (FEP), 2.1 MeV single escape peak (SEP), and 1.62 MeV Bi FEP, can be utilized. It is important to note that these events will exhibit some SSE component due to interactions via the photoelectric effect, but this component is anticipated to diminish rapidly with higher energies, as illustrated in Figure 6. Since we aim to develop pulse shape discrimination techniques that differentiate between signal and background events at the $Q_{\beta\beta}$ value, an ideal proxy for signal and background should possess energies as close to $Q_{\beta\beta}$ as possible to minimize potential energy dependence in PSD performance.

The pulse shape discrimination method in this study is based on differentiating SSE from MSE, specifically on the spatial extension of the energy deposition within the detector material. Subsequently, the SSE fraction in various energy regions of the ^{228}Th spectrum and 0νββ events is investigated using Monte Carlo (MC) simulations, demonstrating that 0νββ events are typically fully absorbed within < 1 mm3.

In this study, Monte Carlo (MC) simulations are employed to investigate the Single Site Event (SSE) fraction in various energy regions of the ^{228}Th spectrum and 0νββ events. The energy depositions from ^{228}Th source in GERDA Phase II calibration runs were simulated using the MaGe framework based on Geant4. The RMS is used as a measure of the spatial extension of energy depositions from an event inside the germanium detector, aiding in distinguishing SSE from Multi-Site Events (MSE).

$$RMS = \sqrt{\frac{1}{E}\sum_i [(x_i - \bar{x})^2 + (y_i - \bar{y})^2 + (z_i - \bar{z})^2].E_i}$$

Each simulated event comprises multiple subsequent energy depositions (termed as hits) in detector volume till all energy from the simulated radiation is dissipated. For each hit i, it has associated energy deposition of E_i and hit position (x_i,y_i,z_i). The barycenter *r* = ($\bar{x}$,$\bar{y}$,$\bar{z}$) of the event is calculated as the energy weighted mean of all individual hit positions. Then, the spatial spread of energy depositions is calculated as energy weighted root mean square difference of all hit positions with barycenter *r* = ($\bar{x}$,$\bar{y}$,$\bar{z}$).

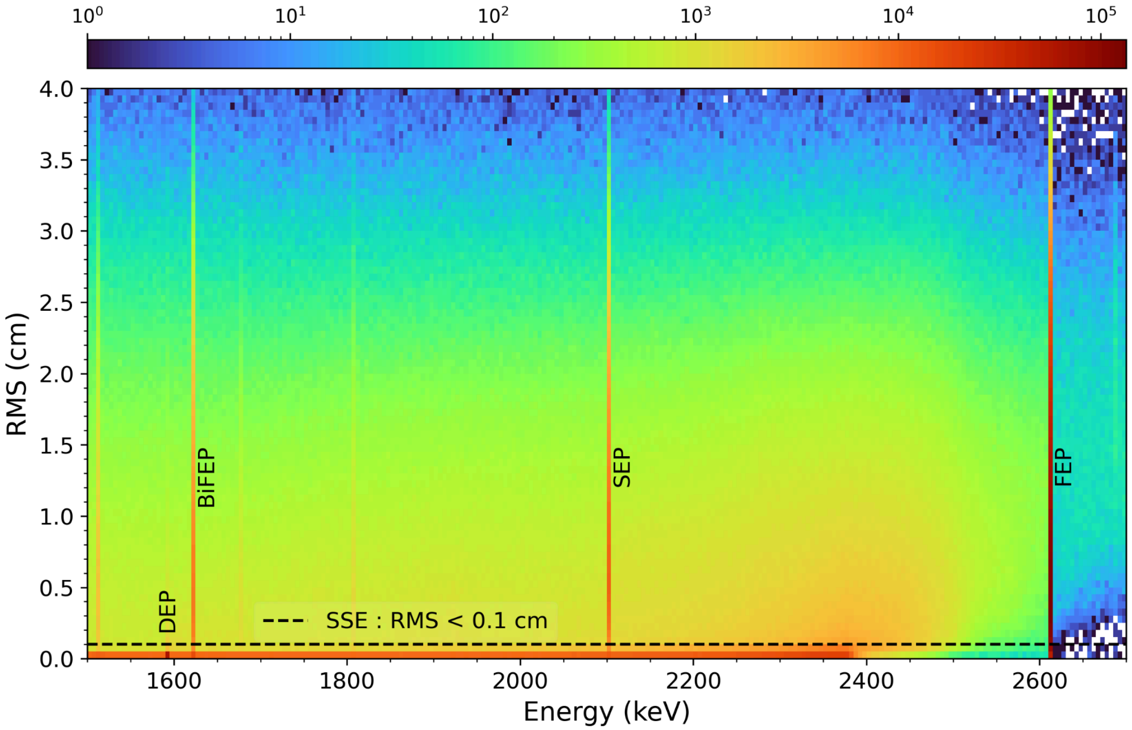

Figure 92: presents a 2-d histogram of simulated MC spectrum for a semi-coaxial detector, ANG2, displaying the Root Mean Square (RMS) as a function of energy. The RMS is calculated as the root-mean-squared distance of all hits within the detector, with each hit position weighted by its energy fraction. The SSE region is defined as events with an RMS < 0.1 cm. Note that the DEP events at 1592.5 keV exhibit an exceptionally high SSE fraction shown by dense population at low RMS values.

It is evident from Figure 92, for the gamma ray peaks of the ^{228}Th spectrum, we observe distinct RMS distributions indicating dissimilar event compositions. The double escape peak features an enhanced fraction of single-site events (SSE). Conversely, other predominant peaks, including the adjacent full energy peak (FEP) from ^{212}Bi and the ^{208}Tl single escape peak (SEP) at 2103.5 keV and FEP at 2614.5 keV, exhibit a broad distribution toward higher values for the root-mean-square (RMS), indicating a tendency toward an increased spread of interaction points of energy deposition. This aligns with the assumption that they are primarily of multi-site event (MSE) in nature.

The simulations demonstrate that 0νββ events are typically fully absorbed within a volume of less than 1 mm^3. However, the analysis provides an estimate of the SSE fraction, and potential influences from noise or electronic response are not considered in the subsequent discussion. The larger the detector, the higher the detection probability of MSE with larger RMS values, while SSE are not significantly affected.

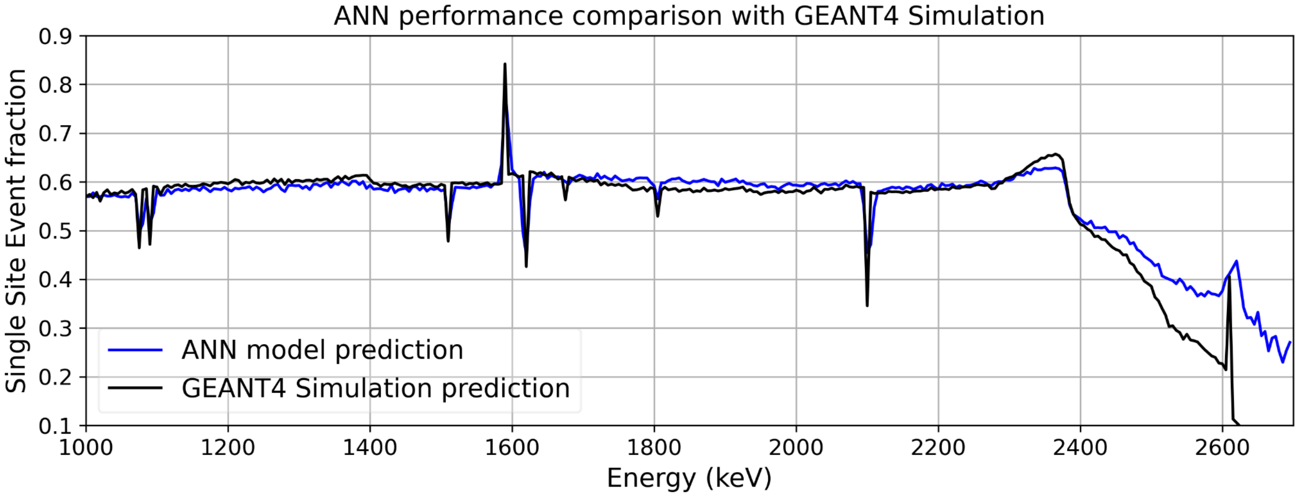

Figure 93: Based on the analysis approach to infer the SSE/MSE composition of various events in the calibration spectra from simulations, the plot compares the performance of our ANN-based models in discriminating between SSE and MSE. To visualize this, the single-site event (SSE) fraction as a function of energy as predicted by the ANN model is plotted, overlaying it with a similar plot derived from the simulated RMS calculations.

For a meaningful comparison and to check for any energy dependence in the ANN model, the cut thresholds were aligned to ensure the same SSE fraction at the $Q_{\beta\beta}$ energy. This alignment is crucial because it standardizes the comparison across different energy levels, ensuring that any observed discrepancies are due to model performance rather than inherent differences in SSE fraction at various energies.

The resulting Figure 93 clearly demonstrates that ANN model effectively discriminates between SSE and MSE. The model's performance closely replicates the SSE fraction distribution predicted by the simulation, indicating that it successfully captures the necessary features to distinguish between single-site and multi-site events. Moreover, this performance shows no significant energy dependence, confirming that the ANN model maintains its discriminative power consistently across the energy spectrum. This consistency is particularly important as it validates that the ANN model can reliably differentiate signal from background events at energies close to $Q_{\beta\beta}$.

The Monte Carlo simulations qualitatively and quantitatively support the pulse shape discrimination approach applied in this analysis. Events from the ^{208}Tl double escape peak and the nearby ^{212}Bi full energy peak serve as reasonably proper proxy samples for the signal and background event classes in the ANN training process, despite the underlying Compton continuum.

Spatial distribution of events of interest inside the detector volume:

An additional critical consideration related to the selection of training or testing samples for event classes, which can be examined using data from Monte Carlo simulations, involves the potential non-uniform distribution of the associated signal event class proxy within the detector material. This issue arises due to particle interaction processes in matter, where, for the double escape peak (DEP) used as a single-site event (SSE) sample, the chance of the two 511 keV photons to escape is larger at the corners. Consequently, a volume dependency of the classifier may be introduced, potentially leading to the selection of events situated at the outer surface instead of identifying single-site events as detailed in Section 4.5.

The position information derived from the MaGe simulation can also be studied to understand the spatial distribution of certain type of events within the detector. This is important, as detailed in Chapter 3, the pulse shapes for semi-coaxial detectors do depend on the interaction position inside the detector. As discussed in section 4.5 and shown by figure 36, DEP events are generally located near the corners of the detector, where annihilation photons have a higher probability of escaping the active volume. In contrast, events from the FEP events tend to have their barycenter situated in the middle of the detector bulk. Considering these distributions of the training samples, a volume-dependent sensitivity in event selection by the ANN classifier seems natural in hindsight. The position dependent ANN-MSE efficiency for simulated 0νββ events is shown in figure 94 below where the models were trained with 208Tl DEP as a signal proxy. To mitigate this issue, in this study, we utilized the closest matching proxy available, which are 0νββ events that are homogenous across detector volume given the homogeneity of ^{76}Ge enrichment.

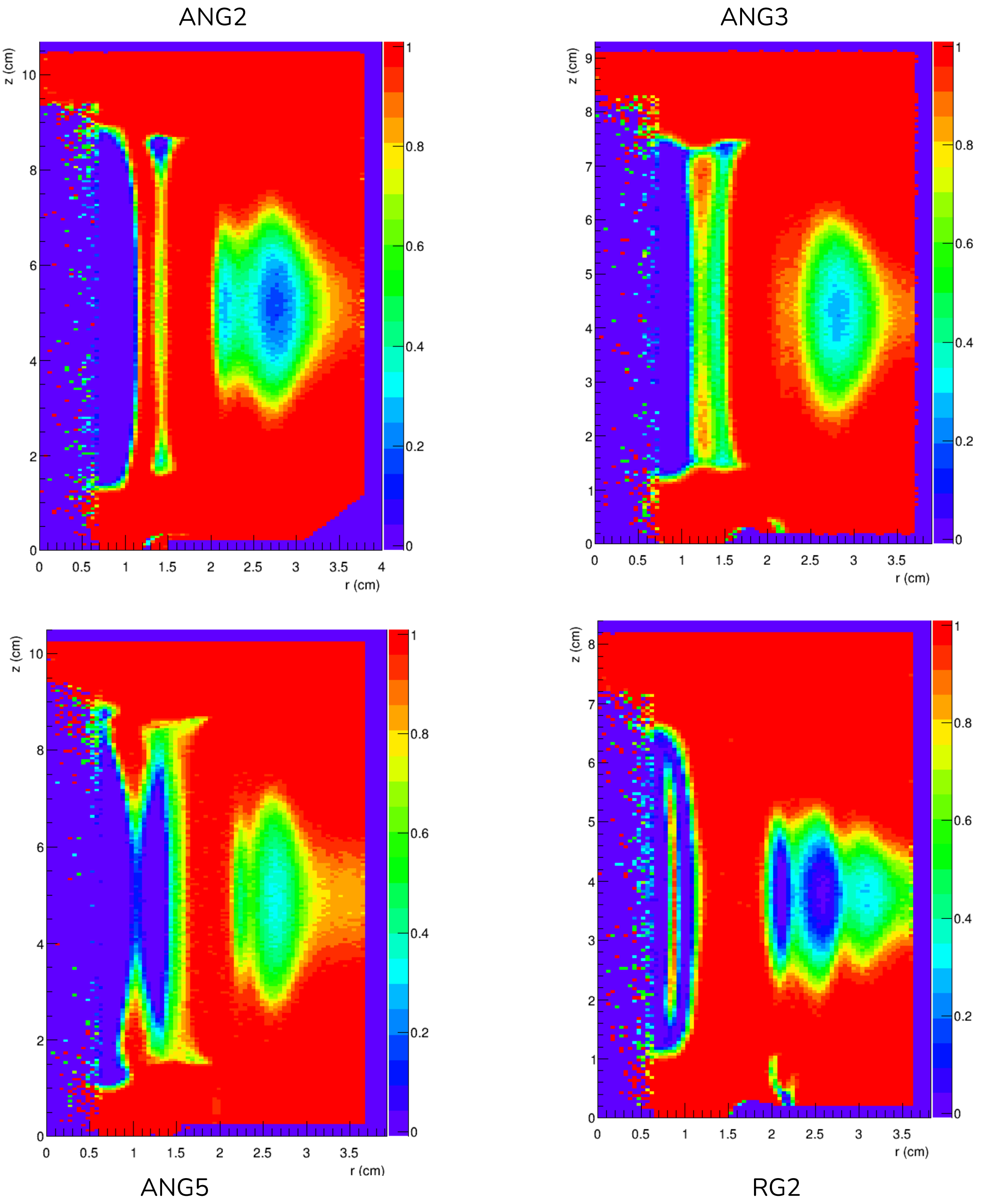

Figure 94: Spatial distribution of ANN-MSE efficiency for homogeneously simulated 0νββ events inside detector volume for each of the semi-coaxial detectors is shown as a function of radial distance (r) and height (z).

Bibliography (Appendix A):

[Bru16] Bruyneel, B., Birkenbach, B. & Reiter, P. Pulse shape analysis and position determination in segmented HPGe detectors: The AGATA detector library. *Eur. Phys. J. A* 52, 70 (2016). https://doi.org/10.1140/epja/i2016-16070-9

[Sal15] M. Salathe, “Study on modified point contact germanium detectors for low background applications” , PhD thesis, University of Heidelberg, 2015

[Kir14] A. Kirch, “Search for the neutrinoless double β -decay in GERDA Phase I using a Pulse Shape Discrimination technique”, PhD thesis, University of Heidelberg, 2014

[Pan18] K.Panas, “Development of Pulse Shape Discrimination Methods as Tools for Background Suppression in High Purity Germanium Detectors used in the GERDA Experiment”, PhD thesis. 2018.

[Wiki] https://en.wikipedia.org/wiki/Bilinear_transform#Genera

[Eme65]F. E. Emery and T. A. Rabson, “Average Energy Expended Per Ionized Electron-Hole Pair in Silicon and Germanium as a Function of Temperature”, Phys. Rev. 140, A2089 – 1965

[Ber05] Berger, M.J., Coursey, J.S., Zucker, M.A., and Chang, J. (2005), ESTAR, PSTAR, and ASTAR: Computer Programs for Calculating Stopping-Power and Range Tables for Electrons, Protons, and Helium Ion. https://physics.nist.gov/PhysRefData/Star/Text/ESTAR.html

Appendix B

Electronic response in pulse shape simulations: computation of impulse response in discrete time domain

In order to get the impulse response in discrete-time *(z)* domain, a bilinear transformation of the transfer function is necessary. For this purpose, a general second-order Biquad transformation is utilized.

For a general second-order filter with the given transfer function,

$$H(s) = \frac{b_0 + b_1 s^{-1} + b_2 s^{-2}}{a_0 + a_1 s^{-1} + a_2 s^{-2}} \quad ,$$

Applying the bilinear transform, $s \leftarrow \frac{2}{T}\frac{1-z^{-1}}{1+z^{-1}}$, gives us a digital biquad filter in a discrete-time domain with coefficients expressed in terms of the coefficients of the original continuous time filter [Wiki]:

$$H(z) = \frac{(b_0K^2 + b_1K + b_2) + (2b_2 - 2b_0K^2)z^{-1} + (b_0K^2 - b_1K + b_2)z^{-2}}{(a_0K^2 + a_1K + a_2) + (2a_2 - 2a_0K^2)z^{-1} + (a_0K^2 - a_1K + a_2)z^{-2}}$$

Normalizing $a_0$and using Direct Form I, the difference equation is expressed as:

$$y[n] = \frac{b_0K^2 + b_1K + b_2}{a_0K^2 + a_1K + a_2}.x[n] + \frac{2b_2 - 2b_0K^2}{a_0K^2 + a_1K + a_2}.x[n-1] + \frac{b_0K^2 - b_1K + b_2}{a_0K^2 + a_1K + a_2}.x[n-2]$$
$$- \frac{2a_2 - 2a_0K^2}{a_0K^2 + a_1K + a_2}.y[n-1] - \frac{a_0K^2 - a_1K + a_2}{a_0K^2 + a_1K + a_2}.y[n-2]$$

Where $K = 2/T$, T is the sampling period which is 10 ns for high frequency waveforms in GERDA. Comparing the transfer function from our model and above equation, the coefficients are evaluated as:

$$b_0 = \frac{1}{C_f} \quad ; \quad b_1 = 0 \quad ; \; b_2 = 0$$

$$a_2 = \alpha \;\; ; \quad a_1 = 1 + \alpha.(\omega_{sum} + \omega_{pre}) \;\; ; \quad a_0 = \alpha.\omega_{sum}.\omega_{pre} + \omega_f$$

Appendix C

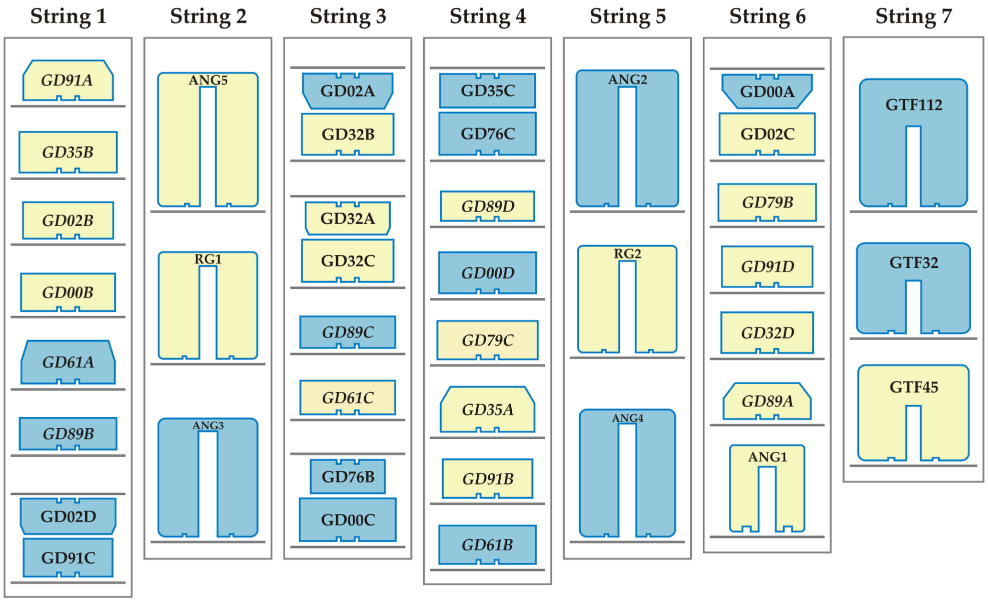

Figure 95: . GERDA detector array in Phase II before the upgrade

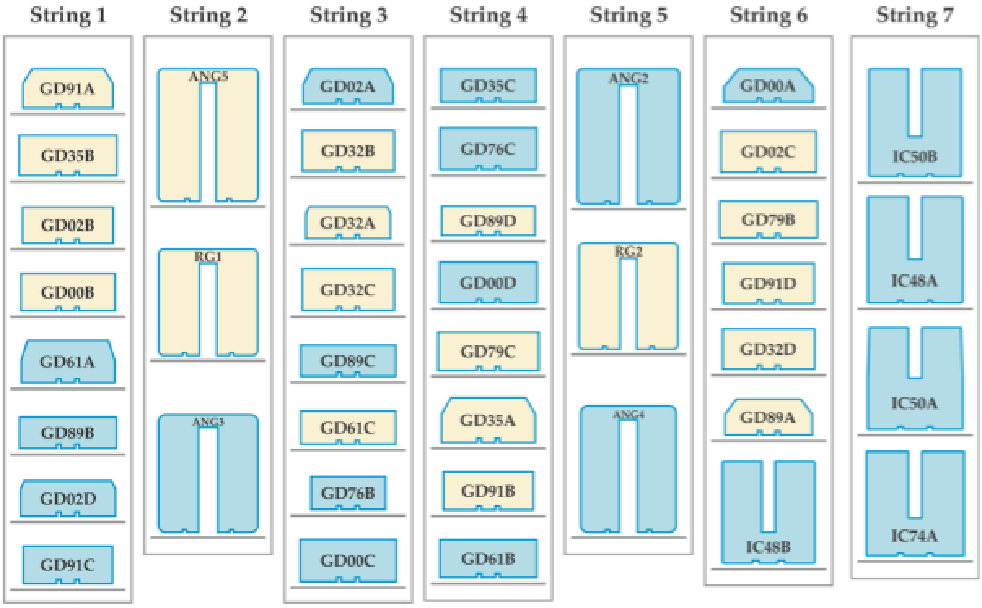

Figure 96: GERDA detector array in Phase II after the upgrade where the non-enriched (GTF series) detectors and ANG1 were replaced by IC detectors.

Acknowledgements

First and foremost, I would like to express my deepest gratitude to Dr. Bernhard Schwingenheuer for his unwavering support and invaluable guidance throughout my PhD journey. His insights and expertise have been instrumental in shaping this work, and his encouragement has continually motivated me to overcome challenges and reach this milestone. I am especially appreciative of his precise suggestions and concerns, which have greatly enhanced the quality of this thesis.

I am also deeply grateful to Prof. Jim Hinton for giving me the opportunity to pursue this PhD. His timely support, along with his pleasant demeanor and patience, has been invaluable throughout this journey. I would like to extend my thanks to Dr. Teresa Marrodán Undagoitia for kindly agreeing to be my second referee; her expertise in rare decay experiments is something I greatly appreciate.

I am particularly grateful to Dr. Yoann Kermaidic for his help in smoothly integrating me into the team and for his invaluable assistance during the initial months of my PhD. His guidance was essential in getting me started and up to speed. I would also like to thank Dr. Simon Sailer for the many enriching discussions over coffee and for his exceptional support with package management and code debugging, which saved me a great deal of time and effort. Additionally, I extend my thanks to Sean Sullivan for the fun discussions and our enjoyable games of Scrabble. I would also like to thank other group members, Prof. Werner Hoffmann, Dr. Thomas Kihm, and Dr. Karl Tasso, for providing their valuable insights during the weekly group meetings.

My heartfelt thanks go to the entire GERDA Collaboration. This experiment, driven by a shared passion for physics, stands as a testament to the collective efforts of numerous individuals. The contributions of every member were integral to this large-scale experimental endeavor and the work presented in this thesis.

A special thanks goes to Ruth Crespo for her tireless efforts in handling administrative tasks—whether it be visa matters or other paperwork, which allowed me to focus on my research. I am truly grateful for your warm and friendly demeanor and everything you do.

I would also like to thank my friends Praveen, Saba, Venky, Apoorva, and Kaustav for making my years in Heidelberg unforgettable. Your companionship brought much joy to this journey and made the years in Heidelberg truly enjoyable.

Finally, I owe my deepest thanks to you, Kalyani. Your constant love and support have been my anchor through the ups and downs of this journey. Thank you for always believing in me and for standing by me through every phase of my doctoral thesis, especially during the final stretch. This achievement would not have been possible without you by my side.